

**PL-TR-96-2016**

**Environmental Research Papers, No. 1186**

---

**WAVEGUIDE EFFECTS OF LARGE-SCALE STRUCTURAL VARIATION,  
ANELASTIC ATTENUATION, AND RANDOM HETEROGENEITY ON SV  
Lg PROPAGATION: A FINITE-DIFFERENCE MODELING STUDY**

Rong-Song Jih

21 DECEMBER 1995

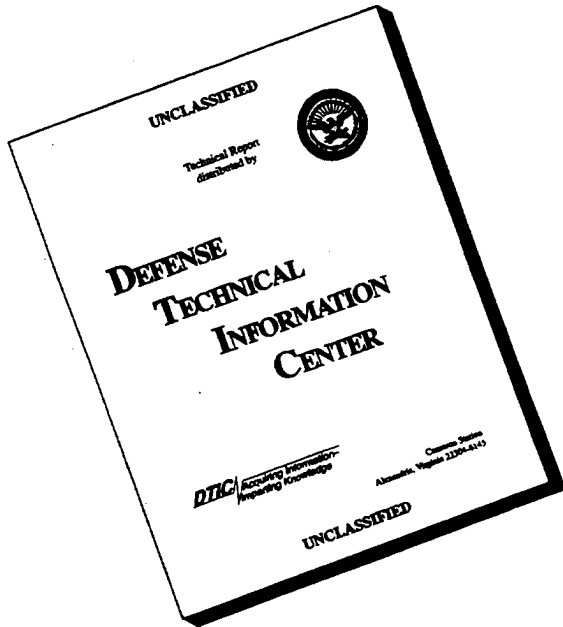
APPROVED FOR PUBLIC RELEASE; DISTRIBUTION UNLIMITED



PHILLIPS LABORATORY  
Directorate of Geophysics  
AIR FORCE MATERIEL COMMAND  
HANSCOM AFB, MA 01731-3010

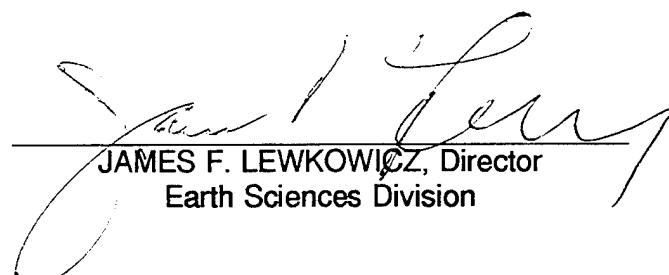
19960712 038

# **DISCLAIMER NOTICE**



**THIS DOCUMENT IS BEST  
QUALITY AVAILABLE. THE  
COPY FURNISHED TO DTIC  
CONTAINED A SIGNIFICANT  
NUMBER OF PAGES WHICH DO  
NOT REPRODUCE LEGIBLY.**

"This technical report has been reviewed and is approved for publication."



JAMES F. LEWKOWICZ, Director  
Earth Sciences Division

This report has been reviewed by the ESC Public Affairs Office (PA) and is releasable to the National Technical Information Service (NTIS).

Qualified requestors may obtain additional copies from the Defense Technical Information Center (DTIC). All others should apply to the National Technical Information Service (NTIS).

If your address has changed, or if you wish to be removed from the mailing list, or if the addressee is no longer employed by your organization, please notify PL/IM, 29 Randolph Road, Hanscom AFB, MA 01731-3010. This will assist us in maintaining current mailing list.

Do not return copies of this report unless contractual obligations or notices on a specific document requires that it be returned.

# REPORT DOCUMENTATION PAGE

Form Approved  
OMB No. 0704-0188

Public reporting burden for this collection of information is estimated to average 1 hour per response, including the time for reviewing instructions, searching existing data sources, gathering and maintaining the data needed, and completing and reviewing the collection of information. Send comments regarding this burden estimate or any other aspect of this collection of information, including suggestions for reducing this burden, to Washington Headquarters Services, Directorate for Information Operations and Reports, 1215 Jefferson Davis Highway, Suite 1204, Arlington, VA 22202-4302, and to the Office of Management and Budget, Paperwork Reduction Project (0704-0188), Washington, DC 20503.

1. AGENCY USE ONLY (Leave blank)			2. REPORT DATE 21 December 1995		3. REPORT TYPE AND DATES COVERED Scientific, Interim, 25 Apr - 24 Oct 1995		
4. TITLE AND SUBTITLE Waveguide Effects of Large-Scale Structural Variation, Anelastic Attenuation, and Random Heterogeneity on SV Lg Propagation: A Finite-Difference Modeling Study			5. FUNDING NUMBERS  PE 35999F      PE 621010 PR TERM      PR 7600 TA GM      TA 09 WU 88      WU 08				
6. AUTHOR(S)  Rong-Song Jih			8. PERFORMING ORGANIZATION REPORT NUMBER  PL-TR-96-2016 ERP, No. 1186				
7. PERFORMING ORGANIZATION NAME(S) AND ADDRESS(ES)  Earth Science Division (GPE) Phillips Laboratory 29 Randolph Road Hanscom AFB, MA 01731-3010			9. SPONSORING / MONITORING AGENCY NAME(S) AND ADDRESS(ES)  HQ AFTAC/TTR 1030 South Highway 1A1 Patrick AFB, FL 32925-6001				
11. SUPPLEMENTARY NOTES  * Supported under AFTAC Project Authorization T/0121			10. SPONSORING / MONITORING AGENCY REPORT NUMBER				
12a. DISTRIBUTION / AVAILABILITY STATEMENT  Approved for Public Release; Distribution Unlimited			12b. DISTRIBUTION CODE				
13. ABSTRACT (Maximum 200 words)  <p><math>L_g</math> is often the most prominent phase on regional seismograms and hence it has been extensively used in various seismic operations: (a) detection and location, (b) source size (earthquake magnitude and explosive yield) estimation, and (c) source type identification (that is, discrimination). However, there have also been many outstanding fundamental questions regarding the excitation and propagation of the <math>L_g</math> phase. This report documents a comprehensive modeling study aimed at quantification of the individual effect of several major factors that affect <math>L_g</math> propagation. Two techniques are specifically designed for this project: [1] a pure <math>L_g</math> wave packet suitable for triggering the linear finite-difference [LFD] calculations, and [2] a simple, causal method to incorporate spatially-varying anelastic attenuation into LFD simulations. A variety of mechanisms responsible for <math>L_g</math> blockage / weakening are carefully evaluated. These mechanisms include [a] large-scale structural variations and discontinuities, [b] anelastic attenuation, and [c] small-scale random heterogeneities. A <math>L_g</math> path-correction procedure is proposed to correct for these effects as well as the geometrical spreading. This procedure has an immediate (that is, operational) application to routine processing of seismic records and it could improve the performance of seismic discriminants based on <math>P/L_g</math> ratios.</p>							
14. SUBJECT TERMS  $L_g$ , Seismic wave propagation, Linear finite-difference method, Blockage, Anelastic attenuation, Q, Random heterogeneity, Path calibration					15. NUMBER OF PAGES 116		
16. PRICE CODE							
17. SECURITY CLASSIFICATION OF REPORT Unclassified		18. SECURITY CLASSIFICATION OF THIS PAGE Unclassified		19. SECURITY CLASSIFICATION OF ABSTRACT Unclassified		20. LIMITATION OF ABSTRACT SAR	

## CONTENTS

SUMMARY .....	1
1. INTRODUCTION .....	3
2. LFD IMPLEMENTATION OF $L_g$ WAVE PACKET .....	5
3. $L_g$ PROPAGATION IN MODELS WITH IRREGULAR WAVEGUIDE GEOMETRY .....	11
4. $L_g$ PROPAGATION IN ANELASTIC MODELS .....	71
5. $L_g$ PROPAGATION IN MODELS WITH RANDOM VELOCITY VARIATION .....	79
6. REMARKS ON OBSERVATIONS OF $L_g$ BLOCKAGE AND A MODEL-BASED CORRECTION PROCEDURE .....	88
7. DISCUSSION AND CONCLUSION .....	91
REFERENCES .....	95
DISTRIBUTION LIST .....	101

## ILLUSTRATIONS

1.	The vertical-component snapshots of $L_g$ wave propagation in a single-layer crustal model taken at a temporal spacing of 10 seconds	7
2.	Synthetic seismogram and corresponding particle motion at five depths for the reference 1-layer model 00	8
3.	Vertical and horizontal seismic sections of $L_g$ displacement synthetics for the reference 1-layer model 00	9
4.	Vertical and horizontal seismic sections of $L_g$ displacement synthetics recorded at a depth of 10 km for the reference 1-layer model 00	10
5.	Five of the canonical crustal models tested in this study (models 00, 0A, 0Aa, 0B, and 0Ba)	12
6.	Same as Figure 5 except for models 0C, 0Ca, 0D, 0Da, and 0Db	13
7.	Same as Figure 5 except for models 0E, 0Ea, 0Eb, 0Ec, and 0Ed	14
8.	Same as Figure 5 except for models 0F, 0Fb, 2a, and 4	15
9.	The vertical-component snapshots of $L_g$ wave propagation in the model 0A, which has an abrupt Moho uplift	21
10.	Record sections of surface synthetics for the model 0A	22
11.	Same as Figure 9 except for the model 0Aa, which has a gentle continental-to-oceanic transition	23
12.	Seismic sections of surface synthetics for the model 0Aa	24
13.	The vertical-component snapshots of $L_g$ wave propagation in model 0B in which the crustal thickness decreases abruptly from 30 to 6 km	25
14.	Seismic sections of surface synthetics for model 0B	26
15.	The vertical-component snapshots of $L_g$ wave propagation in model 0Ba with a crustal thickness gradually decreasing from 30 to 6 km	27
16.	Seismic sections of surface synthetics for model 0Ba	28
17.	The vertical-component snapshots of $L_g$ wave propagation in model 0C, which has a sedimentary layer 16 km thick	29

18.	<b>Seismic sections of surface synthetics for model 0C</b>	30
19.	<b>Same as Figure 17 except that the basin has a gentle edge</b>	31
20.	<b>Seismic sections of surface synthetics for model 0Ca</b>	32
21.	<b>Because of the contained structure of the basin, the <math>L_g</math> that tunnels under the edge of the basin eventually recovers characteristics like a multiply bouncing SmS</b>	33
22.	<b>The contained basin structure removes energy from the "on-time <math>L_g</math>" and converts it to the so-called "late <math>L_g</math>" which has the same phase velocity as the reference <math>L_g</math> but is significantly delayed</b>	34
23.	<b>Same as Figure 21 except for an elliptical basin</b>	35
24.	<b>Similar to Figure 22 except for an elliptical basin</b>	36
25.	<b>The vertical-component snapshots of <math>L_g</math> wave propagation in the basin model 0Db</b>	37
26.	<b>Similar to Figure 22 except that a thin, slow sedimentary layer is added</b>	38
27.	<b>The vertical-component snapshot of <math>L_g</math> wave propagation in model 0E with a thickened crust</b>	39
28.	<b>Seismic sections of model 0E, which has a thickened crust</b>	40
29.	<b>The vertical-component snapshots of <math>L_g</math> wave propagation in model 0Ea with a thickened crust</b>	41
30.	<b>Seismic sections of model 0Ea, which has a thickened crust</b>	42
31.	<b>The vertical-component snapshots of <math>L_g</math> wave propagation in model 0Eb, with a thickened crust</b>	43
32.	<b>Seismic sections of model 0Eb, which has a thickened crust</b>	44
33.	<b>The vertical-component snapshots of <math>L_g</math> wave propagation in model 0Ec, with a thickened crust</b>	45
34.	<b>Seismic sections of model 0Ec, which has a thickened crust</b>	46
35.	<b>The vertical-component snapshots of <math>L_g</math> wave propagation in model 0Ed, with a thickened crust</b>	47

36.	<b>Seismic sections of model 0Ed, which has a thickened crust</b>	48
37.	<b>The vertical-component snapshots of <math>L_g</math> wave propagation in model 0F, which has both a sedimentary basin and a Moho uplift</b>	49
38.	<b>Seismic sections of model 0F, which has a Moho uplift and a sedimentary basin</b>	50
39.	<b>The horizontal-component snapshots of <math>L_g</math> wave propagation in model 0Fa which has both a sedimentary basin and a Moho uplift</b>	51
40.	<b>Seismic sections of model 0Fa, which has a Moho uplift and a sedimentary basin</b>	52
41.	<b>The horizontal-component snapshots of <math>L_g</math> wave propagation in model 0Fb, which has two sedimentary layers and a Moho uplift</b>	53
42.	<b>Seismic sections of model 0Fb, which has a Moho uplift and two sedimentary layers</b>	54
43.	<b>The vertical-component snapshots of <math>L_g</math> wave propagation in model 0Fc which has two sedimentary layers and a Moho uplift</b>	55
44.	<b>Seismic sections of model 0Fb, which has a Moho uplift and two sedimentary layers</b>	56
45.	<b>The vertical-component snapshots of <math>L_g</math> wave propagation of model 2, which has a flat Moho and a moderate free-surface topography</b>	57
46.	<b>Seismic sections of model 2, which has a moderate free-surface topography</b>	58
47.	<b>The vertical-component snapshots of <math>L_g</math> wave propagation of model 2a, in which the Moho is fully compensated</b>	59
48.	<b>Seismic sections of model 2a, which has a moderate free-surface topography and a fully compensated Moho</b>	60
49.	<b>The vertical-component snapshots of <math>L_g</math> wave propagation of model 3</b>	61
50.	<b>Seismic sections of model 3, which has a moderate free-surface topography and a flat Moho</b>	62
51.	<b>The vertical-component snapshots of <math>L_g</math> wave propagation of model 3a, in which the Moho is fully compensated</b>	63
52.	<b>Seismic sections of model 3a, which has a moderate free-surface topography and a fully compensated Moho</b>	64

53.	The vertical-component snapshots of $L_g$ wave propagation of model 4	65
54.	Seismic sections of model 4, which has a trapezoidal topography and a fully compensated Moho	66
55.	Vertical-component synthetic seismograms recorded at 3 depths (0 km, 10 km, and 40 km) and started at 20 seconds for models 00, 0A, 0Aa, 0B, and 0Ba, respectively	67
56.	Same as Figure 55 except for models 0C, 0Ca, 0D, 0Da, and 0Db	68
57.	Same as Figure 55 except for models 0E, 0Ea, 0Eb, 0Ec, and 0Ed	69
58.	Same as Figure 55 except for models 0F, 0Fa, 0Fb, 2a, and 4	70
59.	The vertical-component snapshots of $L_g$ wave propagation in an anelastic mode	75
60.	Seismic sections of model 0Qd,122 which has an attenuating body 100 km long, 30 km thick, with $Q_0(L_g) = 263$	76
61.	Synthetic seismograms recorded at 3 depths (0 km, 10 km, and 40 km) after crossing an anelastic zone 100 km wide and 30 km thick for five attenuative models	77
62.	Similar to Figure 59 except a 15 km-thick attenuative layer	78
63.	The vertical-component snapshots of $L_g$ wave propagation in a single-layer model with a heterogeneous portion 100 km long and 30 km thick embedded in it	82
64.	Seismic sections of the model 0Y, 10%	83
65.	The vertical-component snapshots of $L_g$ wave propagation in a single-layer model with a heterogeneous portion 100 km long and 30 km thick embedded in it	84
66.	Seismic sections of the model 0Y,20%	85
67.	Synthetics recorded at 3 depths (0 km, 10 km, and 40 km) after crossing a heterogeneous zone 100 km wide and 30 km thick	86
68.	Regressing the $L_g$ transmission coefficient, $S_n/L_g$ amplitude ratio, far-P/ $L_g$ amplitude ratio, and far-S/ $L_g$ amplitude ratio	87

## **TABLES**

1.	<b>Major Structural Feature(s) of Each Model</b>	11
2.	<b><math>L_g</math> Propagation Statistics of Deterministic Models</b>	19
3.	<b><math>L_g</math> Propagation Statistics of 7 Anelastic Models</b>	74
4.	<b><math>L_g</math> Propagation Statistics of Random Models</b>	80
5.	<b>Observed <math>L_g</math> Blockage/Weakening and Proposed Mechanisms</b>	88

## ACKNOWLEDGEMENTS

This project benefited from discussion with Bob Blandford (AFTAC), Dave Harkrider (BC), Anton Dainty (PL), Dave Russell (AFTAC), Keith McLaughlin (S-Cubed), and Howard Patton (LLNL). The  $L_g$  eigenfunctions needed to synthesize the pure  $L_g$  wave packet are generated with Bob Herrmann's (1987) software. The PSLIB PostScript library released by Paul Wessel (HIG) and Walter Smith (Scripps) has been used in generating most of the figures. This study was supported by Air Force Technical Applications Center. The views and conclusions contained in this report are those of the author and should not be interpreted as representing the official policies, either expressed or implied, of the U.S. Air Force or the U.S. Government.

## SUMMARY

Many empirical studies have found evidence that abrupt thinning of the crust can weaken the  $L_g$  phase, and that contained sedimentary basins or mountain ranges on the path can completely or partially block the phase. Theoretical (modeling) studies can provide insights for better understanding and interpretations of the physical mechanisms involved (Blandford *et al.*, 1992). This study attempts to quantitatively predict the waveguide effects using extensive two-dimensional linear elastic ( $P$ - $SV$ ) finite-difference [LFD] calculations. Miscellaneous waveguide effects are analyzed and compared, both qualitatively and quantitatively, through visualization and spectral analysis. A pure  $L_g$  wave packet is injected into a stratified portion of the grid as the reference initial condition to trigger all LFD calculations for a suite of heterogeneous crustal structures. An obvious advantage of this approach is that the effects due to different types of heterogeneity on  $L_g$  phase can be isolated and evaluated easily. Each model contains a laterally heterogeneous crust superimposed on the homogeneous mantle. The heterogeneities examined include large-scale lateral structural variations in the crustal waveguide (such as Moho uplift, crustal thickening, rugged free-surface topography, embedded thick sedimentary layers, etc.), anelasticity, and small-scale random heterogeneity.

The LFD results demonstrate that indeed both abrupt changes in the Moho topography and a thick contained sedimentary layer can cause  $L_g$  blockage primarily through strong  $L_g$ -to- $S_n$  conversions (with actually different physical mechanisms). Alluvial basin structures cause strong reverberations as well as very strong  $L_g$ -to- $R_g$  conversions. If the principle of seismic reciprocity is invoked,  $R_g$ -to- $L_g$  conversion could be an important mechanism of  $L_g$  excitation for certain structures. Unlike the case of  $R_g$  waves, a moderate free-surface topography alone does not seem to affect  $L_g$  propagation as much as do other types of heterogeneity. Anelasticity and small-scale random heterogeneity can also explain the  $L_g$  blockage. An RMS velocity variation of 8 percent in the whole crust is equivalent to a  $Q_0(L_g)$  of about 270, which would be sufficient to reduce the peak amplitude of 1Hz  $L_g$  waves by 30 percent for every 100 km it traverses. However, LFD calculations also indicate that these mechanisms exhibit some systematic differences in the couplings of  $L_g$  into other phases. Thus, identifying the actual mechanism responsible for the blockage along a specific path is possible.

---

Received for publication 21 December 1995.

# WAVEGUIDE EFFECTS OF LARGE-SCALE STRUCTURAL VARIATION, ANELASTIC ATTENUATION, AND RANDOM HETEROGENEITY ON SV Lg PROPAGATION: A FINITE-DIFFERENCE MODELING STUDY

## 1. INTRODUCTION

The most prominent regional phase generated by shallow events is the  $L_g$  phase identified by Press and Ewing (1952). The  $L_g$  phase receives considerable attention in recent years because of its potential use in yield estimation (e.g., Nuttli, 1986) and discriminating between earthquakes and explosions at regional distances (e.g., Blandford, 1981; Pomeroy *et al.*, 1982). Based on empirical observations, RMS  $L_g$  has been recognized as a stable relative-yield indicator (Patton, 1988; Hansen *et al.*, 1990). However, it is also recognized that  $L_g$ , like  $R_g$ , is sensitive to changes in structure along its path, which can have deleterious effects on any role as a discriminant (see Lynnes and Baumstark, 1991) or magnitude measure (see Jih and Lynnes, 1993), unless the propagation effects are accurately accounted for. Numerous studies have used the sensitivity of  $L_g$  to structural effects to map regions of anomalous propagation and to try to associate them with crustal structure. Bias in  $L_g$ -based magnitude measurements were reported by Gregersen (1984) in Greenland. Very low  $L_g/S_n$  amplitude ratios have been observed after crossing the Tibetan plateau (Ruzaikin *et al.*, 1977), the North Sea grabens (Gregersen, 1984; Kennett *et al.*, 1985), the Caspian Sea, or the Black Sea (Levshin and Berteussen, 1979; Kadinsky-Cade *et al.*, 1981). Chinn *et al.* (1980) (and Lynnes and Baumstark, 1991) observed that the efficiency of the  $L_g$  propagation is better for paths parallel to the structural trend than for paths in the perpendicular direction. Earlier studies (Press and Ewing, 1952; Oliver and Ewing, 1957; Savarensky and Valdner, 1960) have established that  $L_g$  does not propagate through crust overlain by water deeper than 2 km. On the other hand, propagation across a marginal sea of continental shelf does not completely quench  $L_g$ , but can reduce its amplitude. Baumgardt (1991) compared the crustal cross-sections for  $L_g$  propagation, and he found that the  $L_g$  blockage correlates with thick sediment very well. Basically, his observation is that paths that do not cross basins or for which sediments do not vary by greater than 3 km exhibit little or no  $L_g$  blockage and scattering. Baumgardt (1991) also identified paths for which the surface elevations and crustal thickness change substantially, and yet  $L_g$  propagates efficiently. Thus his observations suggest that the near-surface sediment-thickness variations seem to correlate more strongly with  $L_g$  blockage than do the crustal-thickness variations. Zhang and Lay (1994) used surface topography as a manifestation of the varying crustal structures. They found a strong correlation between  $S_n/L_g$  ratios for Eurasian explosions and roughness or mean altitude of the topography along the path, based on a meager data set.

Despite the long-time interest, there remain many fundamental questions about the excitation and propagation of  $L_g$  waves phases to be answered. Numerical modeling of the  $L_g$  waves (and other regional phases) would complement the empirical studies by providing more accurate interpretations and better insight of the underlying physics. Theoretical studies of  $L_g$  propagation across continental margins have been conducted by Kennett (1986a), Maupin (1989), Regan and Harkrider (1989), Cao and Muirhead (1993), and Gibson and Campillo (1994), using different techniques. A simple geometrical ray theory can be used to predict the kinematic property in a qualitative manner, as Kennett (1986a) has illustrated, but would fail to explain the dynamic properties for complex media. Kennett (1986b, 1989ab) used a modal summation to investigate  $L_g$  propagation in stratified and weakly heterogeneous media. Mitchell and Hwang (1987) computed multi-mode synthetics for 1-D models with various thickness of low-Q sediments. Regan and Harkrider (1989) used a hybrid of propagator matrix and the finite-element [FE] methods to model the  $SH-L_g$ -wave propagation. Cao and Muirhead (1993) applied a 2-dimensional P-SV finite-difference method to explore  $L_g$  blockage and argue that a water column over the crust is an important factor in blocking  $L_g$  propagation. Gibson and Campillo (1994) applied both the dynamic ray tracing and the boundary-integral equation methods to model  $L_g$  blockage in the west Pyrenees Range, near the French-Spanish border. They suggest that the unmodeled scattering by small-scale features within the lower crust is the reason for the observed blockage.

In this study the two-dimensional linear elastic ( $P-SV$ ) finite-difference [LFD] method is utilized to model the propagation and scattering of  $L_g$  waves in a suite of crustal models. Each model contains a laterally heterogeneous crust superimposed on the homogeneous mantle. The heterogeneities examined include anelasticity, random velocity variation, rugged interfaces, rugged free-surface topography, as well as embedded thick sedimentary layers. The pure  $L_g$  wave packet is injected into a stratified portion of the LFD grid as the reference initial condition to trigger all LFD calculations. An obvious advantage of this approach is that the effect due to different types of heterogeneity on the  $L_g$  phase can be easily isolated and evaluated. A number of different output formats are available from the LFD simulation. In fact, one of the advantages of the LFD method (and the finite-element method) is the ability to save particle displacements for any number of receivers in the grid and for all times. A particularly informative way to view wave propagation through the models is by using numerical Schlieren diagrams, or "snapshots". Wavefield snapshots are extensively used as a visualization aid throughout the study.

The procedure of implementing a pure  $L_g$  wave packet is described in Section 2 and validated with a reference crustal model. LFD experiments are then conducted with a suite of canonical models representing a variety of crustal structures. The geometrical effects of various structures on  $L_g$  propagation are analyzed, both qualitatively and quantitatively. In Sections 4 and 5, similar analyses are conducted for anelastic and random models, respectively. All three major categories of structures are compared and equated, regarding their roles in causing  $L_g$  blockage and the coupling of  $L_g$  into other

phases. A brief review on the reported observations of  $L_g$  blockage is given in Section 6. Finally, a quantitative way of describing  $L_g$  blockage is explored, and an improved amplitude/magnitude correcting procedure is presented, which includes a correction to account for the geometrical blockage.

## 2. LFD IMPLEMENTATION OF $L_g$ WAVE PACKET

The LFD method has the advantage that the solution contains all conversions and all orders of multiple scattering. It permits examinations of fairly general models with arbitrary complex variations in material properties and free-surface geometry. Furthermore, it does not require many assumptions commonly invoked in other theoretical approaches. The basic limitations to the LFD method are the computational cost and memory requirements. These constrain the size of the grid and the number of time steps that can be calculated in a reasonable time frame. Several non-standard features have been incorporated into the LFD code used in this study:

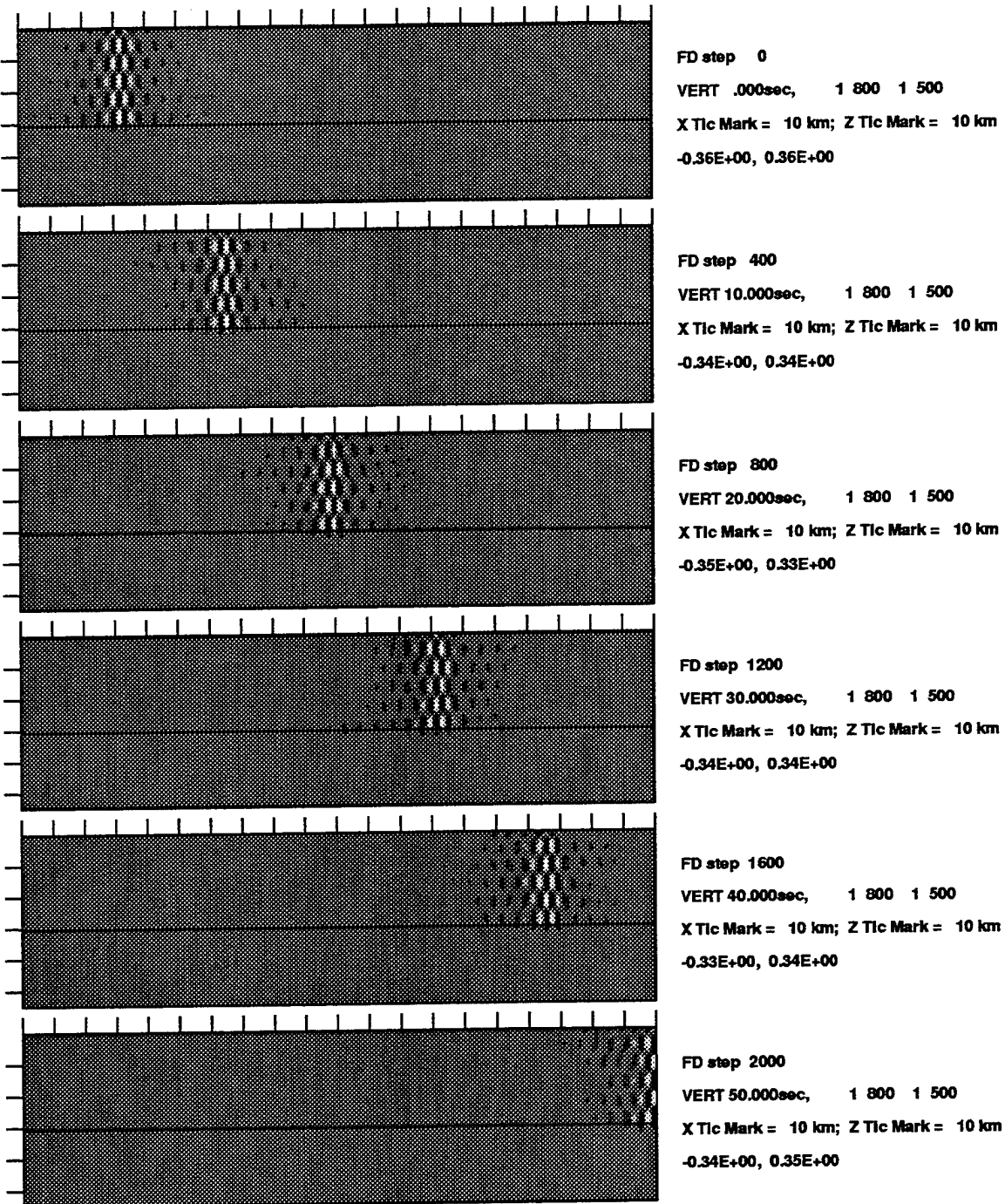
- [1] Explicit boundary conditions for the polygonal free-surface topography.
- [2] The marching-grid technique for stretching the propagation distance in the lateral direction.
- [3] A pure  $L_g$  wave packet suitable for LFD simulations.
- [4] A simple way to incorporate a causal, spatially-varying attenuation operator into LFD simulations.

Detailed descriptions of the explicit boundary conditions and the marching grid technique can be found in Jih *et al.* (1988) and Jih (1993a). Incorporation of the causal, spatially-varying attenuation operator will be described in Section 4 of this report. The algorithm generating the incident  $L_g$  wave packet is analogous to the one Boore (1970) developed for the fundamental-mode Love wave packet. Given a stratified crustal model, the Thomson-Haskell method is used to compute the  $L_g$  dispersion and eigenfunctions associated with this structure. The  $L_g$  eigenfunctions are modulated by a Ricker (1977) wavelet in the wavenumber domain and then converted to the displacement field by the inverse Fourier transform. The resulting wavefield is well localized in both spatial and wavenumber domains, and can be easily embedded in complicated 2-dimensional models (for which other forward-modeling methods may fail) as the initial condition to trigger the LFD simulation. Ever since Boore (1970) outlined the original algorithm in his SH LFD calculations, the same procedure has been adopted frequently in elastic (P-SV) LFD simulations of  $R_g$  propagation/scattering problems. Just a few studies along this line include: Munasinghe and Farnell (1973), Martel *et al.* (1977), Fuyuki and Matsumoto (1980), Fuyuki and Nakano (1984), Levander (1985), Toksoz *et al.* (1986), McLaughlin and Jih (1986, 1987), and Jih (1993b, 1995). The study described herein is an extension to  $L_g$  of the  $R_g$  analysis as presented in McLaughlin and Jih (1986, 1987) and Jih (1993b, 1995). In an earlier study, Jih and McLaughlin (1988) applied the principle of reciprocity to model the excitation of  $L_g$  in various source media. The goal of this study is to investigate various path effects on  $L_g$ , not the excitation.

On real seismograms, the  $L_g$  phase often lacks a clear onset, but it does have a well-defined amplitude maximum with a group velocity around 3.5 km/sec. The  $L_g$  waves are basically the interference of multiply reflected S waves bouncing back and forth between the free surface and the Moho. We can envision that a system of planar S waves is set off at the Moho at equal delay with the same post-critical inclination, while another system of planar S waves is set off at the free surface in a symmetric manner, which corresponds to the bundle of reflected waves. If these two systems of waves (or rays) are properly confined in the same stratified region of the crust, they will establish repetitive reflections (at both the free surface and the Moho) with constructive interferences. By adjusting the time delay between the consecutive S wavefronts, we can obtain a denser (or coarser) interference pattern. The  $L_g$  waves can also be described as the superposition of many higher-mode surface waves which interfere to give the complex observed waveforms. For typical continental paths, the important contributions come from the stationary portions of the group velocity curves for about the first 10 modes up to 1 Hz (Knopoff *et al.*, 1973). These modes correspond to waves trapped in the crustal wave guide.

The  $L_g$  wave packet generated by the procedure described earlier exhibits all these expected features. Figure 1 gives the vertical-component snapshots of  $L_g$  wave propagation in a single-layer crustal model taken at a temporal spacing of 10 seconds. The homogeneous crust is 30 km thick with P- and S-wave velocities of 6.2 and 3.58 km/sec, respectively (see Figure 5). The  $L_g$  wave packet travels at a group velocity of approximately 3.33 km/sec (see Figures 3 and 4), which is appropriate for areas like the western U.S. as suggested by Mitchell and Hwang (1987). Since no scattering mechanism is present, the checkerboard-like pattern due to the constructive interference of repeatedly reflected S waves trapped in the crust is retained at all times (Figure 1). This checkerboard-like pattern undoubtedly indicates that both interpretations of  $L_g$  waves, either as multiply reflected S waves or as higher-mode surface waves, are indeed adequate.

Like the fundamental mode Rayleigh waves ( $R_g$ ), planar body waves incident upon the free surface at an oblique angle also exhibit a retrograde rolling. Since  $L_g$  waves are repetitive reflections (at both the free surface and the Moho) of planar S waves, it shares the same characteristics. At greater depths, however, the particle motion of  $L_g$  is very different from that of  $R_g$ . Figure 2 shows particle motion plots of  $L_g$  synthetics recorded at five depths starting at the free surface and 2 km apart. At the anti-nodes (for example, at 4 km), the particle motion is highly linear.



#### LFD Simulation of Lg Propagation: Model 00

**Figure 1.** The vertical-component snapshots of  $L_g$  wave propagation in a single-layer crustal model taken at a temporal spacing of 10 seconds. The homogeneous crust is 30 km thick with  $P$ - and  $S$ -wave velocities of 6.2 and 3.58 km/s, respectively (see Figure 5). The  $L_g$  wave packet travels at a group velocity of approximately 3.33 km/s. Since no scattering mechanism is present, the checkerboard-like pattern due to the constructive interference of repeatedly reflected  $S$  waves trapped in the crust is retained at all times.

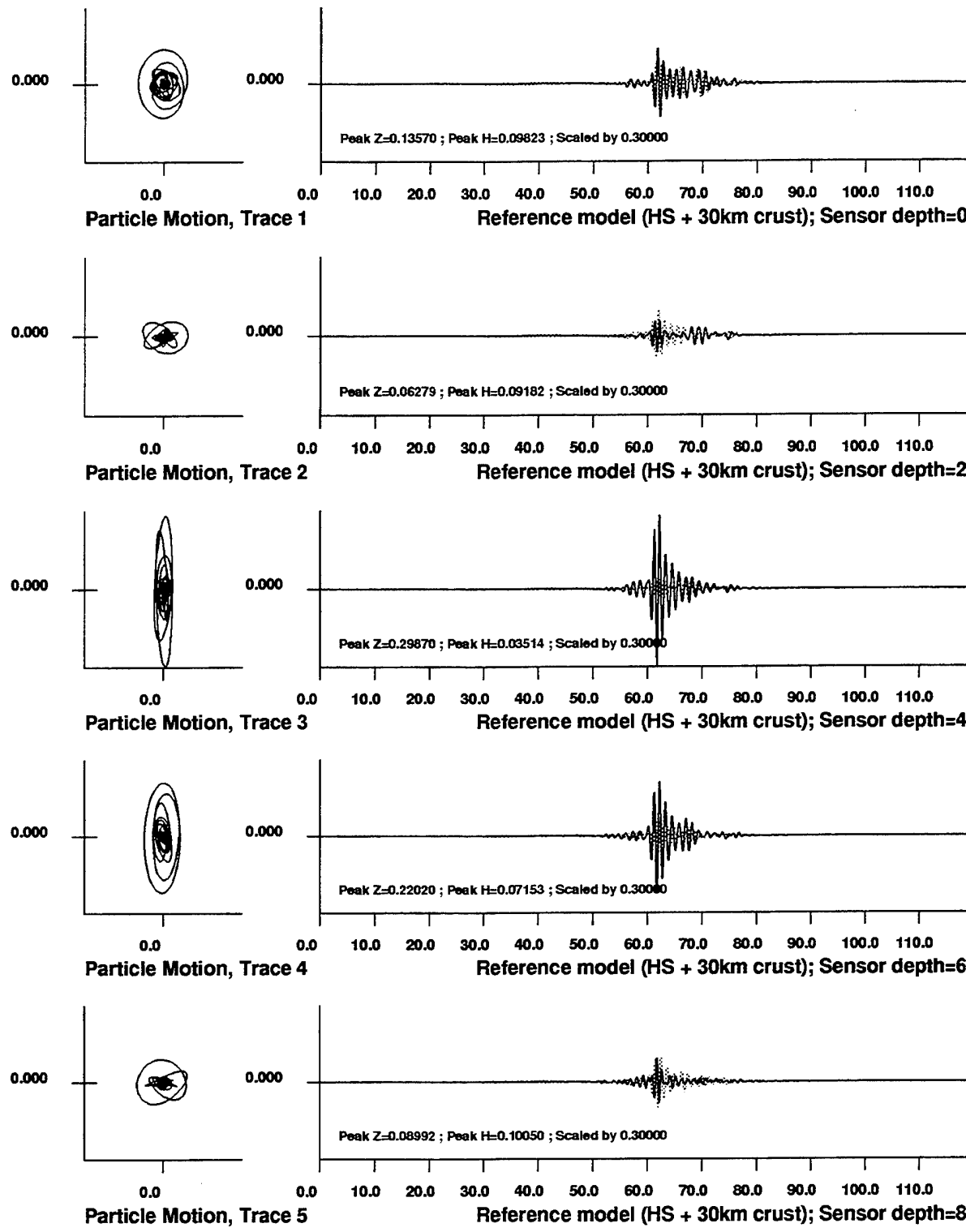
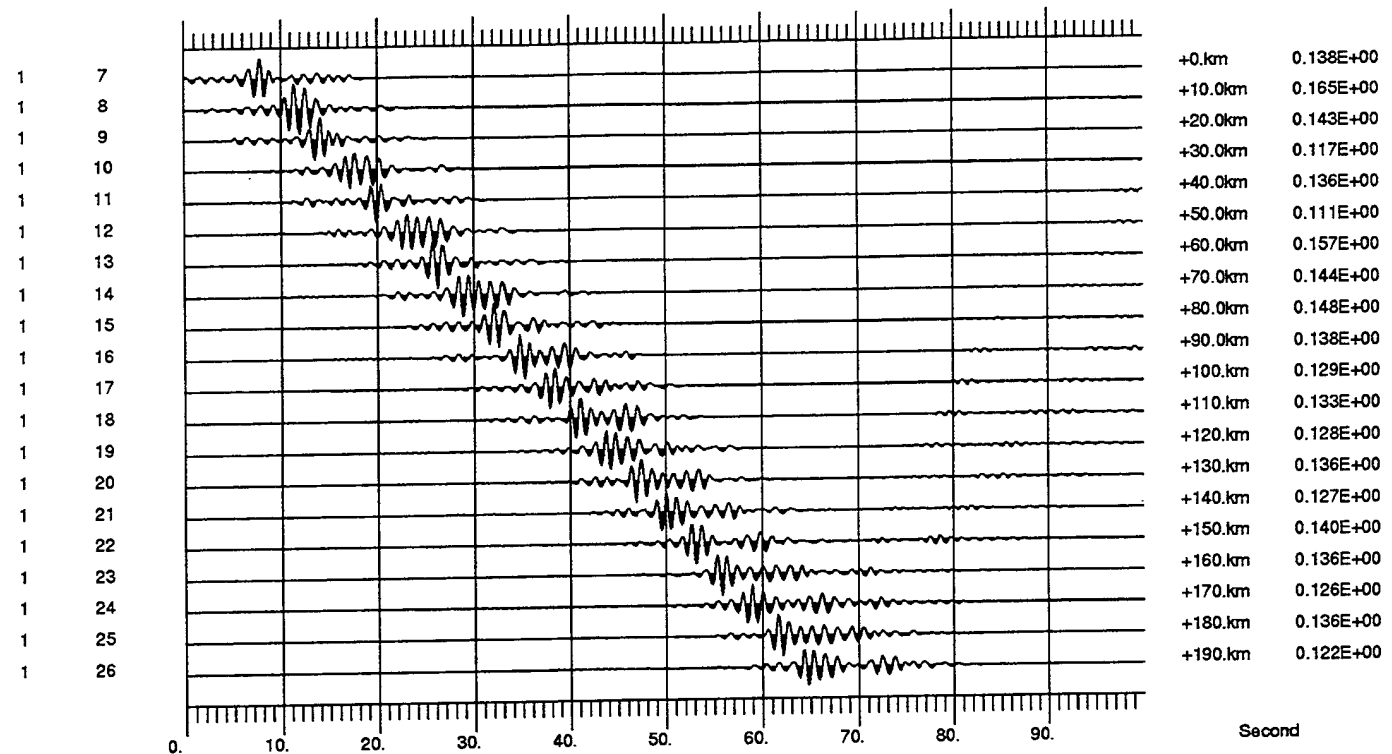


**Figure 2.** Synthetic seismogram (right) and corresponding particle motion (left) at five depths for the reference 1-layer model 00 (see Figure 1). Vertical and horizontal components are shown in solid and dashed lines, respectively. The sensors are 2 km apart. Note the retrograde rolling at the free surface (top) and the highly polarized shear motion at antinodes (for example, at 4-km depth).



Synthetics at 0km Depth, Model 00

VERT, same scale, decimated by 5

+0.km	0.987E-01
+10.0km	0.129E+00
+20.0km	0.106E+00
+30.0km	0.924E-01
+40.0km	0.988E-01
+50.0km	0.795E-01
+60.0km	0.106E+00
+70.0km	0.967E-01
+80.0km	0.107E+00
+90.0km	0.101E+00
+100.km	0.925E-01
+110.km	0.989E-01
+120.km	0.875E-01
+130.km	0.101E+00
+140.km	0.908E-01
+150.km	0.971E-01
+160.km	0.955E-01
+170.km	0.877E-01
+180.km	0.982E-01
+190.km	0.955E-01

Synthetics at 0km Depth, Model 00

HORI, same scale, decimated by 5

Figure 3. Vertical (top) and horizontal (bottom) seismic sections of  $L_g$  displacement synthetics for the reference 1-layer model 00. The  $L_g$  group velocity is about 3.33 (= 190/[65-8]) km/sec.

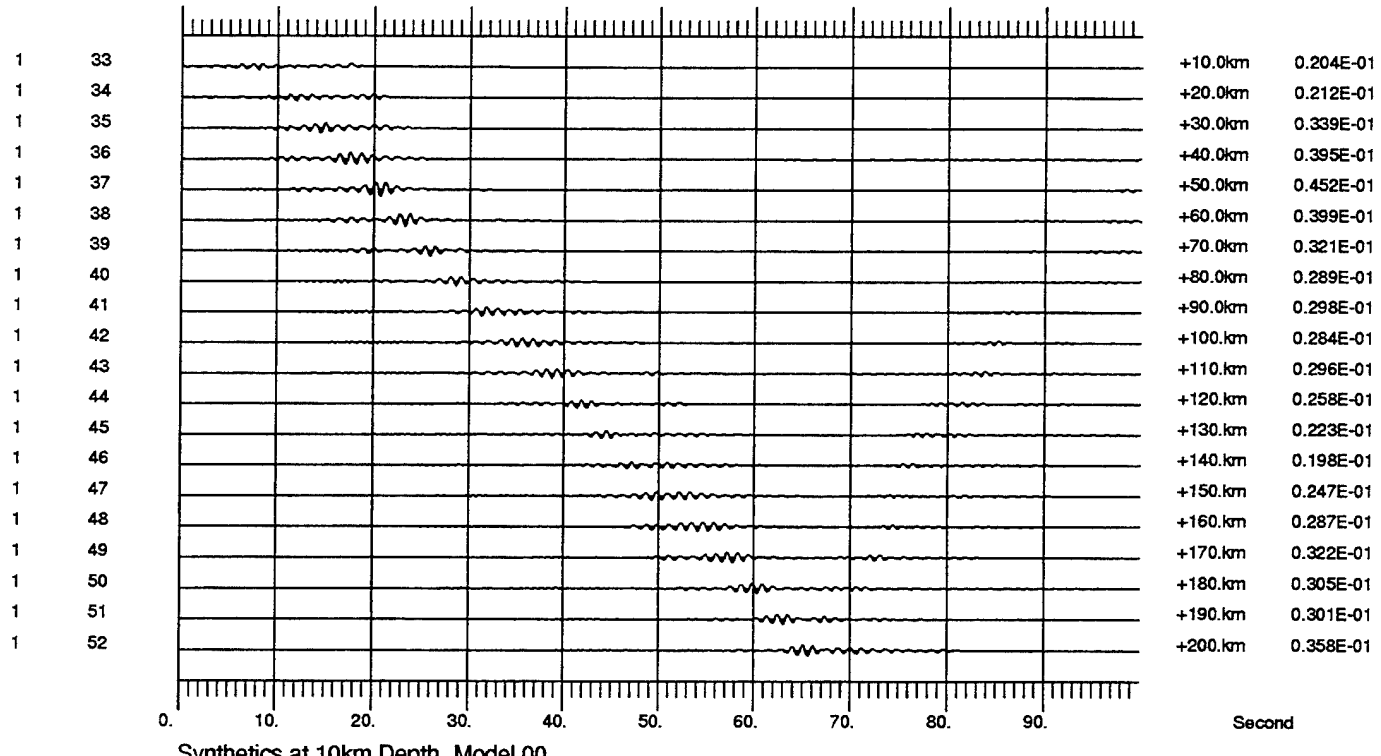
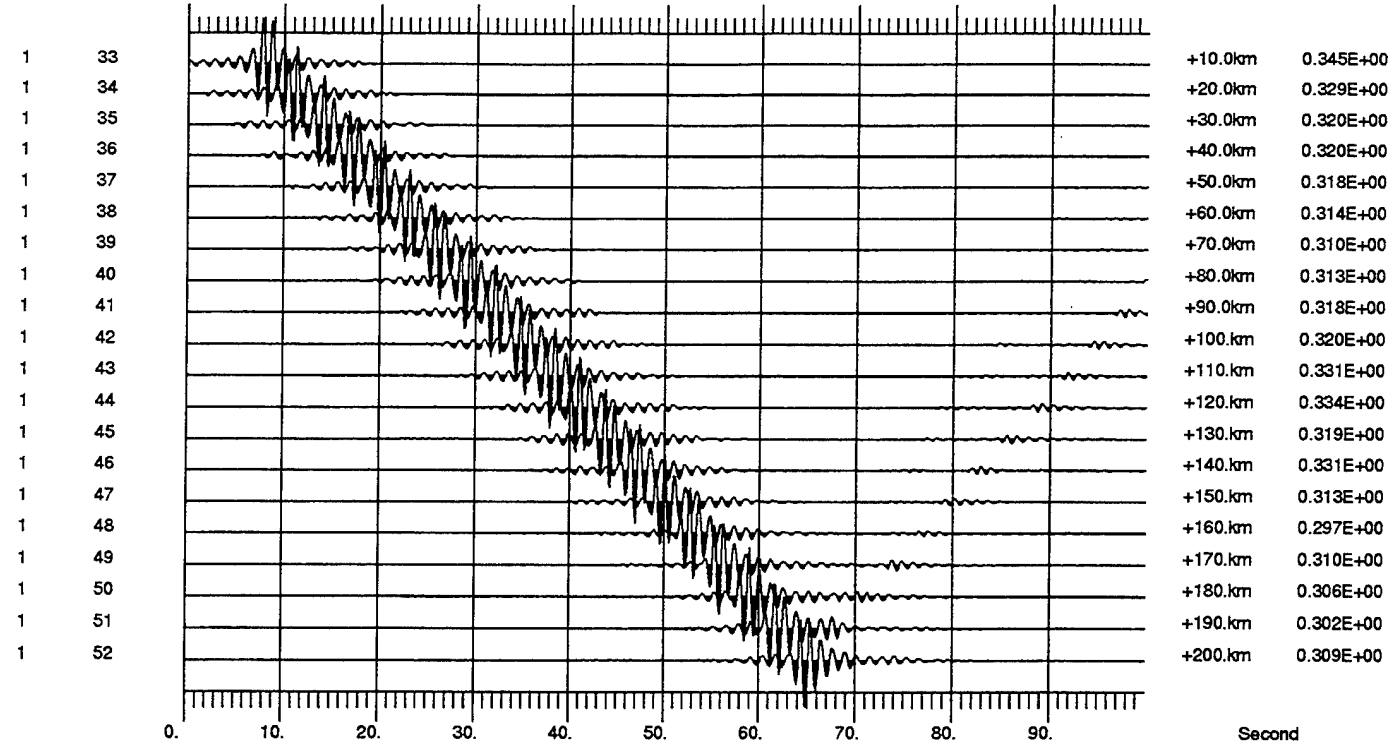


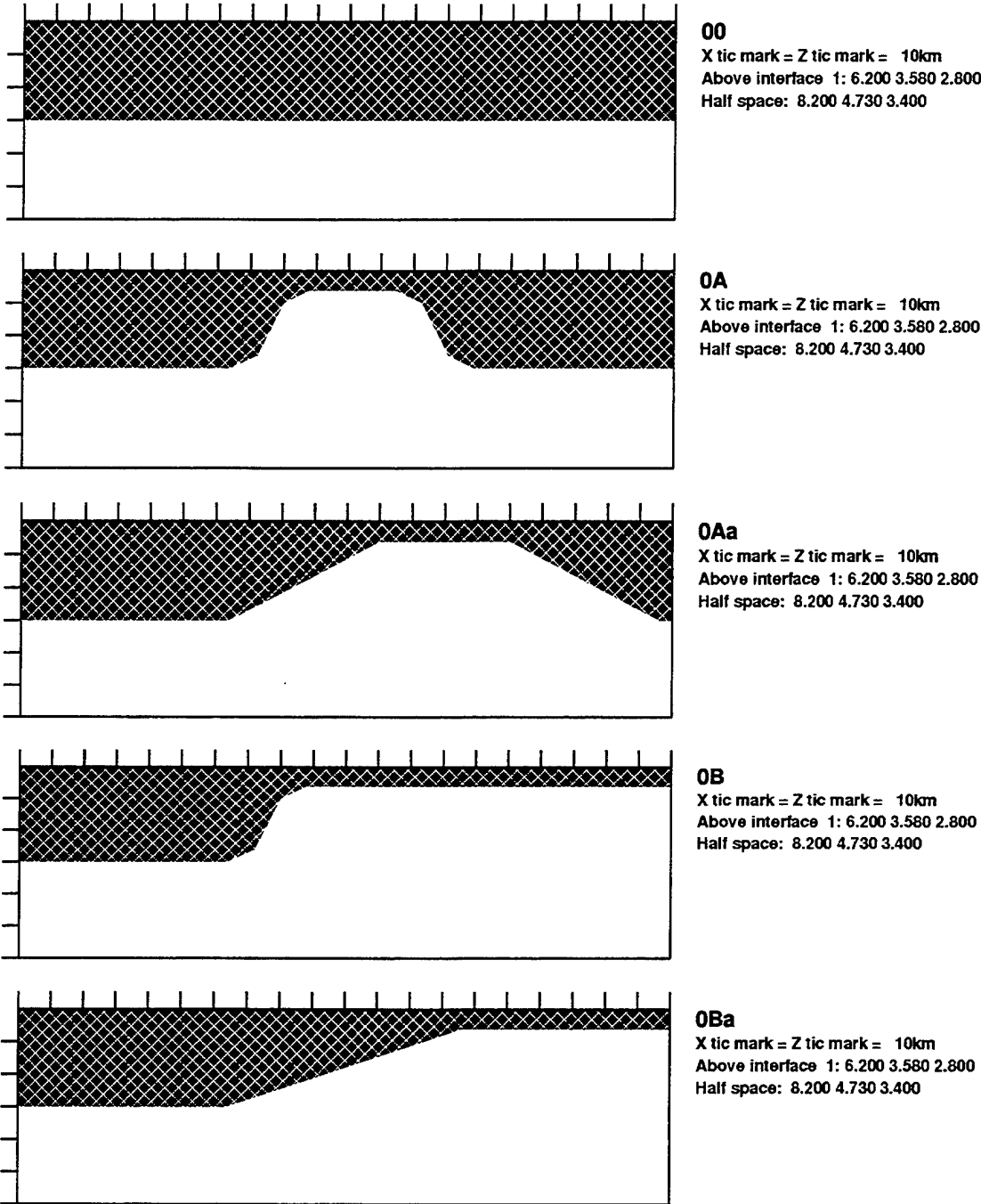
**Figure 4.** Vertical (top) and horizontal (bottom) seismic sections of  $L_g$  displacement synthetics recorded at a depth of 10 km for the reference 1-layer model 00. For the 6th overtone, this depth is very close to an antinode and hence the motion is highly polarized. In later sections of this study, the efficiency of  $L_g$  transmission is measured using a deep receiver to avoid the contamination from the  $R_g$  phase.

### 3. $L_g$ PROPAGATION IN MODELS WITH IRREGULAR WAVEGUIDE GEOMETRY

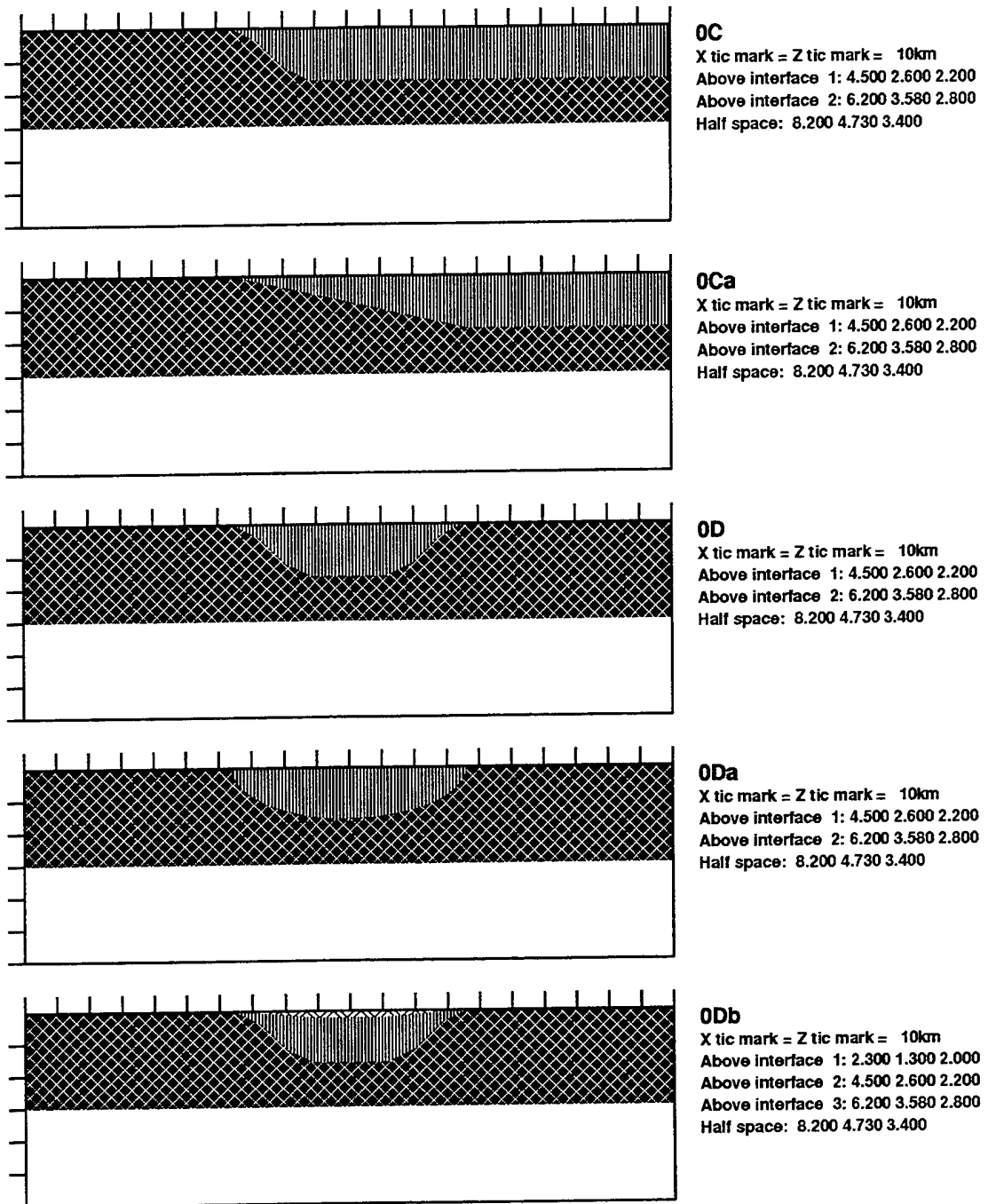
Numerical experiments are first conducted to evaluate the effects of variable crustal thickness, mountainous relief, and sediment thickness on  $L_g$  propagation. In order to isolate these effects, all the crustal models used in the first set of LFD calculations are simple variations of the single-layer crustal model (*viz.* Model 00). Table 1 below gives a brief description of these canonical models. The upper portions of twenty five representative models are shown in Figures 5 through 9.

Table 1. Major Structural Feature(s) of Each Model

00	single-layer (homogeneous) crust of 30 km thick
0A	abrupt Moho uplift (30→6→30)
0Aa	gentle Moho uplift (30→6→30)
0B	a thinning crust (extended Moho uplift) (30→6)
0Ba	similar to 0B, with a gentle transition (30→6)
0C	extended thick sediment
0Ca	similar to 0C, with a gentle, linear transition
0Ca	similar to 0C, with a smooth transition
0D	a contained sedimentary basin
0Da	similar to 0D, with a smooth boundary
0Db	0D + a sedimentary layer
0E	crustal thickening (30→45→30, polygonal Moho)
0Ea	crustal thickening (30→45→30, smooth Moho)
0Eb	crustal thickening (30→40→30, smooth Moho)
0Ec	crustal thickening (30→50→30, smooth Moho)
0Ed	crustal thickening (30→50→30, polygonal Moho)
0F	Moho uplift + a sedimentary basin
0Fa	similar to 0F, with a smooth boundary
0Fb	Moho uplift + a sedimentary basin of slow velocity
0Fc	similar to 0Fb, with a smooth boundary
2	a moderate topography
2a	same topography as 2 with isostatic compensation
3	a moderate topography
3a	same topography as 3 with isostatic compensation
4	thickened crust with a trapezoidal Moho and free surface



**Figure 5.** Five of the canonical crustal models tested in this study. Only the uppermost portion of each model is shown. The actual grid size used in LFD calculation is 1000 by 500, corresponding to 250 km by 125 km. The material parameters of each model are shown on the right. In each LFD experiment, the pure  $L_g$  wave packet is initialized in the stratified portion of the model, near the left edge of the grid. Model 00 is the laterally-invariant reference model.



**Figure 6.** Same as Figure 5 except for models 0C, 0Ca, 0D, 0Da, and 0Db. Both "C" and "D" series of models have a thick sedimentary layer in the structure. The sediment is contained in models of the "D" series.

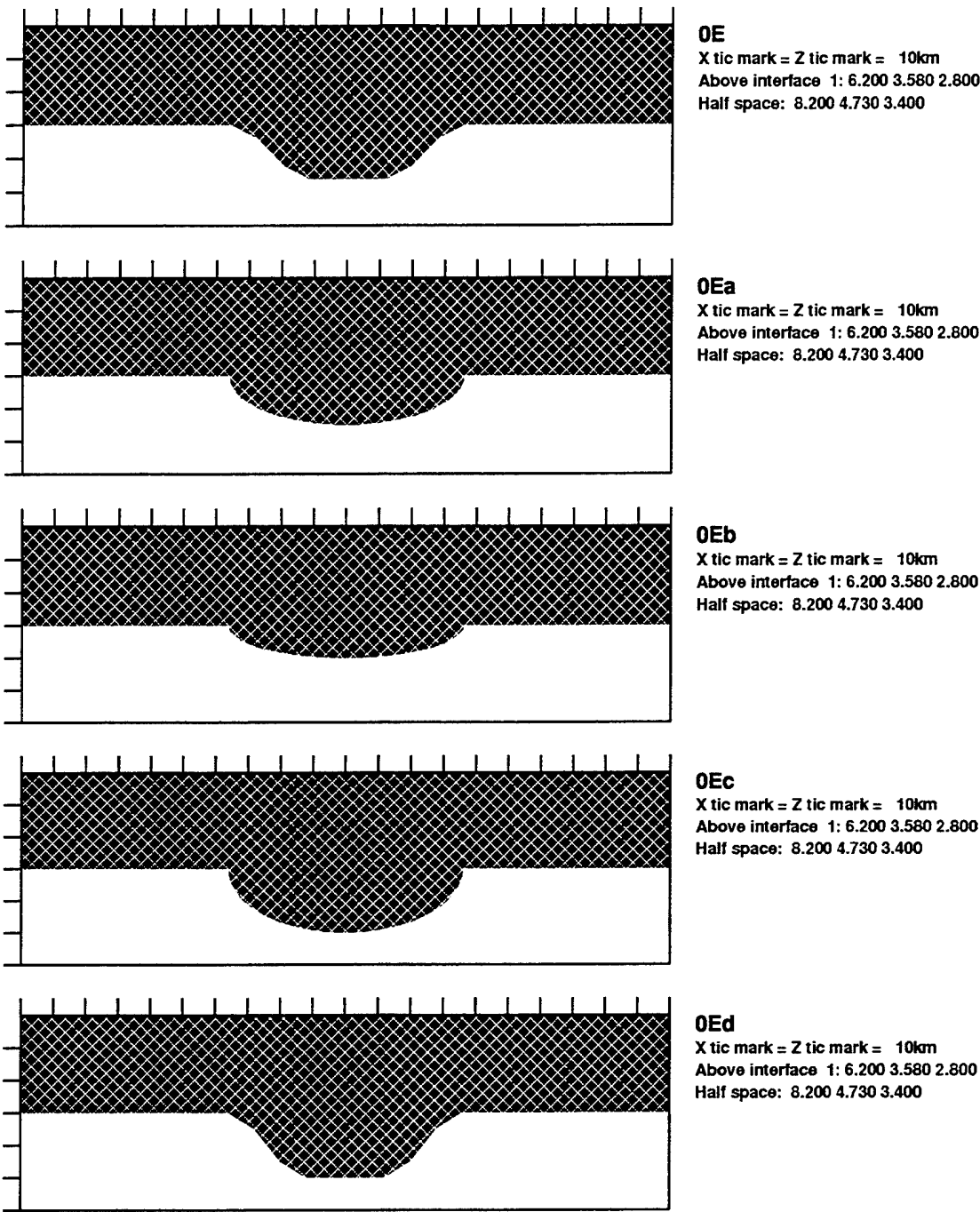


**Figure 7.** Same as Figure 5 except for models 0E, 0Ea, 0Eb, 0Ec, and 0Ed. All "E" series models have thickened crust.

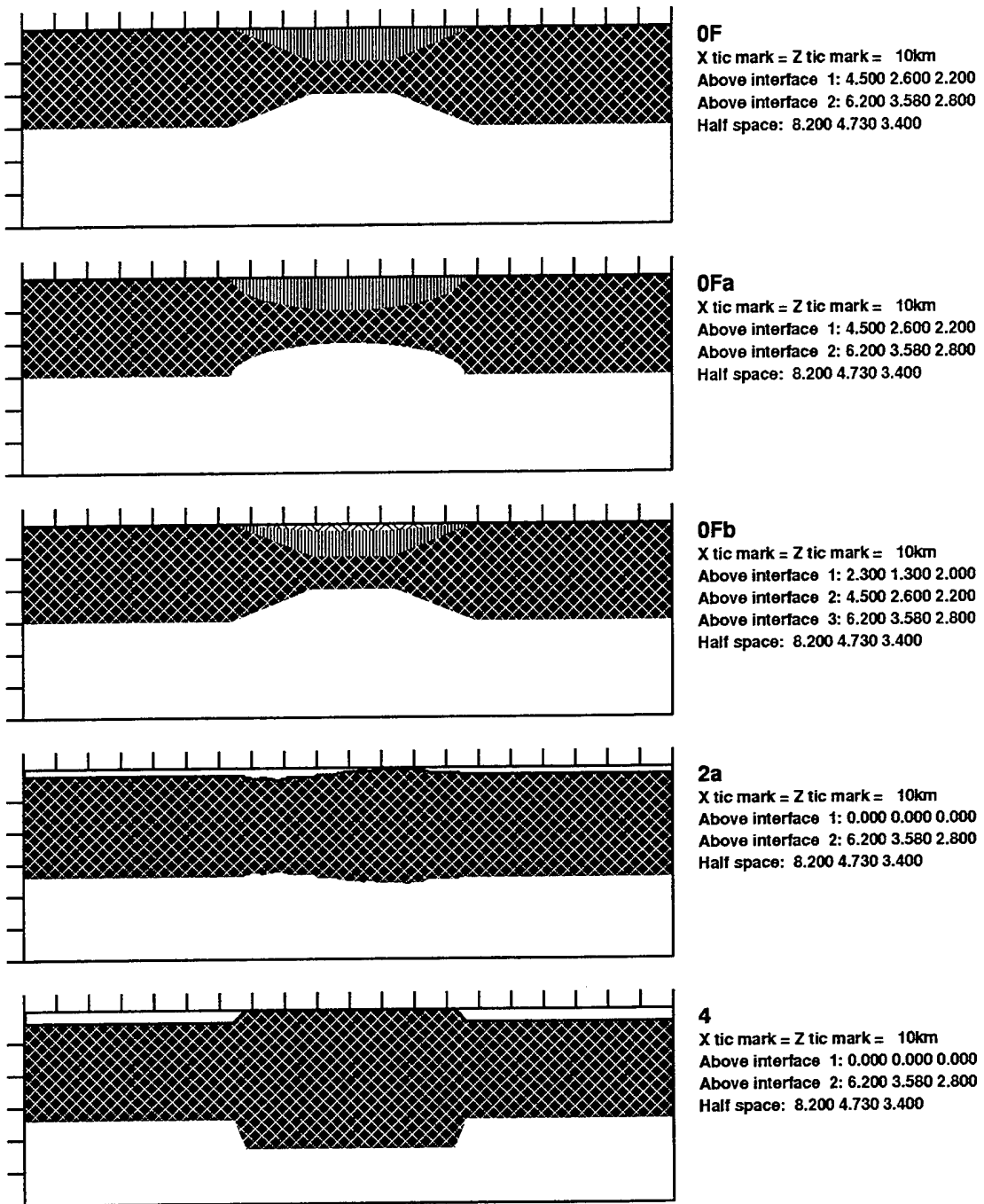


**Figure 8.** Same as Figure 5 except for models OF, OFa, OFb, 2a, and 4. "F" series models are very similar to those of "D" series except that a Moho uplift is added. Model 2a has a moderate topography with a full isostatic compensation. Model 2 (not shown) has an identical free-surface topography with a flat Moho.

Figure 9 shows the vertical-component snapshots of  $L_g$  wave propagation in the model 0A, which has an abrupt Moho uplift. The bulk of the  $L_g$  energy is converted to  $S_n$  at the ascending crust-mantle interface, as shown in Figure 9 at 20 seconds. As a result, the  $L_g$  eigenfunction is broken up and only a fraction of the  $L_g$  energy would enter the oceanic crust. The amplitude of the direct  $L_g$  phase is further reduced, due to the geometric spreading, when it passes the shallow crust to enter the suddenly thickened continental crust (see, at 40 seconds). Record sections of surface synthetics for the model 0A are shown in Figure 10. While  $R_g$  remains intact, the  $L_g$  is effectively blocked, although the oceanic crust is only 50 km long. The majority of  $L_g$  energy is converted to  $S_n$  of which some crosses the descending Moho and re-enters the crust. Due to the post-critical direction, this phase will stay in the crust and become  $L_g$  at a larger distance. This phase is most prominent at 43 seconds on trace 20, and is outside the expected “on-time  $L_g$ ” window.

Model 0Aa is similar to 0A except that a gentle, piecewise-linear Moho is used instead (Figure 11). The  $L_g$ -to- $S_n$  conversion is quite clear at 20 and 30 seconds. The energy which crosses the oceanic crust as the 3rd overtone (see, at 30 seconds) does not touch the free surface as the crust thickens. Instead, it propagates along the descending Moho (see, at 40 and 50 seconds) before it reaches the flat Moho and starts to bounce back to the ground (see, at 60 seconds). The “ $L_g$  blockage” occurs because only  $S_n$  and  $R_g$  could reach ground sensors in the oceanic-to-continental transition zone. Figure 12 shows that the dominating phase of this model is the “early  $L_g$ ” with a group velocity about 4.0 km/sec, followed by  $R_g$  waves with a group velocity of 3.0 km/sec. There is no prominent phase arriving at the expected “on-time”  $L_g$  window of 3.3 km/sec.

Model 0B, shown in Figure 13, has a crust that thins abruptly from a thickness of 30 km to 6 km. As it does in the “A”-series of models, a significant fraction of  $L_g$  energy enters the deeper mantle and detaches from the Moho (see, 30, 40, and 50 seconds of Figure 13). This energy never reaches the surface sensors, and as a result, the most prominent phase is the stabilized 3rd overtone, which stays in the thin crust. Record sections of this model (Figure 14) indicate that no “ $L_g$  blockage” would be observed here since the 3rd overtone has a peak amplitude and a group velocity very similar to those of the “on-time  $L_g$ ” in the reference model. Changing the Moho shape does not affect these observations (see Figures 15 and 16).

All “C”-series models have a sedimentary layer 16 km thick. The sediment slows down the  $L_g$  waves, as expected (Figures 17 and 19). However, this structure does not generate a  $S_n$  conversion as strong as in other models with an irregular Moho or contained basin (Figures 18 and 20).

For models of the “D” series, because of the contained structure of the basin, the  $L_g$  wave that tunnels underneath the basin eventually recovers characteristics like a multiply bouncing SmS (Figure 21). This phase has the same group velocity of the “on-time  $L_g$ ” on those surface sensors co-located

at the bounce points. The amplitude is smaller, however. A more prominent phase comes from the energy that first enters the basin and then leaks out from the ascending edge of the basin. The corner where the pinched basin ends also radiates some body waves. Figure 22 illustrates that the contained basin structure removes some energy of the “on-time  $L_g$ ” and converts it to the so-called “late  $L_g$ ” which has the same phase velocity as the reference  $L_g$  but is significantly delayed. Depending on the location of surface sensors, some seismographs will observe either complete or partial blockage of the “on-time  $L_g$ ”. Figures 23-26 show results for similar structures (models 0Da and 0Db).

Model 0E has a thickened crust and a very strong  $L_g$ -to- $S_n$  conversion occurs along the ascending interface (see, 30, 40, and 50 seconds of Figure 27). Horizontal-component snapshots (not shown) indicate that some focusing of energy occurs at the corner where the Moho turns flat. This corner becomes a secondary point source radiating upgoing body waves. Sensors right above this corner would detect a prominent arrival due to a nearly vertical incidence of shear waves (see traces 16 and 17 of Figure 28). Figures 29-36 show variations of thickened sections of crust (models 0Ea through 0Ed).

“F”-series models have both a sedimentary basin and a Moho uplift. Figure 37 shows the basic geometry. The Moho uplift causes a strong  $S_n$  conversion (see, at 20 seconds of Figure 38). The pinched end of the basin radiates body waves outward, and some of those rays leak into deeper mantle. Figure 39 shows the horizontal-component snapshots of  $L_g$  wave propagation in the model 0Fa which is similar to 0F except for a smooth interfaces. Observations similar to those with the model 0F can be made. The pinched end of the basin radiates body waves outward, and some of those rays leak into deeper mantle (see, at 50 seconds). Some direct P waves are also present (see, at 40 seconds). Direct P waves radiated from the basin’s terminating edge can be seen on the horizontal components of Figure 40. Figure 41-44 show the geometry and results for some other variations (models 0Fb and 0Fc).

Model 2 has a flat Moho and a moderate free-surface topography (Figure 45). The  $L_g$ -to- $S_n$  conversion is relatively weak (see Figure 46). This is very different from the case of  $R_g$  where scattering by rough topography would cause very strong apparent attenuation. Model 2a has a fully compensated Moho added to the model (Figure 47). The fully compensated Moho gives results similar to those from the flat Moho of model 2. Figures 47 through 54 give results from models 2a, 3, 3a, 3a, and 4, which are all similar to model 2.

Figures 55 and 56 display the vertical-component synthetic seismograms recorded at 3 depths (0km, 10km, and 40km) and started at 20 seconds for models 00, 0A, 0Aa, 0B, 0Ba, 0C, 0Ca, 0D, 0Da, and 0Db. Figures 57 and 58 show the same for models 0E, 0F, 0Fa, 0Fc, and 2a starting at time zero. Note that although the “on-time  $L_g$ ” on surface synthetics of models 0B and 0Ba (bottom left) have a peak amplitude in the same order as that of the reference model, they are not the same overtone of the Rayleigh mode. The moderate surface and Moho topography in the model 2a only affect  $L_g$  waveform

characteristics mildly. Note that model 0Fc excites very strong  $R_g$  phase, very similar to the model 0Db. Among all structures tested, "E" series of models (with a thickened crust) excites the strongest  $S_n$  conversion (see Figure 27).

It is interesting to note that all models of the "F" series exhibit significant  $L_g$ -to- $P_g$  conversion. The peak horizontal amplitude on trace No.25 ranges from 10% to 15% of that of the original  $L_g$  wave train. To a lesser extent, models of "C" and "D" series as well as models 0A and 0Ba also generate the same conversion.

For each model, the synthetic seismograms are recorded at three linear arrays at three different depths: 0 km, 10 km, and 40 km. Several parameters are measured to infer the relationship between the major geological/geophysical/geometrical features and possible blockage and  $S_n$  coupling. The amplitude spectrum of a surface synthetic seismogram far away from the heterogeneous structure is computed using a window of 12.8 seconds (512 data points) around the group velocity of 3.33 km/sec. Using the spectrum of model 00 as a reference, the amplitude ratio at 1 Hz is denoted as "BK" in Table 2 to quantify the  $L_g$  blockage. This ratio is also used to compute the equivalent apparent attenuation of the "on-time  $L_g$ ". Both the quality factor  $Q_0$  and the attenuation coefficient  $\gamma$  are printed in Table 2. To measure the total transmitted  $L_g$  energy, a sensor at 10 km depth is used. The spectral amplitude ratio at 1 Hz computed with this sensor is denoted as "T" in Table 2. The converted  $S_n$  energy is measured with a sensor at a depth of 40 km, below the flat Moho. Another sensor, which is near the bottom of the model and under the major heterogeneous feature, records the waveform representing the converted teleseismic energy. Except for the quantity BK, all other ratios are normalized to the 10km-deep synthetic of the model 00 as the reference. The results in Table 2 are sorted by the major structural features of the models. There appear to be some systematic patterns that are very interesting.

Table 2.  $L_g$  Propagation Statistics of Deterministic Models

Model	BK	T	$S_n/L_g$	far-P/ $L_g$	far-S/ $L_g$	$Q_0$	$\gamma$ (1 Hz)
0A	0.349	0.346	0.164	0.110	0.105	91	0.0105
0Aa	0.416	0.689	0.216	0.083	0.087	109	0.0088
0Ab	0.384	0.624	0.233	0.080	0.079	100	0.0096
0B	1.035	—	0.546	0.109	0.103	—	—
0Ba	0.848	—	0.482	0.041	0.044	581	0.0016
0C	0.354	0.790	0.084	0.061	0.048	92	0.0104
0Ca	0.237	0.521	0.076	0.026	0.010	66	0.0144
0Cb	0.307	0.496	0.065	0.051	0.034	81	0.0118
0D	0.595	0.565	0.161	0.075	0.084	185	0.0052
0Da	0.317	0.577	0.185	0.073	0.096	84	0.0115
0Db	0.508	0.409	0.102	0.083	0.086	142	0.0068
0E	0.977	0.779	0.468	0.046	0.051	4136	0.0002
0Ea	0.963	0.723	0.459	0.038	0.082	2534	0.0004
0Eb	0.967	0.649	0.201	0.032	0.050	2821	0.0003
0Ec	0.983	0.719	0.478	0.052	0.070	5558	0.0002
0Ed	0.923	0.741	0.318	0.058	0.039	1191	0.0008
0F	0.228	0.580	0.177	0.058	0.062	65	0.0148
0Fa	0.789	0.595	0.225	0.076	0.084	405	0.0024
0Fb	0.318	0.533	0.157	0.070	0.087	84	0.0115
0Fc	0.473	0.560	0.194	0.078	0.098	128	0.0075
2	1.023	0.574	0.087	0.058	0.127	—	—
2a	1.020	0.717	0.152	0.059	0.138	—	—
3	0.875	0.829	0.091	0.061	0.145	721	0.0013
3a	1.111	0.715	0.133	0.070	0.150	—	—
4	1.738	0.408	0.319	0.050	0.072	—	—

BK: spectral amplitude ratio at 1 Hz of "on-time  $L_g$ " (3.33 km/sec) to that of the reference model.

T: spectral amplitude ratio at 1 Hz of transmitted  $L_g$  (recorded at a depth of 10 km) to that of the reference model.

$S_n/L_g$ : spectral amplitude ratio at 1 Hz of converted  $S_n$  to the reference  $L_g$ .

far-P/ $L_g$ : spectral amplitude ratio at 1 Hz of converted teleseismic P to the reference  $L_g$ .

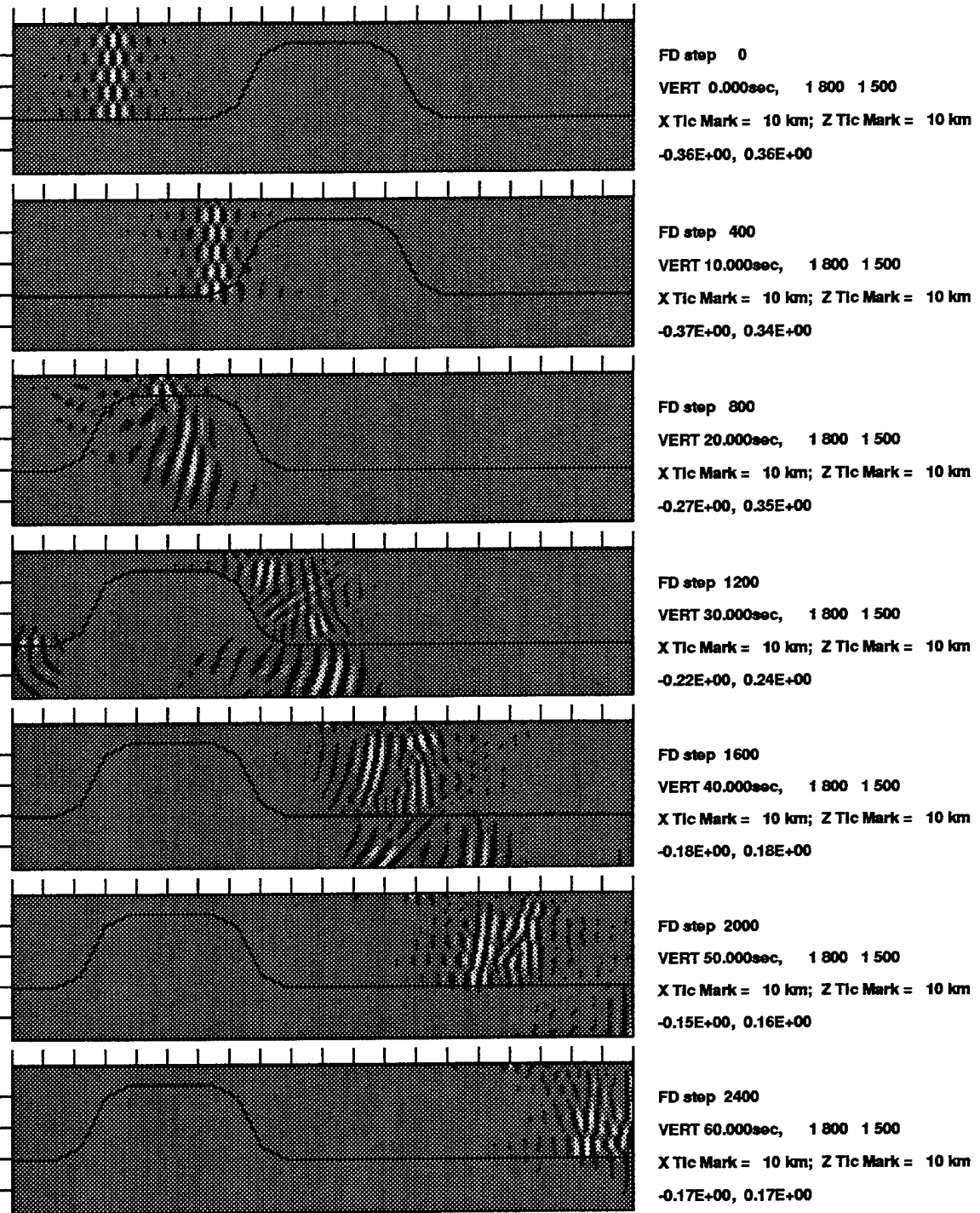
far-S/ $L_g$ : spectral amplitude ratio at 1 Hz of converted teleseismic S to the reference  $L_g$ .

For seismic stations in northern Scandinavia, the 1 Hz  $L_g$  waves from Novaya Zemlya are severely blocked. Based on the coda Q method, Nuttli (1988) deduced a  $Q_0$  value of 252 for the path from Novaya Zemlya to WWSSN station KEV (Kevo, 69.755°N, 27.007°E). Using a joint inversion method with  $L_g$  amplitude measurements, Jih *et al.* (1995) point out that this  $Q_0$  value appears to be appropriate. Assuming that the coda Q method really provides an independent and consistent measure

of  $L_g$  Q, then there should be a  $L_g$ -mb bias of 0.26 magnitude unit [m.u.] between the Eastern U.S. and Novaya Zemlya. The  $Q_0$  value of 252 for station KEV actually includes the gross reduction effects on  $L_g$  amplitude due to both the intrinsic attenuation and the geometrical blockage, of which the latter was not fully studied or documented at the time Nuttl estimated the yield for Novaya Zemlya explosions. The continental path crossing Barents Shelf is a classical example of " $L_g$  blockage" (Baumgardt, 1991). For blockage of the "on-time  $L_g$ " to be noticeable at similar distance, it is reasonable to expect to have a  $Q_0$  value no more than 270, or equivalently, a BK no greater than approximately 0.7.

Using a BK of 0.7 as the threshold, we see that all models of the "A", "C", and "D" series as well as most of the "F" series would block  $L_g$ , while none of the "B" and "E" models or any model with a mild topography would block  $L_g$ . All "E"-type of models, which have a thickened crust, exhibit very little attenuation. Most of the topographic models (that is, models 2, 2a, 3a, and 4) actually exhibit an amplification, instead of reduction, in  $L_g$  amplitude. The thinning of the crust is an important mechanism to block  $L_g$  (Figures 8 and 10), as reported in many observational studies. However, the thinning itself has to be of finite span in the lateral direction. The two "B" series of models either show an amplification or have a BK larger than 0.85 (see Figures 12 and 14).

The comparison of  $L_g$  coupling to teleseismic phases is also described in Table 2. In terms of  $L_g$ -to- $S_n$  conversion, models 0B and 0Ba are the most efficient ones, followed by four models with thickened crust, 0E, 0Ea, 0Ec, and 0Ed. Another "E"-type model, 0Eb, with an elliptical Moho shape as in model 0Ea but only 40 km thick, gives a much weaker  $S_n$  excitation. On the other hand, all these "E" series models have very comparable efficiency in  $L_g$  transmission - either measured at the free surface or at a depth of 10 km. Model 4 has a trapezoidal mountain (5 km high) on the top and a trapezoidal intrusion of 10 km in the bottom of the crust. Thus its overall increase in thickness is identical to that of models 0E and 0Ea. While the level of  $S_n$  conversion is in the same range as other "E" models, the  $L_g$  transmission is actually amplified. If the models are sorted by the corresponding levels of  $S_n$  conversion, we have {0B,0Ba} > {0E,0Ea,0Ec,0Ed} >> 4 > 0A,0Eb > 0F\* > 0D\*,2a,3a > 2,3 > 0C\*.



#### LFD Simulation of Lg Propagation: Model 0A

**Figure 9.** The vertical-component snapshots of  $L_g$  wave propagation in the model 0A, which has an abrupt Moho uplift. The bulk of  $L_g$  energy is converted to  $S_n$  at the ascending crust-mantle interface (see, at 20 seconds). As a result, the  $L_g$  eigenfunction is broken up and only a fraction of the  $L_g$  energy would enter the oceanic crust. The amplitude of the direct  $L_g$  phase is further reduced (due to the geometric spreading) when it passes the shallow crust to enter the suddenly thickened continental crust (at 40 seconds). Although the oceanic crust is only 50 km long, it effectively blocks the  $L_g$ .

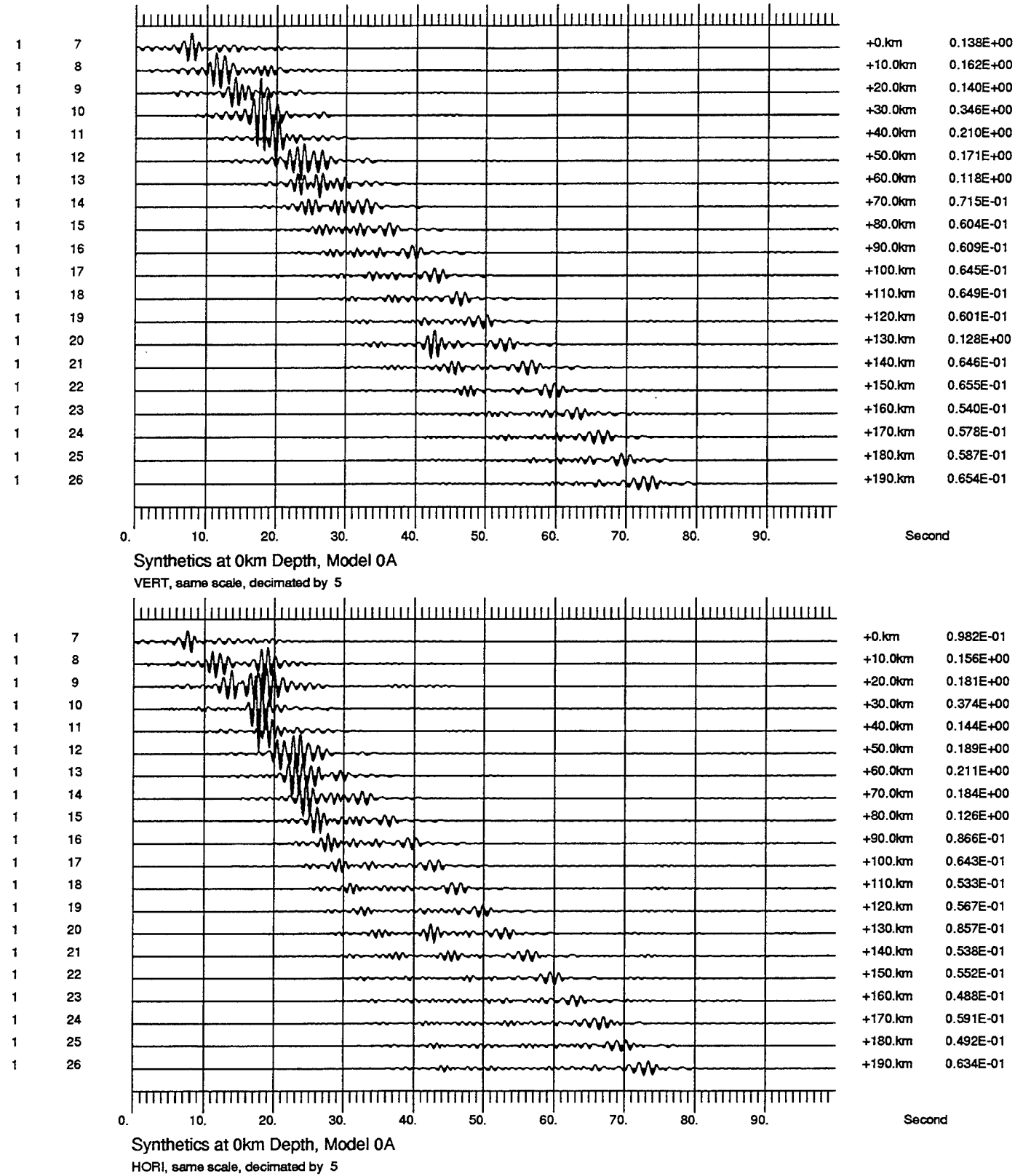
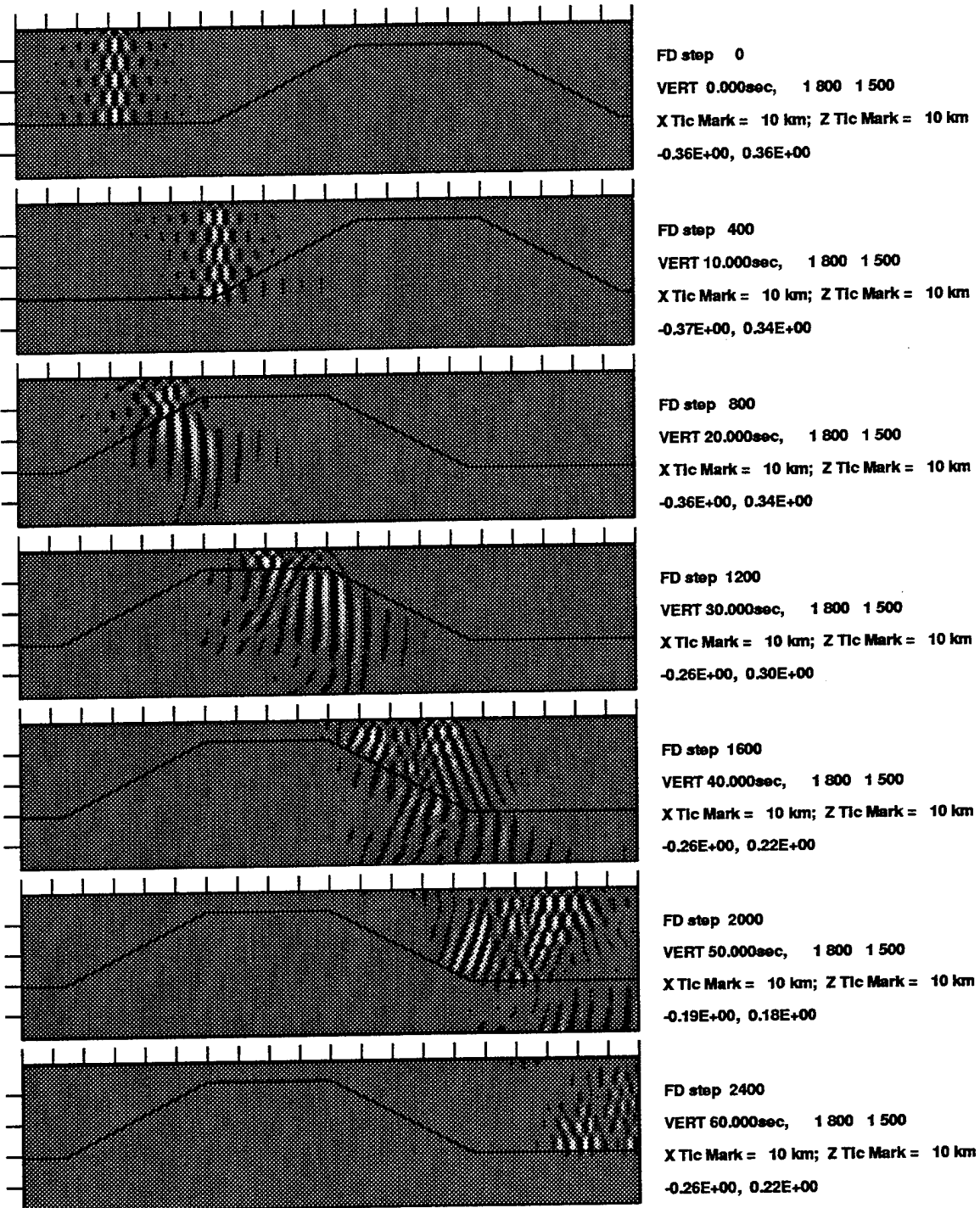
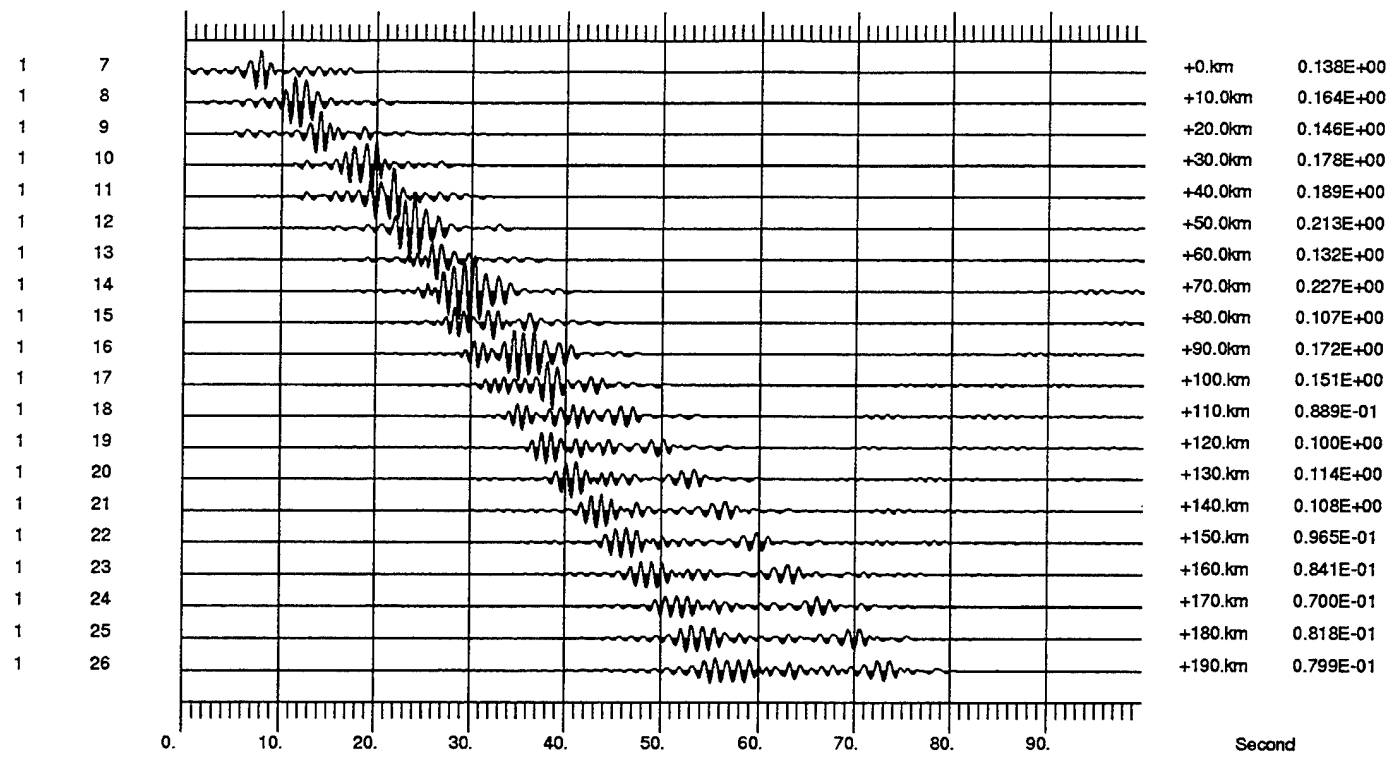


**Figure 10.** Record sections of surface synthetics for the model 0A. While  $R_g$  is intact, the  $L_g$  is effectively blocked. The majority of  $L_g$  energy is converted to  $S_n$ , of which some crosses the descending Moho and re-enters the crust. Due to the post-critical direction, this phase will stay in the crust and become  $L_g$  at a larger distance. This phase is most prominent at 43 seconds on trace 20, and is outside the expected "on-time  $L_g$ " window.



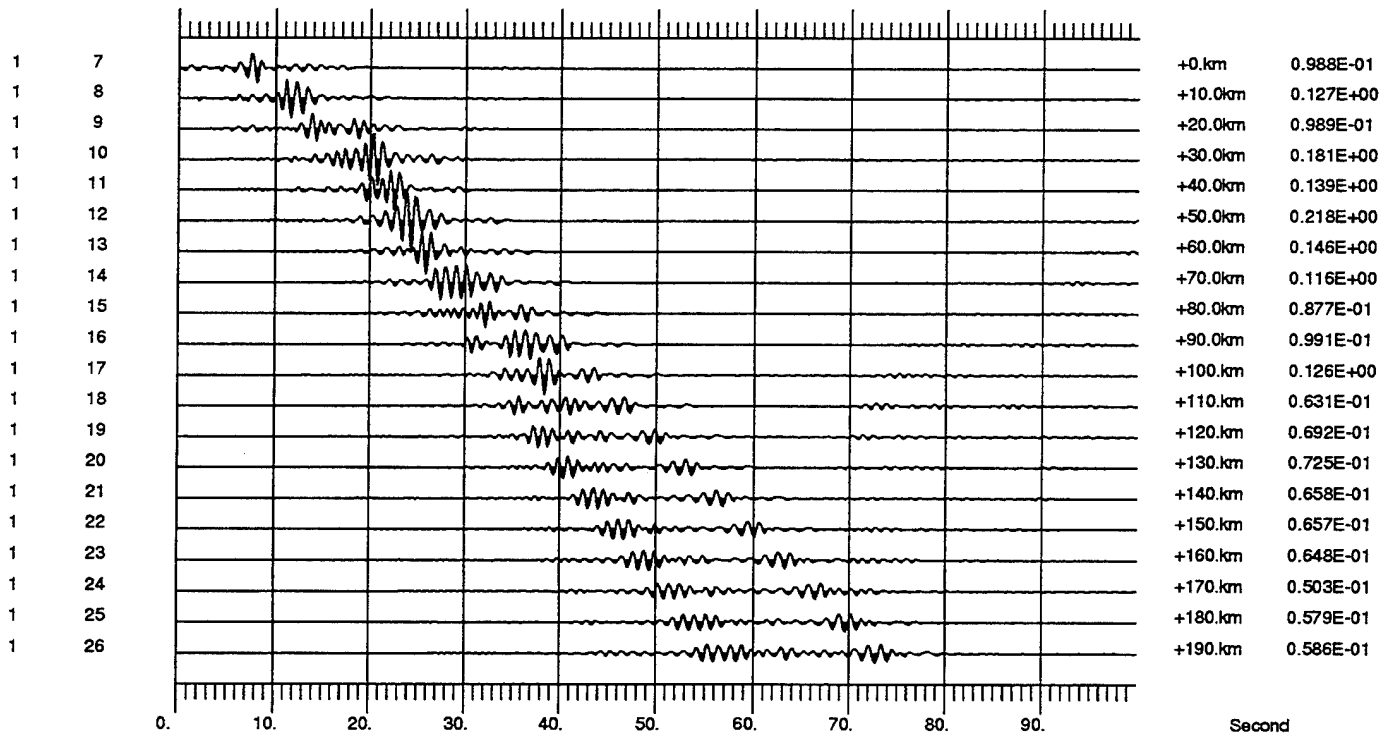
LFD Simulation of Lg Propagation: Model 0Aa

**Figure 11.** Same as Figure 9 except for the model 0Aa, which has a gentle continental-to-oceanic transition. The  $L_g$ -to- $S_n$  conversion is quite clear at 20 and 30 seconds. The energy that crosses the oceanic crust as the 3rd overtone (see, at 30 seconds) does not touch the free surface as the crust thickens. Instead, it propagates along the descending Moho (at 40 and 50 seconds) before it reaches the flat Moho and starts to bounce back to the ground (see, at 60 seconds). The “ $L_g$  blockage” occurs because only  $S_n$  and  $R_g$  could reach ground sensors in the oceanic-to-continental transition zone.



Synthetics at 0km Depth, Model 0Aa

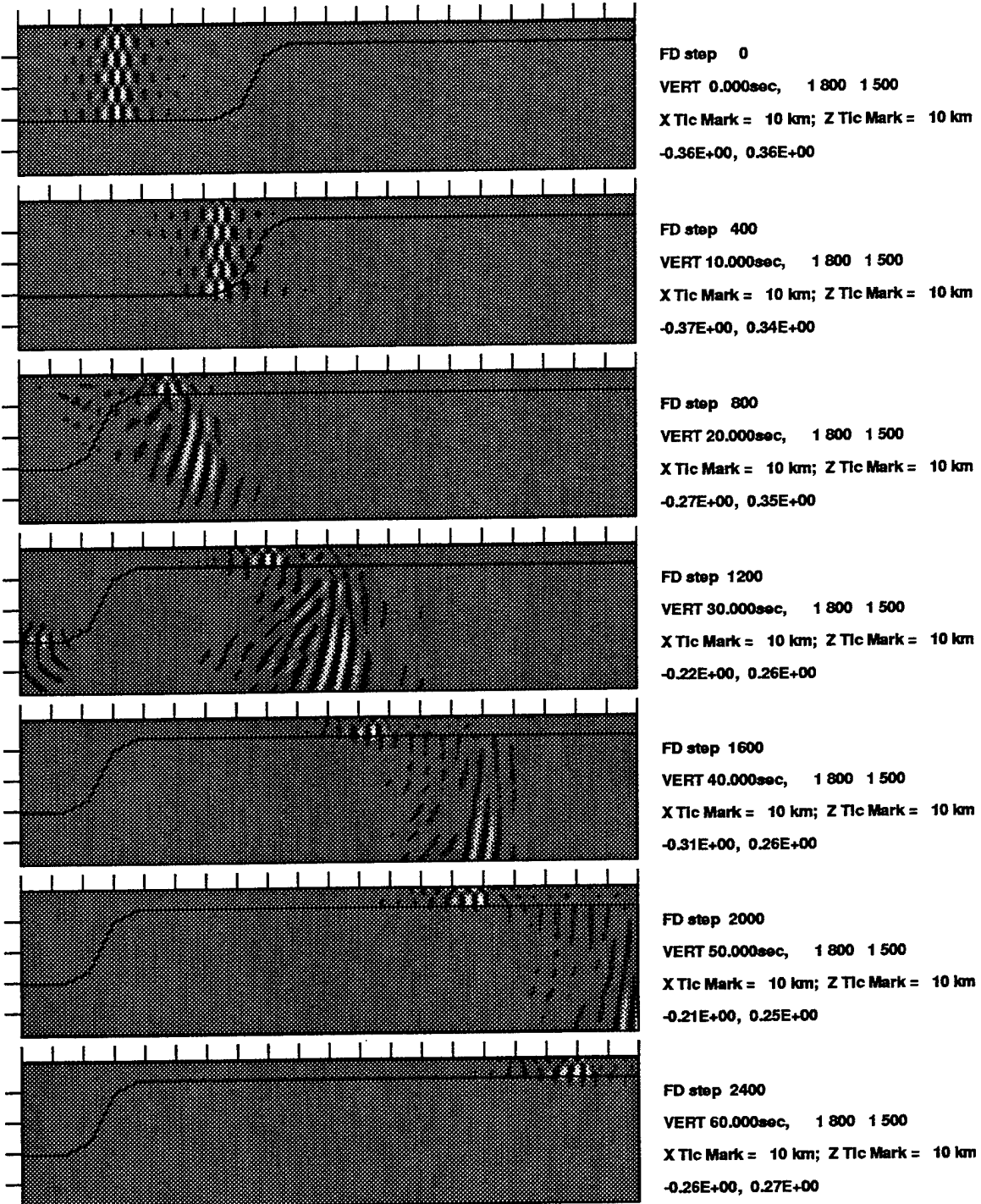
VERT, same scale, decimated by 5



Synthetics at 0km Depth, Model 0Aa

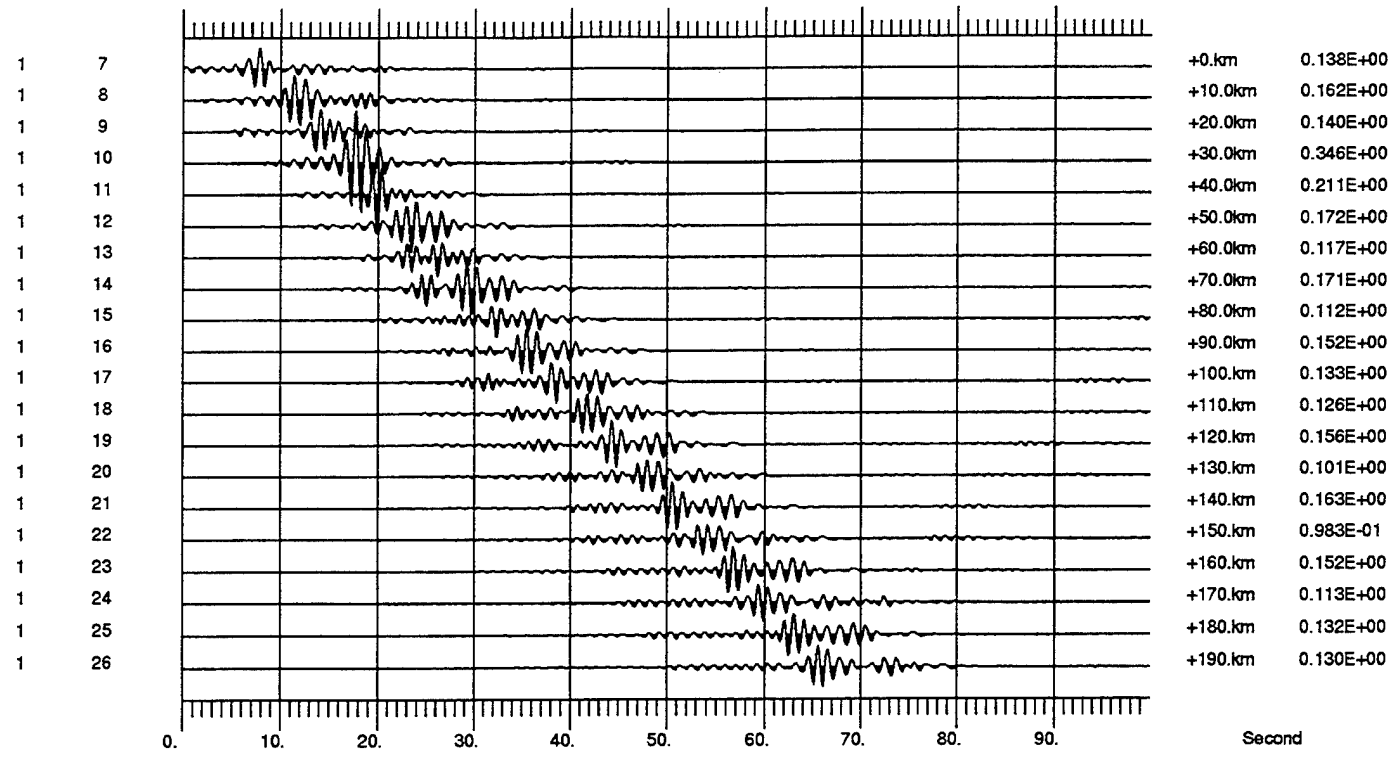
HORI, same scale, decimated by 5

**Figure 12.** Seismic sections of surface synthetics for the model 0Aa. The dominating phase is the "early  $L_g$ " with a group velocity about 4.0 km/sec, followed by  $R_g$  waves with a group velocity of 3.0 km/sec. There is no prominent phase arriving at the expected "on-time"  $L_g$  window at 3.3 km/sec.



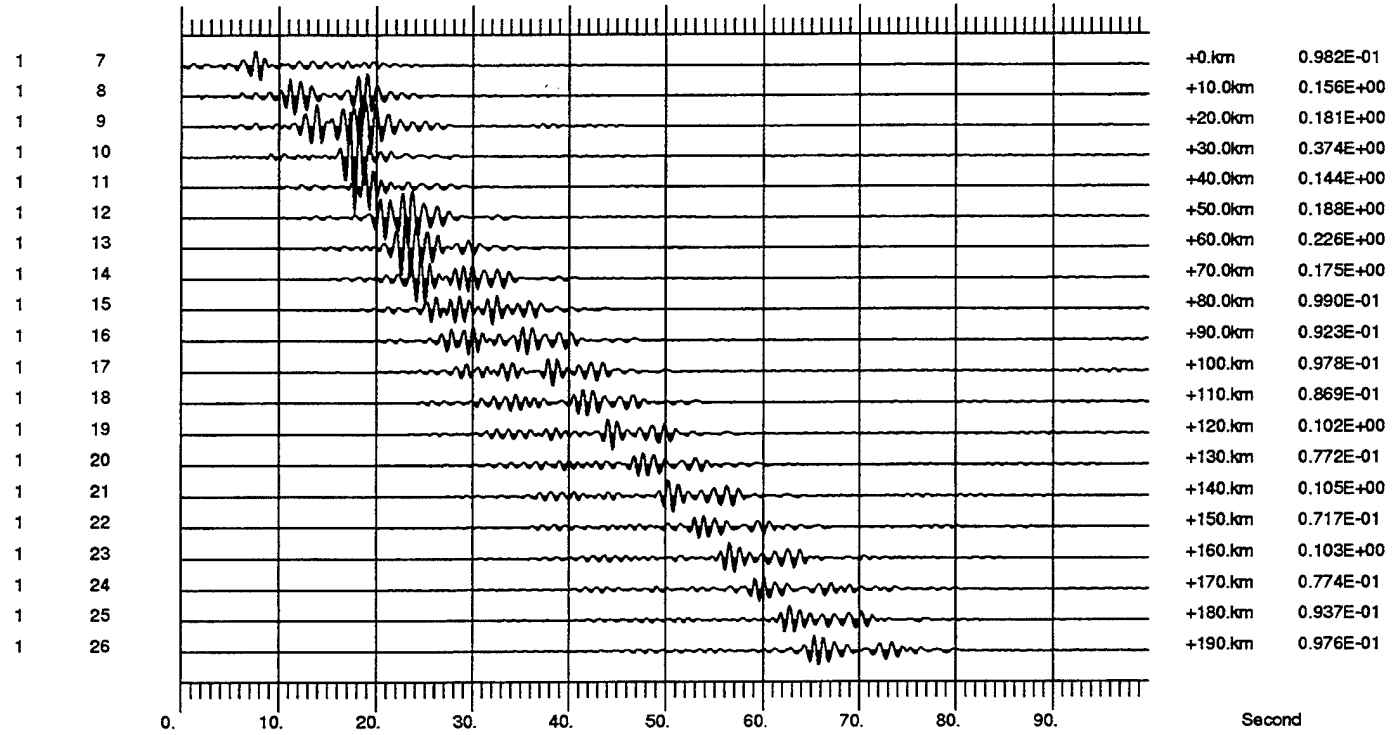
#### LFD Simulation of Lg Propagation: Model 0B

**Figure 13.** The vertical-component snapshots of  $L_g$  wave propagation in model 0B in which the crustal thickness decreases abruptly from 30 to 6 km. A significant fraction of  $L_g$  energy enters the deeper mantle and detaches from the Moho (see 30, 40, and 50 seconds). This energy never reaches the surface sensors, and as a result, the most prominent phase is the stabilized 3rd overtone, which stays in the thin crust.



Synthetics at 0km Depth, Model 0B

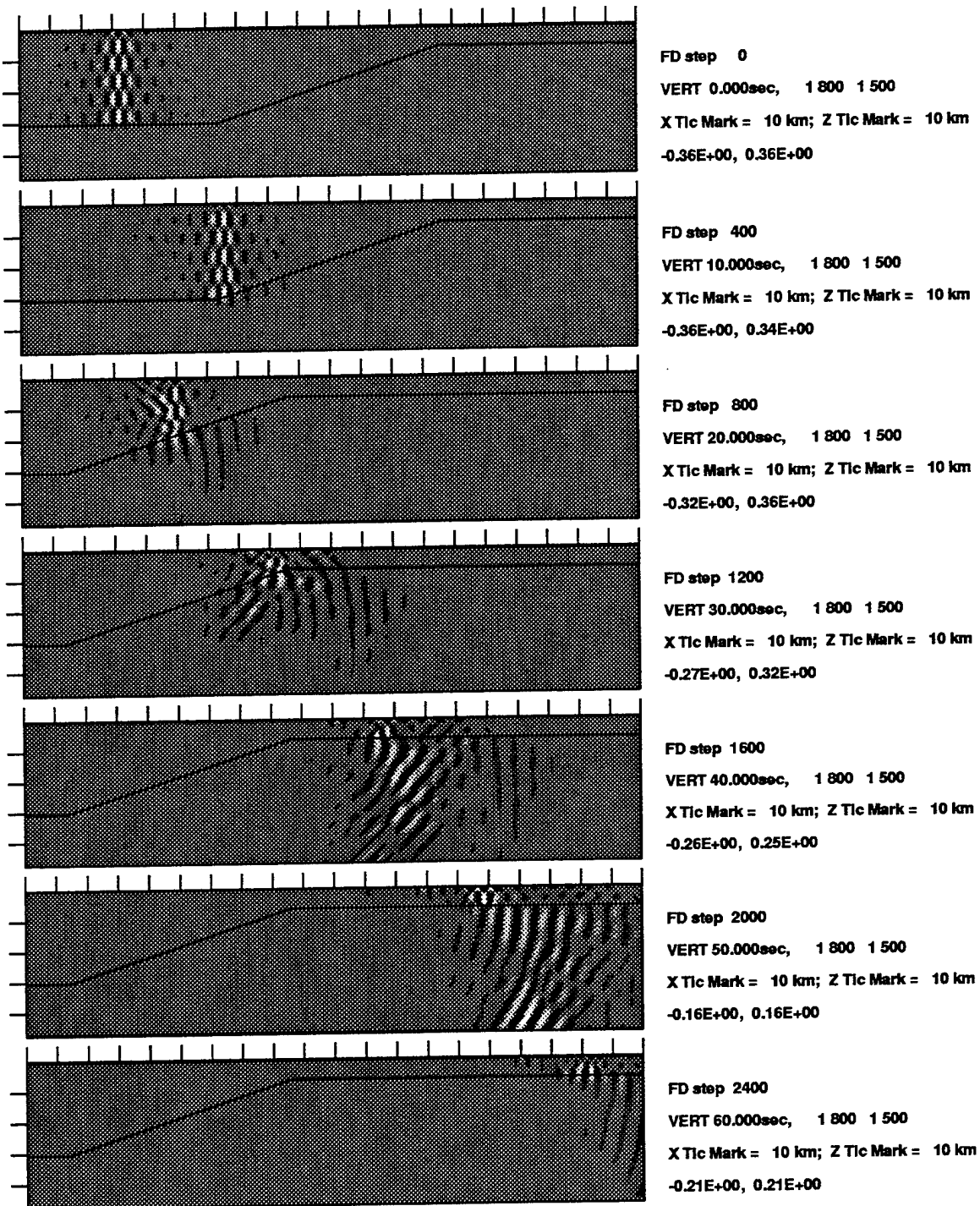
VERT, same scale, decimated by 5



Synthetics at 0km Depth, Model 0B

HORI, same scale, decimated by 5

**Figure 14.** Seismic sections of surface synthetics for model 0B. The most prominent phase is the 3rd overtone converted from the original  $L_g$ . Note that no “ $L_g$  blockage” would be observed here since this 3rd overtone has a peak amplitude and a group velocity very similar to those of the “on-time  $L_g$ ” in the reference model (see Figure 3).



#### LFD Simulation of Lg Propagation: Model 0Ba

**Figure 15.** The vertical-component snapshots of  $L_g$  wave propagation in model 0Ba with a crustal thickness gradually decreasing from 30 to 6 km. As in model 0B, the  $L_g$  is only partially blocked with some energy traveling within the thin crust as the 3rd overtone. Much of the energy leaks into deeper mantle apparently in the form of body waves radiating from the corner where the thin crust starts, which is easier to see on the horizontal component.

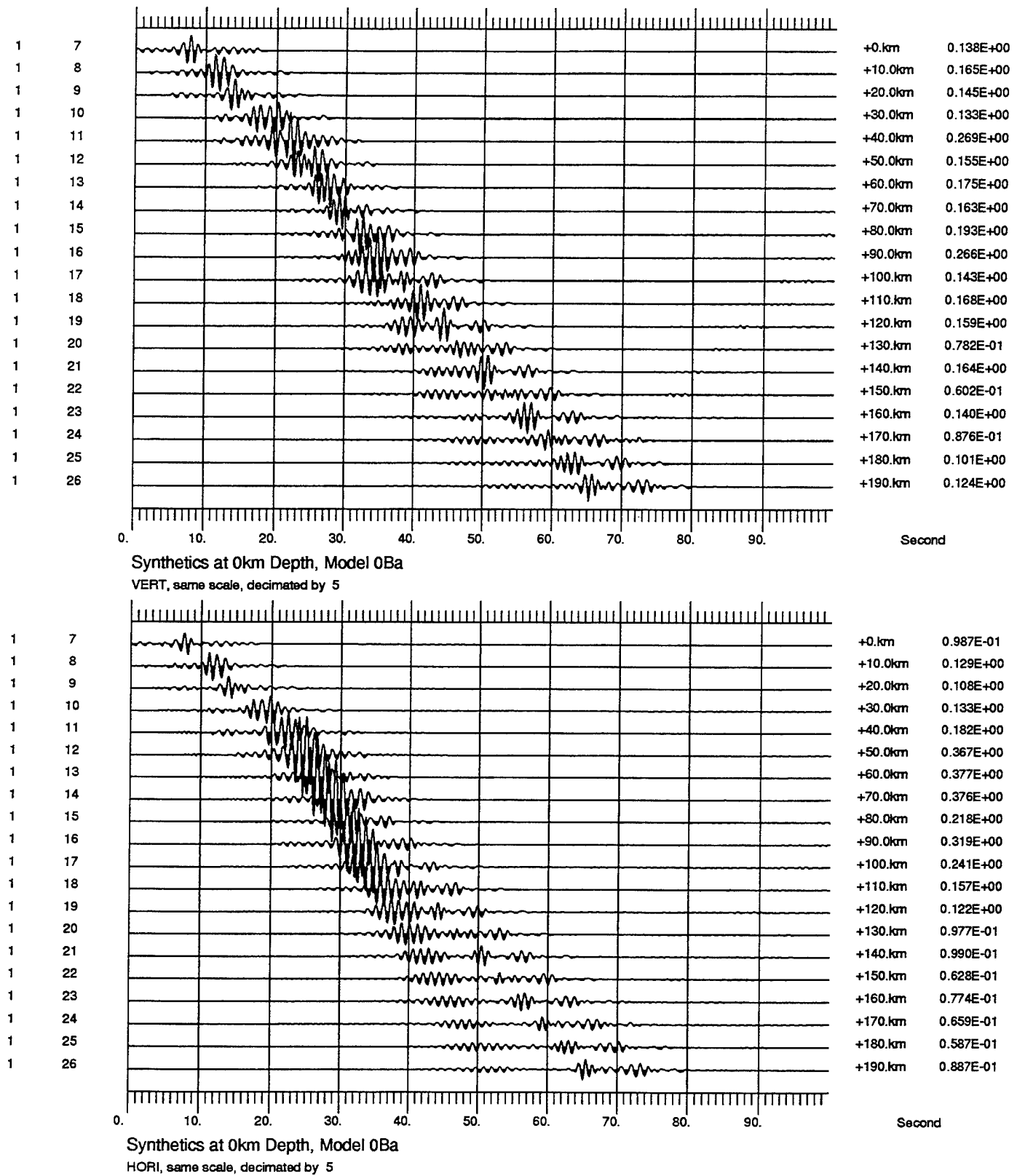
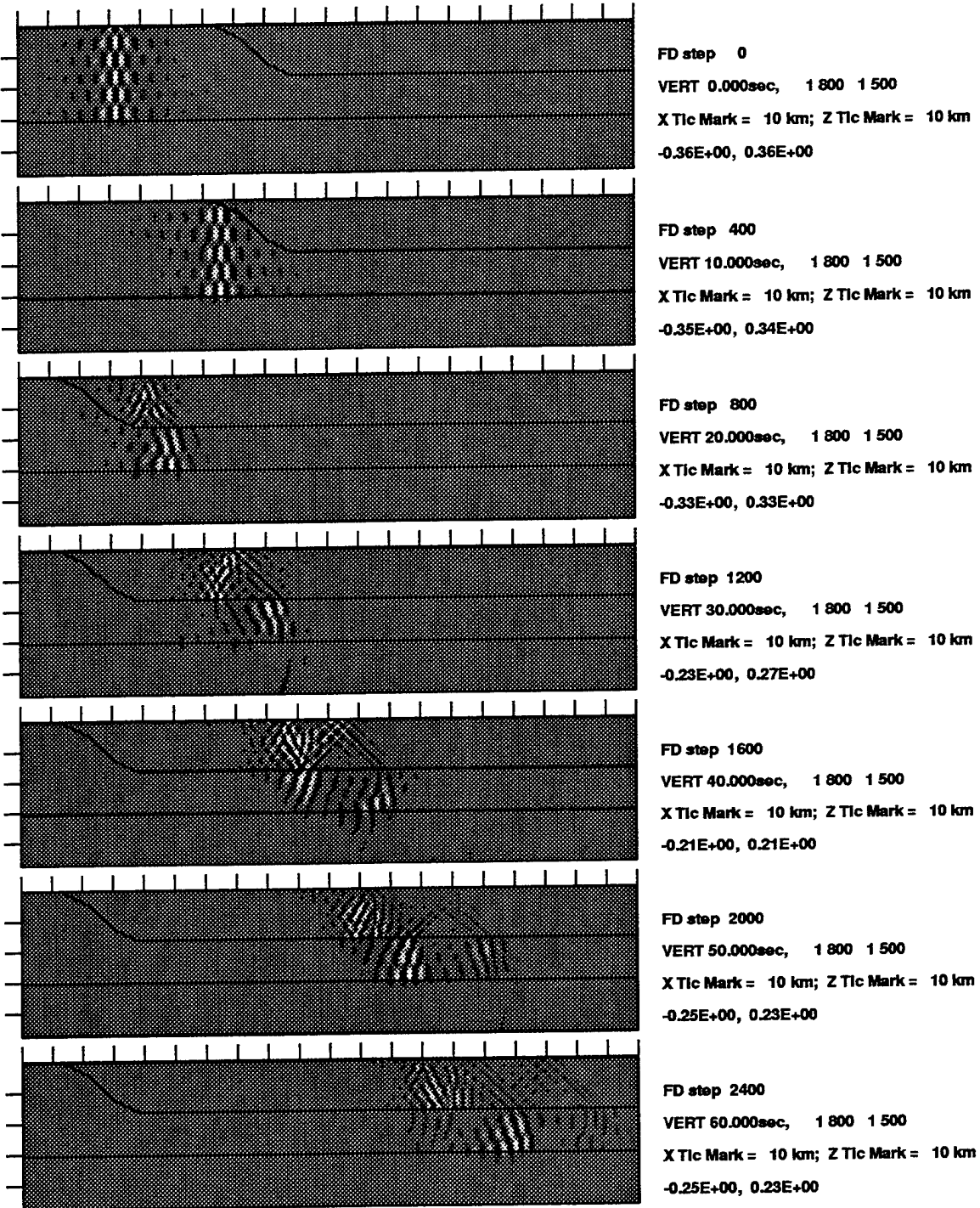
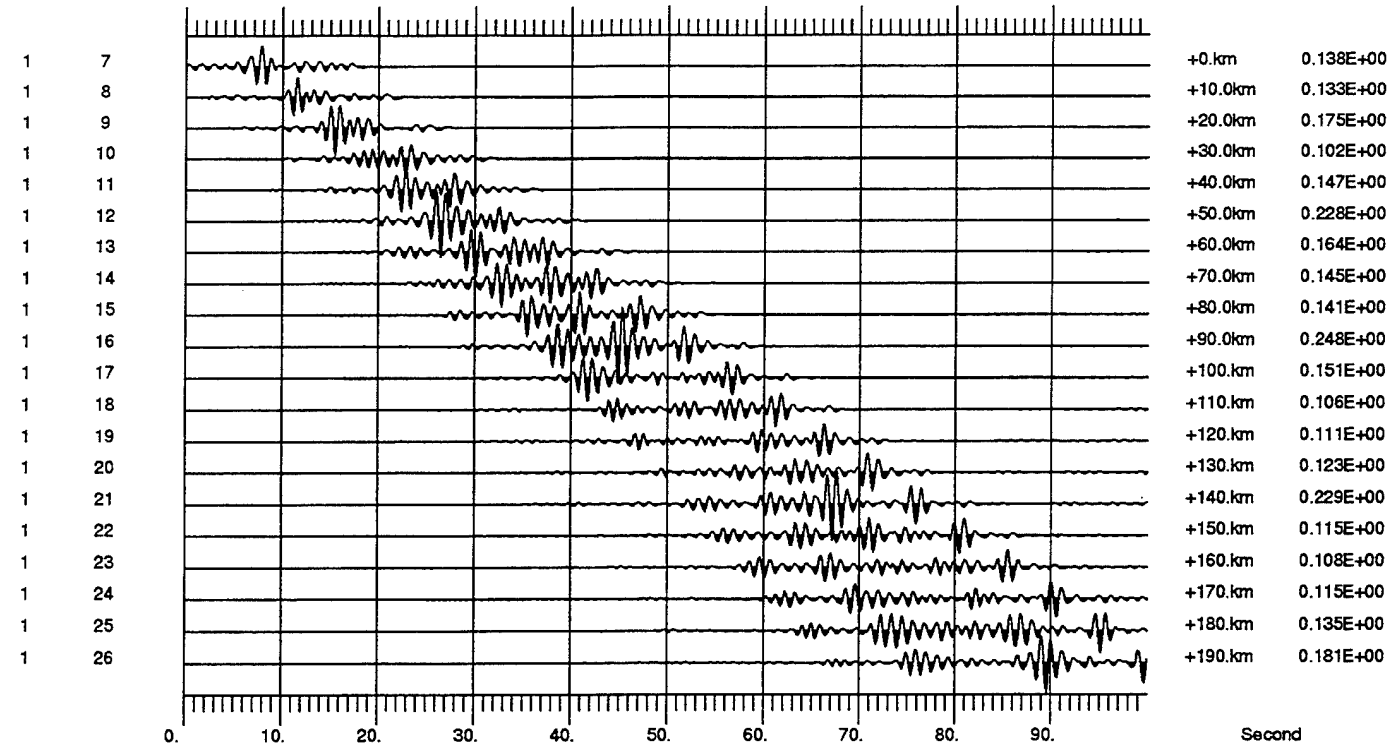


**Figure 16.** Seismic sections of surface synthetics for model 0Ba. The most prominent phase on trace No. 26 is the 3rd overtone converted from the original  $L_g$ , which arrives “on-time” and hence only a partial blockage is observed. A strong  $L_g$ -to-P conversion at the corner generates a very prominent arrival on the horizontal component. This phase dies out very fast on the surface recordings.



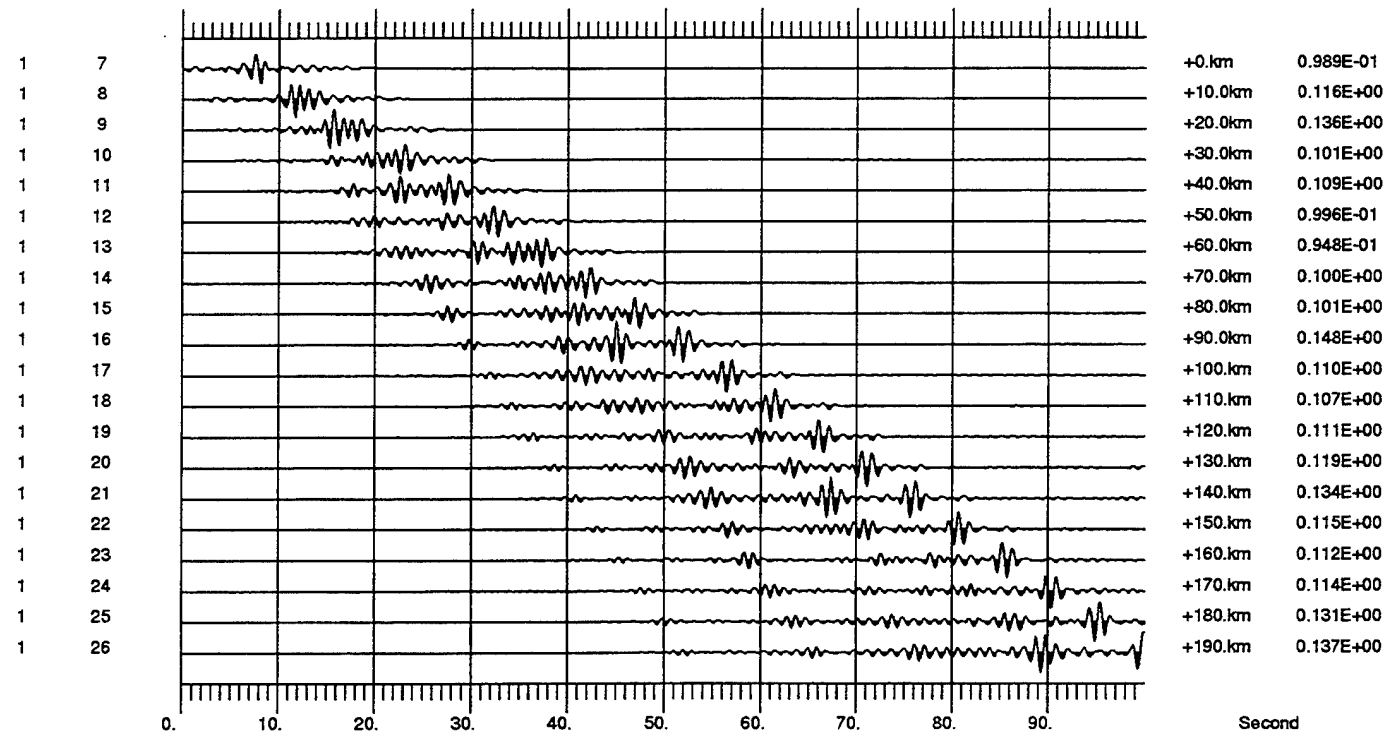
#### LFD Simulation of Lg Propagation: Model 0C

**Figure 17.** The vertical-component snapshots of  $L_g$  wave propagation in model 0C, which has a sedimentary layer 16 km thick. The sediment slows down the  $L_g$  waves, as expected. However, this structure does not generate a  $S_n$  conversion as strong as in other models with irregular Moho or contained basin.



Synthetics at 0km Depth, Model 0C

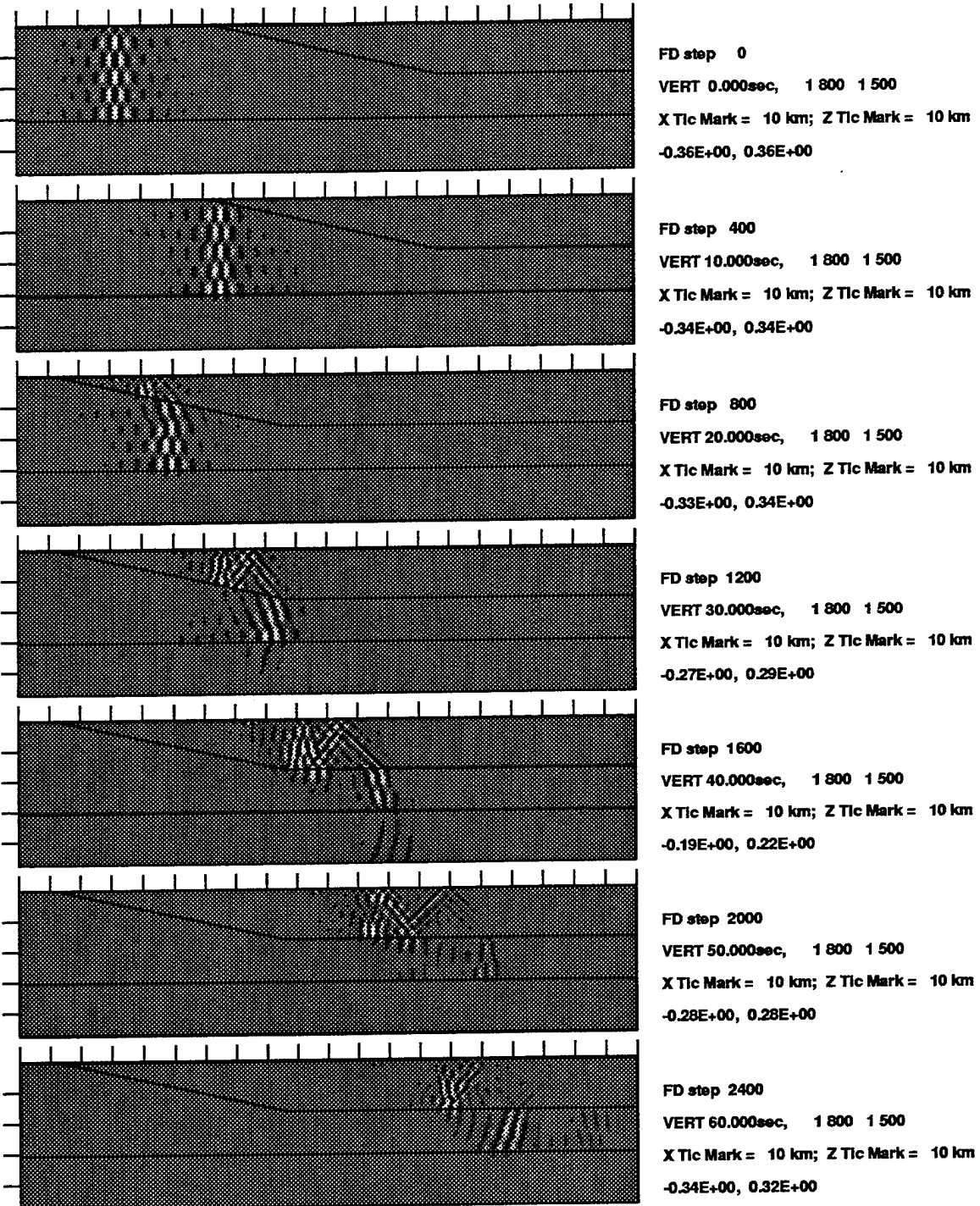
VERT, same scale, decimated by 5



Synthetics at 0km Depth, Model 0C

HORI, same scale, decimated by 5

**Figure 18.** Seismic sections of surface synthetics for model 0C.



LFD Simulation of Lg Propagation: Model 0Ca

Figure 19. Same as Figure 17 except that the basin has a gentle edge.

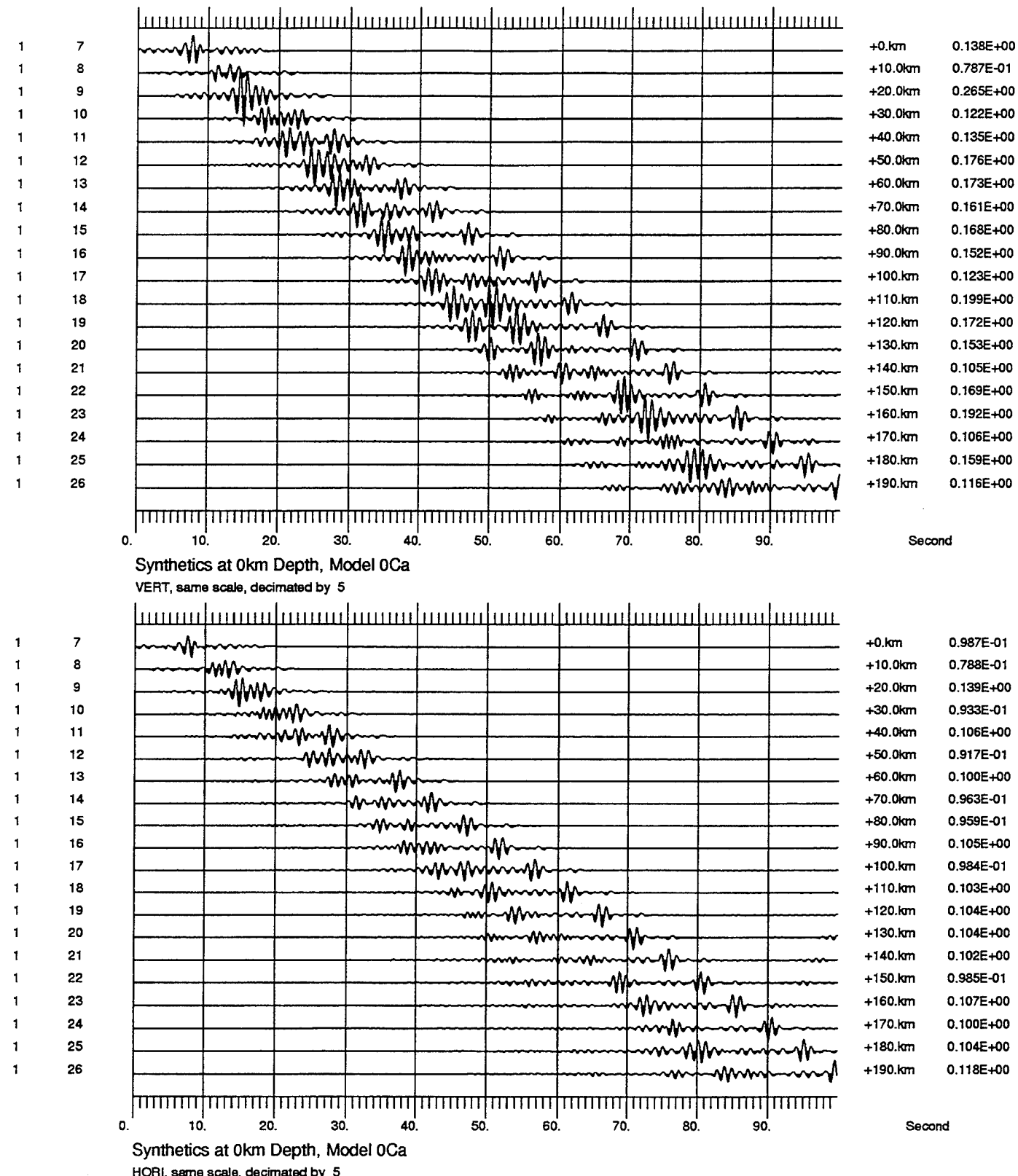
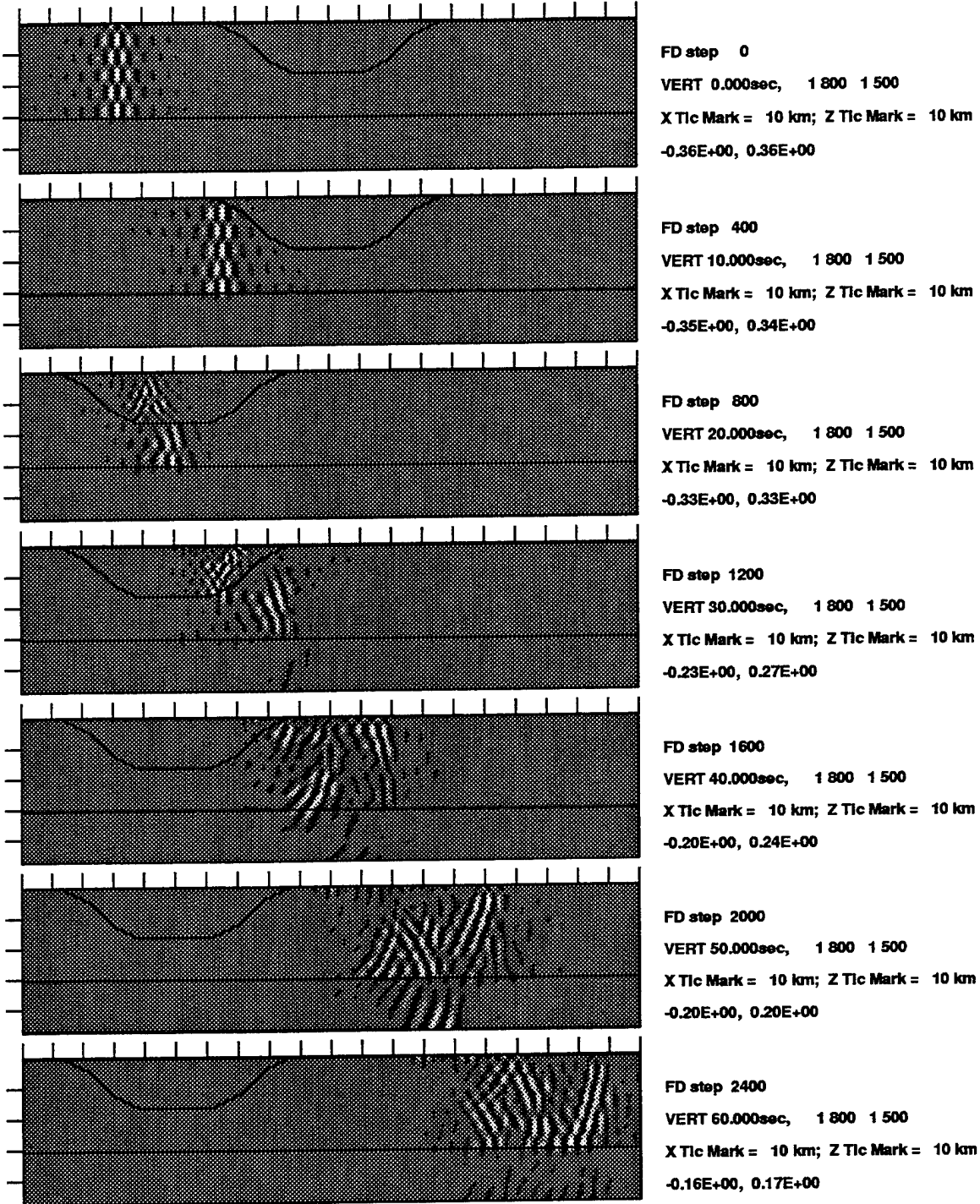
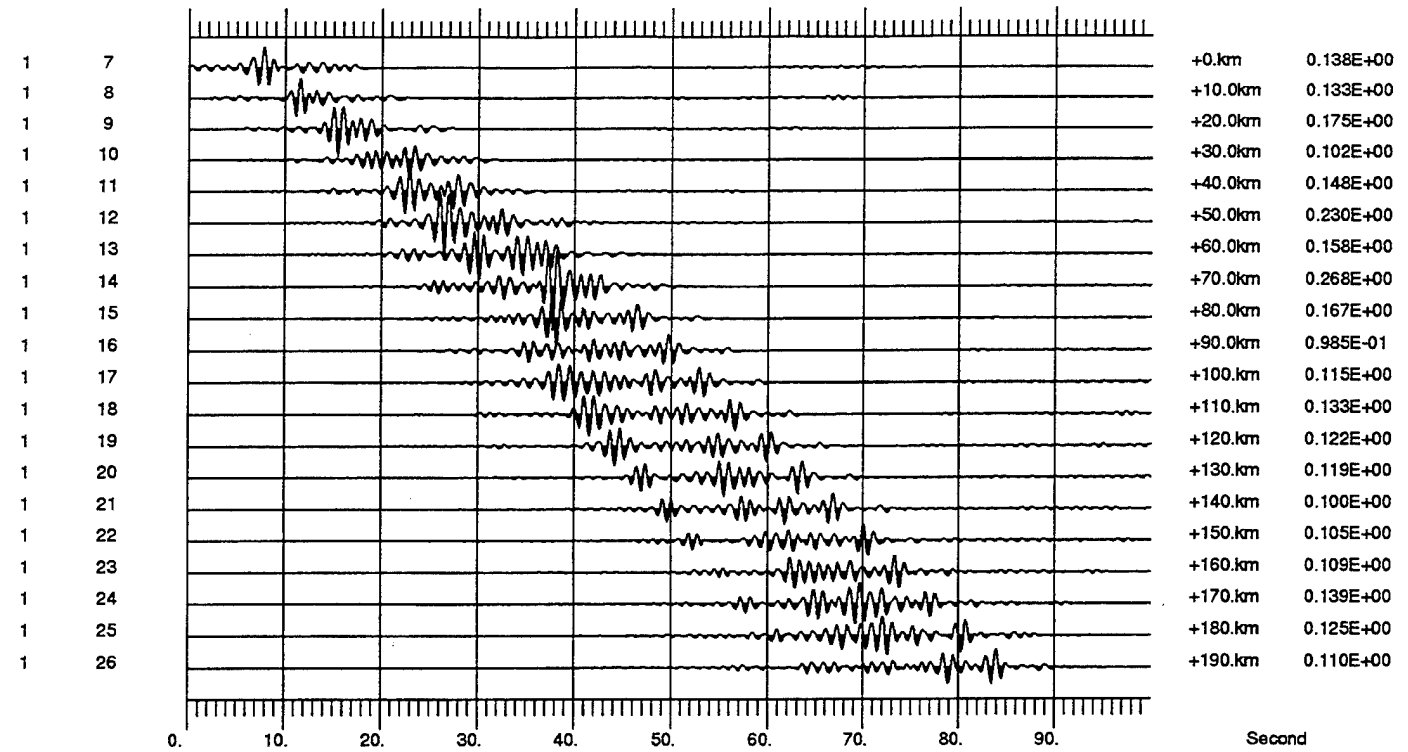


**Figure 20.** Seismic sections of surface synthetics for model 0Ca.



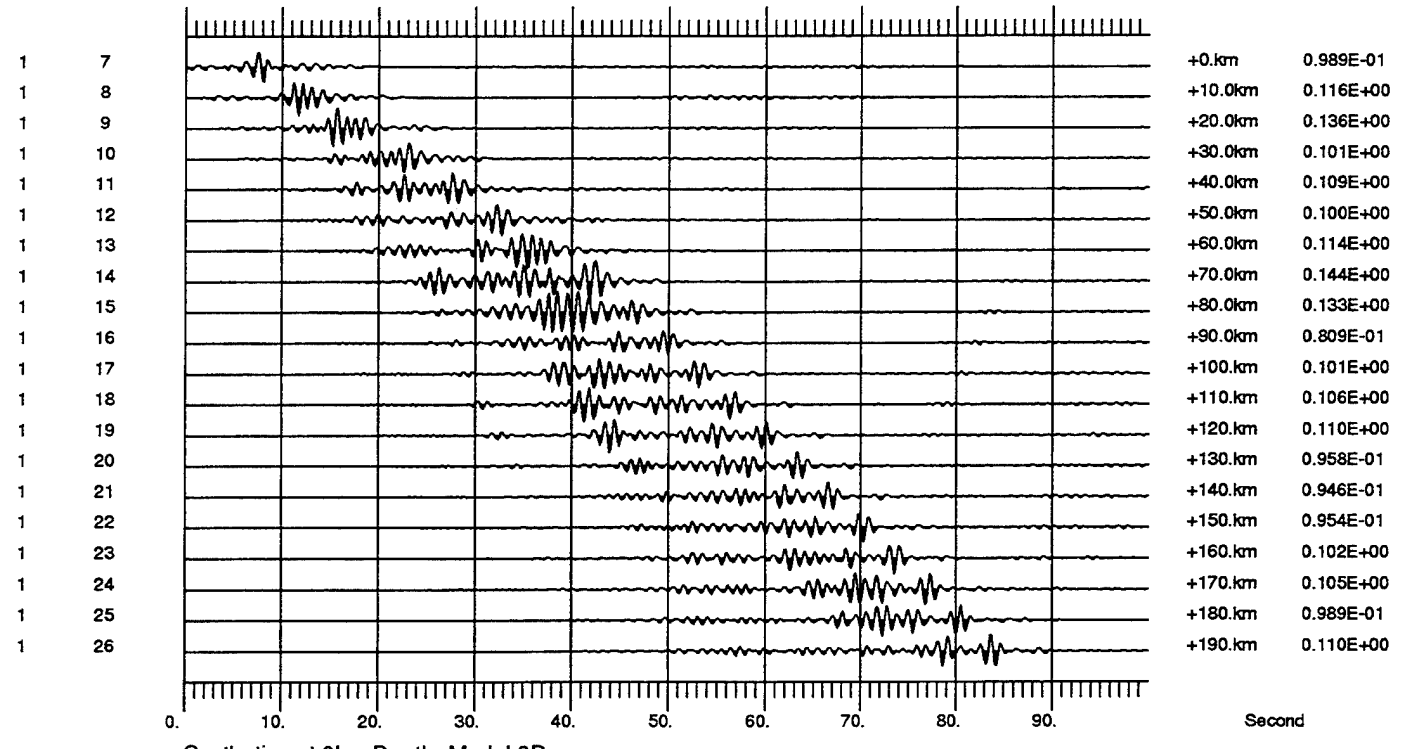
#### LFD Simulation of Lg Propagation: Model 0D

**Figure 21.** Because of the contained structure of the basin, the  $L_g$  that tunnels underneath the basin eventually recovers characteristics like a multiply bouncing SmS. This phase has the same group velocity as the “on-time  $L_g$ ” on those surface sensors co-located at the bounce points. The amplitude is smaller, however. A more prominent phase comes from the energy that first enters the basin and then leaks out from the ascending edge of the basin. The corner where the pinched basin ends also radiates some body waves.



Synthetics at 0km Depth, Model 0D

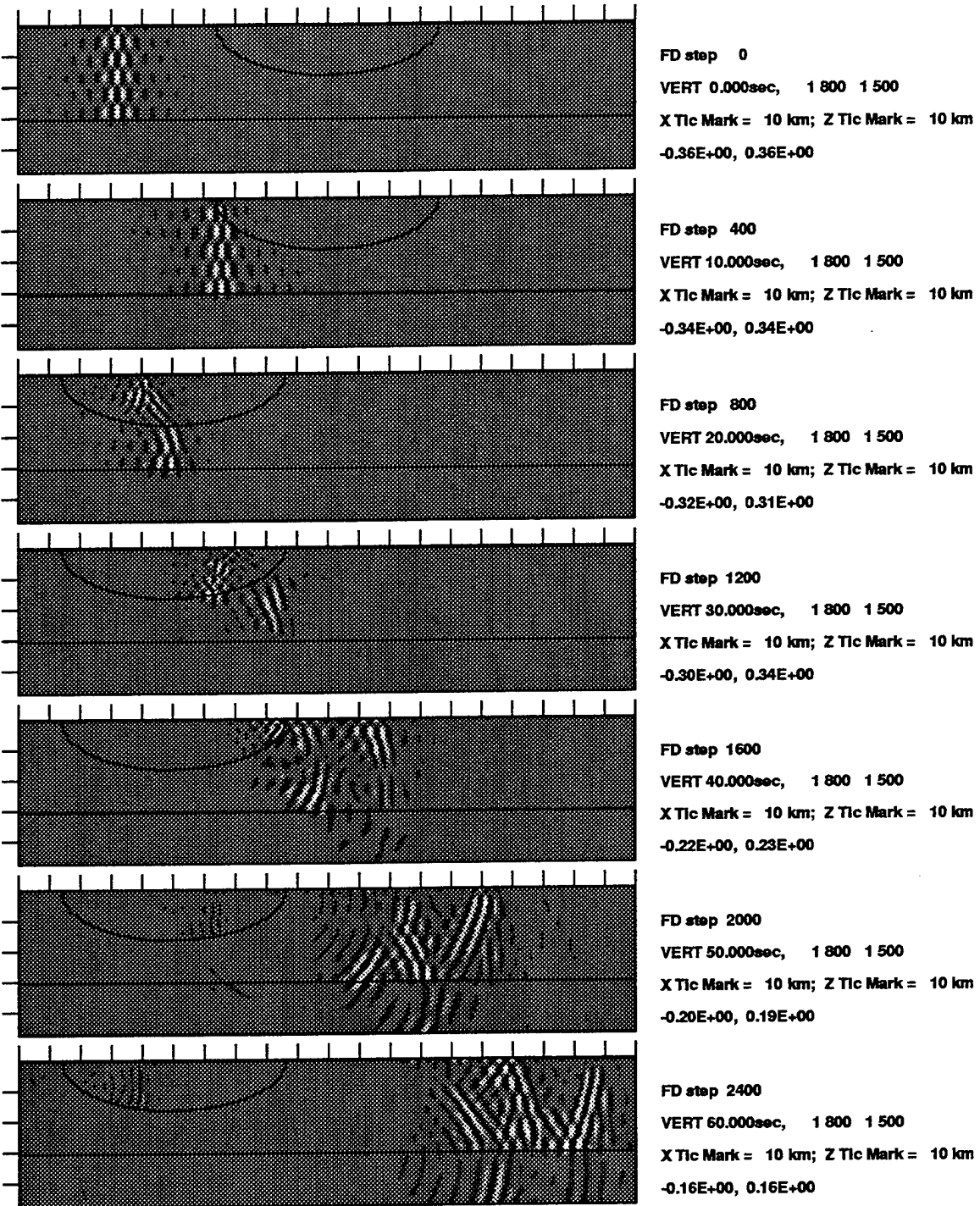
VERT, same scale, decimated by 5



Synthetics at 0km Depth, Model 0D

HORI, same scale, decimated by 5

**Figure 22.** The contained basin structure removes some energy from the "on-time  $L_g$ " and converts it to the so-called "late  $L_g$ " which has the same phase velocity as the reference  $L_g$  but is significantly delayed. Depending on the location of surface sensors, some sensors will observe either complete or partial blockage of the "on-time  $L_g$ ".



#### LFD Simulation of Lg Propagation: Model 0Da

**Figure 23.** Same as Figure 21 except for an elliptical basin. The results are very similar to those of model 0D. Thus the details of the basin shape appear to be not that important.

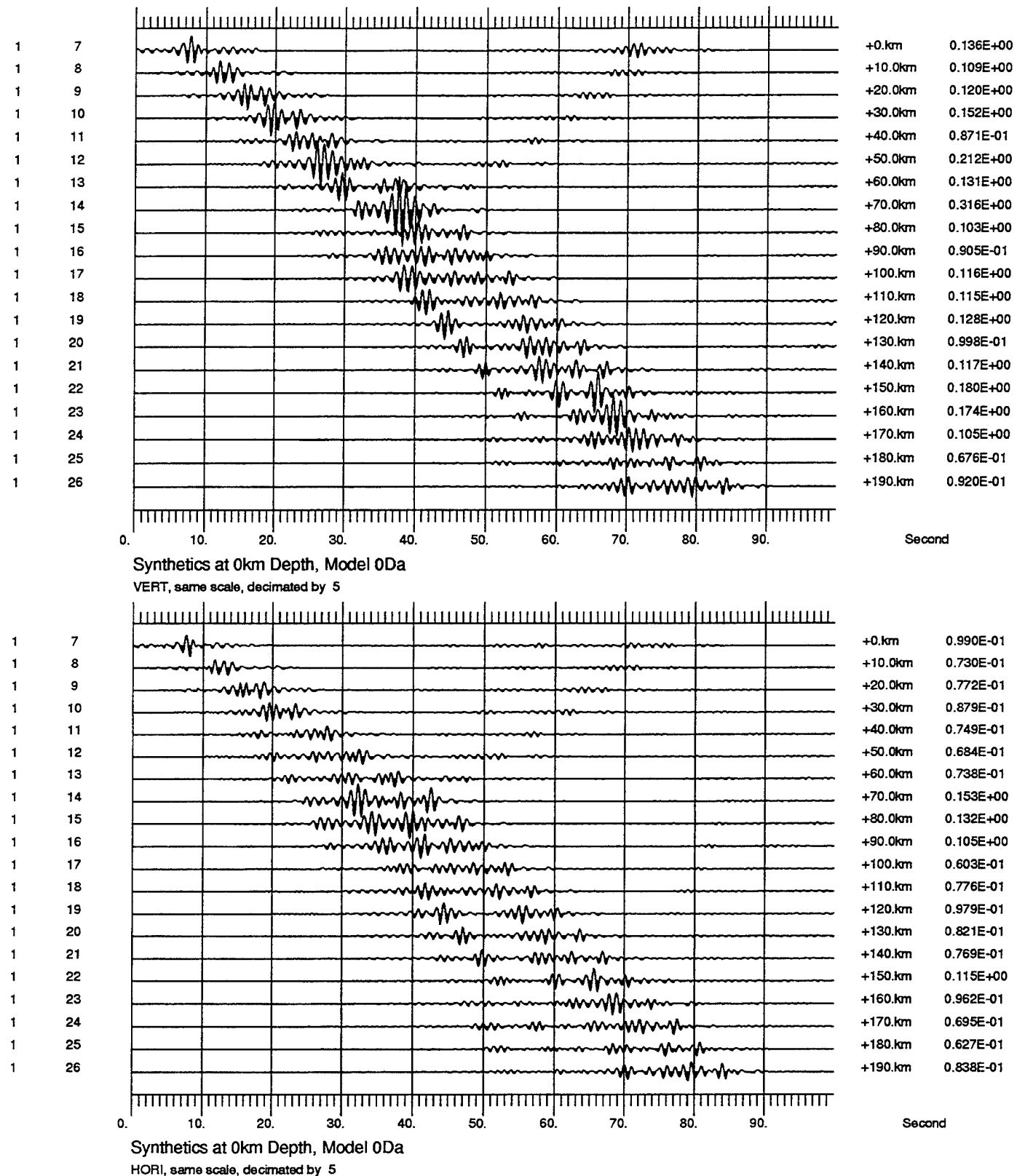
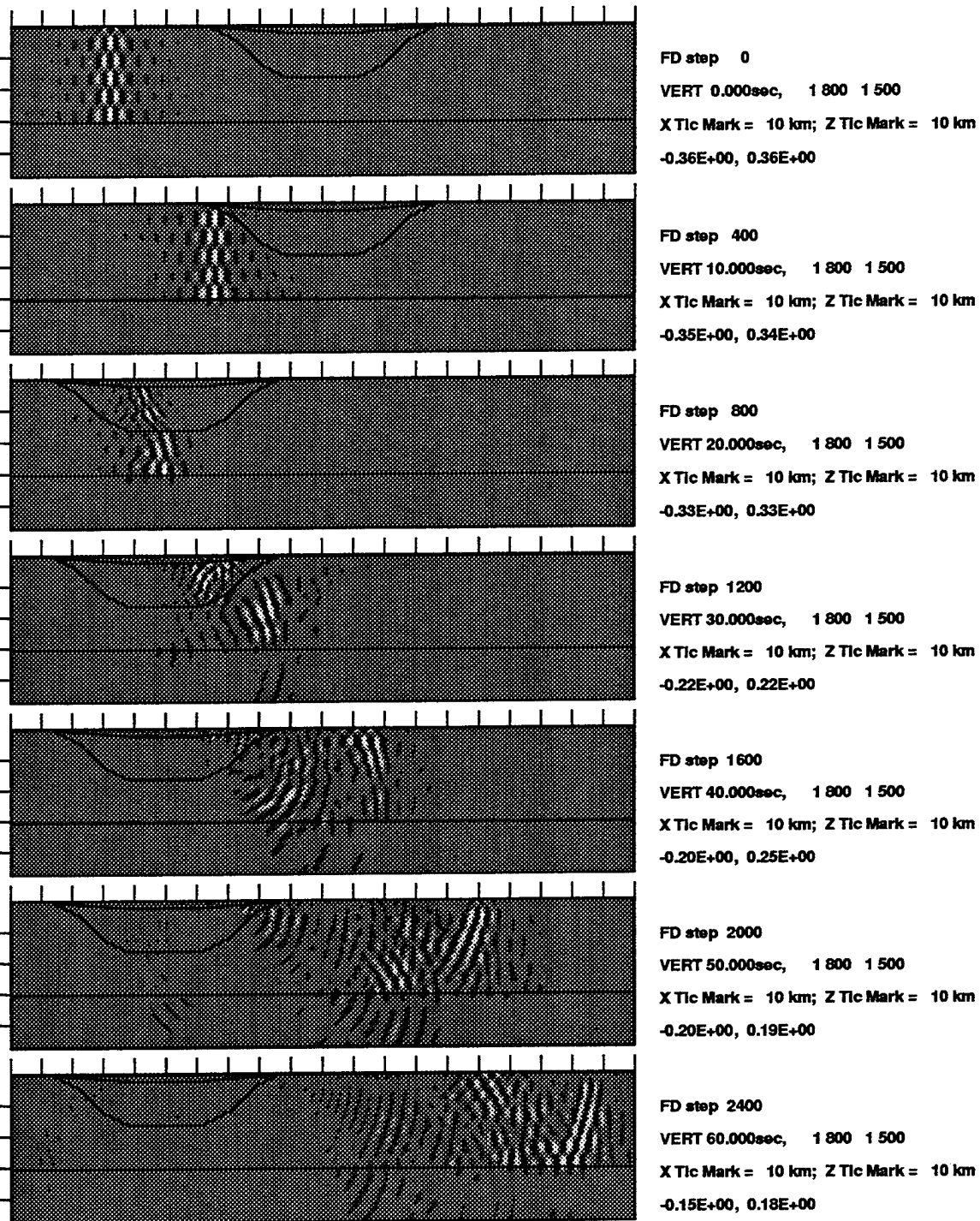


**Figure 24.** Similar to Figure 22 except for an elliptical basin. Although the results are very similar to those of model 0D, the blockage of the “on-time  $L_g$ ” is more apparent. Also note the strong backscattering at the terminating edge of the basin.



#### LFD Simulation of Lg Propagation: Model 0Db

**Figure 25.** The vertical-component snapshots of  $L_g$  wave propagation in the basin model 0Db. As in models 0D and 0Da, the bodywave coupling occurs at the pinched end of the basin where part of the energy that traverses the basin starts to leak out (at 40 and 50 seconds). This suggests that even in a model with no lateral variation in the Moho, the lateral structural heterogeneity in the uppermost crust still can produce mantle phases through scattering. The pinched edge is essential in this mechanism.

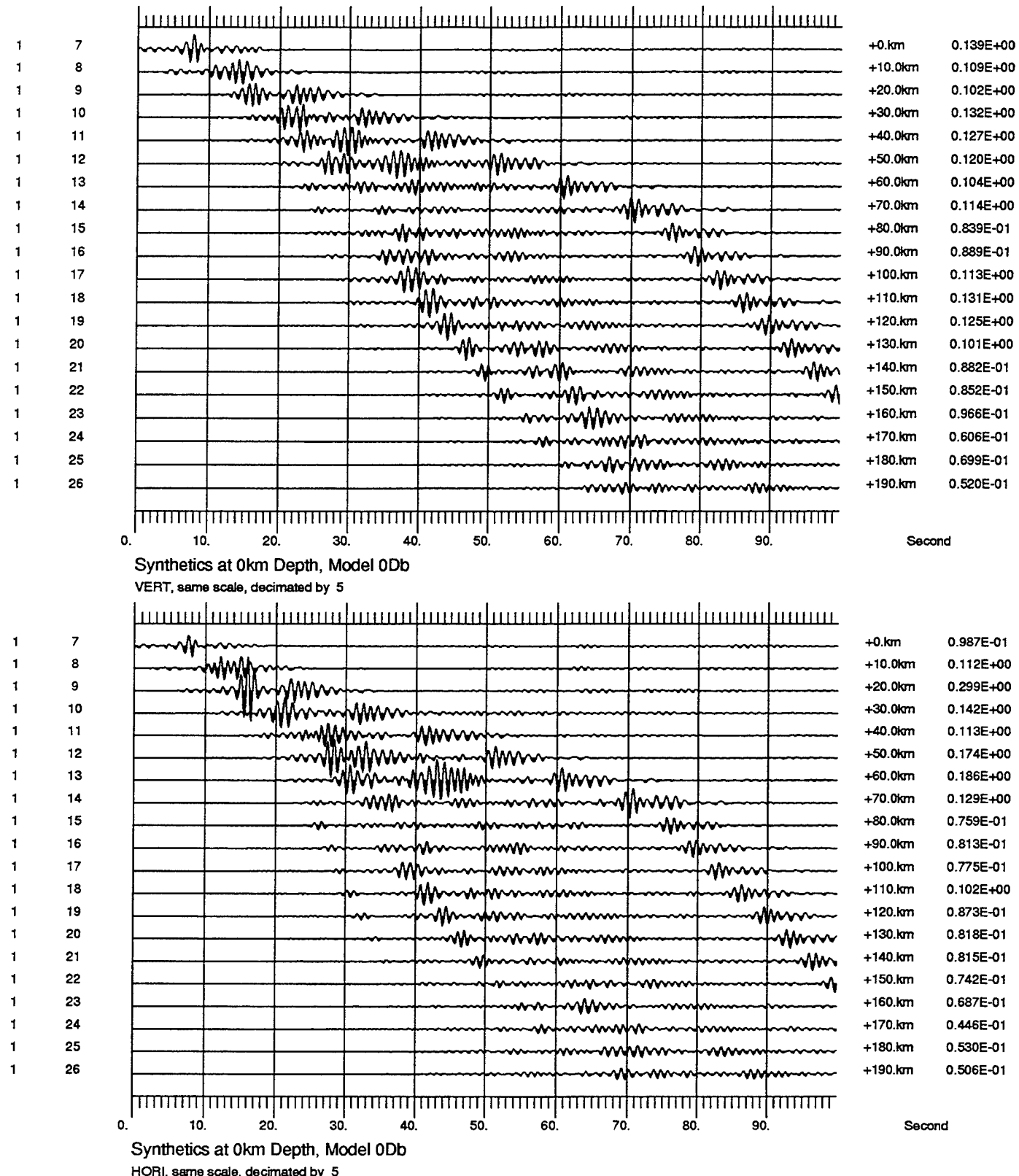
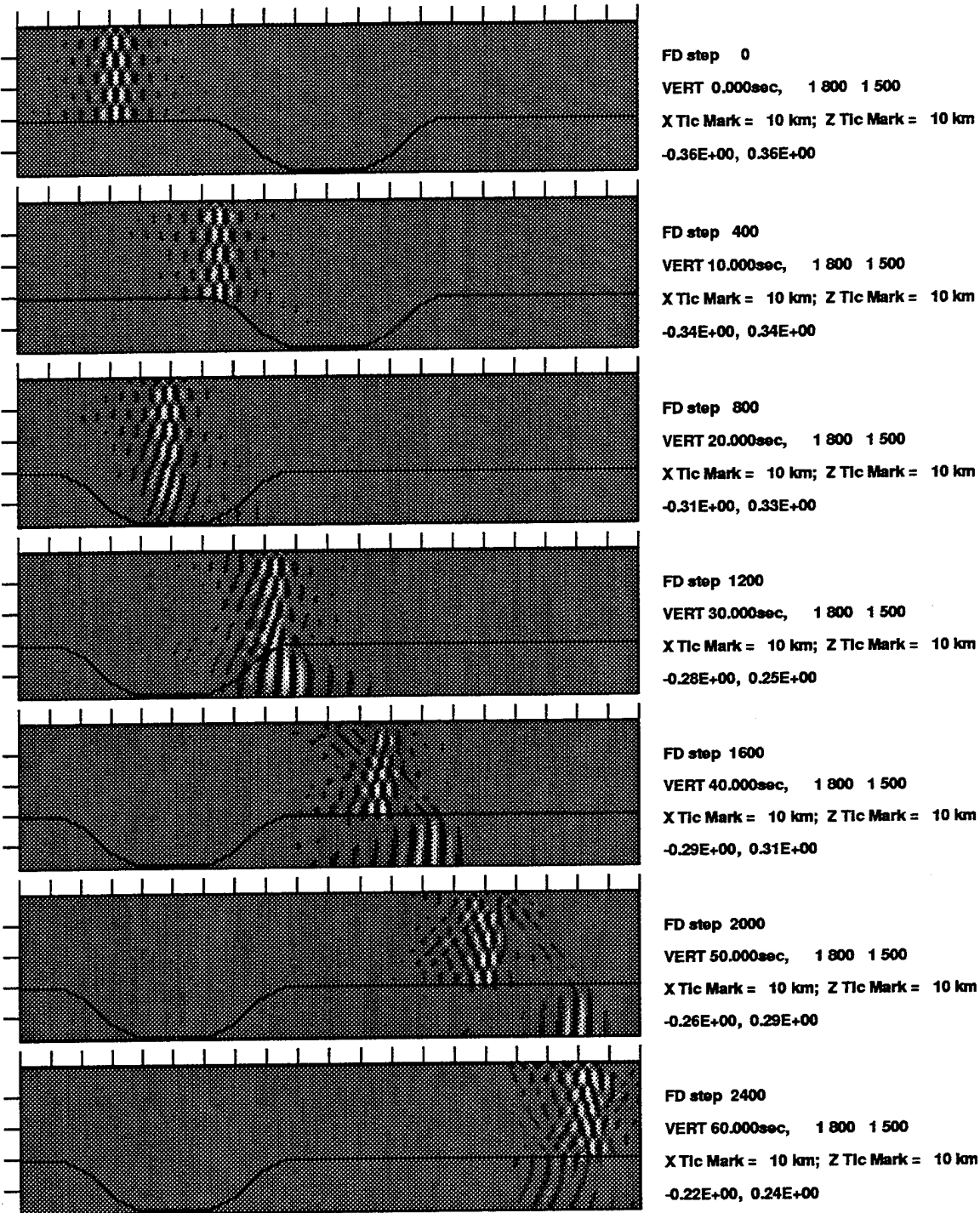
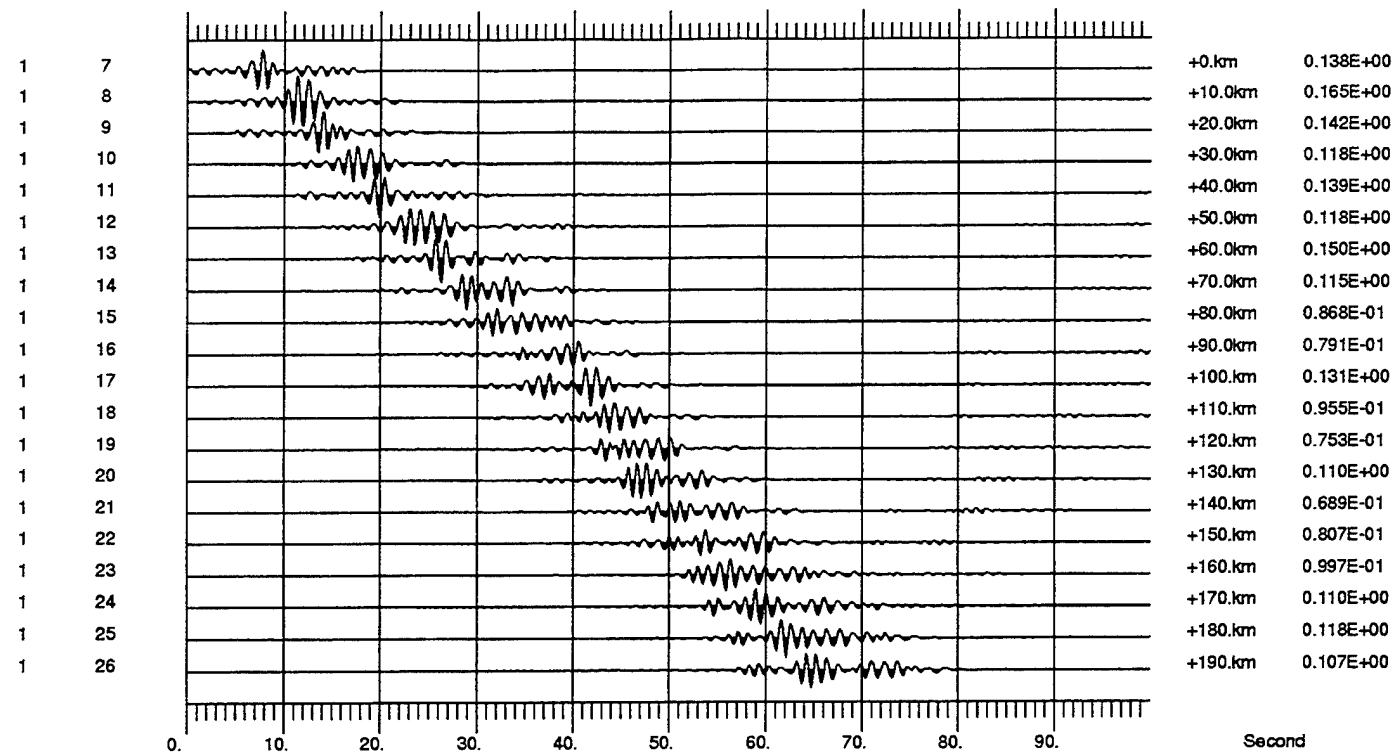


**Figure 26.** Similar to Figure 22 except that a thin, slow sedimentary layer is added. Both the  $R_g$  phase and the “late  $L_g$ ” become prominent in this case. The “on-time  $L_g$ ” wave is weakened and only certain surface sensors at the right locations can observe it.



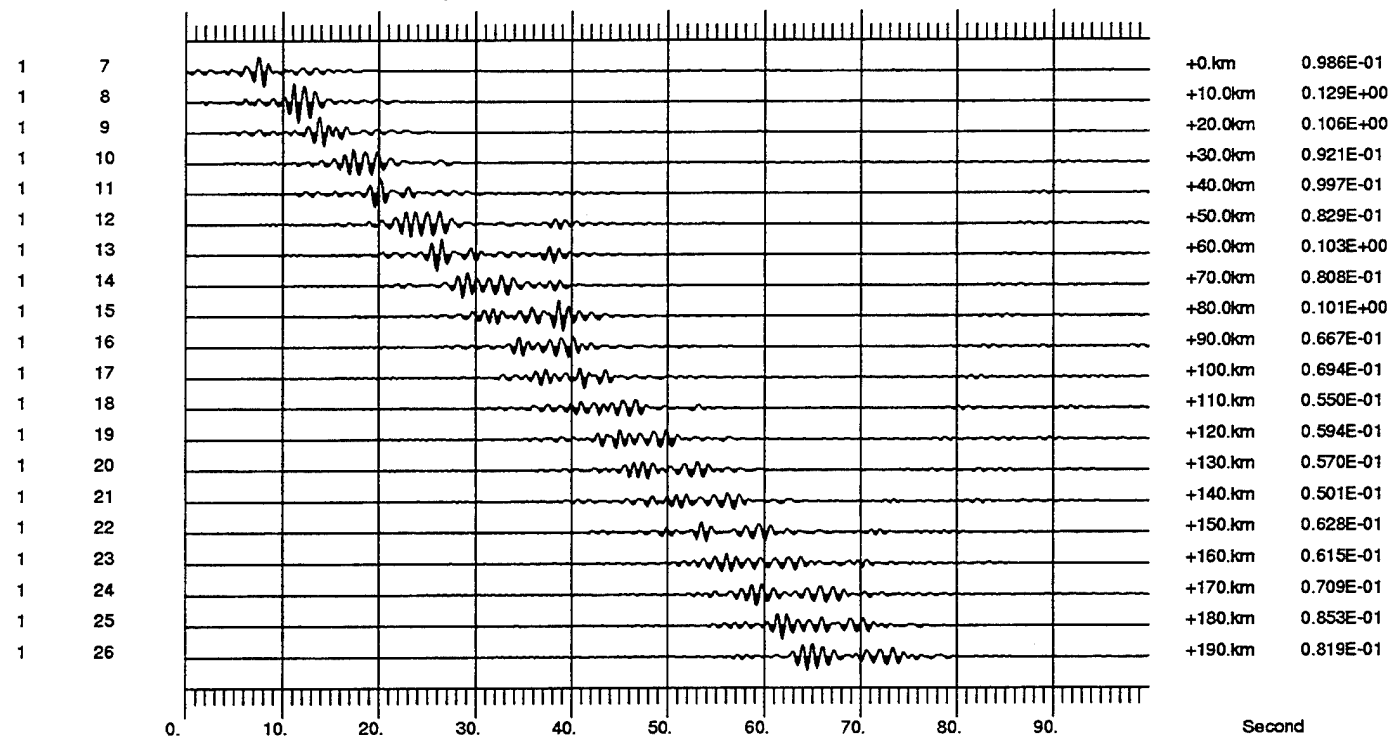
#### LFD Simulation of Lg Propagation: Model 0E

**Figure 27.** The vertical-component snapshots of  $L_g$  wave propagation in model 0E with a thickened crust. A very strong  $L_g$ -to- $S_n$  conversion occurs along the ascending interface (see, 30, 40, and 50 seconds). Horizontal-component snapshots (not shown) indicate that some focusing of energy occurs at the corner where the Moho turns flat. This corner becomes a secondary point source, radiating upgoing body waves. Sensors right above this corner would detect a prominent arrival due to a nearly vertical incidence of shear waves (see traces No. 16 and 17 of Figure 28).



Synthetics at 0km Depth, Model 0E

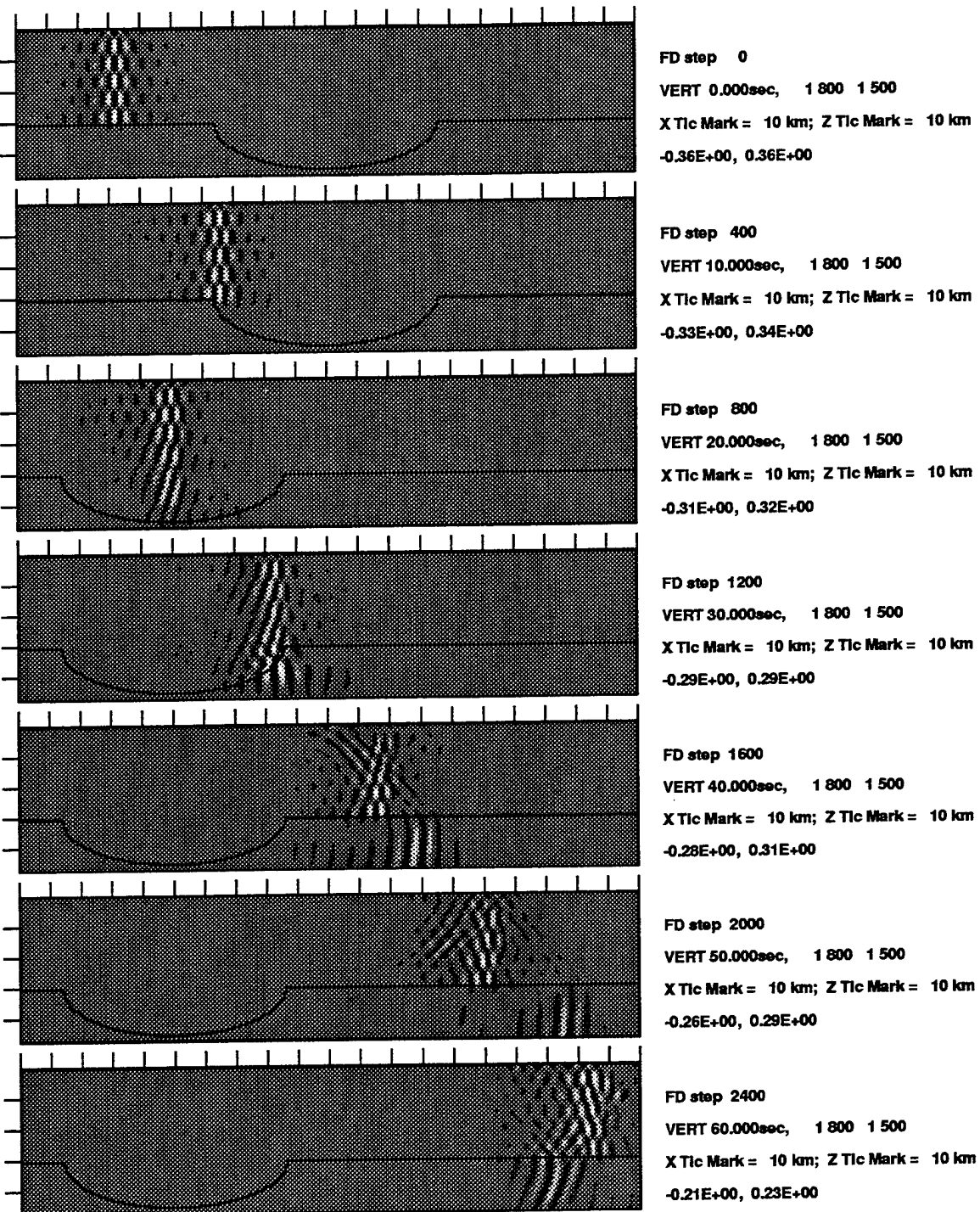
VERT, same scale, decimated by 5



Synthetics at 0km Depth, Model 0E

HORI, same scale, decimated by 5

**Figure 28.** Seismic sections of model 0E, which has a thickened crust. The corner where the Moho turns flat is a secondary point source radiating upgoing body waves. The prominent arrival on traces 16 and 17 has a very large apparent velocity, due to a nearly normal incidence. The “on-time  $L_g$ ” is only partially blocked.



#### LFD Simulation of Lg Propagation: Model 0Ea

**Figure 29.** The vertical-component snapshots of  $L_g$  wave propagation in model 0Ea with a thickened crust.

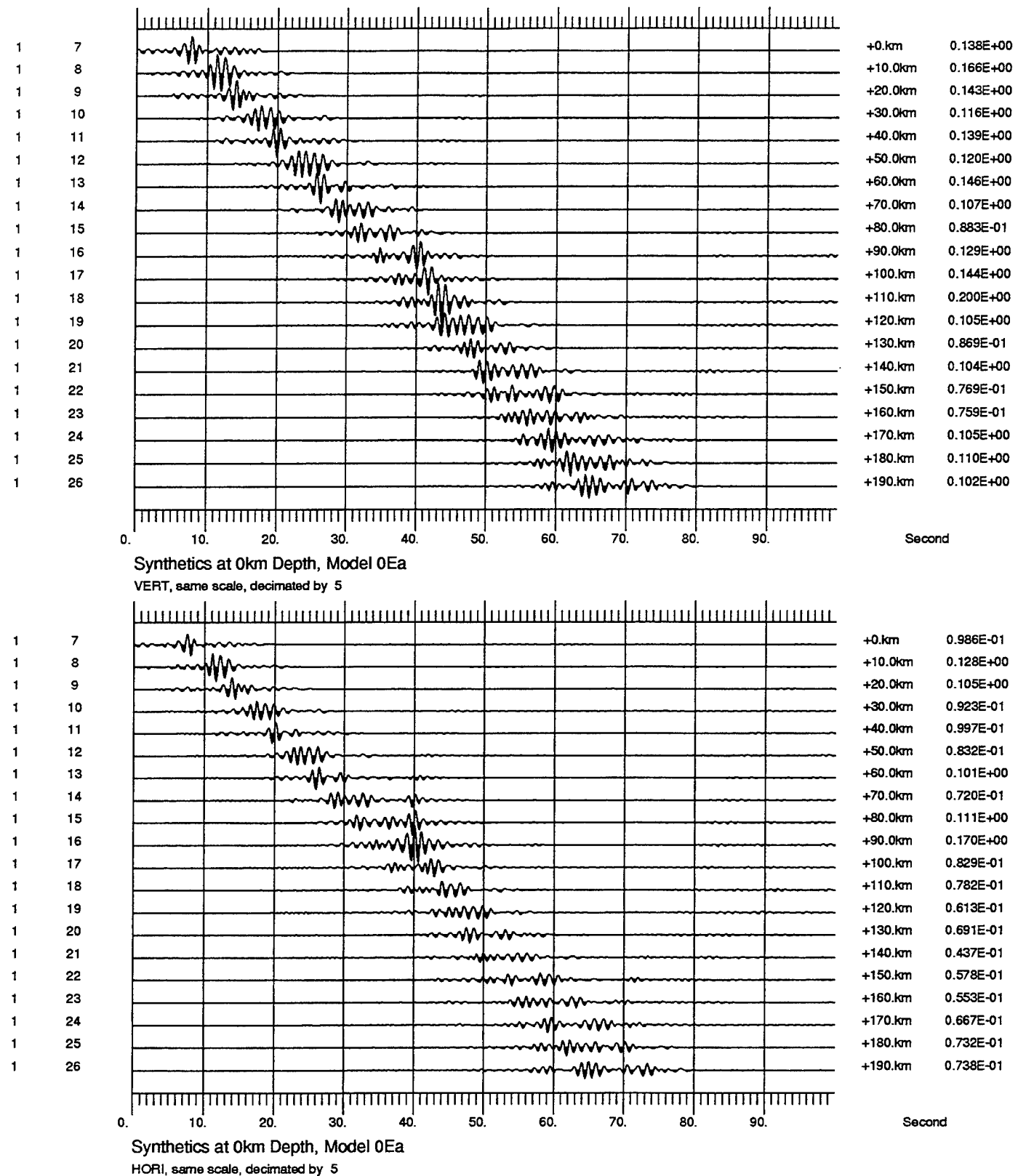
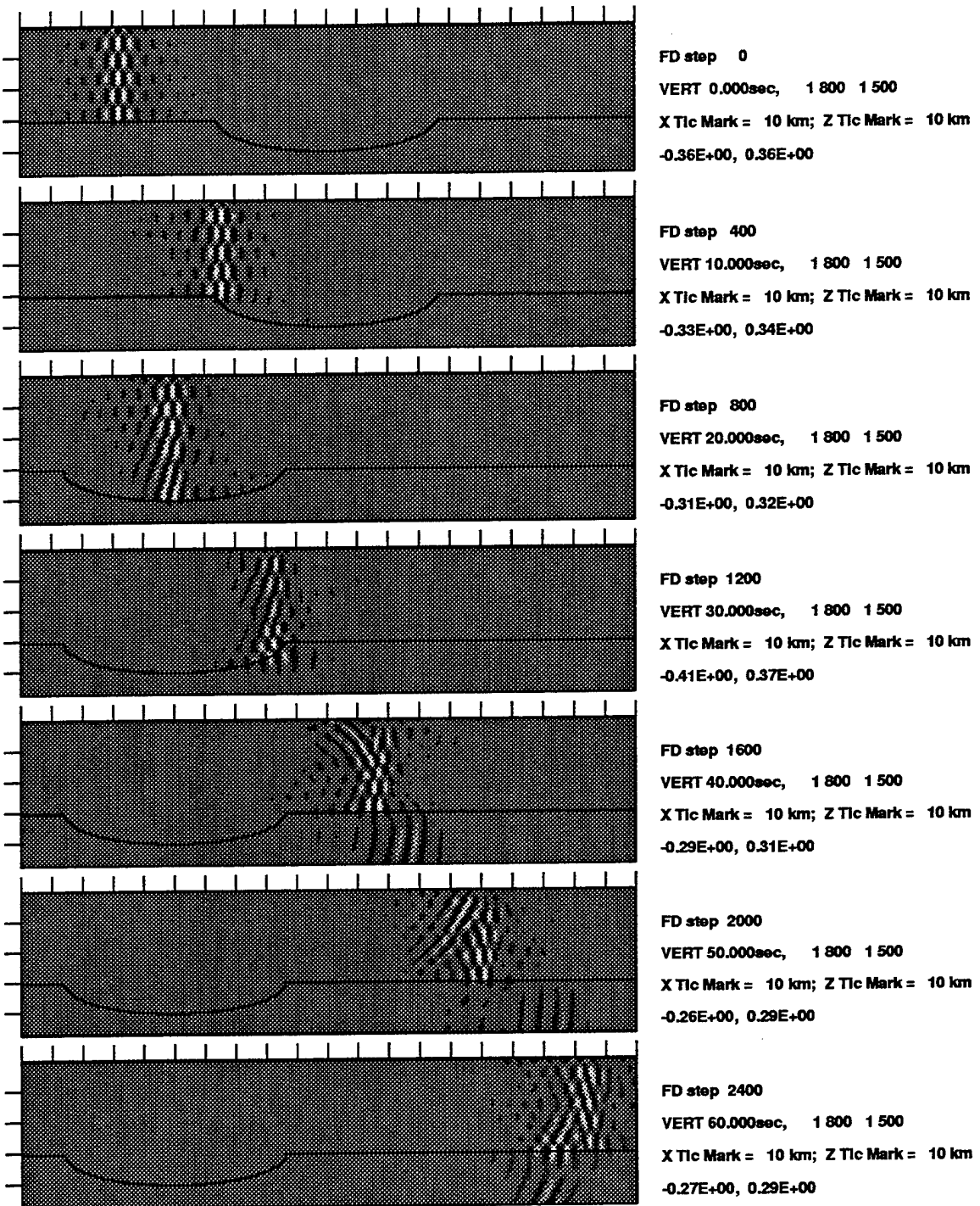
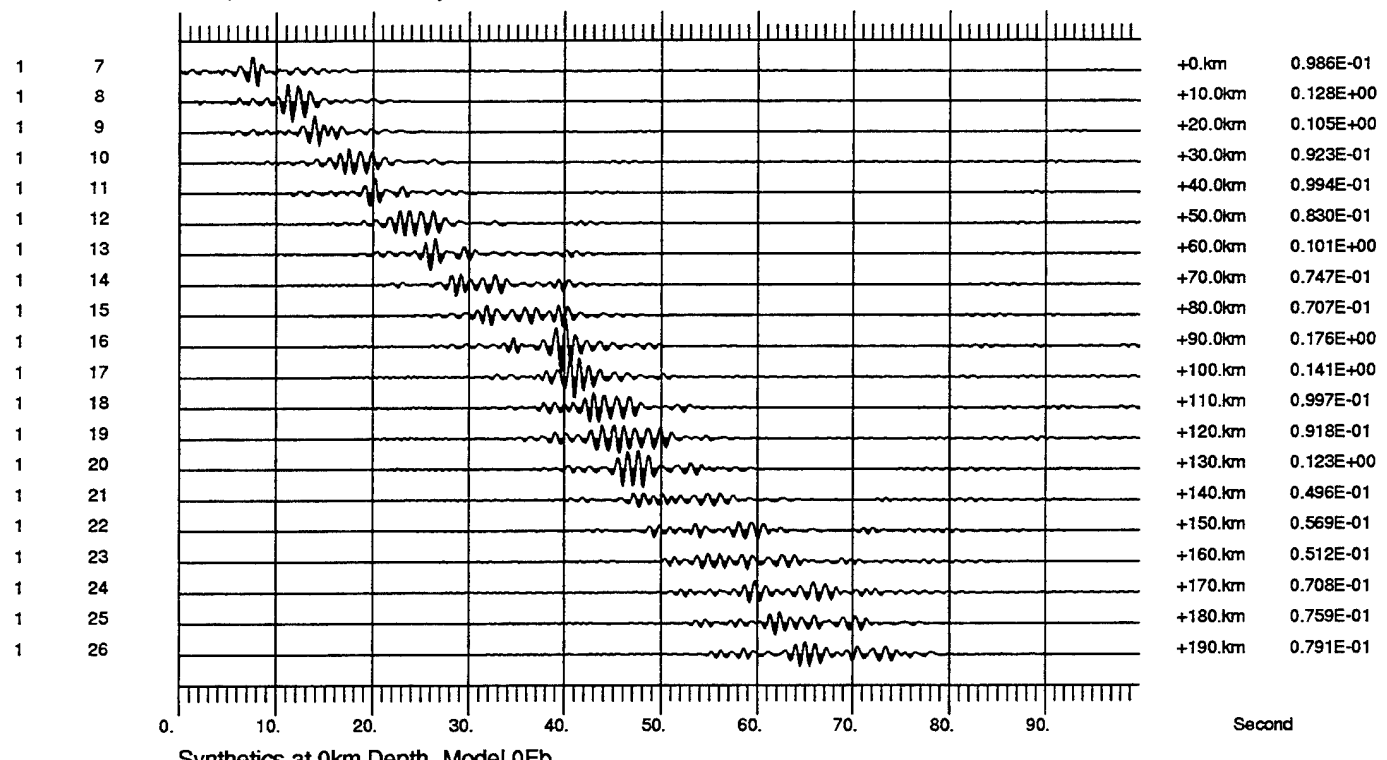
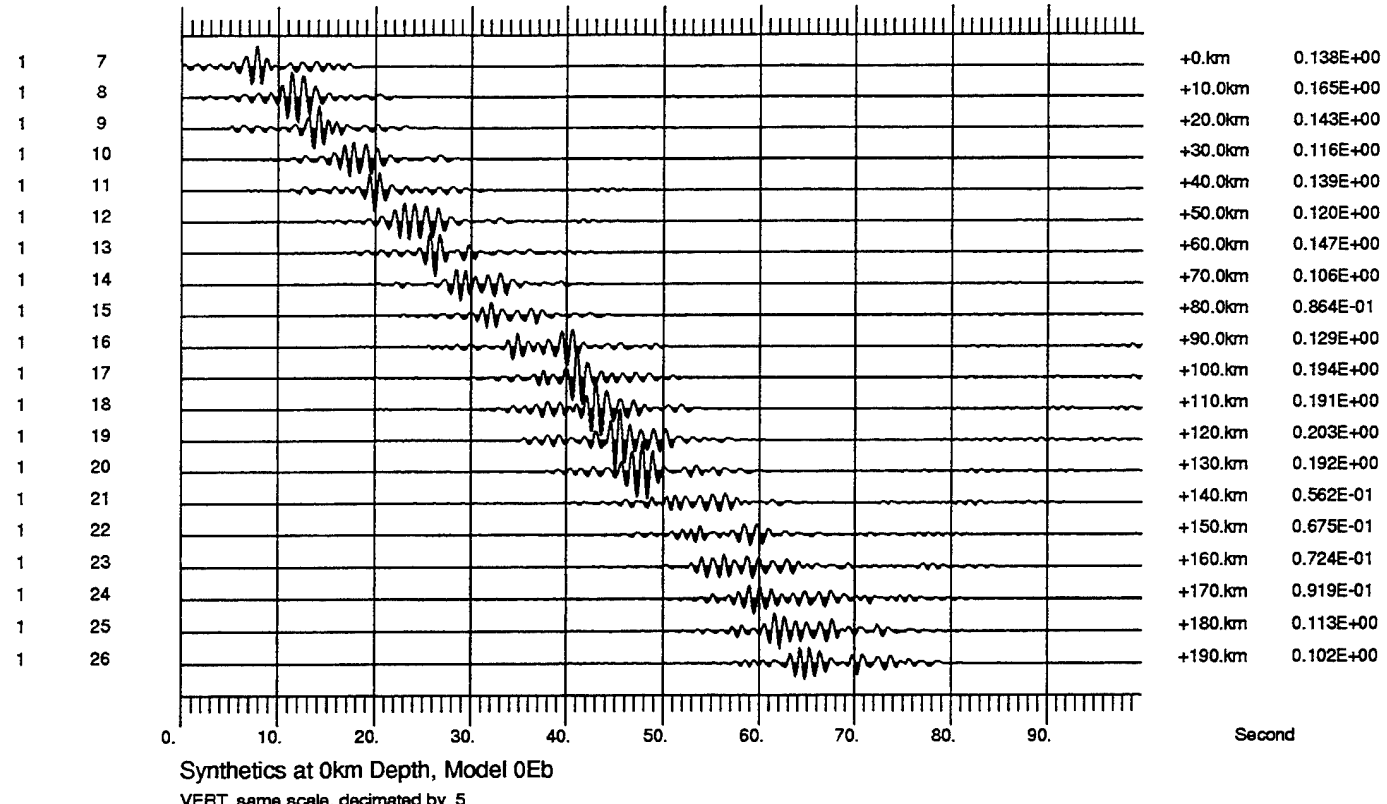


Figure 30. Seismic sections of model 0Ea, which has a thickened crust. The corner where the Moho turns flat is a secondary point source radiating upgoing body waves. The prominent arrival on traces 16 and 17 has a very large apparent velocity, due to a nearly normal incidence. The “on-time  $L_g$ ” is only partially blocked.

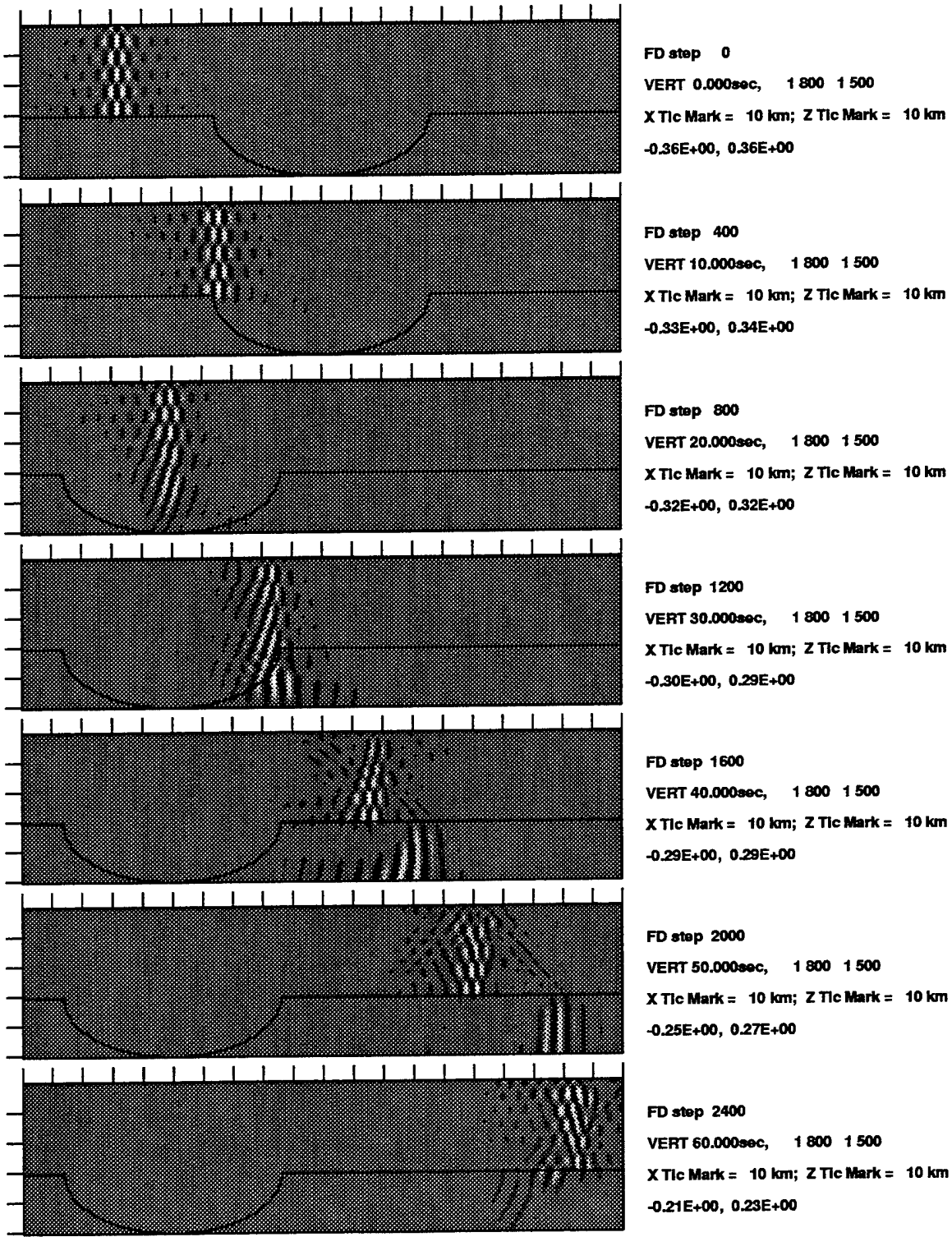


#### LFD Simulation of Lg Propagation: Model 0Eb

**Figure 31.** The vertical-component snapshots of  $L_g$  wave propagation in model 0Eb, with a thickened crust.



**Figure 32.** Seismic sections of model 0Eb, which has a thickened crust. The corner where the Moho turns flat is a secondary point source radiating upgoing body waves. The prominent arrival on traces 16 and 17 has a very large apparent velocity, due to a nearly normal incidence. The “on-time  $L_g$ ” is only partially blocked.



#### LFD Simulation of Lg Propagation: Model 0Ec

Figure 33. The vertical-component snapshots of  $L_g$  wave propagation in model 0Ec, with a thickened crust.

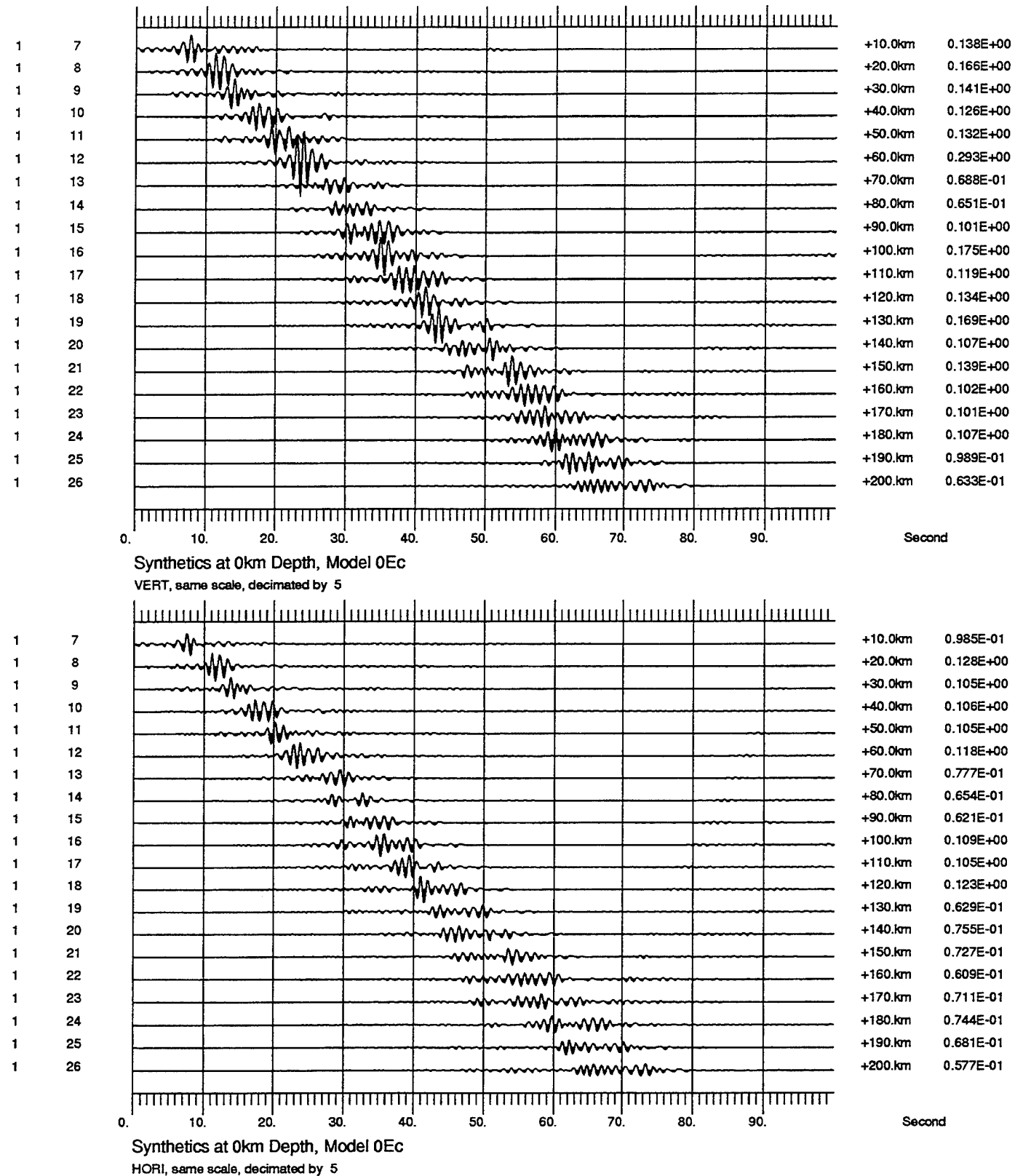
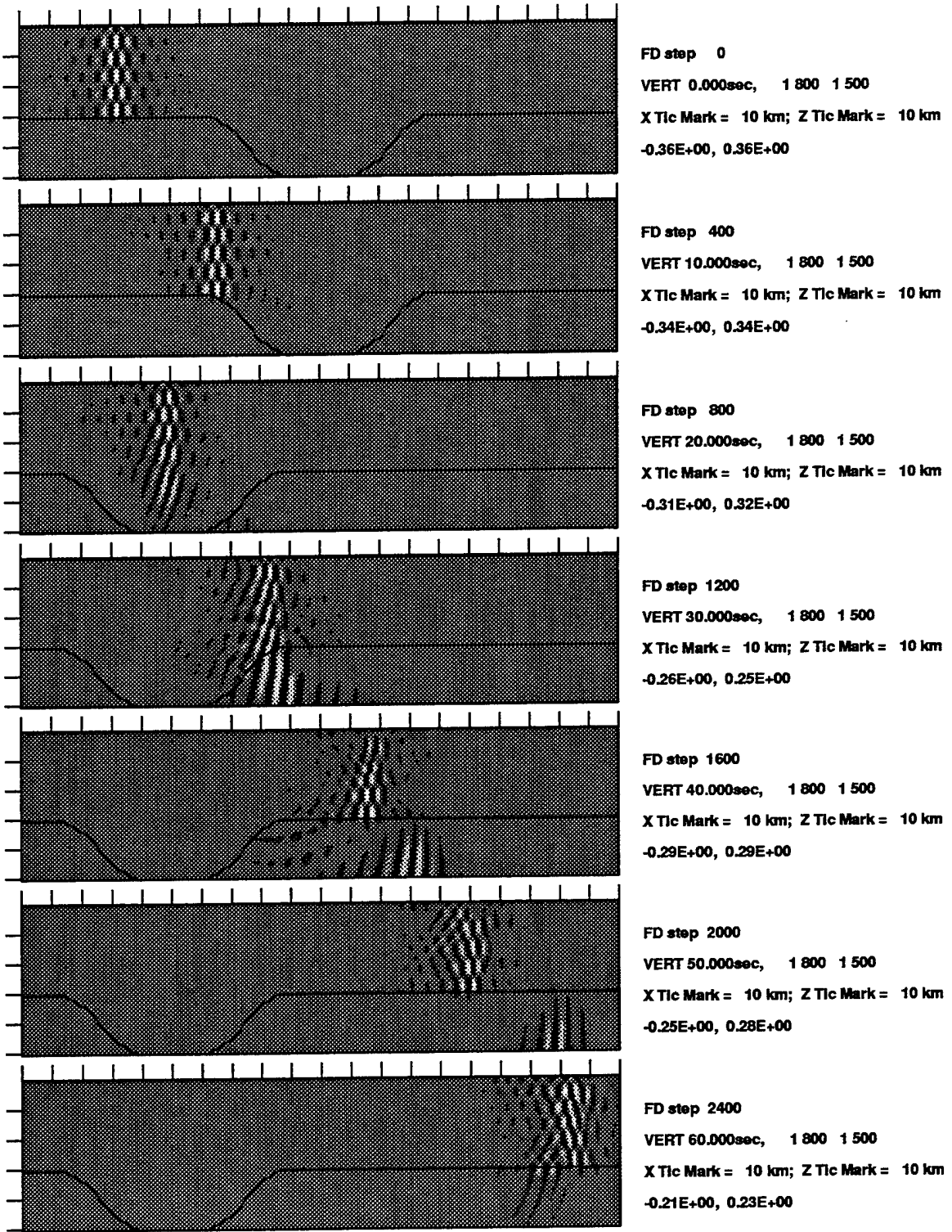
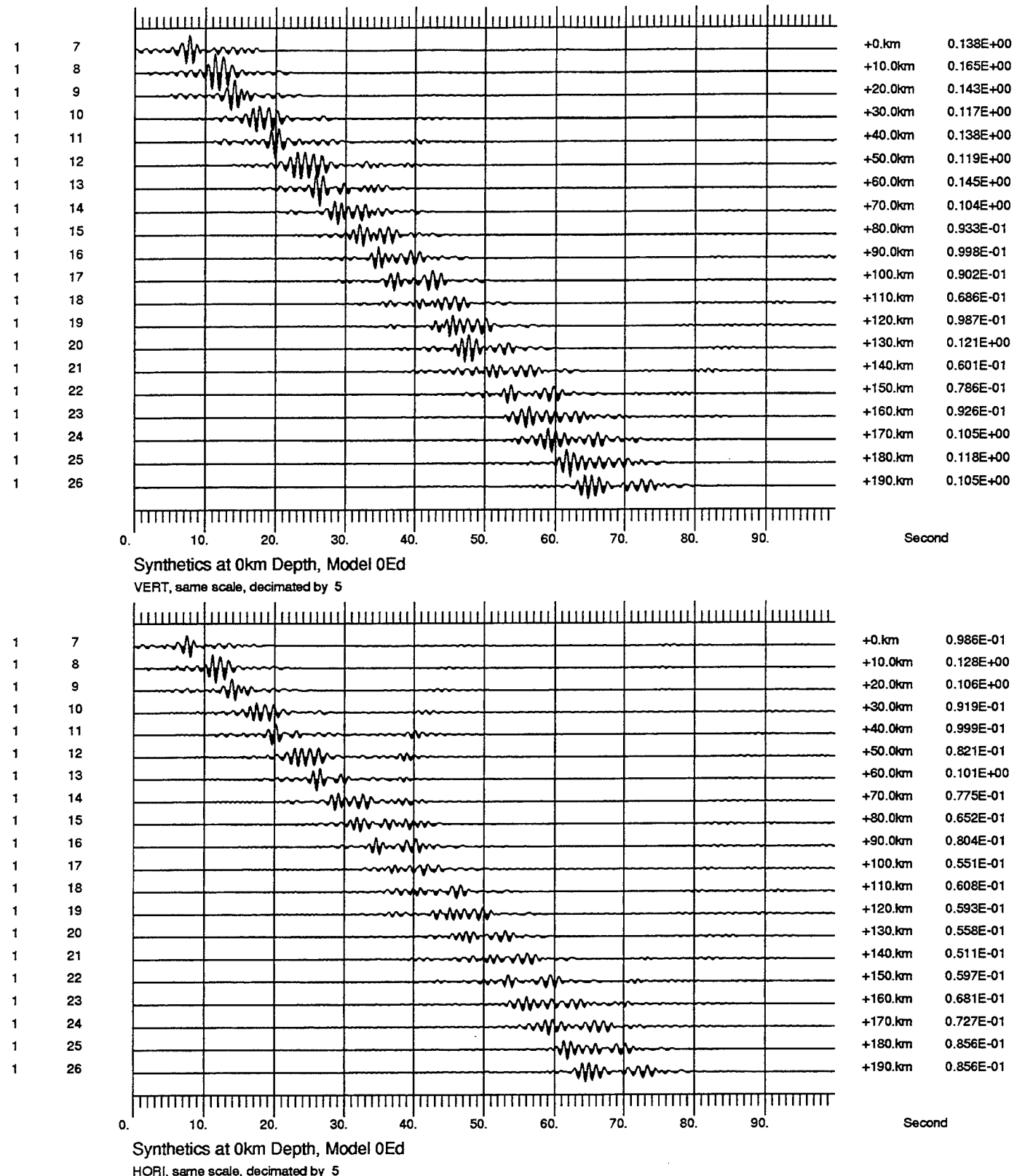


Figure 34. Seismic sections of model 0Ec, which has a thickened crust. The “on-time  $L_g$ ” is only partially blocked.

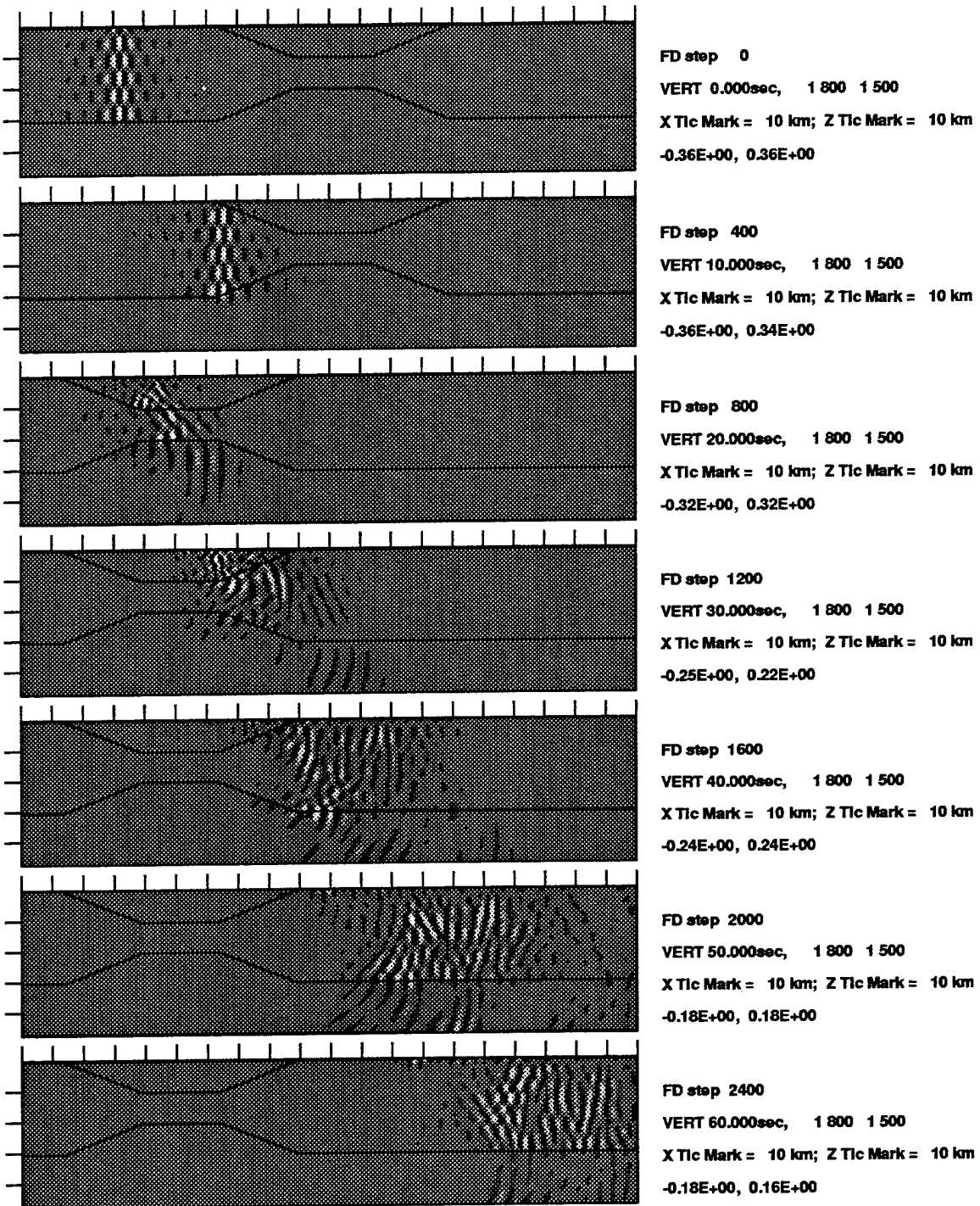


#### LFD Simulation of Lg Propagation: Model 0Ed

Figure 35. The vertical-component snapshots of  $L_g$  wave propagation in model 0Ed, with a thickened crust.



**Figure 36.** Seismic sections of model 0Ed, which has a thickened crust. The corner where the Moho turns flat is a secondary point source radiating upgoing body waves. The prominent arrival on traces 16 and 17 has a very large apparent velocity, due to a nearly normal incidence. The "on-time  $L_g$ " is only partially blocked.



#### LFD Simulation of $L_g$ Propagation: Model OF

**Figure 37.** The vertical-component snapshots of  $L_g$  wave propagation in model OF, which has both a sedimentary basin and a Moho uplift. The Moho uplift causes a strong  $S_n$  conversion (see, at 20 seconds). The pinched end of the basin radiates body waves outward, and some of those rays leak into deeper mantle.

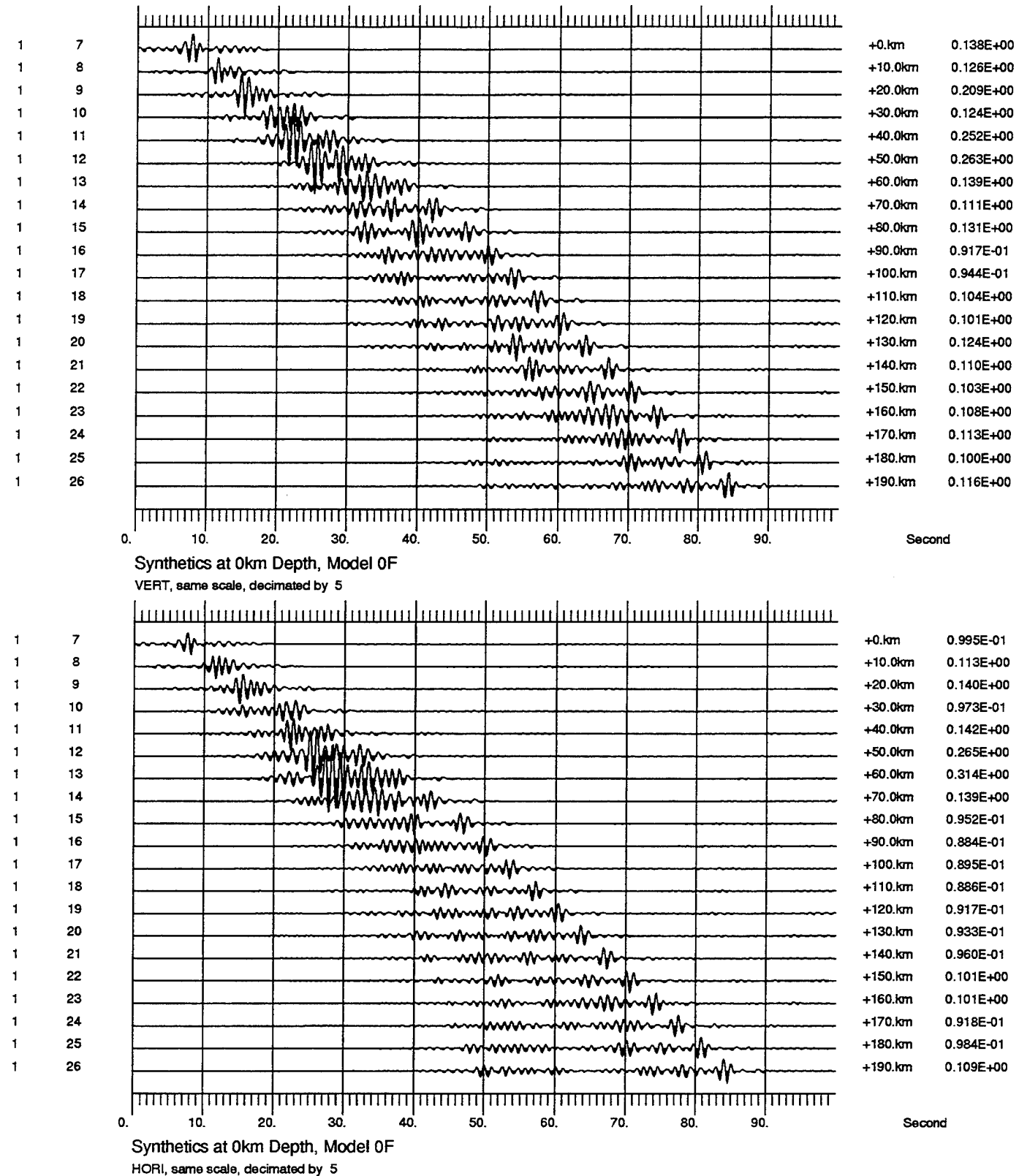
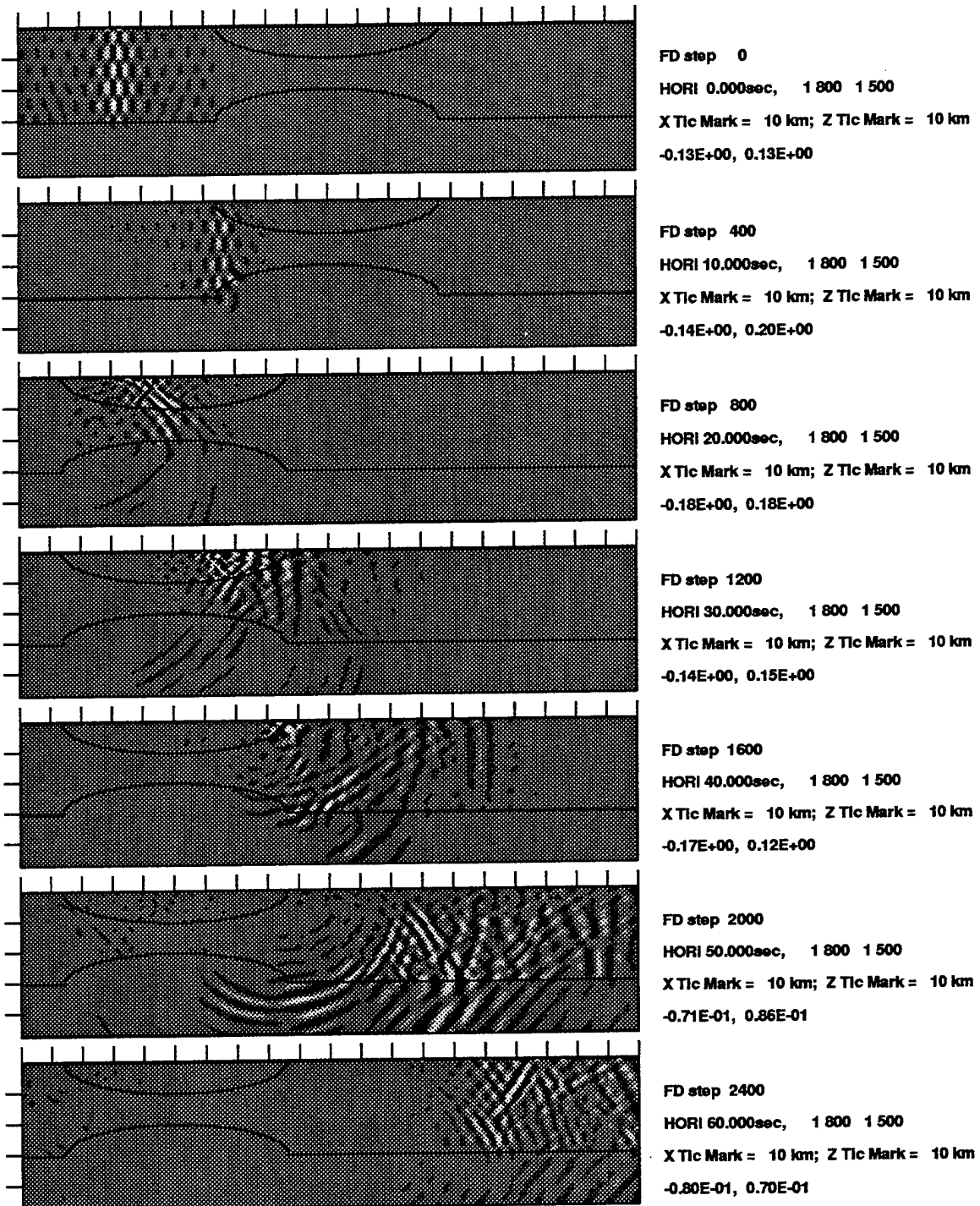


**Figure 38.** Seismic sections of model OF, which has a Moho uplift and a sedimentary basin.



#### LFD Simulation of Lg Propagation: Model 0Fa

**Figure 39.** The horizontal-component snapshots of  $L_g$  wave propagation in model 0Fa, which has both a sedimentary basin and a Moho uplift. Observations similar to those with the model 0F can be made. The pinched end of the basin radiates body waves outward, and some of those rays leak into deeper mantle (see, at 50 seconds). Some direct P waves are also present (see, at 40 seconds).

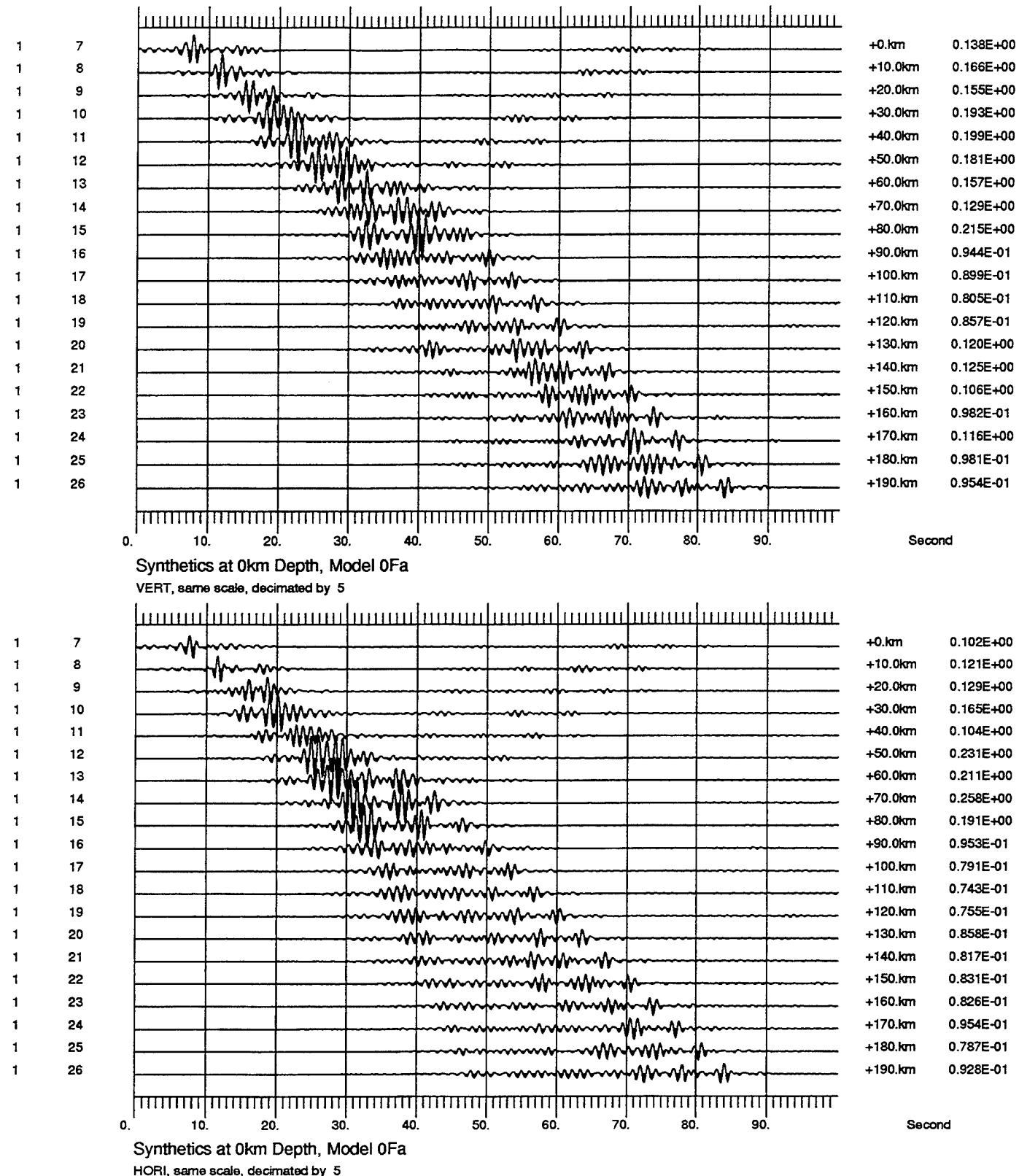
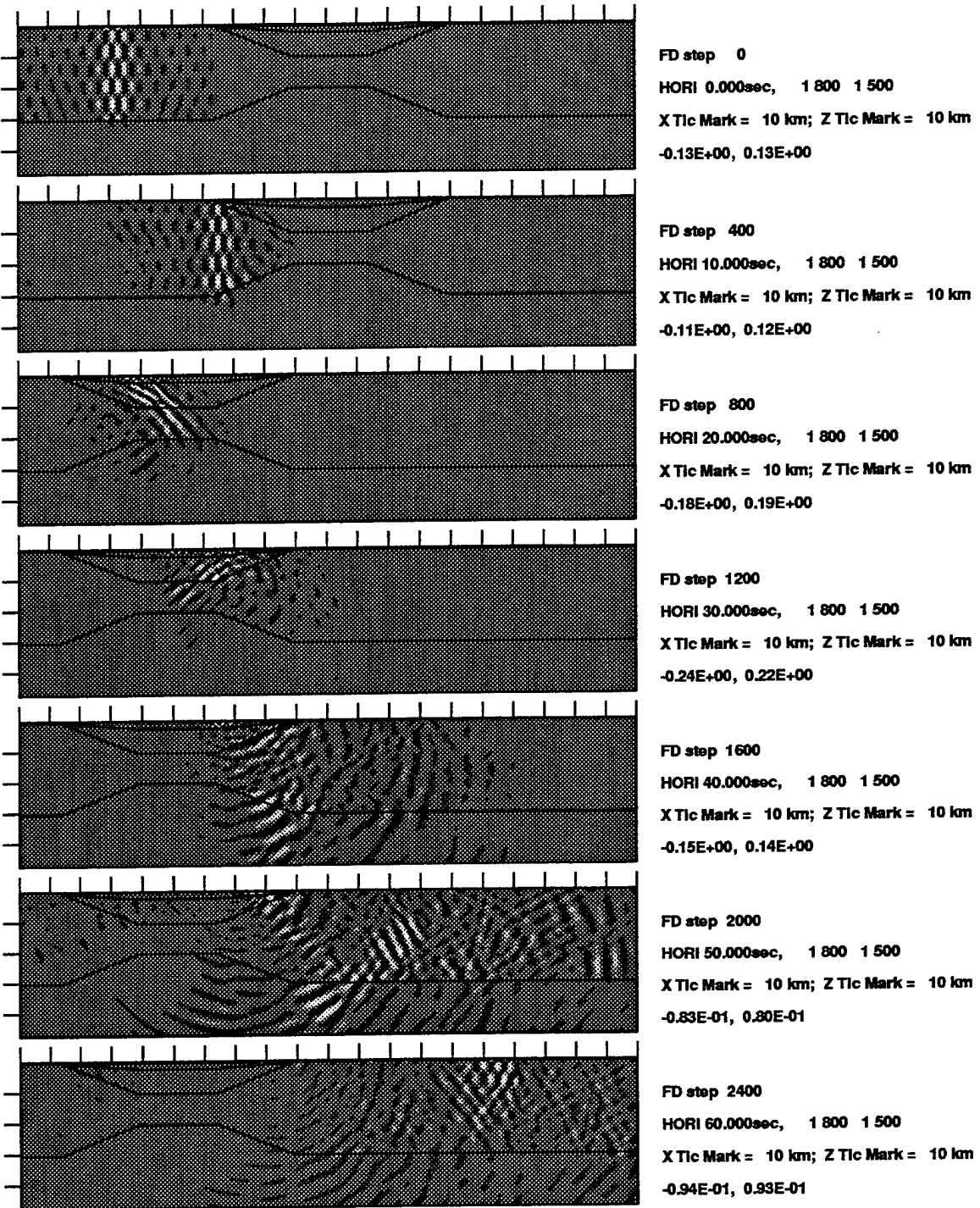
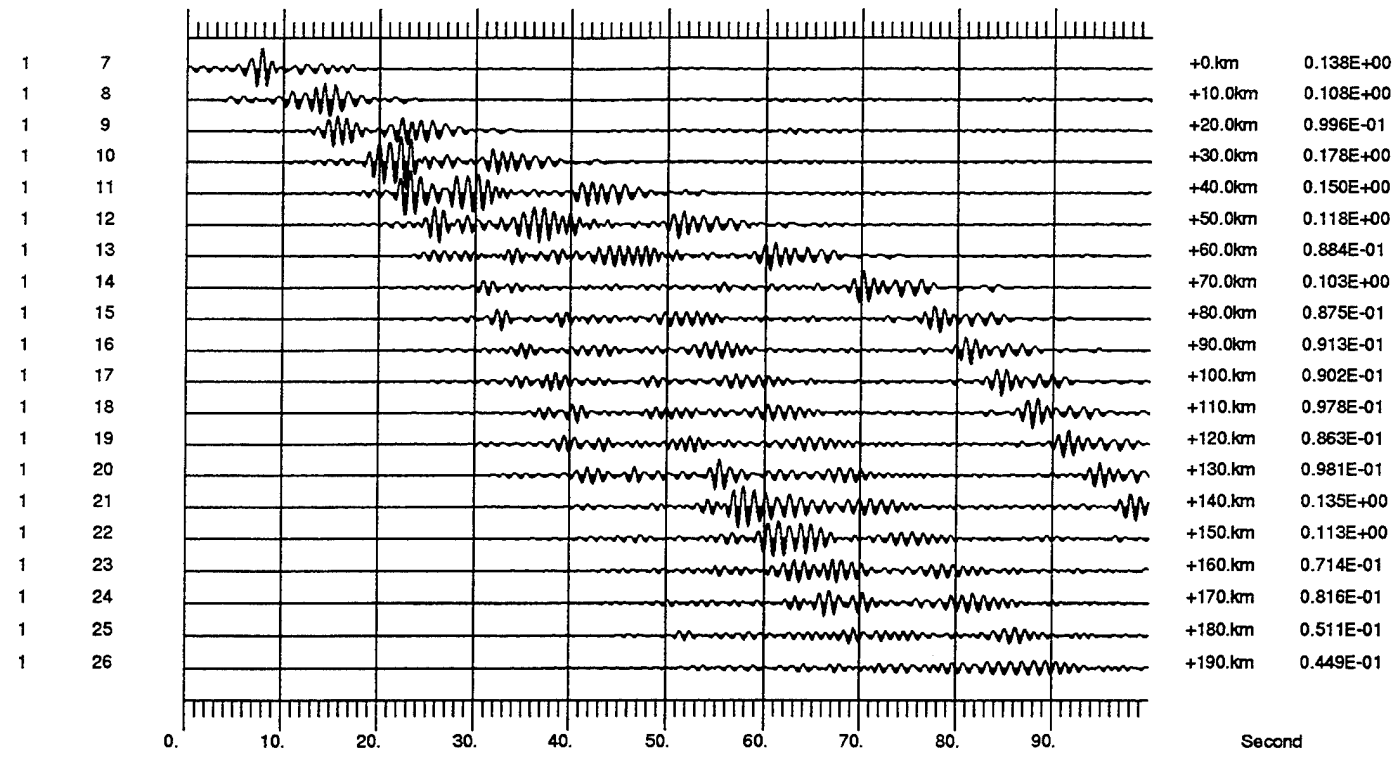


**Figure 40.** Seismic sections of model OFa, which has a Moho uplift and a sedimentary basin. Partial blockage of “on-time  $L_g$ ” is observable. Much of the energy is delayed because of the sedimentary basin. Direct P waves radiated from the basin’s terminating edge can be seen on the horizontal components.



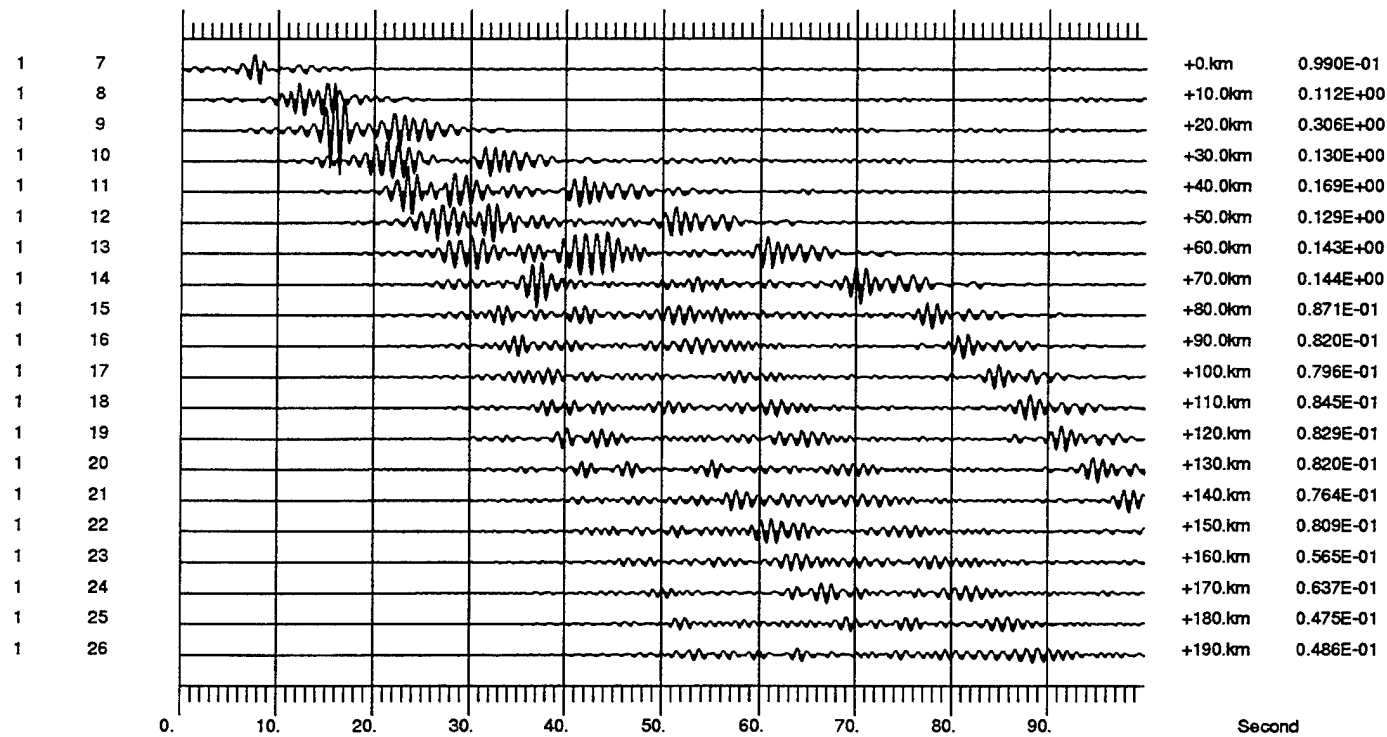
#### LFD Simulation of Lg Propagation: Model 0Fb

**Figure 41.** The horizontal-component snapshots of  $L_g$  wave propagation in model 0Fb, which has two sedimentary layers and a Moho uplift. Observations similar to those with the models 0F and 0Fa can be made: the basin edge acts like a secondary point source. A prominent SmS-mode of propagation is quite clear at 50 seconds. The visibility of this phase is distance-dependent.



Synthetics at 0km Depth, Model 0Fb

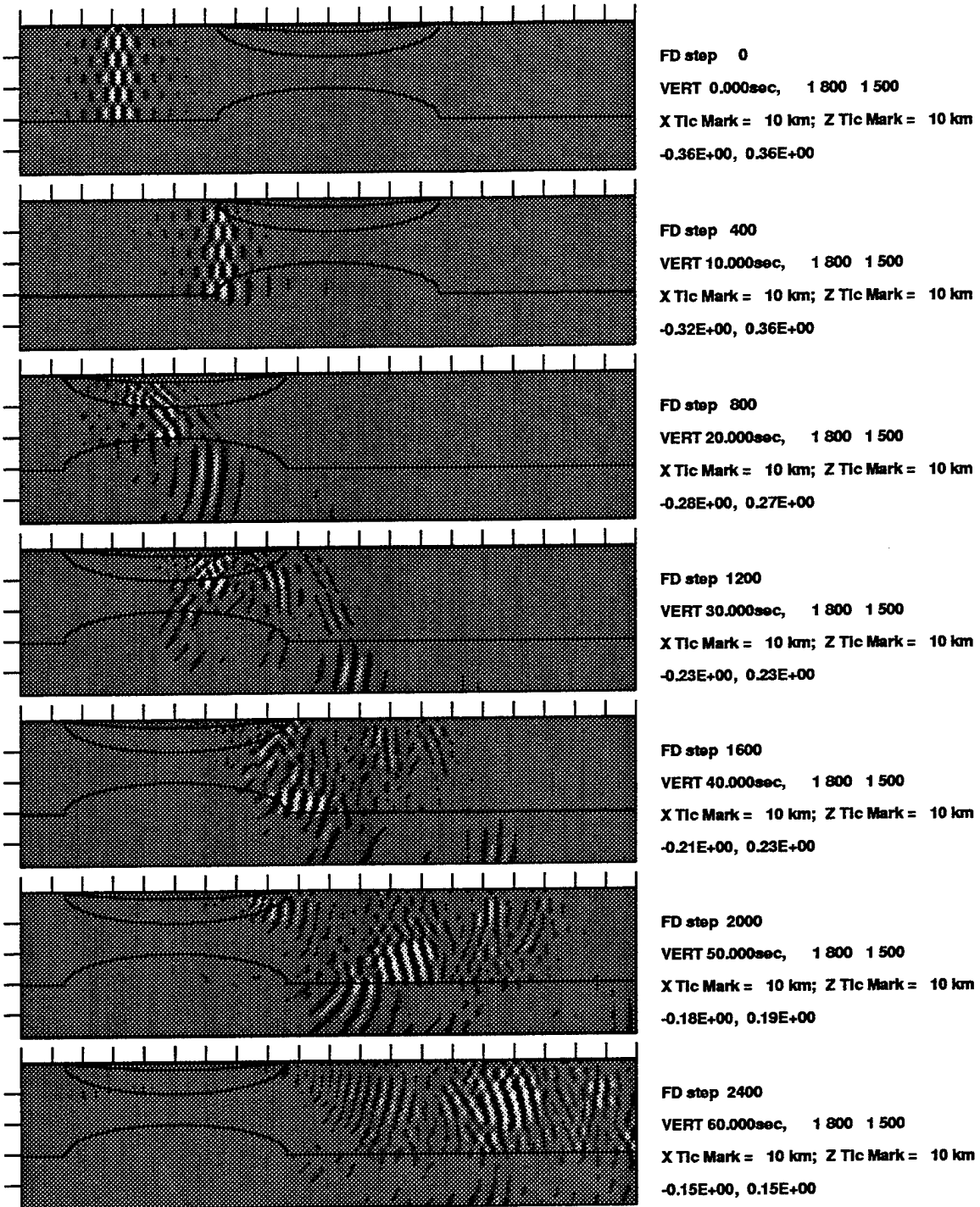
VERT, same scale, decimated by 5



Synthetics at 0km Depth, Model 0Fb

HORI, same scale, decimated by 5

**Figure 42.** Seismic sections of model 0Fb, which has a Moho uplift and two sedimentary layers. "On-time  $L_g$ " is essentially blocked whereas two groups of "late  $L_g$ " waves as well as the further delayed  $R_g$  are present. The prominent phase arriving between 55 and 70 seconds on traces 20 through 24 is a SmS phase originated from the basin edge.



#### LFD Simulation of Lg Propagation: Model 0Fc

**Figure 43.** The vertical-component snapshots of  $L_g$  wave propagation in model 0Fc, which has two sedimentary layers and a Moho uplift. Observations similar to those with model 0Fb can be made: the basin edge acts like a secondary point source. A prominent SmS-mode of propagation is quite clear at 50 and 60 seconds. The visibility of this phase is distance-dependent, however.

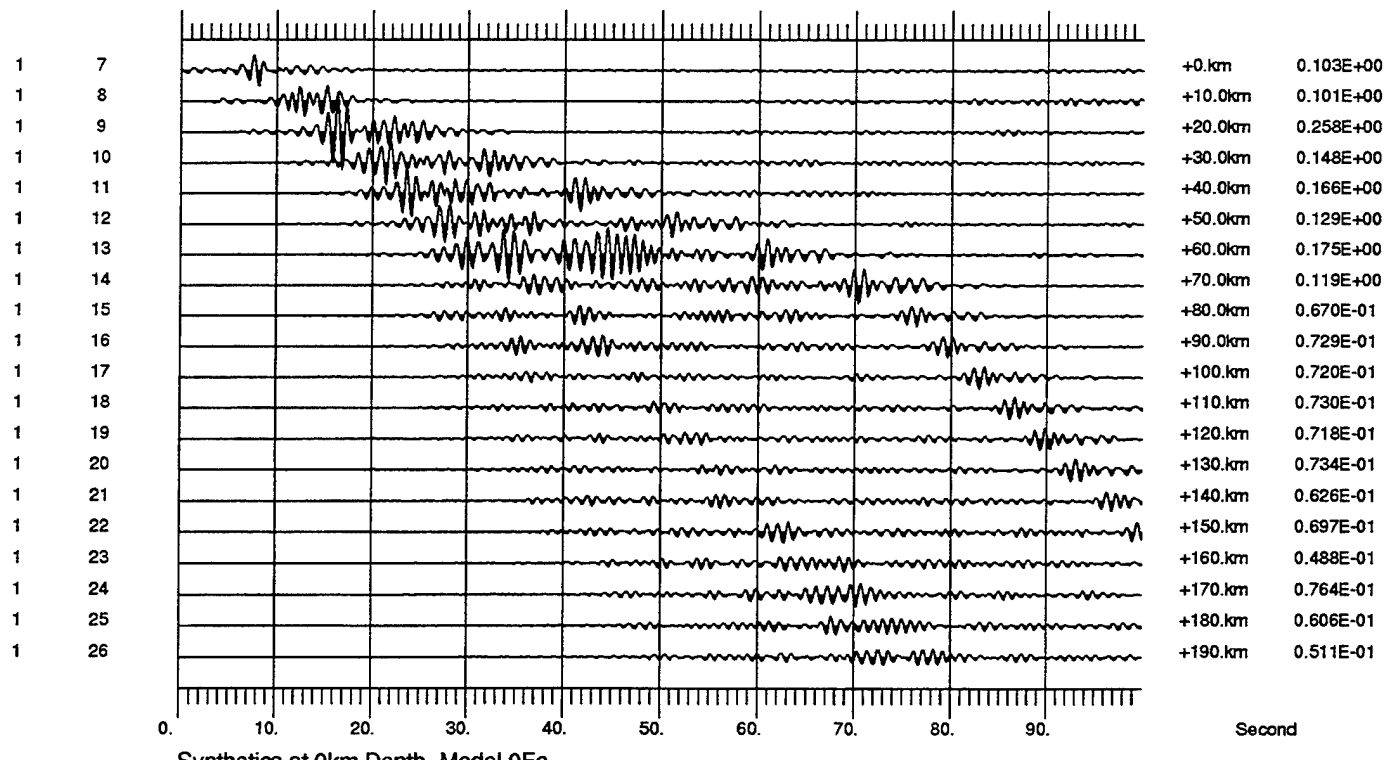
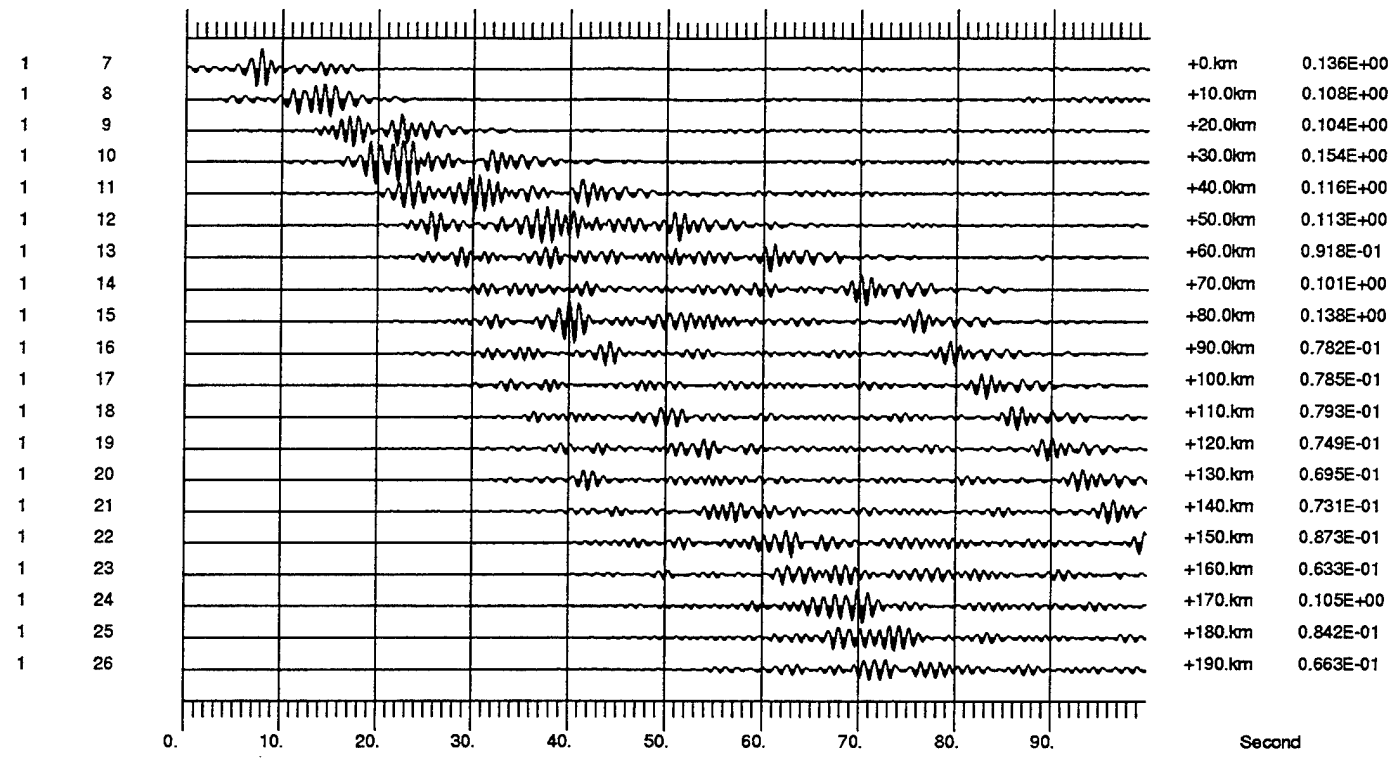
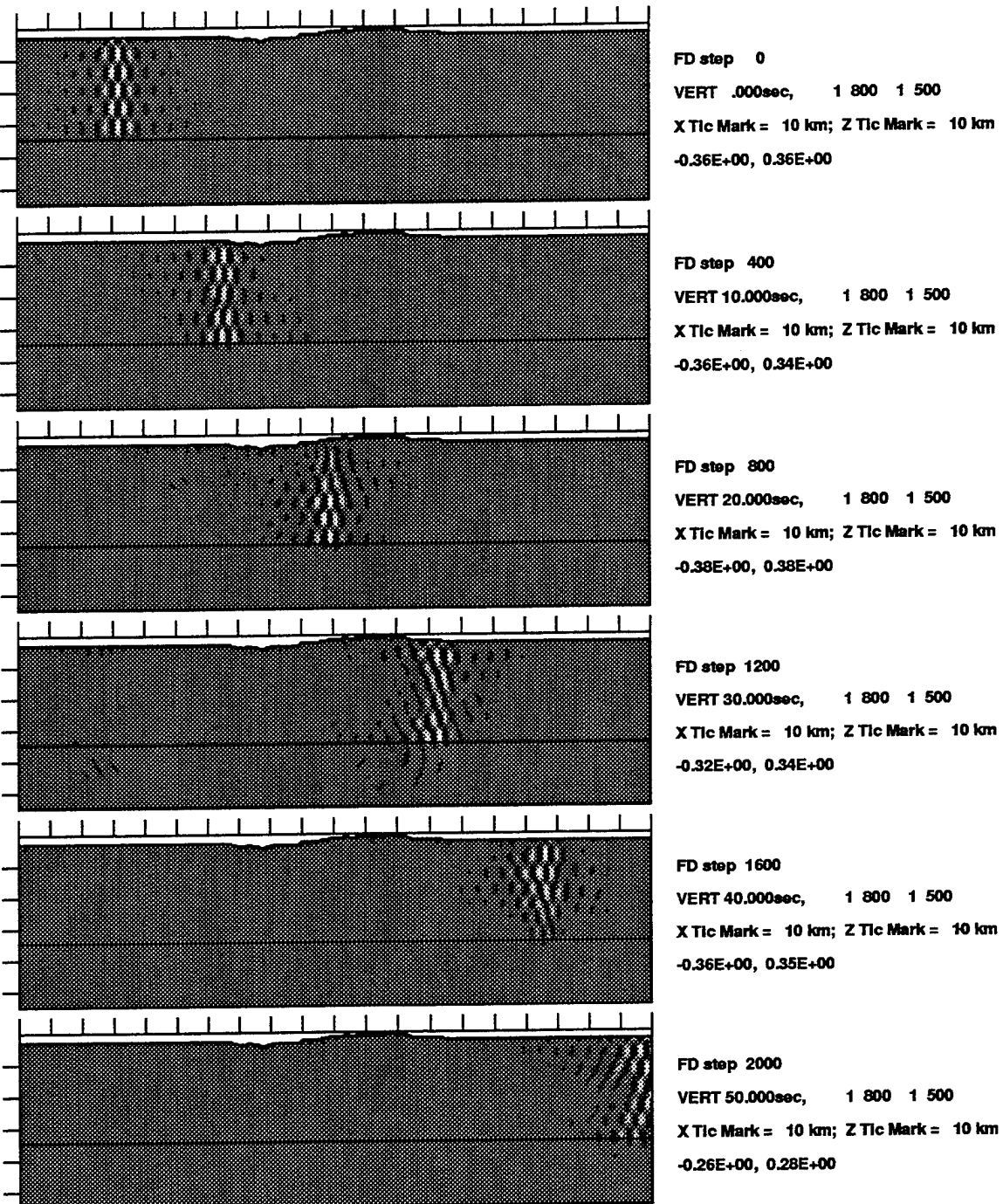
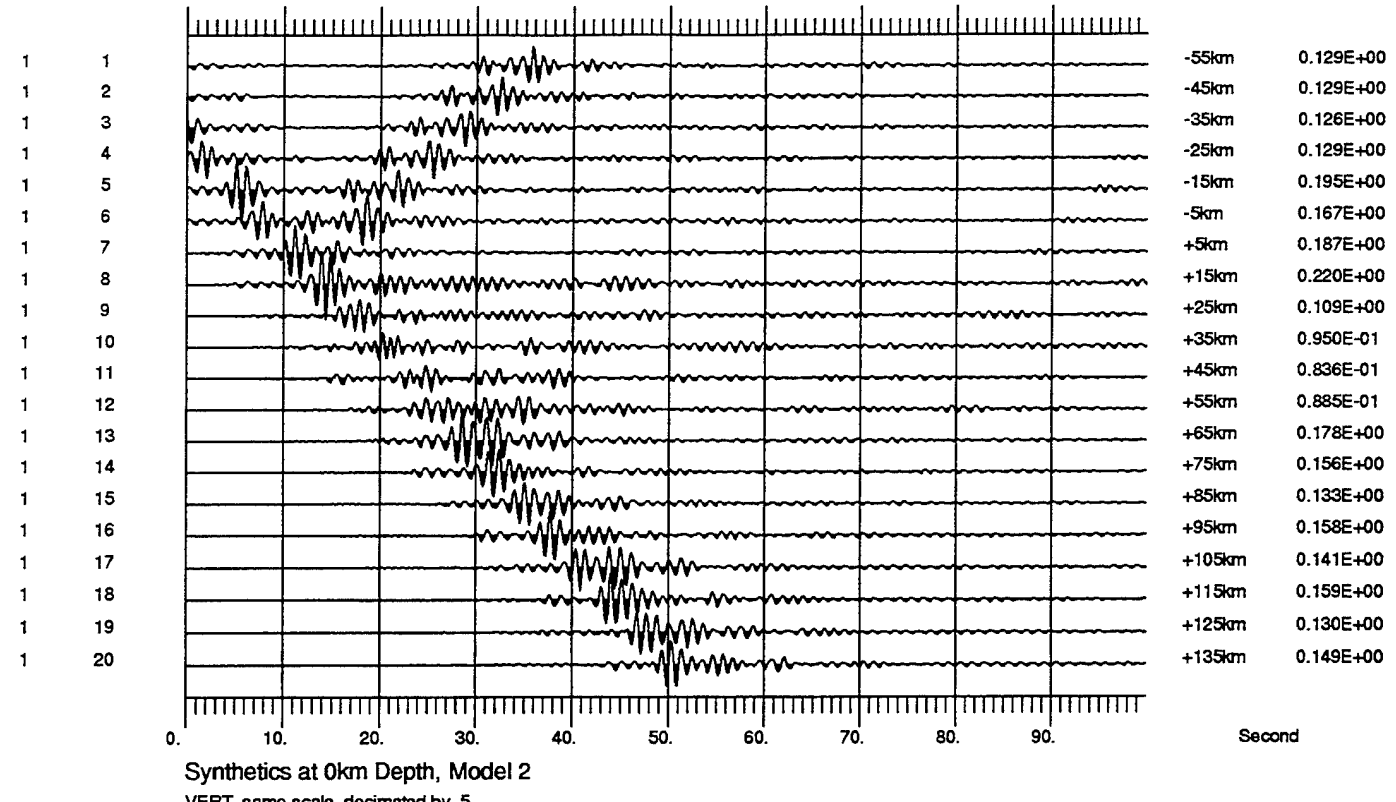


**Figure 44.** Seismic sections of model 0Fc, which has a Moho uplift and two sedimentary layers. The most prominent phase before  $R_g$  is the SmS radiated from the basin edge, which can be seen at certain receivers, depending on the distance (see traces No. 21 through 26).



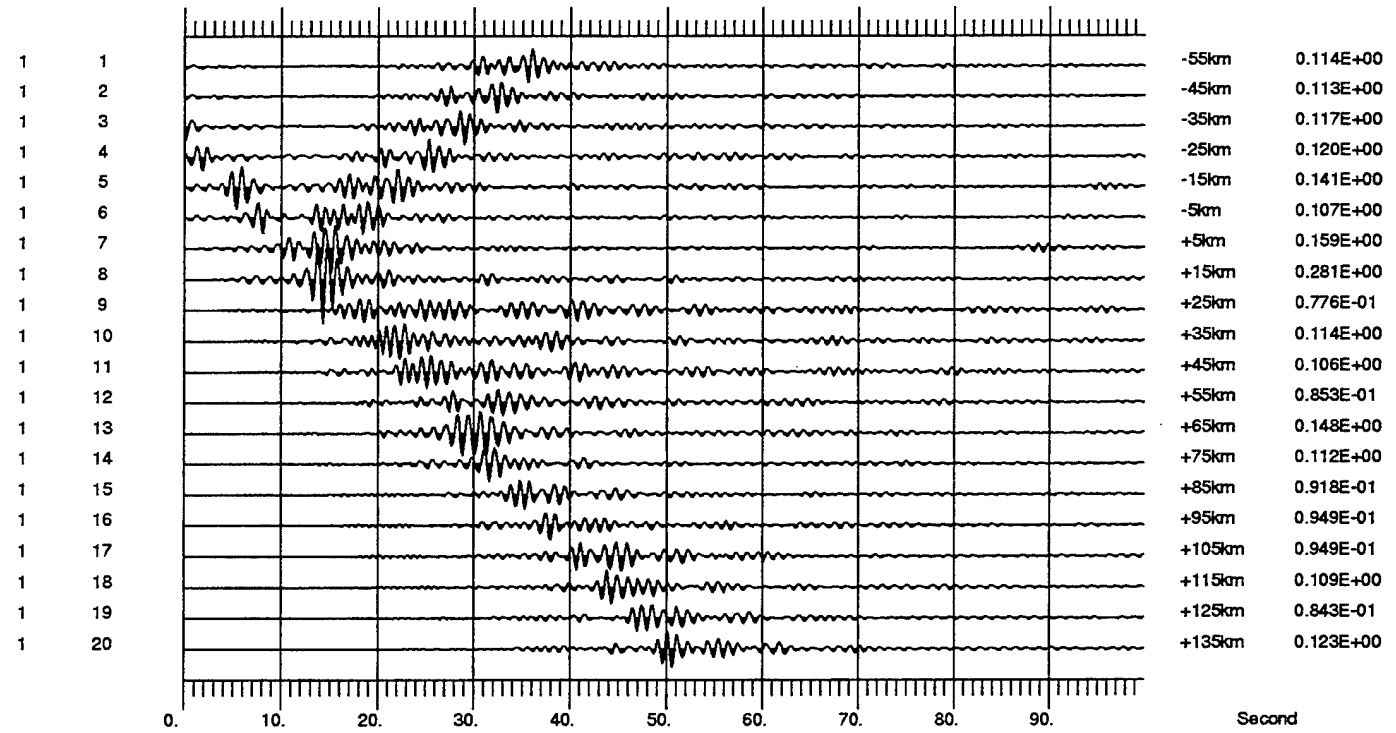
LFD Simulation of Lg Propagation: Model 2

**Figure 45.** The vertical-component snapshots of  $L_g$  wave propagation of model 2, which has a flat Moho and a moderate free-surface topography. The  $L_g$ -to- $S_n$  conversion is relatively weak. This is very different from the case of  $R_g$  where scattering by rough topography would cause very strong apparent attenuation.



Synthetics at 0km Depth, Model 2

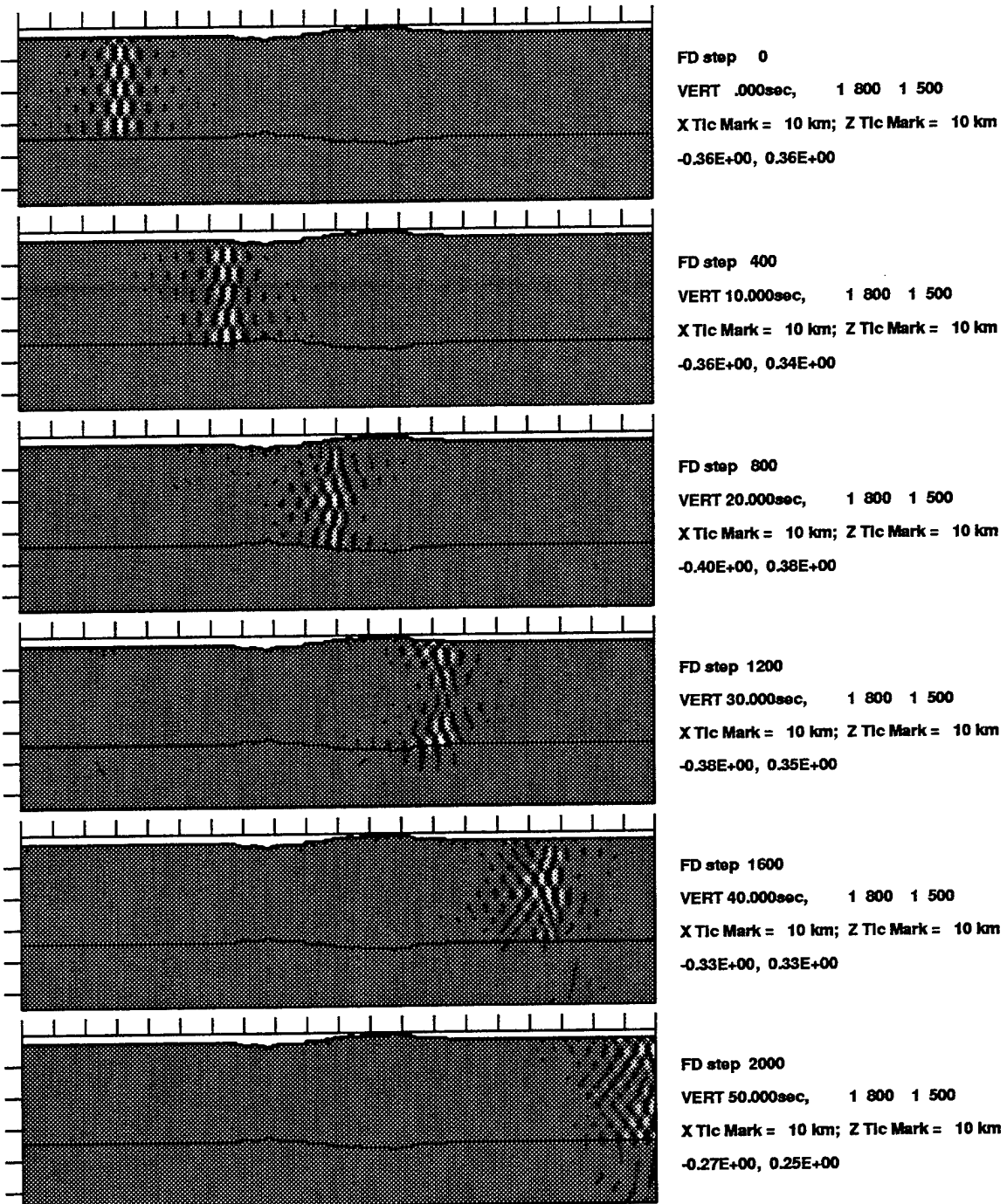
VERT, same scale, decimated by 5



Synthetics at 0km Depth, Model 2

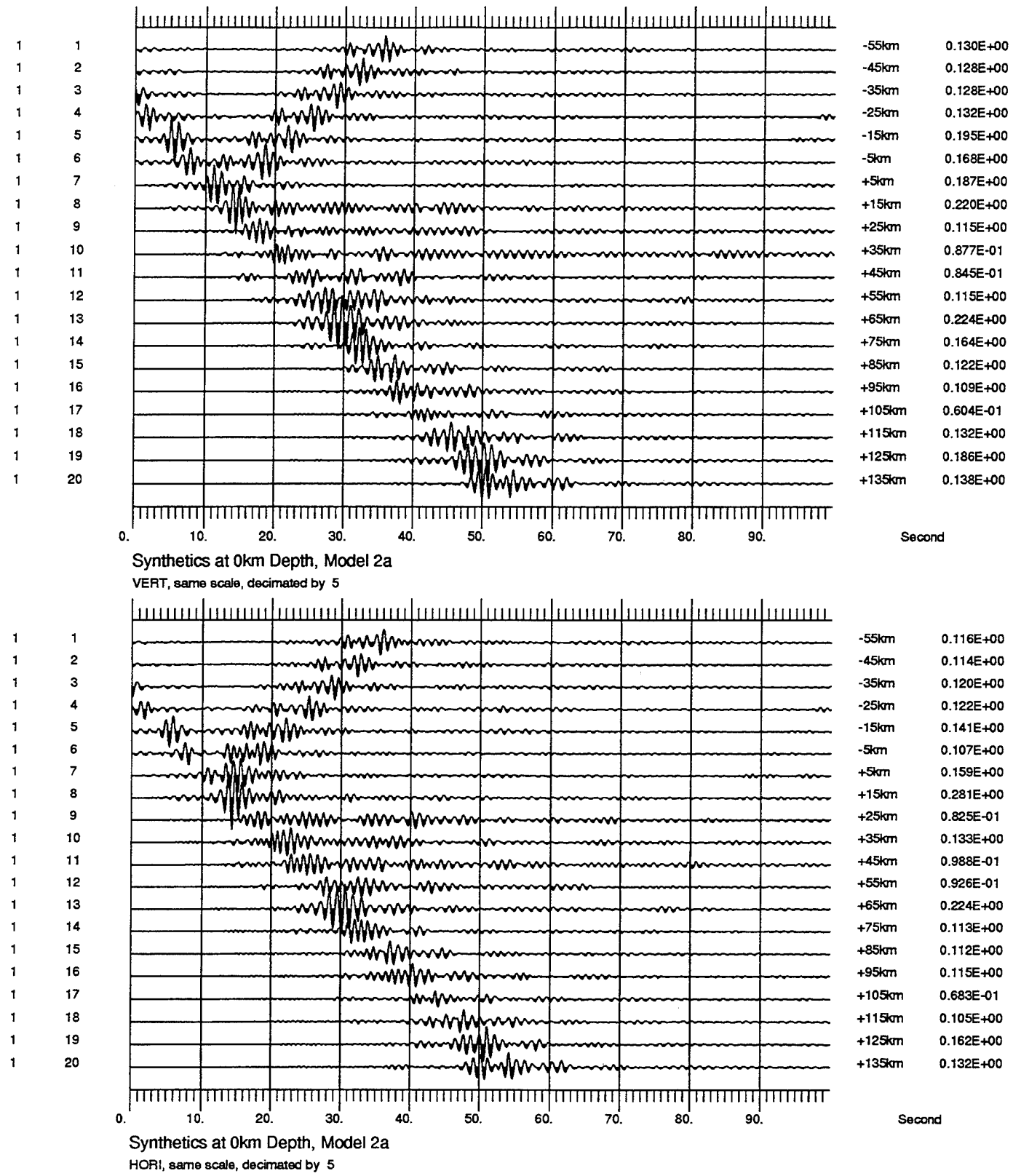
HORI, same scale, decimated by 5

**Figure 46.** Seismic sections of model 2, which has a moderate free-surface topography. The scattering effects of topography on  $L_g$  are not as strong as those due to large-scale structural discontinuities.

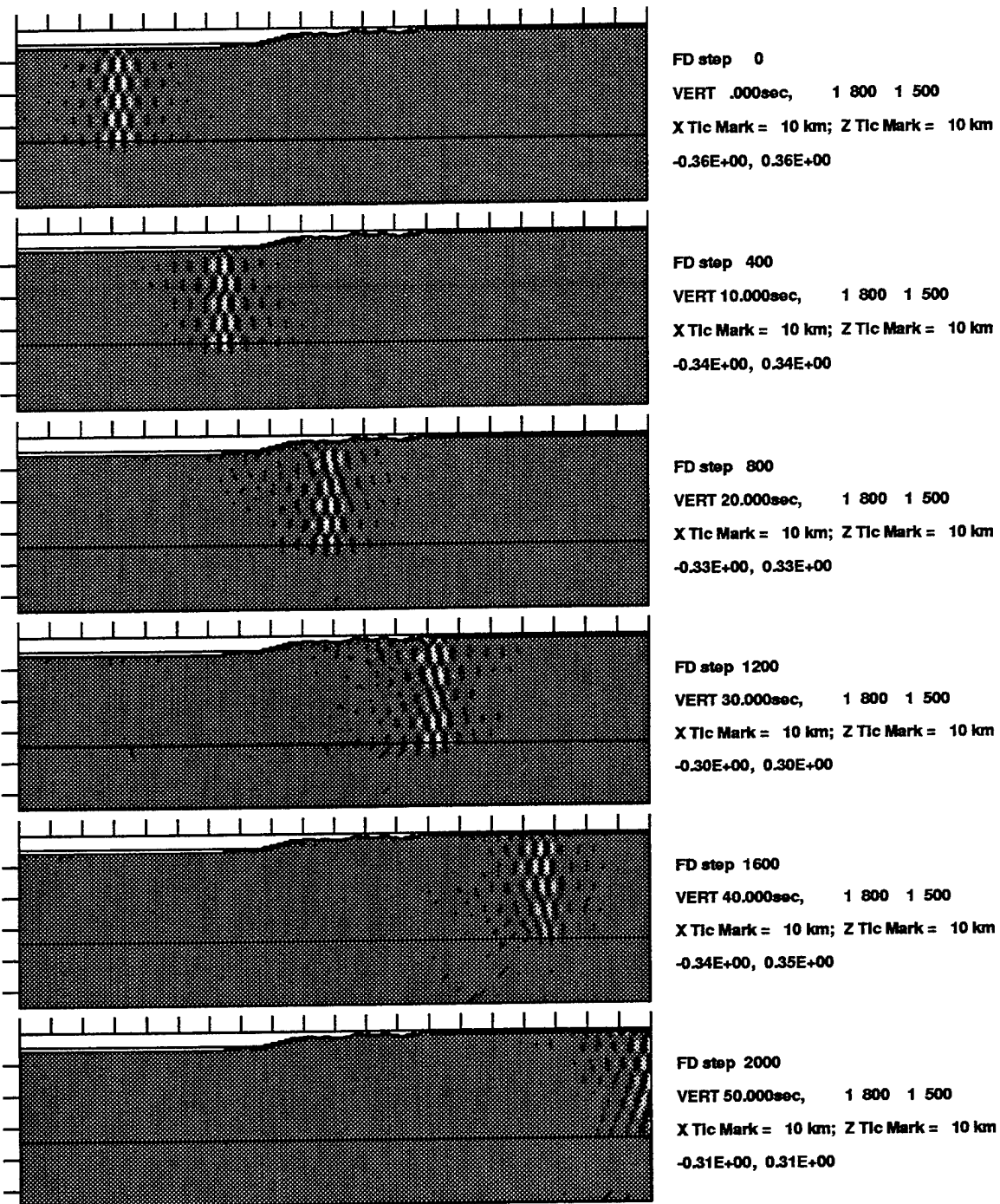


LFD Simulation of  $L_g$  Propagation: Model 2a

**Figure 47.** The vertical-component snapshots of  $L_g$  wave propagation of model 2a, in which the Moho is fully compensated. The elevation change of this topographic profile is relatively small compared to the thickness of the homogeneous crust, and hence the transmission of  $L_g$  is still fairly efficient.

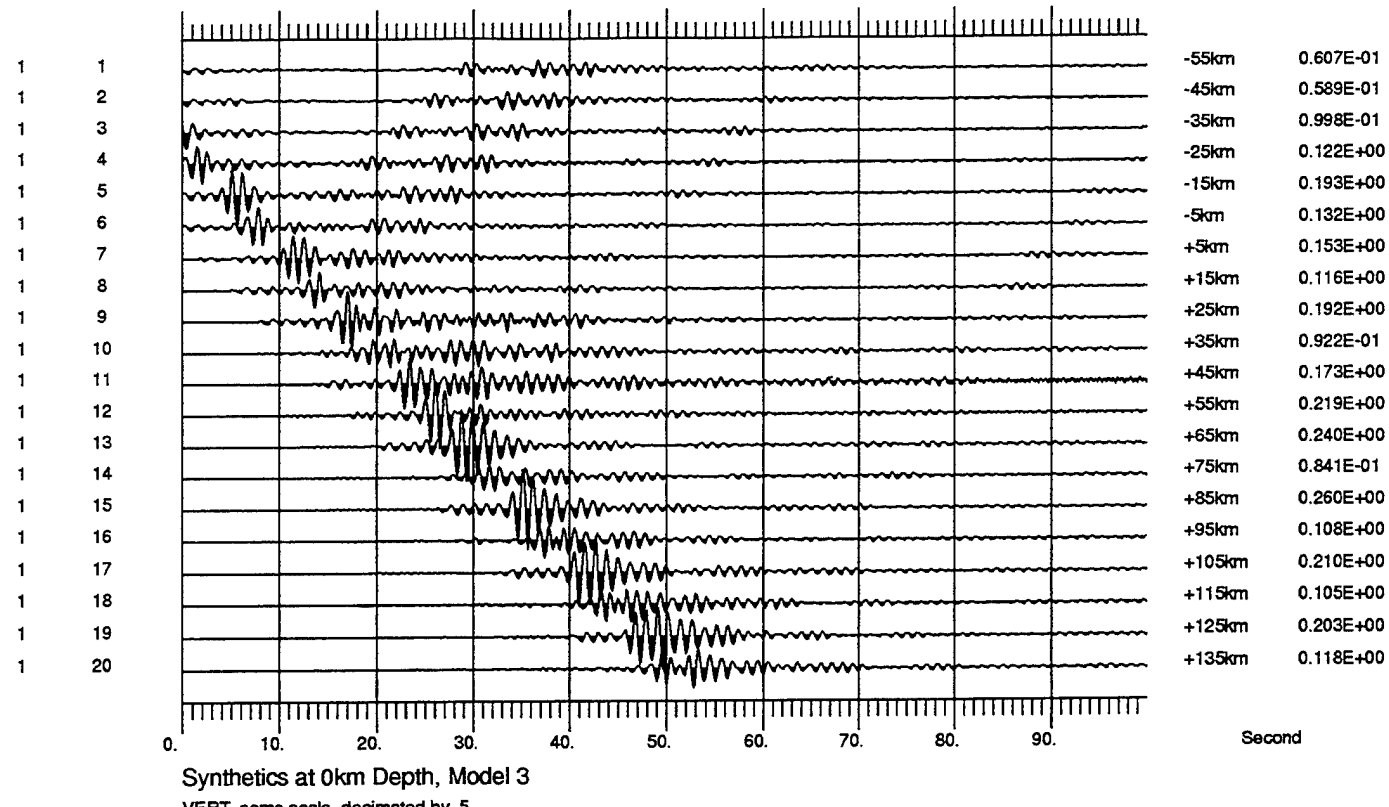


**Figure 48.** Seismic sections of model 2a, which has a moderate free-surface topography and a fully compensated Moho. The scattering effects of topography on  $L_g$  are not as strong as those due to large-scale structural discontinuities.



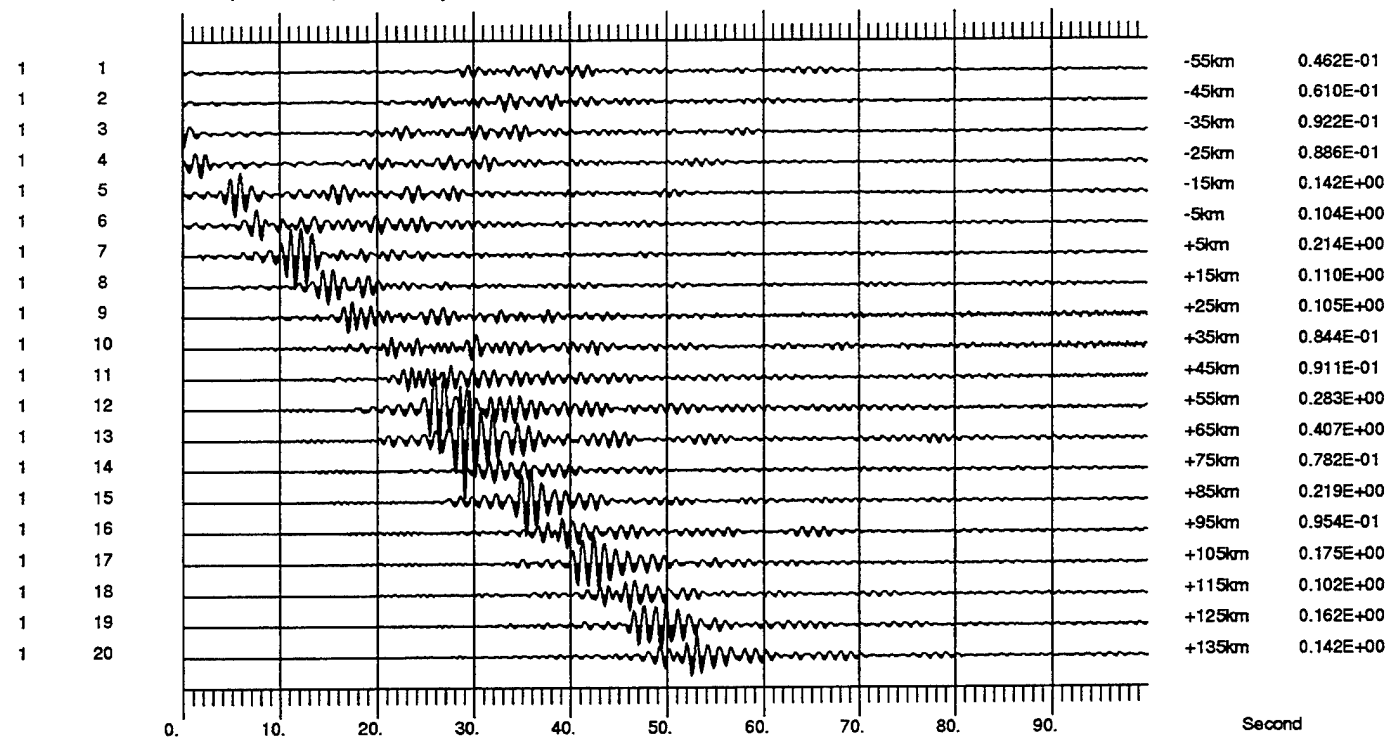
LFD Simulation of Lg Propagation: Model 3

Figure 49. The vertical-component snapshots of  $L_g$  wave propagation of model 3. The elevation change of this topographic profile is relatively small compared to the thickness of the homogeneous crust, and hence the transmission of  $L_g$  is still fairly efficient.



Synthetics at 0km Depth, Model 3

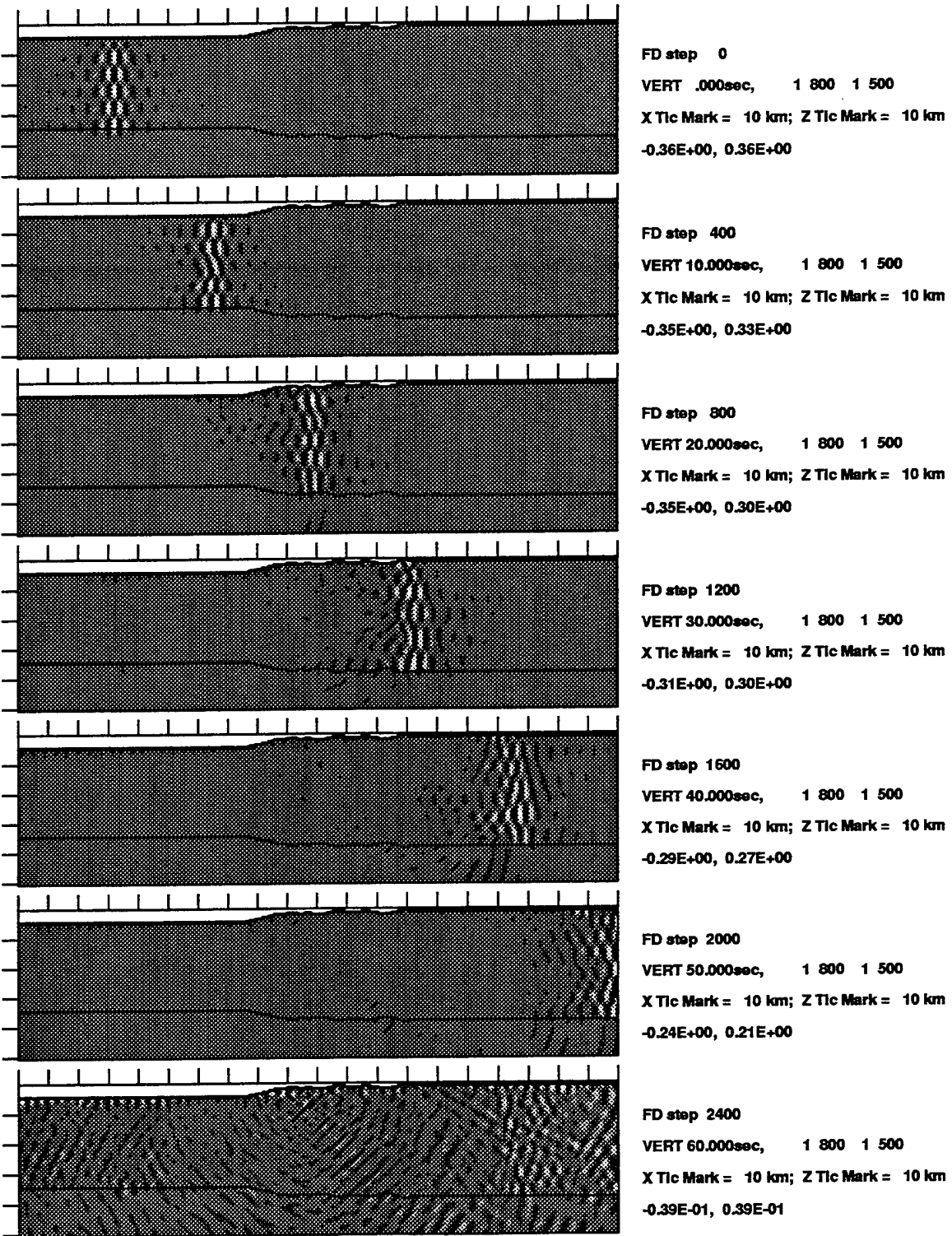
VERT, same scale, decimated by 5



Synthetics at 0km Depth, Model 3

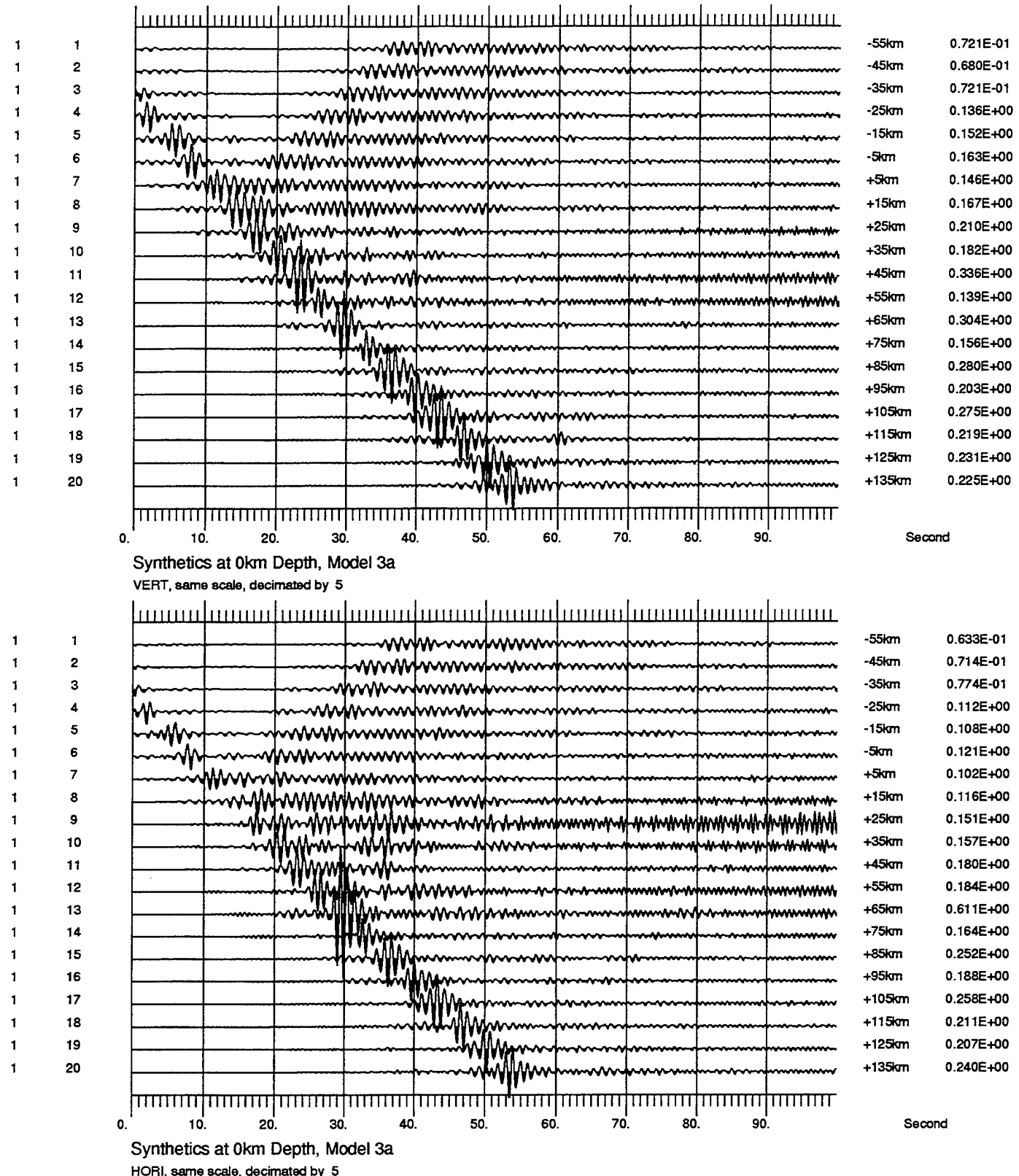
HORI, same scale, decimated by 5

**Figure 50.** Seismic sections of model 3, which has a moderate free-surface topography and a flat Moho. The scattering effects of topography on  $L_g$  are not as strong as those due to large-scale structural discontinuities.

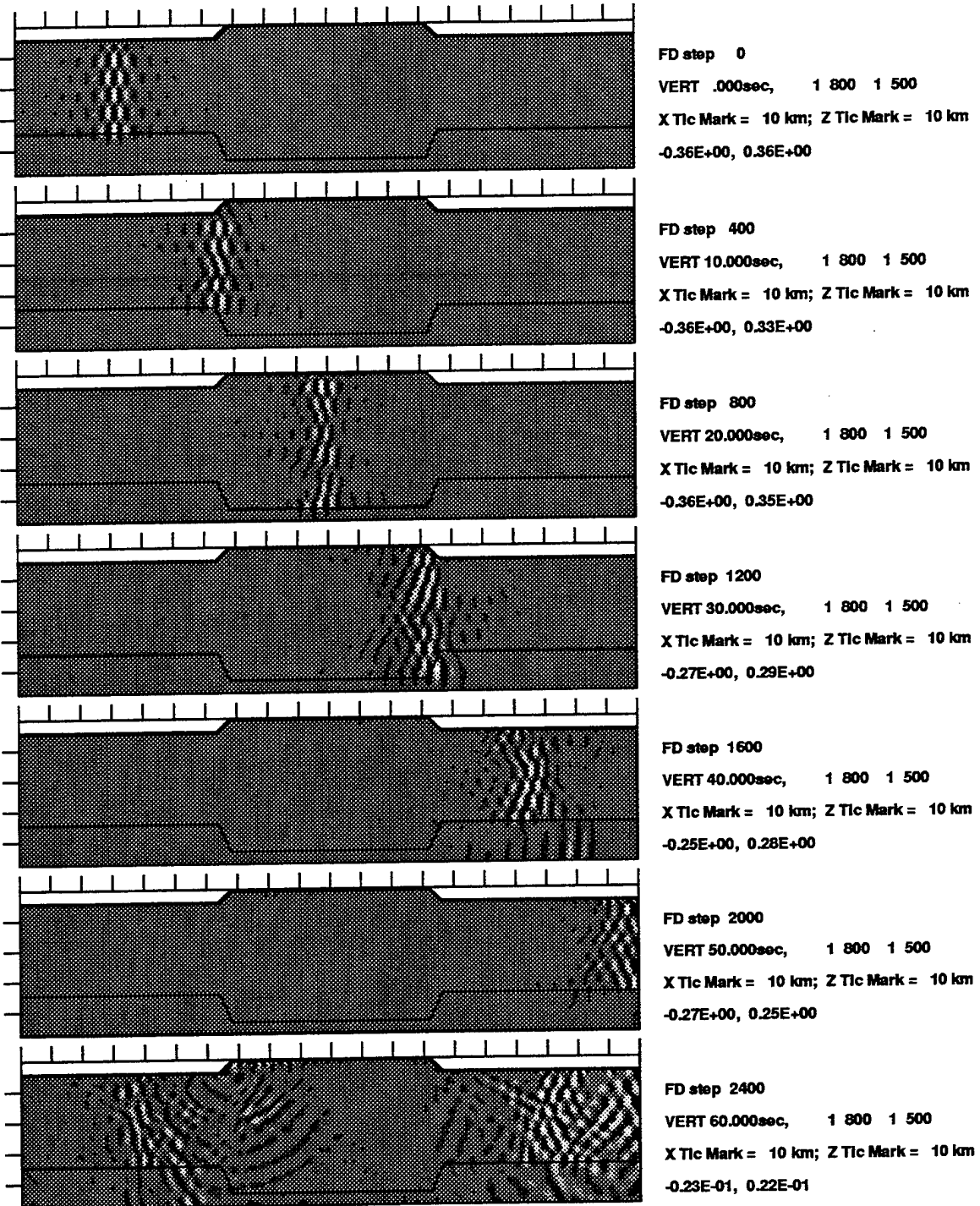


#### LFD Simulation of Lg Propagation: Model 3a

Figure 51. The vertical-component snapshots of  $L_g$  wave propagation of model 3a, in which the Moho is fully compensated. The elevation change of this topographic profile is relatively small compared to the thickness of the homogeneous crust, and hence the transmission of  $L_g$  is still fairly efficient.

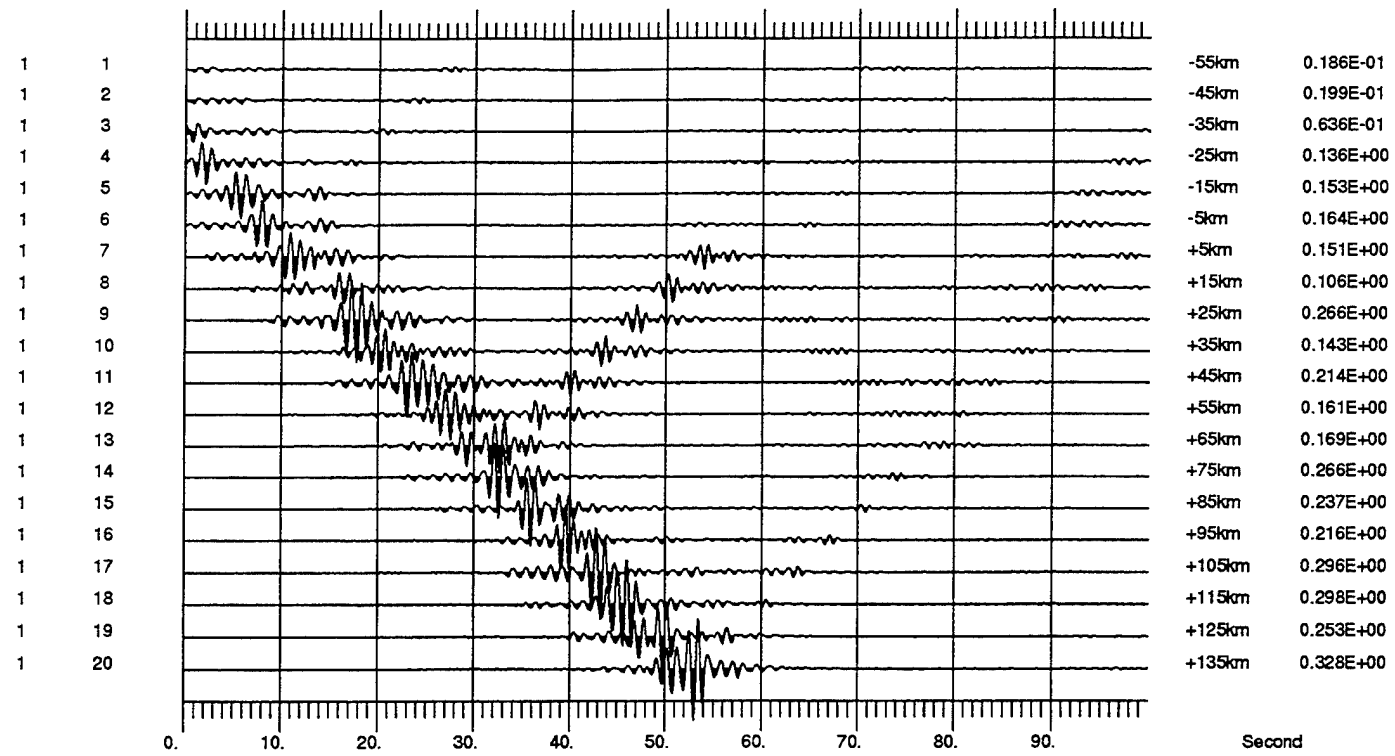


**Figure 52.** Seismic sections of model 3a, which has a moderate free-surface topography and a fully compensated Moho. The scattering effects of topography on  $L_g$  are not as strong as those due to large-scale structural discontinuities.



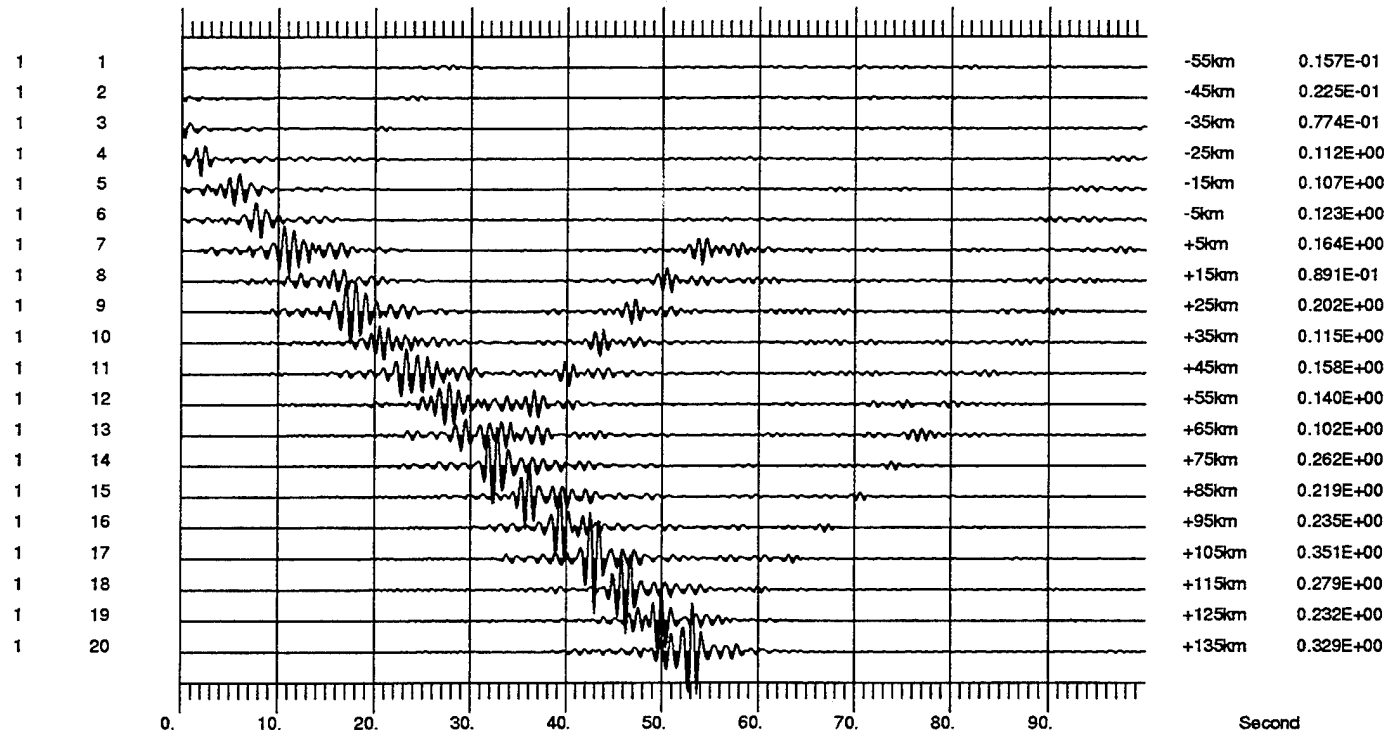
#### LFD Simulation of Lg Propagation: Model 4

Figure 53. The vertical-component snapshots of  $L_g$  wave propagation of model 4.



Synthetics at 0km Depth, Model 4

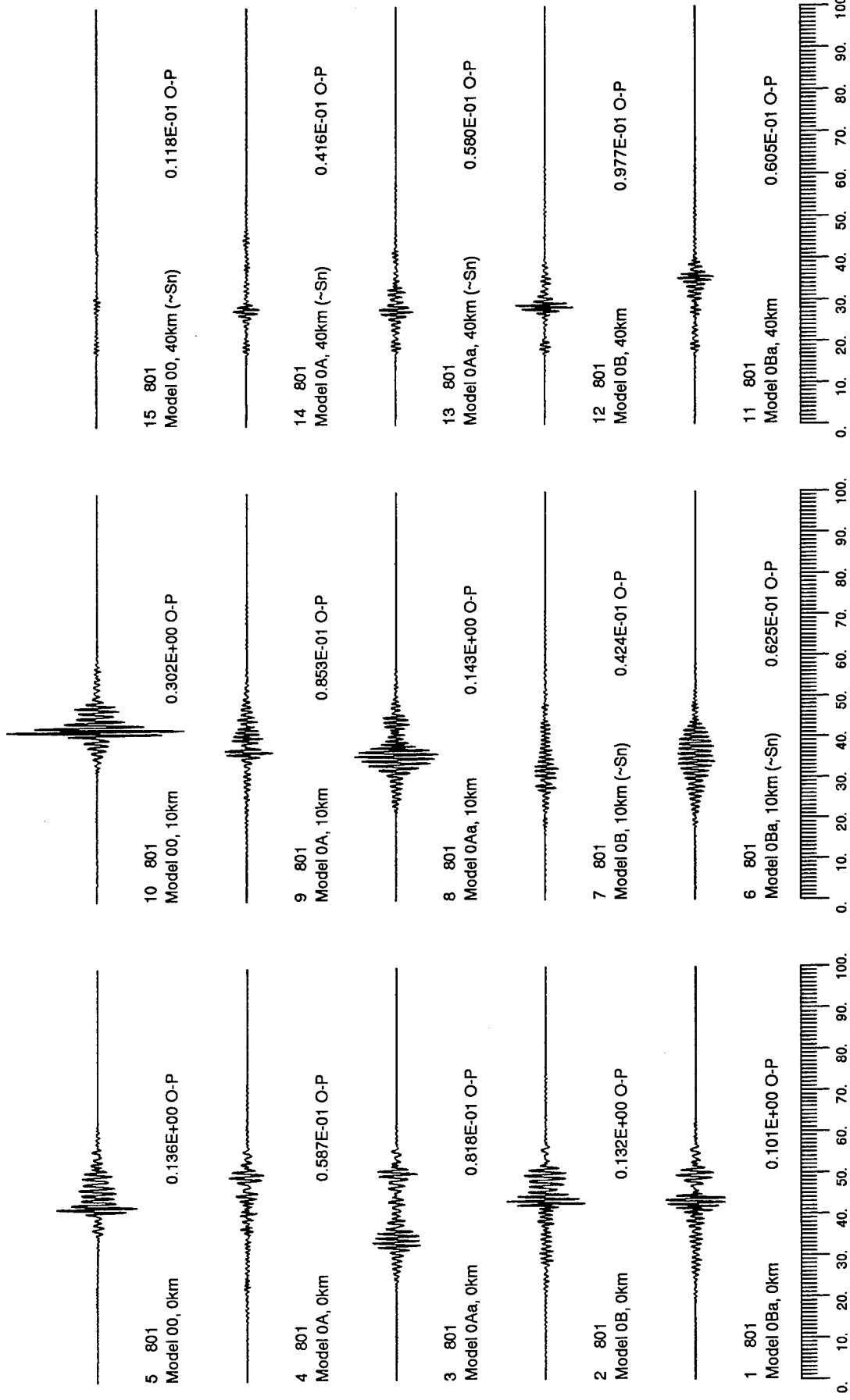
VERT, same scale, decimated by 5



Synthetics at 0km Depth, Model 4

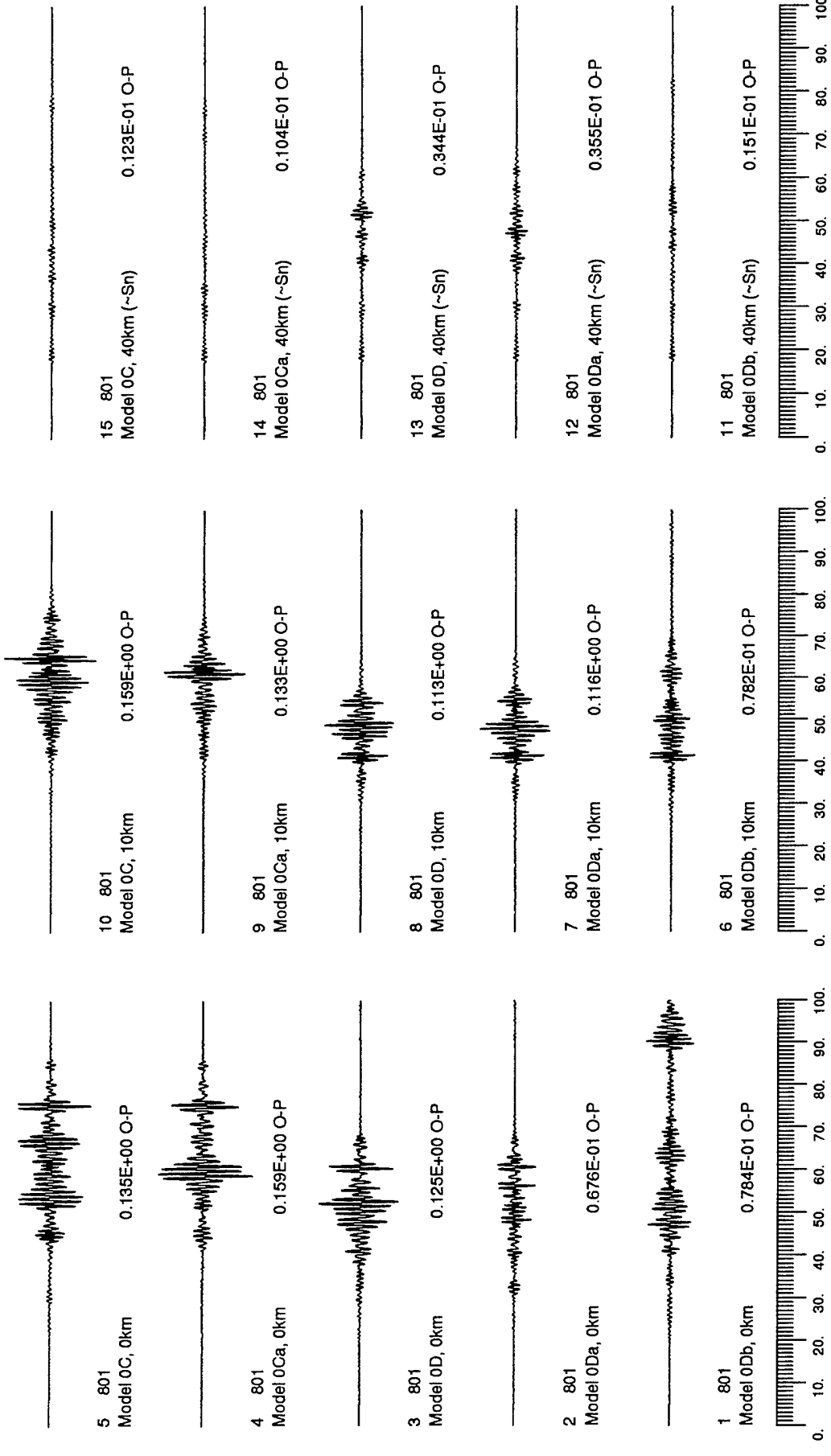
HORI, same scale, decimated by 5

Figure 54. Seismic sections of model 4, which has a trapezoidal topography and a fully compensated Moho.



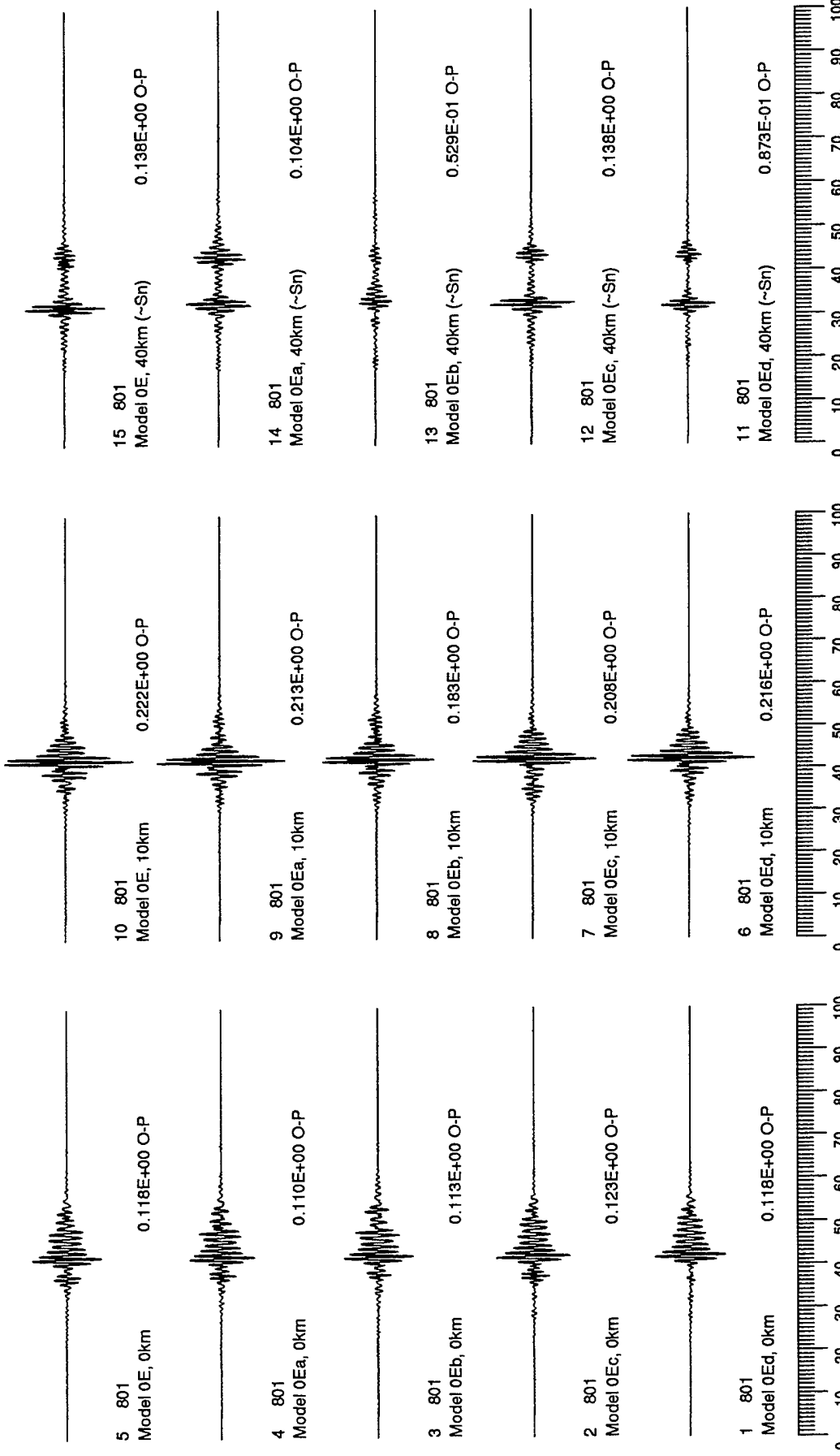
### Synthetics (@ 3 Depths) of Various Crustal Models: 0Ba, OB, OAa, OA, OO

**Figure 55.** Vertical-component synthetic seismograms recorded at 3 depths (0km, 10km, and 40km) and started at 20 seconds for models 00, OA, OAa, OB, and 0Ba, respectively. While both models with Moho uplift (OA and OAa) clearly exhibit a blockage for the “on-time  $L_g$ ”, only model 0Aa generates the “early  $L_g$ ” (left). Although the “on-time  $L_g$ ” on surface synthetics of models OB and 0Ba (bottom left) have a peak amplitude in the same order as that of the reference model, they are not the same overtone of the Rayleigh mode.



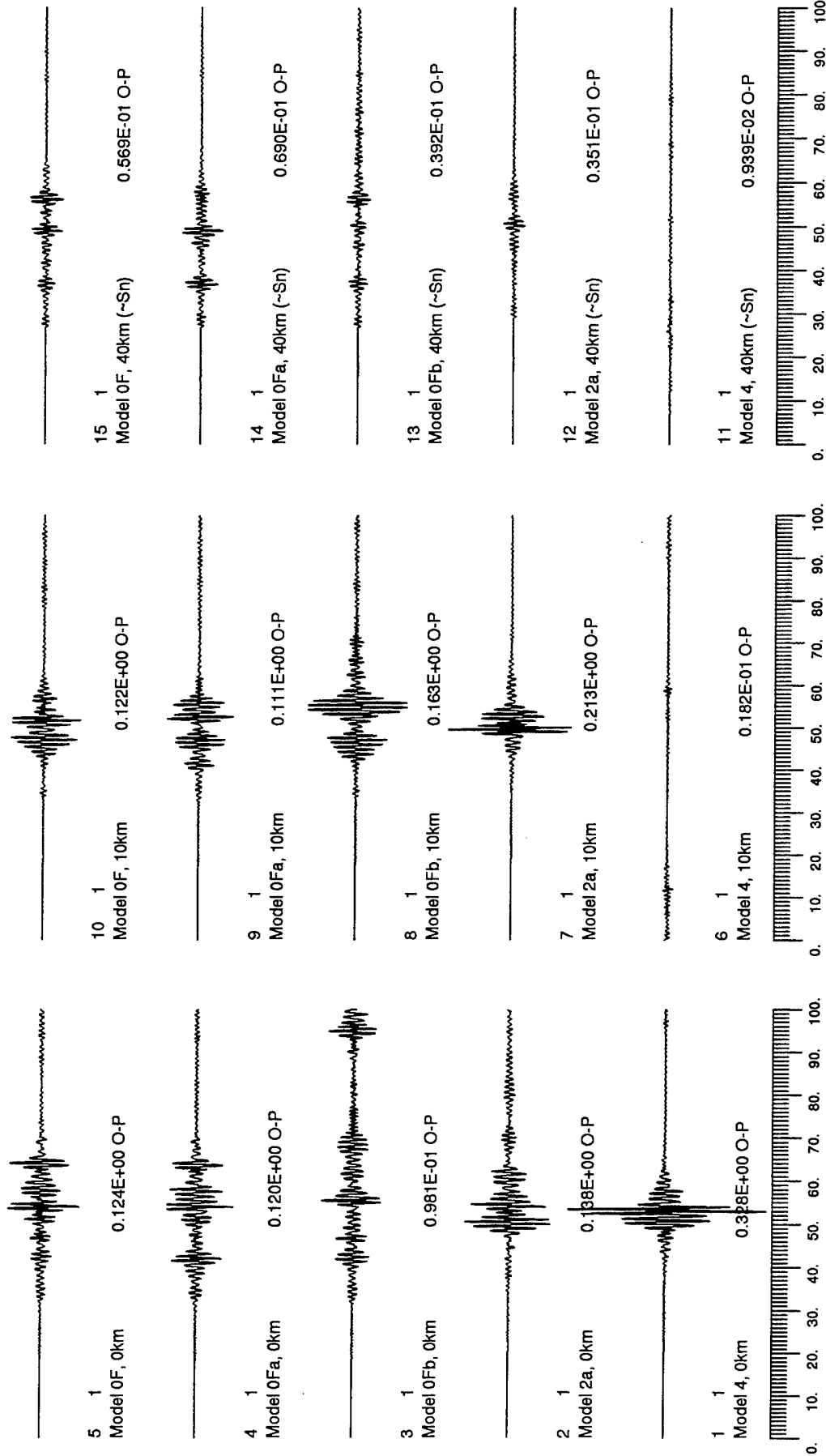
**Figure 56.** Same as Figure 55 except for models 0C, 0Ca, 0D, 0Da, and 0Db. All these models have embedded sedimentary layer(s) and hence the  $L_g$  energy is delayed. There is relatively less energy that would penetrate the Moho, as shown on the waveforms at 40 km. The model 0Db generates enhanced  $R_g$  waves (bottom left).

### Synthetics (@ 3 Depths) of Various Crustal Models: 0Db, 0Da, 0D, 0Ca, 0C



### Synthetics (@ 3 Depths) of Various Crustal Models: 0Ed, 0Ec, 0Eb, 0Ea, 0E

**Figure 57.** Same as Figure 55 except for models 0E, 0Ea, 0Eb, 0Ec, and 0Ed. Models of the "E" series excite very strong Sm phase.



### Synthetics (@ 3 Depths) of Various Crustal Models: 4, 2a, OFb, OFa, OF

**Figure 58.** Same as Figure 55 except for models OF, OFa, OFb, 2a, and 4. The moderate surface and Moho topography in model 2a effect  $L_g$  waveform characteristics only mildly. Model OFb excites very strong  $R_g$  phase, very similar to model ODb (see bottom left of Figure 56).

## 4. $L_g$ PROPAGATION IN ANELASTIC MODELS

The incorporation of intrinsic attenuation due to an arbitrary absorption law is believed to be straightforward in frequency-domain methods. However, so far many codes used in waveform synthesis (such as the reflectivity method and the wavenumber-integration method) can only handle a frequency-independent  $Q$ .<sup>1</sup> Bache *et al.* (1981) found that  $L_g$  synthetics made for models with frequency-independent  $Q$  do not attenuate with the proper frequency dependence. If models are constructed that match  $L_g$  amplitude-distance relationship at 1 Hz, then  $L_g$  synthetics would attenuate too rapidly at higher frequencies.

For the time-domain-based numerical methods, it has been very difficult to add the intrinsic attenuation because the anelastic stress-strain relation has the form of a convolution integral, which is intractable in a numerical computation. Vidale and Helmberger (1988) convolved finite-difference synthetics with a time-varying operator to model the effect of anelastic attenuation. This method is not suitable for media with spatially-varying  $Q$ . This method is also not appropriate when there are significant wave conversions (P to S etc.) in media where  $Q_p$  is not equal to  $Q_s$ . The first successful attempt to incorporate realistic attenuation laws into time-domain methods was made by Day and Minster (1984) based on the method of Pade approximation, which yields an expansion of the frequency-dependent viscoelastic modulus into a rational function. Emmerich and Korn (1987) propose a slightly different method based on the rheological model of the generalized Maxwell body, which has a modulus of the desired rational form. The major inconvenience of these approaches is that they demand a continual storage of five or more time steps of the wave field, depending on the accuracy of the approximation. The non-causal nature of some of these techniques is another fundamental drawback, at least conceptually, since in reality the anelastic attenuation of the Earth should act in a causal manner. That is, the dissipation of energy should occur as soon as the seismic wave arrives, and that the resulting displacement at the current time step should not be dependent on future displacement.

With all these considerations in mind, a different procedure is developed in this study to incorporate the anelastic attenuation. It turns out that if we drop the ambitious attempt of imposing an arbitrary (that is, user-defined) frequency-dependence on the  $Q$  operator, then it becomes very easy to implement a causal, phase-independent damping operator which is quite suitable for the LFD calculation. Several researchers have readily demonstrated that the performance of commonly used absorbing boundary conditions can be greatly improved if a viscous damping zone is added to the grid boundary (Cerjan *et al.*, 1985; Levander, 1985a). The damping zone simply reduces the amplitude in a pointwise manner. There is no reason why this technique can not be exploited to model the anelastic attenuation.

---

<sup>1</sup> A wavenumber-integration code with this limitation lifted is being developed at S-Cubed by K. McLaughlin.

Different seismic waves are used as the initial pulse in these examples to demonstrate the effectiveness of this algorithm.

Consider the simplest isotropic homogeneous medium in which the amplitude of seismic waves decays exponentially with traveling distance:

$$A(f, \Delta) = A_0(f) \cdot G = A_0(f) \cdot e^{-\gamma \cdot \Delta}, \quad [1]$$

where  $\gamma = \frac{\pi \cdot f}{U \cdot Q}$ ,  $U$  is the group velocity, and  $\Delta$  is the distance traveled. In LFD calculations,  $\Delta$  is taken to be the distance that the seismic wave would travel within one temporal step of the LFD iteration, that is,  $\Delta = U \cdot dt$ . Thus  $G$  can also be written as  $e^{-\frac{\pi \cdot f \cdot dt}{Q}}$ . There exists a constant  $\eta$  such that

$$G = e^{-\gamma \cdot \Delta} = 1 - \eta \cdot \gamma \cdot \Delta. \quad [2]$$

It implies that  $G = 1 - \frac{\eta \cdot \pi \cdot dt \cdot f}{Q}$  and hence  $Q = Q_0 \cdot f$  if we define  $Q_0$  to be  $\frac{\eta \cdot dt \cdot \pi}{1 - G}$ . If the damping term  $G$  is a function of the grid coordinate only and invariant with frequency, then we would have a  $Q$  increasing linearly with frequency. If, however, a frequency-dependent  $G$  is used at separate LFD simulations, then combining the band-limited LFD results would produce the solution for that particular frequency-dependent  $Q$  model. Here the parameter  $\eta$  is a function of  $\gamma$  or  $G$ , and the means of determining  $\eta$  will be discussed later. In practice, however, the users only need to specify a multiplicative constant  $G$  slightly less than 1 for each grid point. These localized damping factors are used to modify the displacement field pointwise at each iteration step. The decay rate ( $\gamma$ ) and the quality factor ( $Q$ ) can be determined later, after the finite-difference calculation is done. A possible drawback of this approach is that if a specific frequency-dependent  $Q$  model is desired, then several separate LFD simulations need to be carried out for each frequency- $Q$  pair of interest, as discussed above. Nevertheless, this possible shortcoming of this approach is outweighed by its simplicity. More importantly, this procedure preserves the causality. Another characteristic of this approach is that, given a damping factor  $G$  in a P-SV LFD calculation,  $Q_0 = \frac{\eta \cdot dt \cdot \pi}{1 - G}$  would be applicable to both P and S phases. Thus,  $Q_P$  and  $Q_S$  should be about the same.

So far we have derived several necessary conditions for an anelastic attenuation model, based on the desired exponential decay of seismic amplitude. In the following, we shall take a schematic view of this proposed algorithm. Consider the heterogeneous acoustic wave equation in the nondissipative medium:

$$\frac{\partial^2 P}{\partial t^2} = c^2(x, z) \left[ \frac{\partial^2 P}{\partial x^2} + \frac{\partial^2 P}{\partial z^2} \right], \quad [3]$$

where  $P$  is the acoustic displacement potential, and  $c(x, z)$  is the acoustic velocity at the node  $(x, z)$ .

LFD iteratively solves for the current pressure at  $(x, z)$  using that of the past within a spatially-limited region surrounding the grid  $(x, z)$ . The actual size of the temporal and spatial buffers required depends on the order of the LFD scheme. At each time step, the resulting unattenuated pressure  $P$  is then multiplied by the damping  $G$  to get the dissipated  $\tilde{P}$ . Once the whole pressure field is updated and dissipated (grid by grid) with the corresponding spatial damping factors, the standard LFD iteration restarts for the next pressure field without damping, and then damping factors are applied again. The procedure for the P-SV LFD calculation is exactly the same. It should be obvious that the extra calculation and memory required in this procedure are minimum. We can envision the pointwise damping factor as a degenerate digital filter which has only one point of temporal span (that is, memory). It can be regarded as the limiting case of the convolutional integral of many attenuation operators typically used in the frequency-domain approach.

The attenuated pressure,  $\tilde{P} = P \cdot G$ , can also be written as

$$\tilde{P} = P - \frac{\eta \cdot \pi \cdot dt \cdot f}{Q} \cdot P . \quad [4]$$

That is,  $\tilde{P}$  can be obtained by adjusting the undissipated  $P$  a little. The coefficient of pressure loss,  $\frac{\eta \cdot \pi \cdot dt \cdot f}{Q}$  is very similar to the coefficient of friction term that Levander (1985) (and Frankel and Wennerberg, 1987) used in the telegraphy equation. The difference is that we have added the  $\eta$  term here to account for the correct relationship between  $Q$  and the damping effect. Jih (1996) gives a more detailed discussion as well as several examples using different seismic waves as input to demonstrate the effectiveness of this algorithm.

Seven models with  $Q_0$  values varying from 60 to 500 are tested in this study. The attenuative portion is 100 km long and 30 km thick. In each case, a significant fraction of the energy is lost due to absorption. Nevertheless, the chessboard pattern of the initial  $L_g$  wave packet is retained for all models. In fact, none of these seven models exhibits any notable scattering (see Figures 59 through 62). Also, the linear frequency-dependence of the resulting  $Q$  is quite clear, so is the frequency-independent  $\gamma$  (Table 3). These observations strongly indicate that the simple attenuation operator proposed for the LFD method is adequate for operational purposes.

Following the same quantification procedure as in the previous section, amplitude ratios representing the  $L_g$  transmission and coupling to other phases are computed. Instead of using the surface synthetic to measure the quality factor and  $\gamma$ , the amplitude ratio of transmitted  $L_g$  waves is based on that at a depth of 10 km, which we find to be a more stable measure of the transmitted energy. The results are summarized in Table 3 below.

Table 3.  $L_g$  Propagation Statistics of 7 Anelastic Models

Model, $e^{-\gamma \Delta}$	BK	T	$S_n/L_g$	far-P/ $L_g$	far-S/ $L_g$	$Q_0$	$\gamma$ (1 Hz)	Q(2 Hz)	$\gamma$ (2 Hz)
0Qa, 0.99747	0.175	0.200	0.053	0.026	0.014	59	0.0162	139	0.0138
0Qb, 0.99873	0.418	0.445	0.049	0.026	0.013	117	0.0082	249	0.0077
0Qc, 0.99916	0.590	0.614	0.056	0.027	0.014	196	0.0049	398	0.0048
0Qd, 0.99937	0.672	0.695	0.059	0.028	0.015	263	0.0036	531	0.0036
0Qe, 0.99949	0.718	0.739	0.060	0.028	0.017	316	0.0030	635	0.0030
0Qf, 0.99958	0.770	0.786	0.060	0.028	0.018	396	0.0024	796	0.0024
0Qh, 0.99968	0.826	0.835	0.060	0.029	0.020	530	0.0018	1054	0.0018

BK: spectral amplitude ratio at 1 Hz of "on-time  $L_g$ " (3.33 km/sec) to that of the reference model.

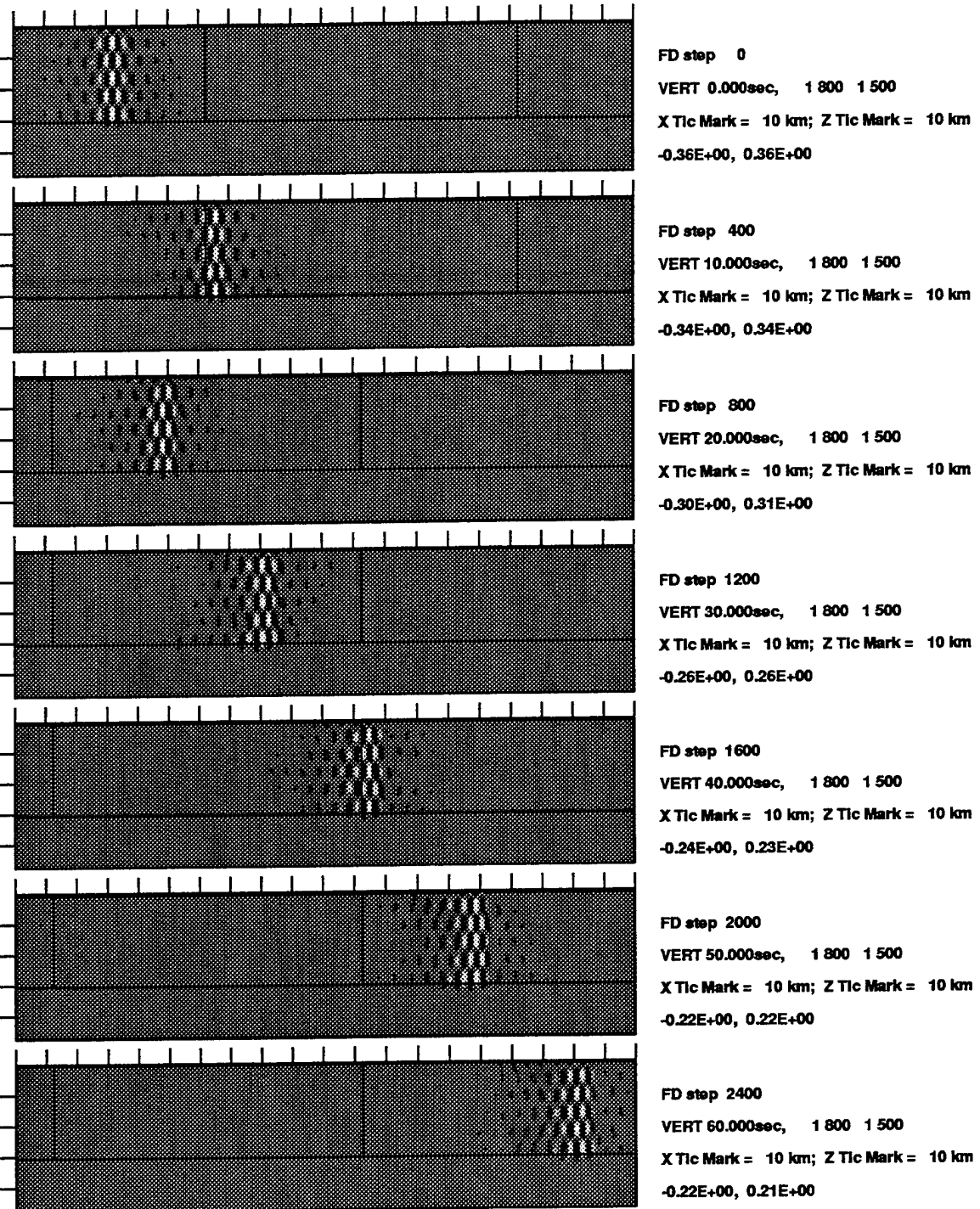
T: spectral amplitude ratio at 1 Hz of transmitted  $L_g$  (recorded at a depth of 10 km) to that of the reference model.

$S_n/L_g$ : spectral amplitude ratio at 1 Hz of converted  $S_n$  to the reference  $L_g$ .

far-P/ $L_g$ : spectral amplitude ratio at 1 Hz of converted teleseismic P to the reference  $L_g$ .

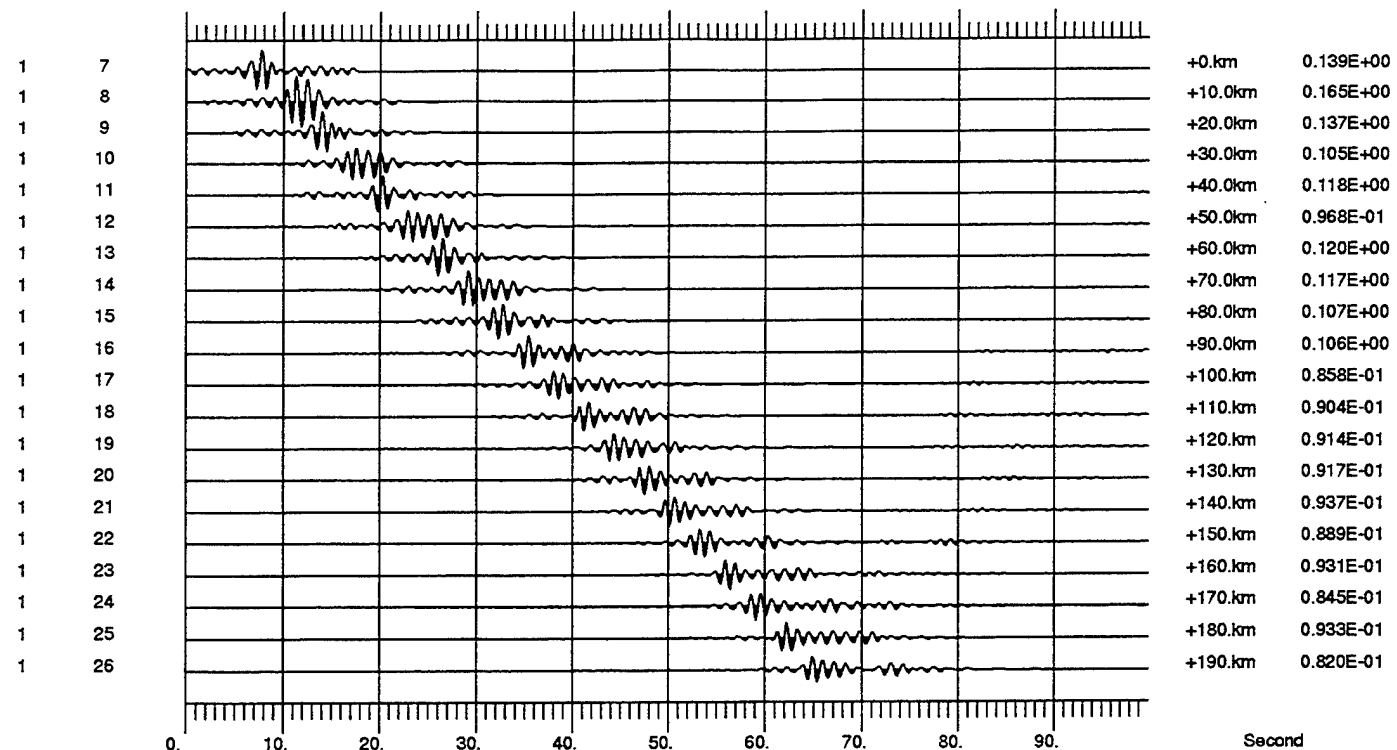
far-S/ $L_g$ : spectral amplitude ratio at 1 Hz of converted teleseismic S to the reference  $L_g$ .

As Q increases, the transmission efficiency (T) also increases, as expected. However, the coupling of  $L_g$  into  $S_n$  or teleseismic phases does not seem to be affected. Reducing the thickness of the attenuating body does not seem to change this observation (Figure 62). This is different from the case of  $R_g$  in which Jih (1995, 1996) reported that the undissipated  $R_g$  energy could actually be converted into S or  $L_g$  waves. The reason for this difference is not clear as yet. A possible explanation is that it has to do with the fundamental difference between  $R_g$  and the higher modes. The particle motion of  $R_g$  is very localized in that the energy causing retrograde (or prograde) rolling at greater depths does not interact with the shallow portion of the crust. When the rolling at shallow depths is dissipated, the "waveguide" is actually changed and the undissipated energy at greater depth can no longer propagate in the same mode as  $R_g$ . As a result, it is converted into a pure shear or  $L_g$ -like wave (see Jih, 1995). On the other hand,  $L_g$  waves are the interference of planar S waves multiply reflected at the free surface and the Moho. This mode of propagation is more robust in that even if part of the energy on the wavefront is dissipated in the upper crust, the remaining part of the wavefront might still be able to propagate more or less along the original direction.  $L_g$  energy in the deeper crust will also be dissipated when it eventually reaches the upper crust. Likewise, the  $L_g$  energy in the shallow portion of the crust will be dissipated first and then eventually enter the deeper crust and so forth. Thus the shallow attenuating layer will affect the whole  $L_g$  wavefield in a relatively more uniform manner without breaking up the mode (eigenfunction). As a result, there will be no notable enhancement of  $S_n$  or teleseismic coupling.



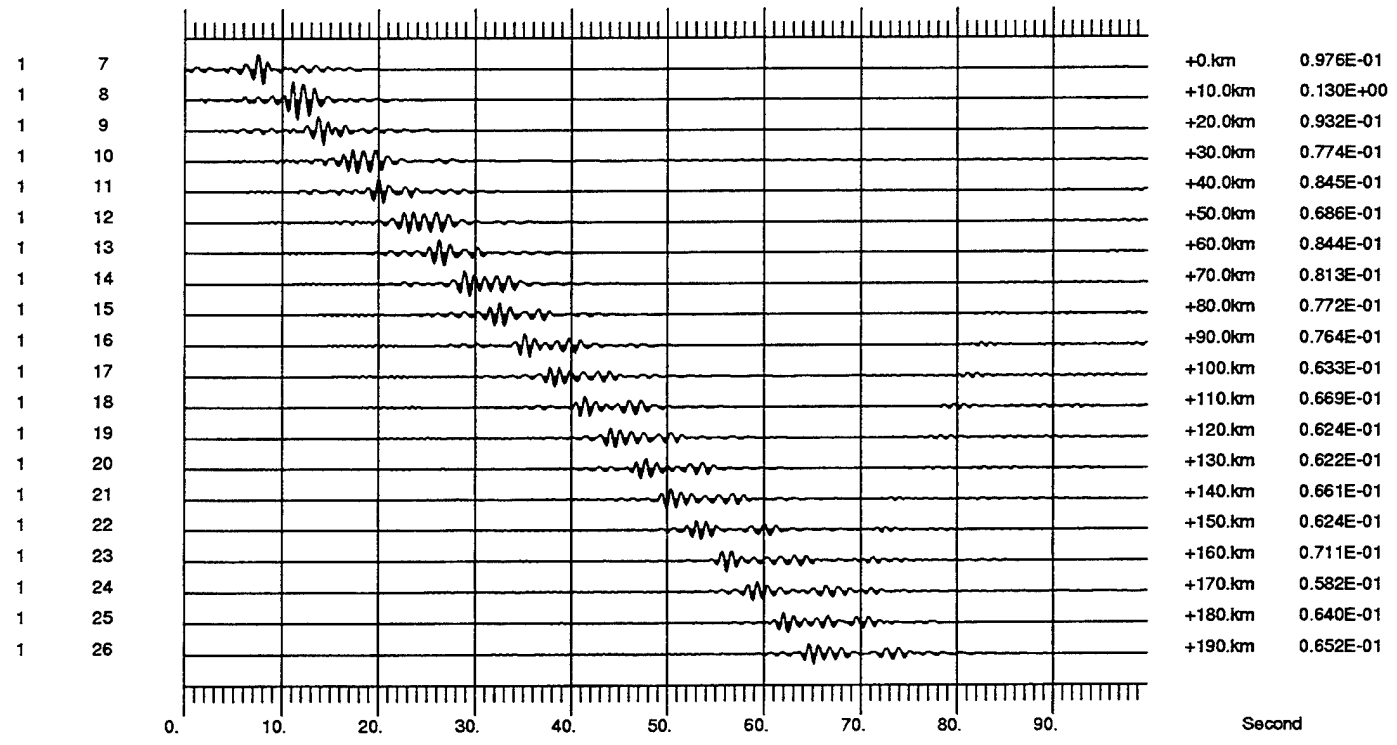
#### LFD Simulation of Lg Propagation: Model 0Qd,122

**Figure 59.** The vertical-component snapshots of  $L_g$  wave propagation in an anelastic mode, 0Qd, with  $Q_0(L_g) = 263$  for  $L_g$  waves. The anelastic portion of the model is 100 km long and 30 km thick. In this case, the effect of the intrinsic attenuation is to reduce the amplitude through dissipation. No significant scattering is observed.



Synthetics at 0km Depth, Model 0Qd,122

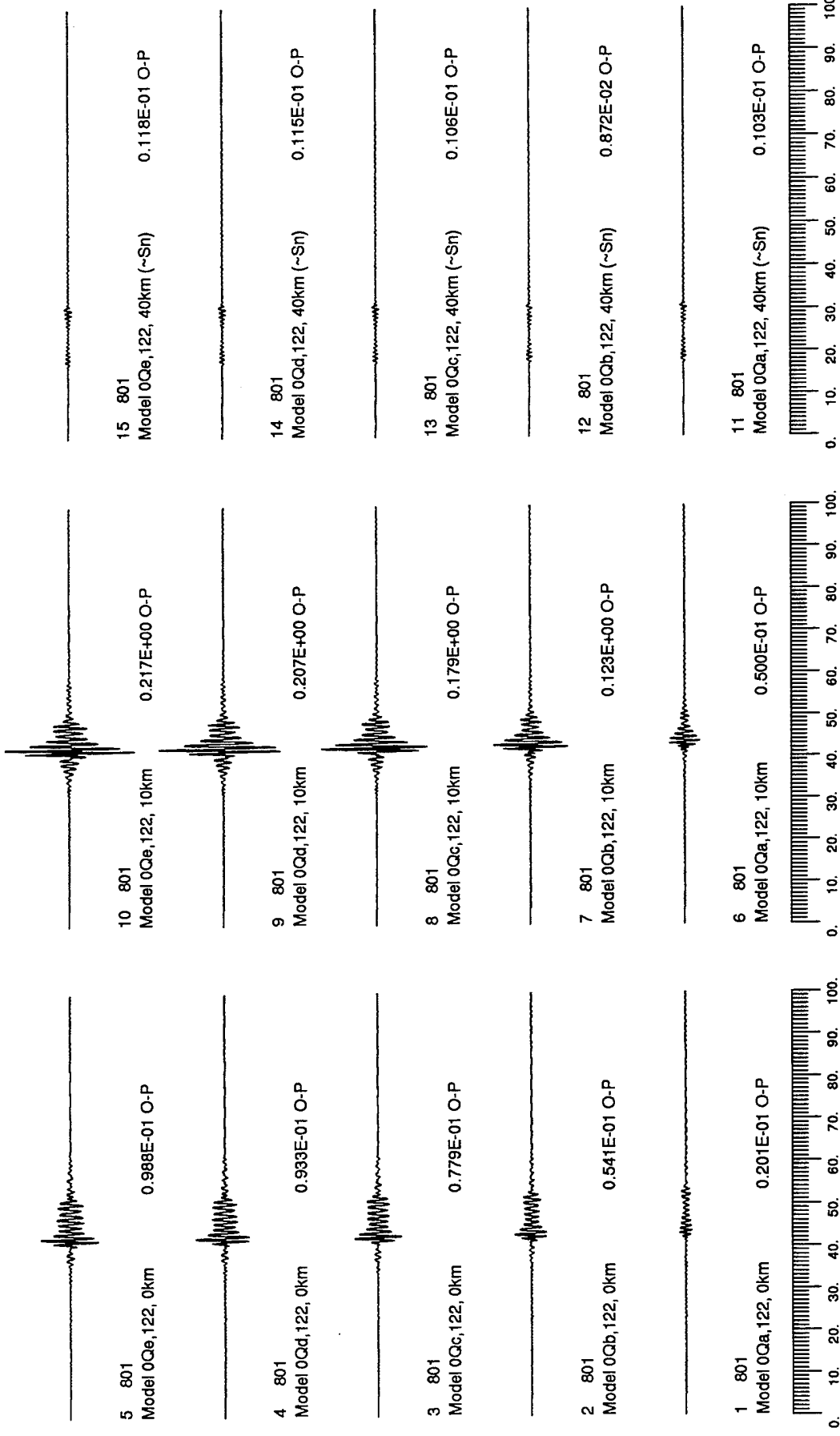
VERT, same scale, decimated by 5



Synthetics at 0km Depth, Model 0Qd,122

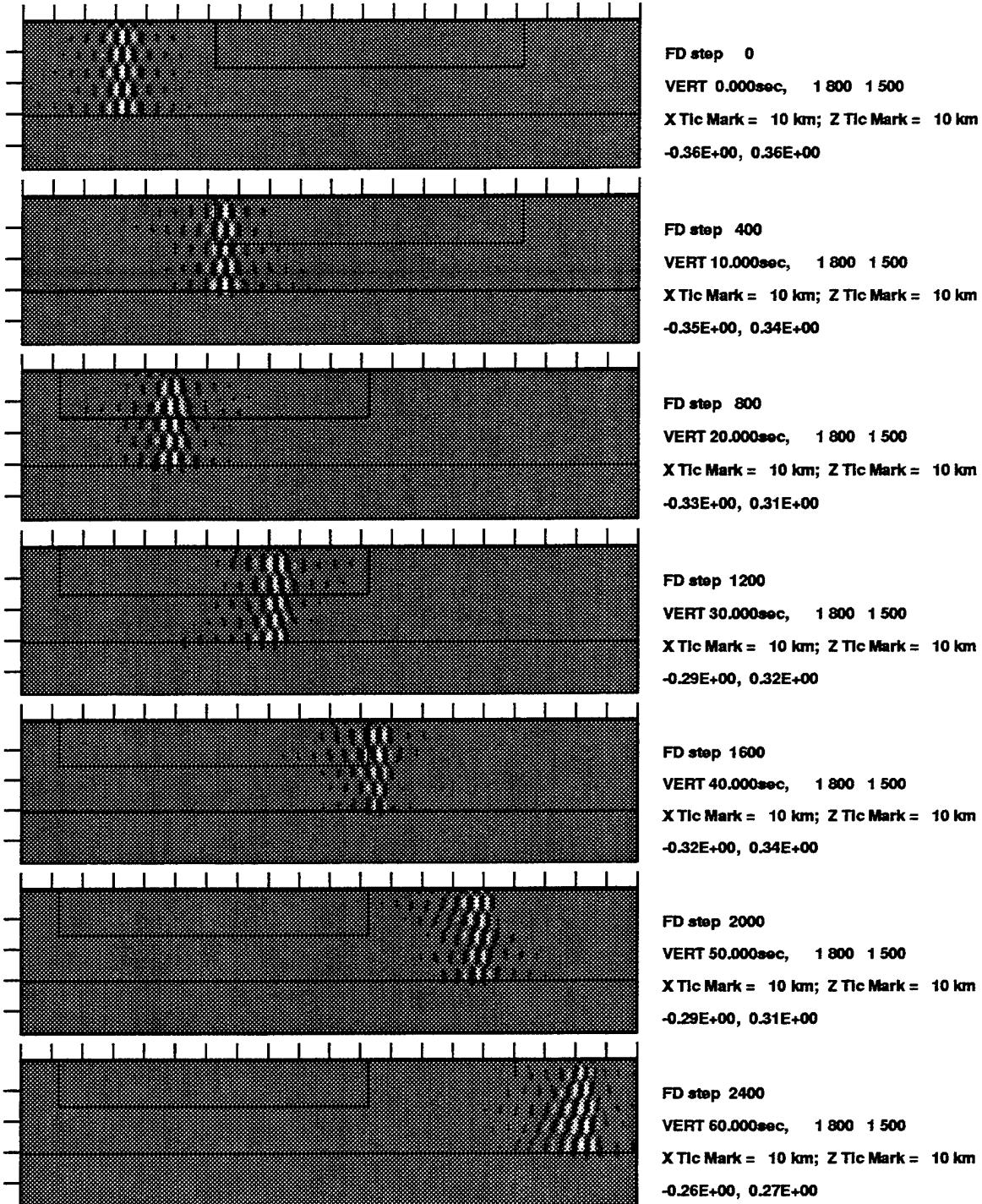
HORI, same scale, decimated by 5

**Figure 60.** Seismic sections of model 0Qd,122 which has an attenuating body 100 km long, 30 km thick, with  $Q_0(L_g) = 263$ .



### Synthetics (@ 3 Depths) of Various Crustal Models: 0Qa, 0Qb, 0Qc, 0Qd, 0Qe

**Figure 61.** Synthetic seismograms recorded at 3 depths (0km, 10km, and 40km) after crossing an anelastic zone 100 km wide and 30 km thick for five attenuative models. From top to bottom, the corresponding  $Q_0(Lg)$  values of these five models are 316, 263, 196, 117, and 59, respectively. Intrinsic attenuation reduces the  $L_g$  amplitude but does not cause any mode conversion.



#### LFD Simulation of Lg Propagation: Model 0Qd,62

**Figure 62.** Similar to Figure 59 except a 15km-thick attenuative layer. For the  $L_g$  phase, the effect of intrinsic attenuation is to reduce the amplitude through dissipation. Changing the volume size (that is, the thickness) of the attenuating body does not seem to cause more mode conversion. This is very different from the case for  $R_g$ .

## 5. $L_g$ PROPAGATION IN MODELS WITH RANDOM VELOCITY VARIATION

In an attempt to model the  $L_g$  blockage observed in the west Pyrenees Range, Chazalon *et al.* (1993) and Gibson and Campillo (1994) suggest that scattering by small-scale features within the lower crust is the primary reason for the observed blockage. In this section, several heterogeneous models with various RMS random velocity fluctuations are tested to quantify the scattering effects of small-scale heterogeneity on  $L_g$ . Figure 63 shows the vertical-component snapshots of  $L_g$  wave propagation in a single-layer model with a heterogeneous portion 100 km long and 30 km thick embedded in it. The self-similar random heterogeneity in this sandwiched portion has an RMS velocity fluctuation of 10 percent and a scale length of 1 km. The random medium is generated with the procedure described in Frankel and Clayton (1986).

As the RMS velocity variation increases to, say 20 percent, the scattered field becomes very complicated (*cf.* Figures 63 and 65). Contrary to the case with intrinsic attenuation alone, the small-scale random heterogeneity causes many kinds of coupling (scattering) (Figure 65). Table 4 below summarizes all the results. The “blocking” parameter (BK) was computed at two different depths, 0 and 10 km, and the latter is used in determining  $Q_0$  and  $\gamma$ . Both the transmission of  $L_g$  and the coupling of other phases are directly affected by the change in the RMS velocity variation. As the RMS velocity variation increases, the amplitude ratio of transmitted  $L_g$  to the reference  $L_g$  wave drops significantly. The scattered energy enhances the coupling of  $S_n$  as well as those of teleseismic phases. It is interesting to note that  $L_g$ -to- $S_n$  coupling is not a simple linear function of RMS velocity variation, unlike the coupling of teleseismic phases or  $L_g$  transmission. Figure 68 and Table 4 indicate that below 10%, the  $L_g$ -to- $S_n$  coupling does exhibit a highly linear trend with the increasing complexity of the medium. The coupling drops as the RMS variation goes beyond 10%. Intuitively this could be because the scattered wavefield would become dominant and the isotropic point scatterers would radiate the energy in all directions.

Another observation is that as the RMS variation increases, the delay of the centroid of the  $L_g$  wave packet on the surface synthetics (see Figure 67) becomes very obvious. This is similar to the “stochastic dispersion” phenomenon McLaughlin and Anderson (1987) reported for P waves. In theory, the apparent attenuation and the dispersion should form a Hilbert transform pair, according to the Kramers-Kronig relation (Jacobson, 1987). This can be tested if the frequency band is broad enough.

Table 4.  $L_g$  Propagation Statistics of Random Models

Model	BK(0)	BK(10)	$S_n/L_g$	far-P/ $L_g$	far-S/ $L_g$	Q(1 Hz)	$\gamma$ (1 Hz)
0Y, 2%	1.020	0.978	0.065	0.040	0.042	3934	0.0002
0Y, 3%	1.032	0.952	0.075	0.048	0.055	1878	0.0005
0Y, 4%	1.044	0.917	0.086	0.057	0.069	1088	0.0009
0Y, 5%	1.059	0.873	0.097	0.065	0.083	707	0.0014
0Y, 6%	1.077	0.822	0.108	0.073	0.096	494	0.0019
0Y, 7%	1.095	0.766	0.118	0.081	0.108	365	0.0026
0Y, 8%	1.114	0.706	0.126	0.089	0.118	280	0.0034
0Y, 9%	1.132	0.644	0.133	0.097	0.127	222	0.0043
0Y, 10%	1.146	0.583	0.138	0.106	0.134	181	0.0053
0Y, 11%	1.154	0.524	0.141	0.115	0.140	150	0.0064
0Y, 12%	1.154	0.471	0.143	0.126	0.144	128	0.0075
0Y, 13%	1.141	0.423	0.143	0.136	0.147	111	0.0086
0Y, 14%	1.115	0.381	0.142	0.145	0.150	98	0.0098
0Y, 15%	1.075	0.344	0.138	0.154	0.155	88	0.0108
0Y, 16%	1.020	0.313	0.133	0.161	0.161	81	0.0118
0Y, 17%	0.949	0.285	0.126	0.167	0.167	75	0.0127
0Y, 18%	0.859	0.260	0.118	0.171	0.173	70	0.0136
0Y, 19%	0.749	0.235	0.110	0.174	0.177	66	0.0146
0Y, 20%	0.625	0.210	0.103	0.174	0.181	61	0.0158

BK(0): spectral amplitude ratio at 1 Hz of "on-time  $L_g$ " (3.33 km/sec) to that of the reference model.

BK(10): spectral amplitude ratio at 1 Hz of transmitted  $L_g$  (recorded at a depth of 10 km) to that of the reference model.

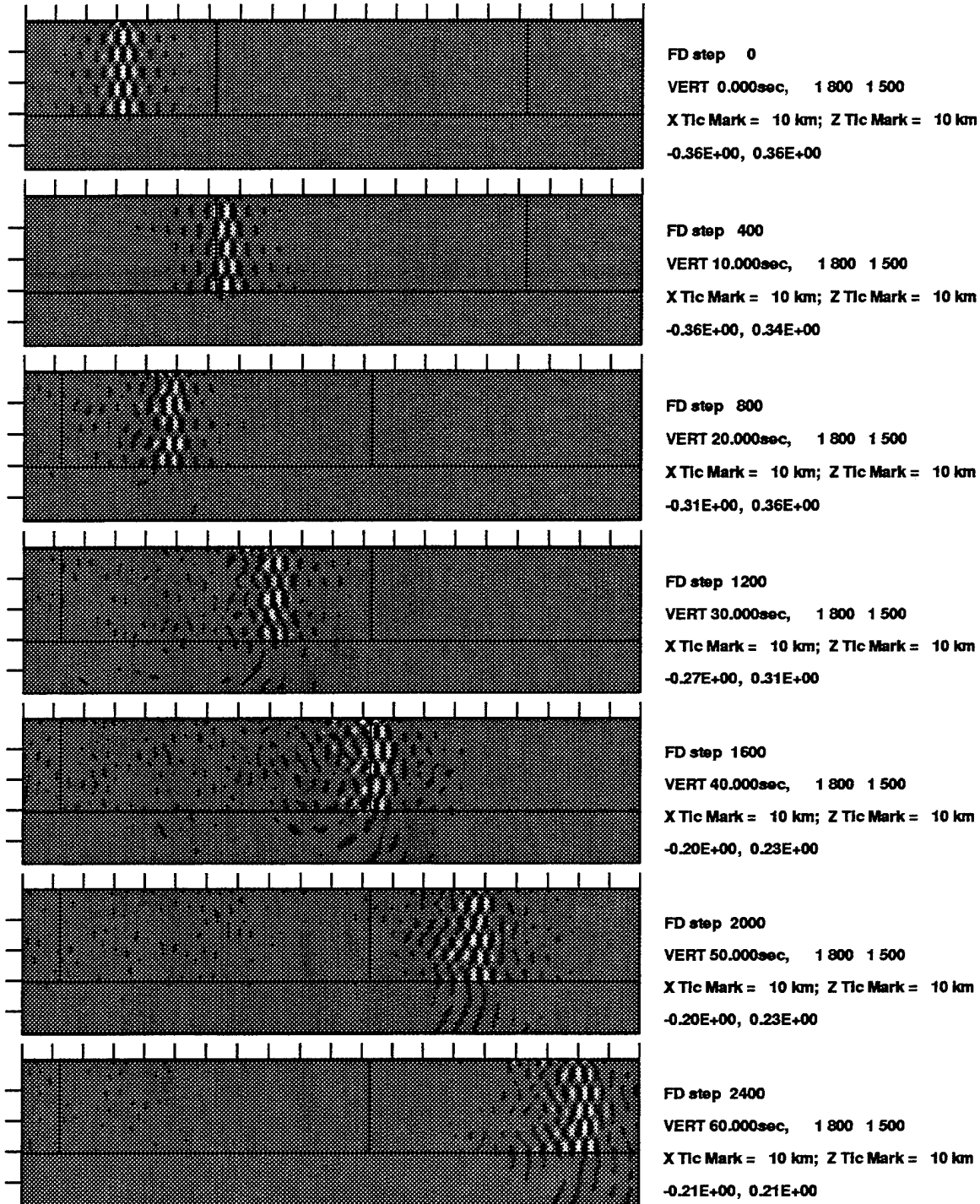
$S_n/L_g$ : spectral amplitude ratio at 1 Hz of converted  $S_n$  to the reference  $L_g$ .

far-P/ $L_g$ : spectral amplitude ratio at 1 Hz of converted teleseismic P to the reference  $L_g$ .

far-S/ $L_g$ : spectral amplitude ratio at 1 Hz of converted teleseismic S to the reference  $L_g$ .

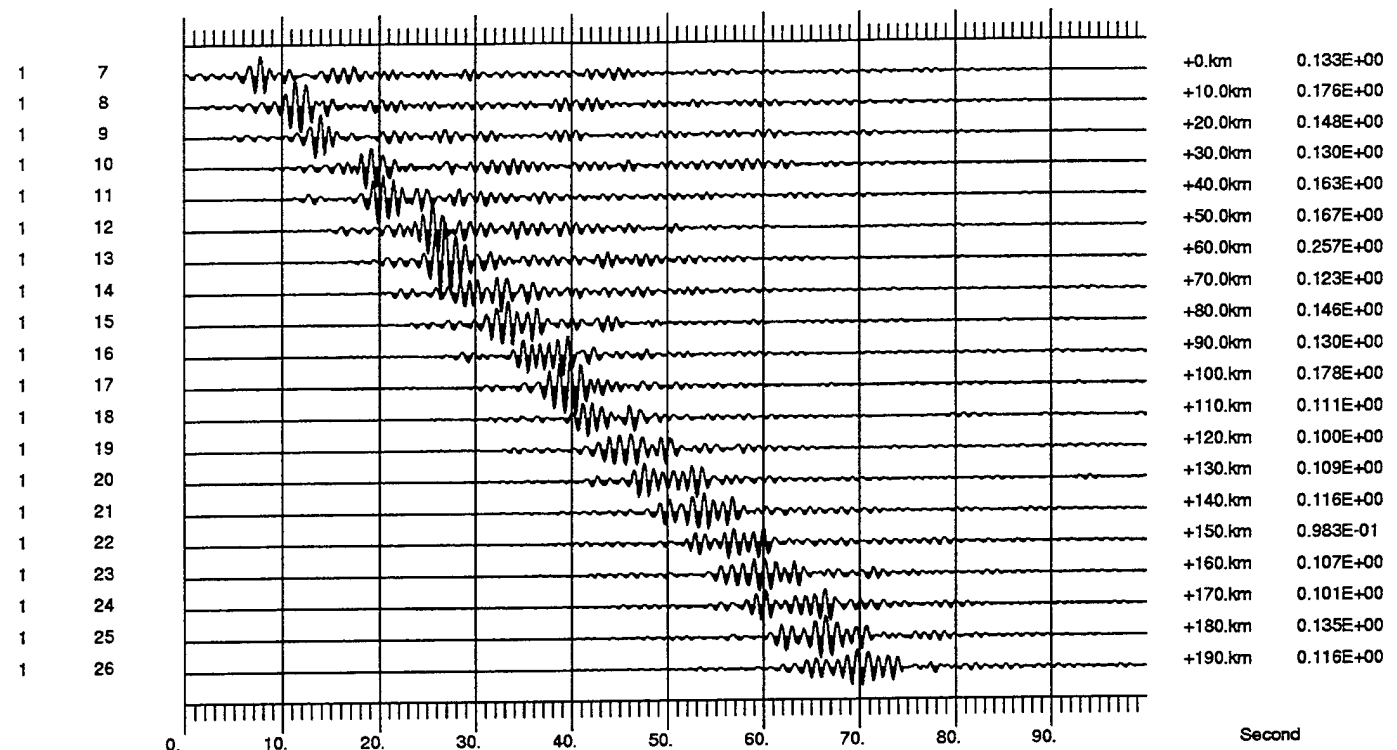
Both anelasticity and small-scale random heterogeneity can contribute to the so-called " $L_g$  blockage". Note that in practice the  $L_g$  blockage occurs whenever the peak  $L_g$  amplitude is below the signal level of other phases surrounding  $L_g$ . It certainly does not require the signal level in the predicted  $L_g$  window to be far below the noise level. In our calculations, a velocity variation of 8 percent or higher leads to an equivalent spatial Q of 270 or less, which would be sufficient to reduce the  $L_g$  amplitude by 30 percent or more for every 100 km it traverses (see the parameter T in Table 3). The classical example of " $L_g$  blockage" along the path from the Novaya Zemlya test site to northern Scandinavia has a  $Q_0(L_g)$  about 252, as discussed before. Based on Table 4, this level of attenuation is approximately equivalent to a model with a velocity variation of 8 percent alone. Stable shield regions are reported to have an RMS velocity variation less than 5 percent. For such paths, the corresponding spatial  $Q_0$  value would be 700 or larger.

Some comparisons of various conversion mechanisms may be interesting. For a mountainous model,  $L_g$ -to-S is twice as strong as  $L_g$ -to-P (Table 2). (Here P and S refer to the teleseismic P and S, respectively.) For the "A" and "B" series of models, as well as the random media, these two mechanisms are about equally strong (see Tables 2 and 4). Anelastic models and "C"-type models have a  $L_g$ -to-S weaker than the  $L_g$ -to-P (Table 3), whereas models of the "D", "E", and "F" series show the opposite trend (Table 2).



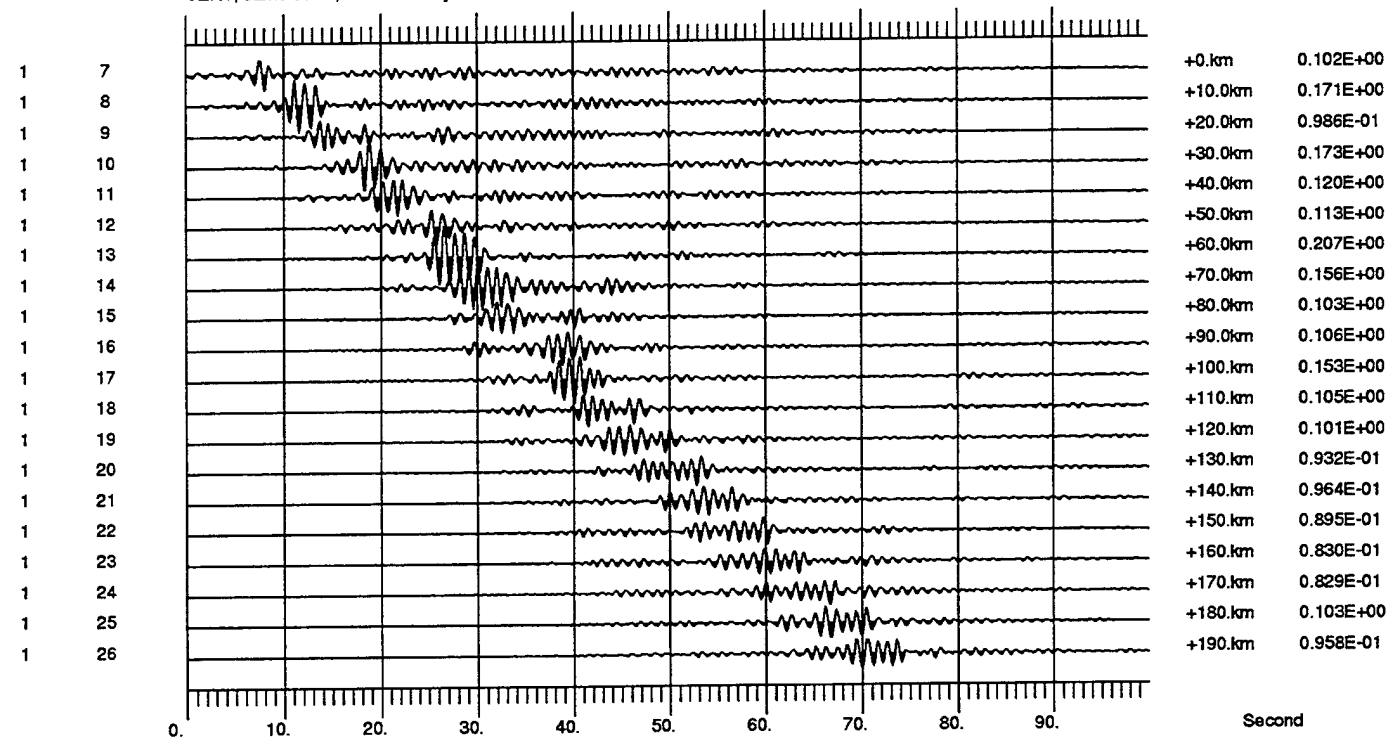
#### LFD Simulation of Lg Propagation: Model 0Y,10%

**Figure 63.** The vertical-component snapshots of  $L_g$  wave propagation in a single-layer model with a heterogeneous portion 100 km long and 30 km thick embedded in it. The self-similar random heterogeneity in this sandwiched portion has an RMS velocity fluctuation of 10 percent and a scale length of 1 km.



Synthetics at 0km Depth, Model 0Y,10%

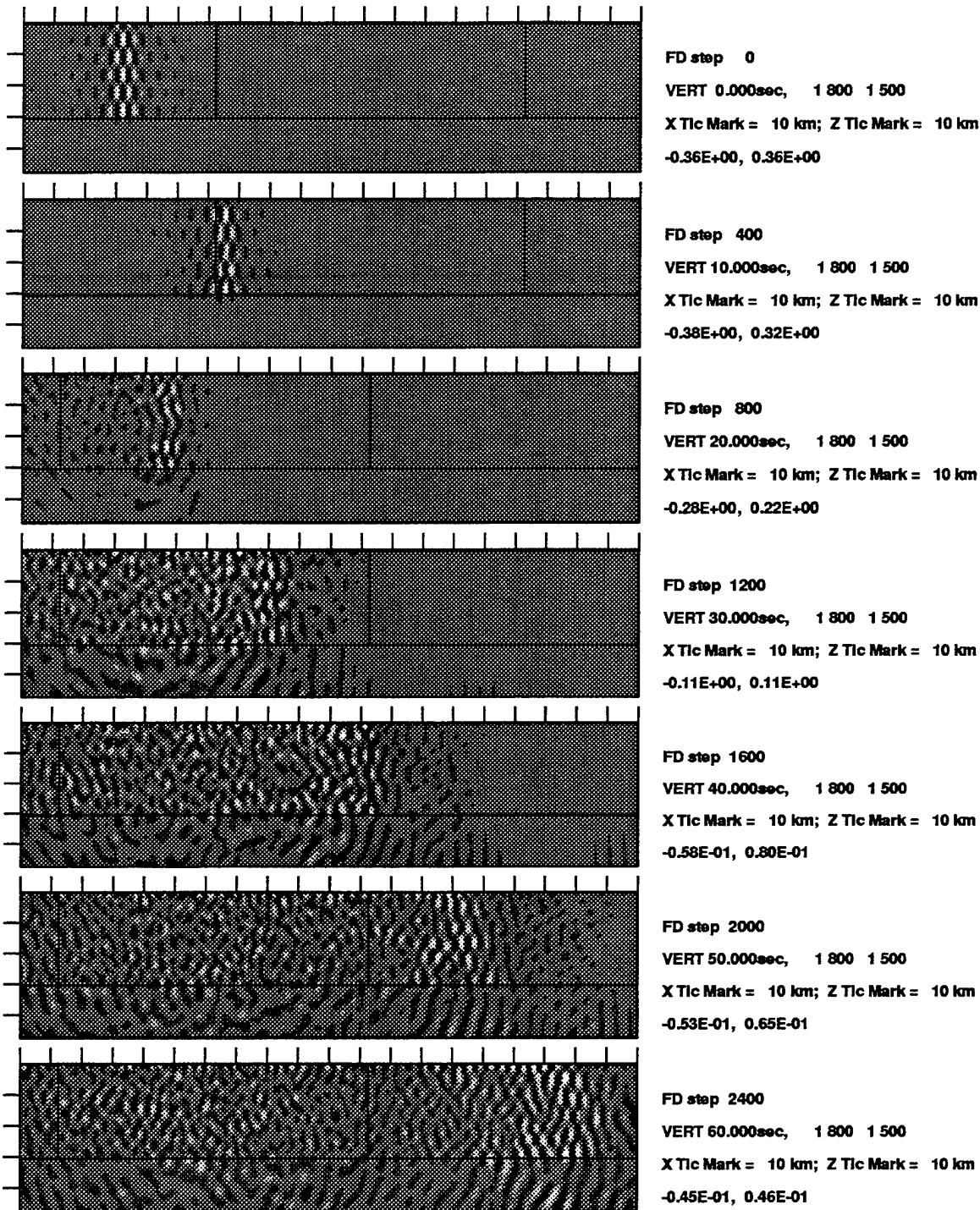
VERT, same scale, decimated by 5



Synthetics at 0km Depth, Model 0Y,10%

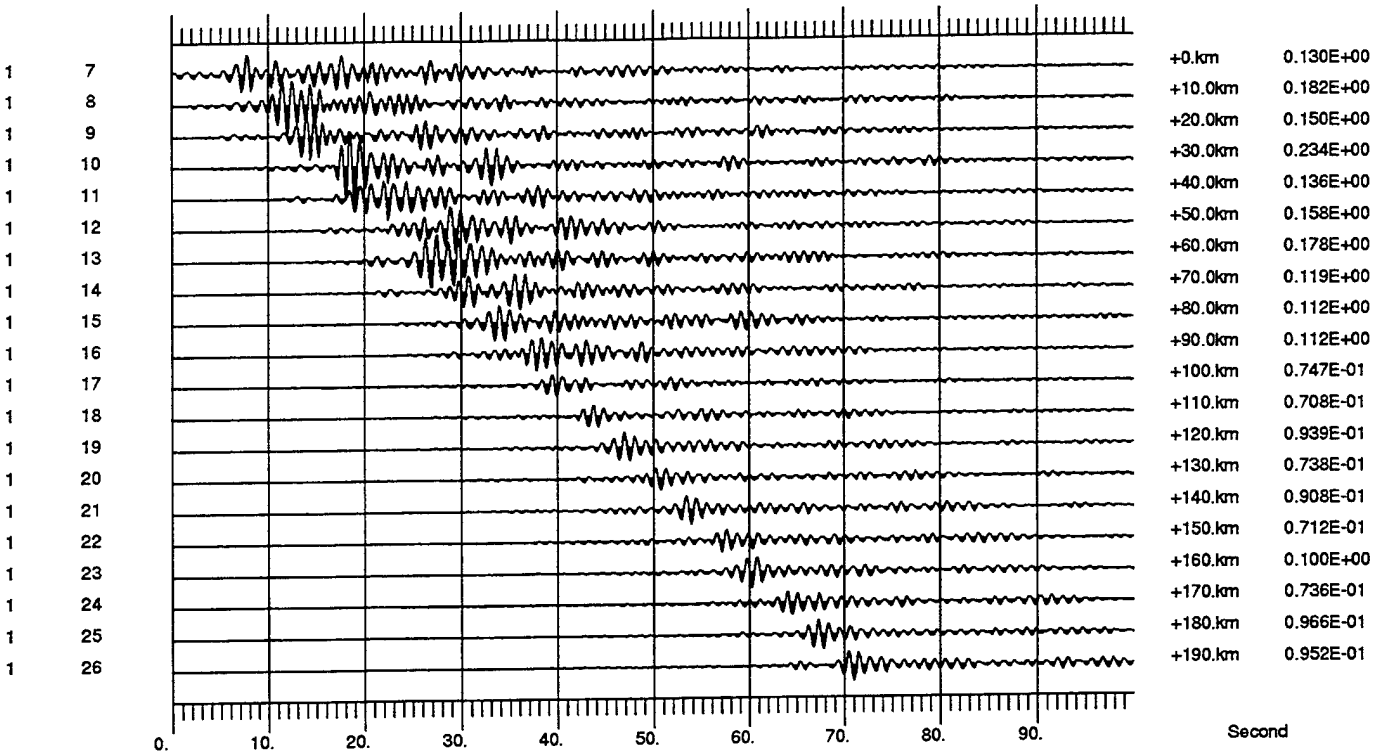
HORI, same scale, decimated by 5

Figure 64. Seismic sections of the model 0Y,10%. This model has 10 percent velocity variation in an embedded heterogeneous volume which is 100 km long and 30 km thick.



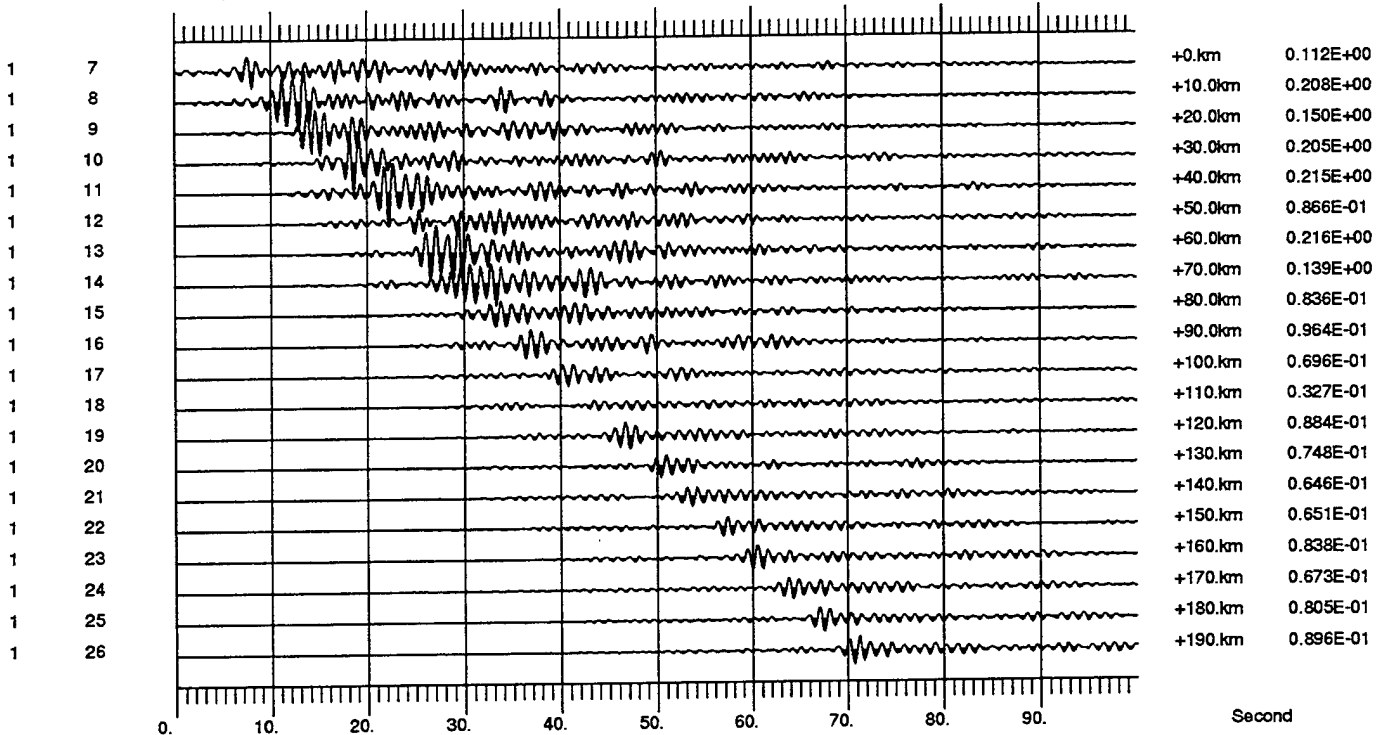
#### LFD Simulation of Lg Propagation: Model 0Y,20%

**Figure 65.** The vertical-component snapshots of  $L_g$  wave propagation in a single-layer model embedded with a heterogeneous portion 100 km long and 30 km thick in it. The self-similar random heterogeneity in this sandwiched portion has an RMS velocity fluctuation of 20% and a scale length of 1 km. The strong scattering generates a very complicated wavefield (as compared to Figure 63). Much of the scattered energy would contribute to coda waves.



Synthetics at 0km Depth, Model 0Y,20%

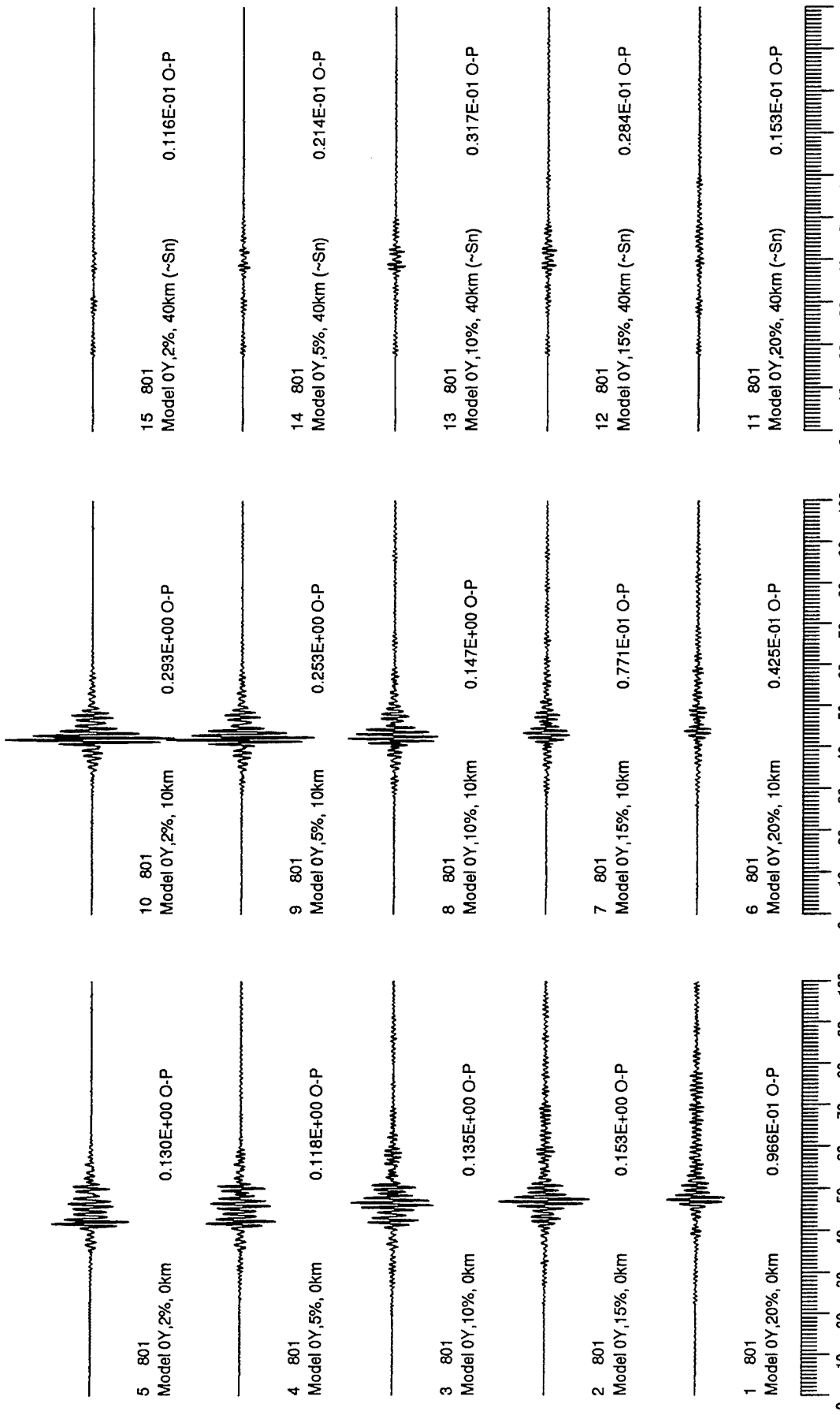
VERT, same scale, decimated by 5



Synthetics at 0km Depth, Model 0Y,20%

HORI, same scale, decimated by 5

**Figure 66.** Seismic sections of the model 0Y,20%. This model has 20% velocity variation in an embedded heterogeneous volume which is 100 km long and 30 km thick. This model generates very long coda, as expected. Also note that the centroid of the  $L_g$  wave packet is delayed.



### Synthetics (@ 3 Depths) of Various Crustal Models: 0Y,20%, 0Y,15%, 0Y,10%, 0Y,5%, 0Y,2%

**Figure 67.** Synthetics recorded at 3 depths (0km, 10km, and 40km) after crossing a heterogeneous zone 100 km wide and 30 km thick. As the velocity fluctuation increases from 2 percent (top) to 20 percent (bottom), the  $L_g$  amplitude decreases (as expected). The centroid of the  $L_g$  wave train also gets delayed somewhat. The  $L_g$ -to- $S_n$  coupling decays once the RMS variation is greater than 13-15 percent, presumably because most of the energy has already been lost to scattering in all directions. A variation of 2 percent leads to very little scattering and hence the synthetics are very similar to those of the reference model (see Figure 61).

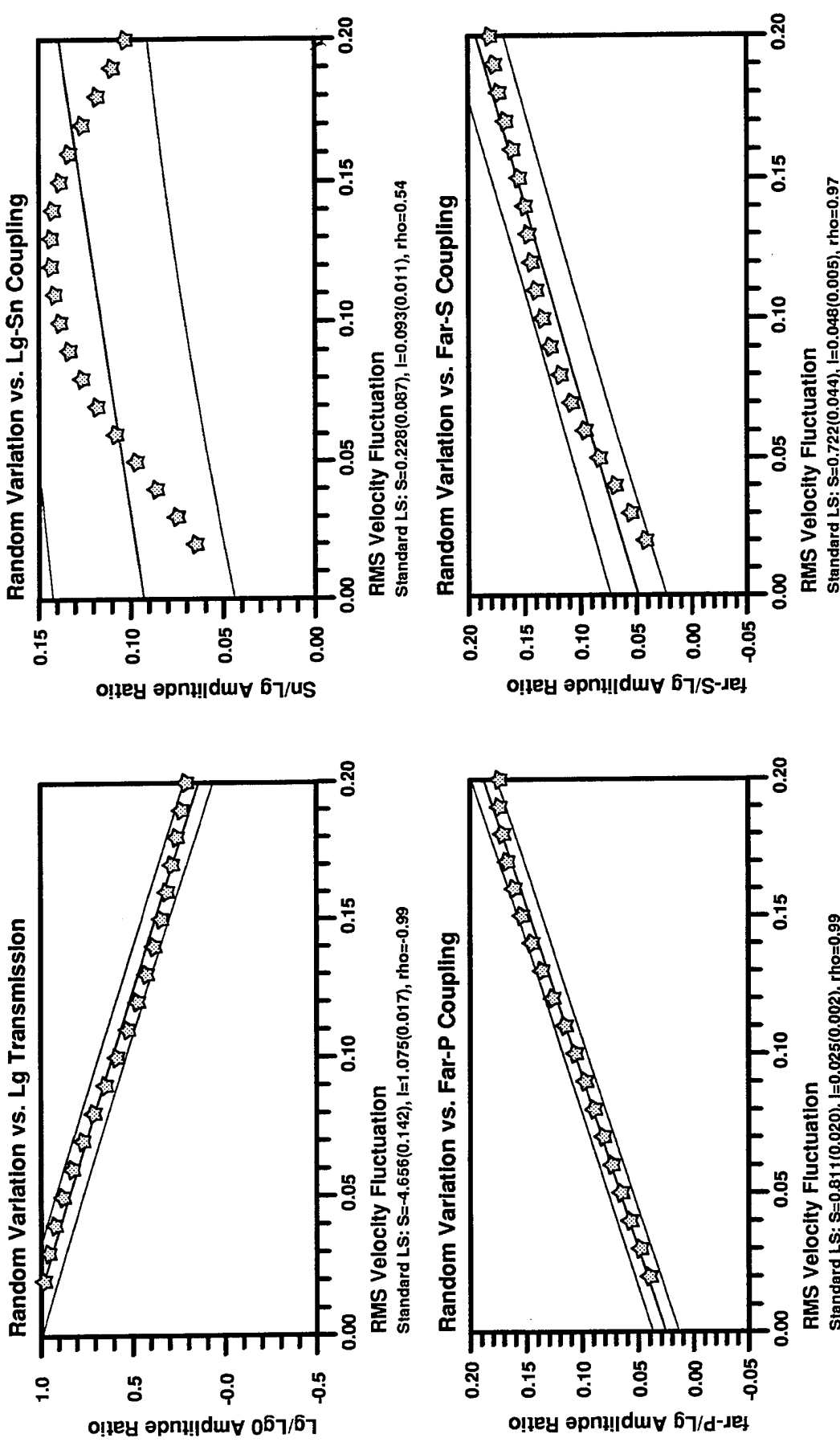


**Figure 68.** Regressing the  $L_g$  transmission coefficient (top left),  $S_n/L_g$  amplitude ratio (top right), far-P/ $L_g$  amplitude ratio (bottom left), and far-S/ $L_g$  amplitude ratio (bottom right). As the model becomes more heterogeneous (that is, has a larger RMS velocity variation), the  $L_g$ -to- $S_n$  coupling as well as the coupling to teleseismic phases become more prominent.

## 6. REMARKS ON OBSERVATIONS OF $L_g$ BLOCKAGE AND A MODEL-BASED CORRECTION PROCEDURE

Baumgardt (1991) conducted a thorough observational study of  $L_g$  blockage for Soviet explosions recorded at regional or far-regional distances. He documented several examples of partial and complete blockage and carefully related the possible cause of each case to geological and geophysical characteristics along the path. Baumgardt found that in every instance of partial or complete blockage, the great-circle path of  $L_g$  between the source and the receiver crosses contained sedimentary basins and adjacent topographic discontinuities.  $L_g$  blockage does not seem to relate to variations in total crustal thickness. Blockages result from basins where there are unusually thick sediments, usually in excess of 10 km, where the basin is fully contained and the sediments pinch out at the edges of the basin, and/or where there are topographic inhomogeneities at the edges of the basin. He observed less blockage for events occurring inside sedimentary basins themselves, where the basins are not particularly thick, or where the sediments thin very gradually with distance. Table 4 below summarizes observations of  $L_g$  blockage and weakening, along with the possible mechanism that has been proposed.

Table 5 Observed  $L_g$  Blockage/Weakening and Proposed Mechanism(s)

Mechanism Proposed	Author(s)	Region Studied
Dramatic thinning of waveguide	Ewing <i>et al.</i> (1957)	continent-ocean margin
Pure oceanic paths	Knopoff <i>et al.</i> (1979)	Atlantic & Pacific Oceans
Missing granitic layer	Piwinski (1981)	Caspian Sea
Crustal thickening	Ruzaikin <i>et al.</i> (1977)	Himalayan Belt
Variations in crustal thickness (+Q?)	Gregersen (1984)	North Sea Graben
Variations in crustal thickness	Kennett <i>et al.</i> (1985)	North Sea Graben
Anelastic attenuation in sediments	Mitchell & Hwang (1987)	U.S.
Scattering by small-scale heterogeneity	Campillo <i>et al.</i> (1993)	SW Alpine Range
Scattering by small-scale heterogeneity	Chazalon <i>et al.</i> (1993)	Western Pyrenean Range
Scattering from tectonic boundaries	Kadinsky-Cade <i>et al.</i> (1981)	Turkish & Iranian Plateaus
Scattering from tectonic boundaries	Ni & Barazangi (1983)	Tibetan Plateau
Scattering from tectonic boundaries	Baumgardt (1985, 1990)	Ural Mountains
Contained thick sedimentary basin	Baumgardt (1991)	Barents Shelf
Contained thick sediments (+low Q?)	Baumgardt (1991)	North Caspian Depression

The importance of understanding crustal waveguide effects on  $L_g$  waves has motivated many modeling studies of blockage in recent years (Kennett, 1986a; Maupin, 1989; Regan and Harkrider, 1989; Chazalon *et al.*, 1993; Gibson and Campillo, 1994; and Cao and Muirhead, 1993). Some of these authors suggest that the observed blockage is not straightforward to simulate, and that the unmodeled small-scale random heterogeneity is required to account for the blockage, on top of the large-scale structural (that is, geometrical) variation of the waveguide. Although either low Q or large velocity variation can be invoked to explain the  $L_g$  blockage of many paths, we might be able to narrow down the possible mechanisms with some additional diagnostic information. For instance, if a pronounced  $L_g$ -to- $S_n$  conversion is observed along with the  $L_g$  blockage, then it is likely that the blocking mechanism is not due to low Q.

One the major challenges in monitoring a Comprehensive Test Ban Treaty [CTBT] is discriminating small events at regional distances. Various forms of compressional/shear (P/S) ratios have been proposed and extensively tested as candidate discriminants. In tackling such problems, a better amplitude (or, equivalently, magnitude) scale of the regional phase of interest, with respective path effects carefully accounted for, is definitely useful or sometimes even necessary. Along this line of thought, Jih *et al.* (1995) (and also Jih and Lynnes, 1993) suggest a simple, convenient magnitude scale for  $L_g$ :

$$m_{L_g} = 4.0272 - \text{Bias} + \log A(\Delta) + \frac{1}{3} \log(\Delta(\text{km})) + \frac{1}{2} \log[\sin(\frac{\Delta(\text{km})}{111.1(\text{km}/\text{deg})})] + \frac{\gamma(\Delta-10\text{km})}{\ln(10)}, \quad [5]$$

$$\text{where } \gamma = \frac{\pi \cdot f}{Q \cdot U}, \quad Q(f) = Q_0 \cdot f^c,$$

$\Delta$  is the epicentral distance in km and  $A(\Delta)$  is the observed raw  $L_g$  amplitude measured in the time domain in  $\mu\text{m}$  [microns] at the epicentral distance of  $\Delta$  km. Or, equivalently,

$$\hat{A}_{L_g} = A(\Delta) \cdot 10^{4.0272 - \text{Bias}} \cdot (\Delta(\text{km}))^{\frac{1}{3}} \cdot [\sin(\frac{\Delta(\text{km})}{111.1(\text{km}/\text{deg})})]^{\frac{1}{2}} \cdot e^{\gamma(\Delta-10\text{km})}. \quad [5a]$$

The "Bias" term in Eqs. (5) and (5a) is meant to account for the different  $L_g$  excitation (relative to  $m_b$ ). It is set to zero for the Eastern U.S. Thus a seismic source with 1-sec  $L_g$  amplitude of 110  $\mu\text{m}$  at 10 km (extrapolated) epicentral distance would correspond to a  $m_{L_g}$  of  $4.0272 + 2.0414 + 0.3333 - 1.4019 + 0.0000 = 5.000$ , which has been suggested to be appropriate for both Eastern North America and Semipalatinsk. That is to say, a seismic source in these two regions with  $m_b$  5.0 would have a  $m_{L_g}$  approximately the same. Jih *et al.* (1995) suggest use of 0.34 and 0.26 m.u. for the "Bias", respectively, for Pahute Mesa and Novaya Zemlya explosions. For earthquakes in the Iranian Plateau, Nuttl (1980) suggested a bias value of 0.39 m.u., which includes both the bias due to regional tectonics as well the  $L_g$ -mb bias due to source type.

If the regionalized  $\gamma$  map is available (such as those in Singh and Herrmann, 1983; Jih and Lynnes, 1993; and many others) a path-specific  $\gamma$  for an arbitrary source-station pair can simply be computed as the weighted sum of the  $\gamma_k$ 's of the subregions that the ray path traverses:

$$\gamma = \sum_{k=1}^K \gamma_k \cdot \frac{\Delta_k}{\Delta} . \quad [6]$$

However, it is clear from Eq. (2) that an erroneous path  $\gamma$  would yield a  $m_{L_g}$  bias that increases with the distance. Furthermore, this error is independent of the actual source size or the quality of the raw amplitude measured at the recording station. It is *the bias* solely due to inaccurate calibration of the propagation effect. Jih and Lynnes (1993) gave several examples showing how  $L_g$  amplitude measurements could be severely biased if a poor estimate of the path  $\gamma$  is used or if the path  $\gamma$  is not used at all. Baumgardt (1995) recently demonstrated that by incorporating a distance-correction term, which is essentially the  $e^{\gamma \cdot \Delta}$  in Eq. (5a), into his  $P_g/L_g$  ratio computation, a much better discrimination result was obtained. In fact, this is exactly the same reason why Nuttli's (1986, 1988) absolute yield estimates of underground nuclear explosions using path-corrected  $m_{L_g}$  are good.

The seismic discrimination problem is actually intertwined with the source-size determination problem, despite the misperception that the estimation of source size in general (and the estimation of explosive yield in particular) may no longer be as important in the CTBT context. P/S-ratio-based discrimination is a procedure to discern differences in energy partitioning among phases and among frequency bands. Miscellaneous amplitude measurements needed to identify the event are actually reflecting different parts of the focal sphere and/or frequency contents of the seismic source itself. These parameters are often obscured by the path effects. Thus, a better path-calibration procedure would always benefit the discrimination, for just the same reason it would benefit the source-size determination.<sup>2</sup>

In a situation where some geometrical blockage occurs along the path, that is, there is a major structural variation along the path, it may be possible to further refine Eq. (5). As an example, the  $\gamma(\Delta - 10\text{km})/\ln(10)$  term for the path from Novaya Zemlya to KEV can be broken down into  $\gamma_1 \cdot (\Delta_1 - 10\text{km})/\ln(10) + \gamma_2 \cdot \Delta_2/\ln(10)$ , where  $\gamma_2 = 0.0052$  (that is,  $Q_0 = 185$ ; see the model 0D in Table 2),  $\Delta_2$  is the lateral span of the Terrigenous Sediments (Baumgardt, 1991), and  $\gamma_1$  is the average  $L_g$  attenuation along the great-circle path excluding the sedimentary segment. Obviously it is necessary to acquire relevant geological and geophysical information along the path before applying this model-based correction.

---

<sup>2</sup> See discussion in Dainty (1995) and Blandford *et al.* (1992).

## 7. DISCUSSION AND CONCLUSIONS

An accurate prediction of the regional phases in areas of high proliferation concern requires a decent understanding of the attenuation and scattering mechanisms along the propagation paths. Synthetic data have been of great benefit in gaining physical insight into discriminants, and may be the only means of evaluating evasion scenarios. Synthetic seismograms are particularly useful for regions where earthquake or explosion data are not available. There is no doubt that both geometrical blockage (due to large-scale lateral structural variation), intrinsic attenuation, and small-scale random heterogeneity in the crust affect  $L_g$  propagation. But it is often very difficult to separate these effects observationally. Again, numerical modeling could be the only means to quantitatively identify the respective roles played by these factors.

In this study, the two-dimensional LFD method has been used to model the propagation and scattering of  $L_g$  waves in a suite of crustal models, including rough interfaces, rugged free-surface topography, and embedded thick sedimentary layers. Two non-standard techniques have been specifically developed for this study: [1] a pure  $L_g$  wave packet (for triggering LFD calculations), and [2] a crude, causal attenuation operator. The pure  $L_g$  wave packet is injected into a stratified portion of the grid as the reference initial condition to trigger all LFD calculations. This is a natural extension of Jih's (1993b) work on  $R_g$  to  $L_g$  problems. In addition to those commonly recognized advantages of LFD method, another obvious advantage of this approach is that the effect due to different types of heterogeneity on the seismic phase of interest can be isolated and evaluated easily. The other tool tested in this study is a new attenuation operator suitable for time-domain numerical calculations. As a crude approximation, it applies to only a narrow band within which it gives a nearly frequency-independent  $\gamma$ , as expected. The most notable advantage is its simplicity to implement. Furthermore, it is a causal operator which, at least conceptually, is more realistic. Overall it appears to perform reasonably well. Major observations made with LFD calculations are summarized in the following:

**Early  $L_g$ :** The Moho uplift, which is common in models of the "A" and "F" series, breaks down the  $L_g$  waveguide and causes  $L_g$ -to- $S_n$  coupling at the ascending interface. When the converted  $S_n$  waves encounter the descending Moho of these models, some energy penetrates the interface again, either as a leg of  $S_n$  or as converted  $L_g$ . The Moho uplift in "F"-series models is not as dramatic as in "A"-series models. Nevertheless, both the  $L_g$ -to- $S_n$  and possibly  $S_n$ -to- $L_g$  conversions are still apparent. The early  $L_g$  observed for paths from Novaya Zemlya to Scandinavia can be explained with this mechanism. The fact that  $L_g$  can be excited at continental margins from oceanic  $S_n$  conversion has long been observed and reported (for example, Isacks and Stephens, 1975).

**Late  $L_g$  and longer coda waves:** The sedimentary layer, which is present in all "C"-series models and some of "D" and "F" models, is the apparent cause of late  $L_g$  arrivals. For models 0Db, 0Fb and 0Fc, the uppermost soft layer causes strong reverberations as well as a very strong  $L_g$ -to- $R_g$  conversion. By seismic reciprocity, there should be some structures that would cause strong  $R_g$ -to- $L_g$  conversion. Part of this issue has been addressed in Jih (1995). Regarding the coda decay rate, intrinsic attenuation and scattering (particularly, that by random heterogeneity) appear to have different effects. Increased scattering attenuation causes more energy to be distributed into the coda from the direct phase with increasing time. On the other hand, increased intrinsic attenuation entails a greater loss of elastic energy with time from both the coda and the direct wave. This observation can be verified by comparing synthetic seismograms in Figures 61 and 67, and is in agreement with Frankel and Wennerberg (1987).

**$S_n$  excitation and  $S_n/L_g$  ratios:** Except for models 00, 2, 2a, 3, 3a, 0C, 0Ca, and 0Cb, all other models excite significant  $S_n$  waves through the  $L_g$ -to- $S_n$  conversion. A thick sedimentary layer by itself does not necessarily cause strong  $L_g$ -to- $S_n$  conversion. Models of the "C"-series are such examples. However, if the thick sediment layer is contained, such as in models of "D" series, then some  $S_n$  waves can be generated at the pinched interface. Models with irregular Moho topography generate  $S_n$  with a different mechanism, as discussed above. Most models excite converted  $S_n$  waves in the forward direction. However, models 0A and 0B also excite some  $S_n$  in the backward direction. The extremely large  $S_n/L_g$  ratio associated with models 0E, 0Ea, and 0Ec (all with a thickened crust) offers an excellent demonstration for the observation Ruzaikin *et al.* (1977) made.

**Topographic relief:** Models with a mild free-surface topography alone (for example, models 2 and 3) generate a relatively weak  $L_g$ -to- $S_n$  conversion comparable to that of "C" models. Comparing the synthetics in Figures 55 and 58, it appears that the transmitted  $L_g$  wave trains of models with mild mountainous topography are very similar to those of the reference model 00. In fact, these mountainous models and models with weak random heterogeneity as well as anelastic models would stand out among all models in that the checkerboard-like interference pattern of the original  $L_g$  wave train is (somewhat) retained (see Figures 45, 49, 59, and 62). This is very different from the case of  $R_g$  for which the rugged free-surface topography is shown to be a strong scatterer (Jih, 1993b, 1995).

**$Lg$  to  $Pg$  conversion:** All models of the "F" series exhibit significant  $L_g$ -to- $P_g$  conversion. The peak horizontal amplitude on trace No. 25 ranges from 10 to 15 percent of that of the original  $L_g$  wave train. To a lesser extent, models of "C" and "D" series as well as models 0A and 0Ba also generate the same conversion.

**Coupling to teleseismic phases:** For mountainous models,  $L_g$ -to-S is twice as strong as  $L_g$ -to-P. For the "A" and "B" series of models, as well as the random media, these two mechanisms are

about equally strong. For anelastic models and "C"-type models,  $L_g$ -to-S is weaker than the  $L_g$ -to-P, whereas models of the "D", "E", and "F" series show the opposite trend (Table 2).

**Lg blockage:** Both abrupt changes in the Moho topography and a thick contained sedimentary layer can cause strong  $L_g$ -to- $S_n$  conversions. The physical mechanisms underlying the conversion are different for these two structures, however. The early  $L_g$  observed for paths from Novaya Zemlya island to Scandinavia is illustrated with LFD calculations. Alluvial basin structures cause strong reverberations as well as very strong  $L_g$ -to- $R_g$  conversions. Valley structures with large depth to width ratios and large velocity contrast with the substrate support very large amplitude lateral resonance modes. If we invoke the principle of seismic reciprocity,  $R_g$ -to- $L_g$  conversion could be an important mechanism of  $L_g$  excitation for certain structures. Recent observational study by Patton and Taylor (1995) suggests that this is the case, at least for Yucca Flat explosions.

Other than major structural discontinuities in the crustal waveguide, both anelasticity and small-scale random heterogeneity can also contribute to the so-called " $L_g$  blockage". For instance, an RMS velocity variation of 8 percent in the whole crust is equivalent to a  $Q_0(L_g)$  of about 270, which would be sufficient to reduce the peak amplitude of 1Hz  $L_g$  waves by 30 percent for every 100 km they traverse. The classical example of an  $L_g$ -blocking path between Novaya Zemlya and northern Scandinavia has a  $Q_0(L_g)$  about 252 and could be modeled with an RMS velocity variation of 8 percent alone.

Unlike  $R_g$  waves,  $L_g$  propagation is not affected by a moderate free-surface topography alone as much as other types of heterogeneity. Topographic relief has been shown to be a very strong scatterer for the  $R_g$  phase (Jih, 1993b, 1995). This is because  $R_g$  energy is confined in the uppermost layer. The energy of  $L_g$  is evenly distributed in the crust, and the surface topography variations are generally small relative to the crustal thickness. Thus it may be expected that the topographic variations alone should have relatively weaker influence on  $L_g$  propagation, as compared to  $R_g$ . This is illustrated with models 2 and 3 of this study. However, the topography may reflect the crustal thickness through isostasy. Zhang and Lay (1994) suggest that  $S_n/L_g$  ratios may be correlated to some roughness measures of the paths, based on a limited data set. LFD appears to be the ideal tool to test the existence of any correlation between some roughness measure and the propagation characteristics of regional phases, as demonstrated with the very few mountainous models tested in this study. Similar statistical analysis should also be conducted to examine the effects of water column, random Moho topography, and irregular intra-crustal interfaces, as well as the combination of all these factors.

## REFERENCES

Bache, T. C., H. Swanger, and B. Shekoller (1981). *Synthesis of  $L_g$  in Eastern United States crustal models with frequency independent Q*, Report SSS-R-81-4668. S-Cubed, La Jolla, CA.

Baumgardt, D. R. (1985), Comparative analysis of teleseismic P coda and  $L_g$  waves from underground nuclear explosions in Eurasia: *Bull. Seism. Soc. Am.*, **75**, 1413-1434.

Baumgardt, D. R. (1991). *High frequency array studies of long range  $L_g$  propagation and the causes of  $L_g$  blockage and attenuation in the Eurasian continental craton*, Report PL-TR-91-2059(II), Phillips Laboratory, Hanscom AFB, MA (ADA 236984).

Baumgardt, D. R. (1995). Cross region analysis, path corrections and the transportability of regional seismic discriminants, in *Proceedings of 17th PL/AFOSR Seismic Research Symposium* (12-15 Sept 1995, Scottsdale, AZ; J. Lewkowicz, J. McPhetres, and D. Reiter eds.), *Report PL-TR-95-2108*, Phillips Laboratory, Hanscom AFB, MA, pp. 27-35.

Blandford, R. R. (1981). Seismic discrimination problems at regional distances, in *Identification of Seismic Sources - Earthquake or Underground Explosion*, (E. S. Husebye and S. Mykkeltveit, eds.), D. Reidel Publishing Co., Dordrecht, The Netherlands, 695-740.

Blandford, R. R., A. Dainty, R. Lacoss, R. Maxion, A. Ryall, B. Stump, C. Thurber, and T. Wallace (1992). *Report on the DARPA Seismic Identification Workshop*, DARPA/NMRO Special Topical Report, 28 pp.

Boore, D. (1970). Love waves in nonuniform wave guides: finite-difference calculations, *J. Geophys. Res.*, **75**, 1512-1527.

Bouchon, M. (1982). The complete synthesis of seismic crustal phases at regional distances, *J. Geophys. Res.*, **87**, 1735-1741.

Campillo, M., B. Feignier, M. Bouchon, and N. Bethoux (1993). Attenuation of crustal waves across the Alpine range, *J. Geophys. Res.*, **98**, 1987-1996.

Campillo, M., M. Bouchon, and B. Massinon (1984). Theoretical study of the excitation, spectral characteristics, and geometrical attenuation of regional seismic phases, *Bull. Seism. Soc. Am.*, **74**, 79-90.

Cao, S. and K. J. Muirhead (1993). Finite difference modeling of  $L_g$  blockage, *Geophys. J. Int.*, **115**, 85-96.

Cerjan, C., D. Kosloff, R. Kosloff, and M. Reshef (1985). A nonreflecting boundary condition for discrete acoustic and elastic wave equations, *Geophysics*, **50**, 705-708.

Chazalon, A., M. Campillo, R. Gibson, and E. Garnero (1993). Crustal wave propagation anomaly across the Pyrenean Range - comparison between observations and numerical simulations, *Geophys. J. Int.*, **115**, 829-838.

Dainty, A. M. (1981). A scattering model to explain seismic Q observations in the Lithosphere between 1 and 30 Hz, *Geophys. Res. Lett.*, **8-11**, 1126-1128.

Dainty, A. M. (1995). The influence of seismic scattering on monitoring, in "Monitoring a Comprehensive Test Ban Treaty" (E. S. Husebye and A. M. Dainty (eds), NATO ASI Series E: Applied Sciences, Vol. 303, pp.663-688, Kluwer Academic Press, Dordrecht, The Netherlands.

Day, S. M. and J. B. Minster (1984). Numerical simulation of wavefields using a Pade approximation method, *Geophys. J. R. Astr. Soc.*, **78**, 105-118.

Emmerich, H. and M. Korn (1987). Incorporation of attenuation into time-domain computation of seismic wave fields, *Geophysics*, **52**, 1252-1264.

Ewing, M., W. S. Jardetsky, and F. Press (1957). *Elastic Waves in Layered Media*, McGraw Hill, New York.

Frankel, A. and R. W. Clayton (1986). Finite-difference simulation of seismic scattering: implications for the propagation of short-period seismic waves in the crust and models of crustal heterogeneity, *J. Geophys. Res.*, **91**, 6465-6489.

Frankel, A. and L. Wennerberg (1987). Energy-flux model of seismic coda: separation of scattering and intrinsic attenuation, *Bull. Seism. Soc. Am.*, **77**, 1223-1251.

Fuyuki, M. and Y. Matsumoto (1980). Finite-difference analysis of Rayleigh wave scattering at a trench, *Bull. Seism. Soc. Am.*, **70**, 2051-2069.

Fuyuki, M. and M. Nakano (1984). Finite-difference analysis of Rayleigh wave transmission past an upward step change, *Bull. Seism. Soc. Am.*, **74**, 893-911.

Gibson, R. and M. Campillo (1994). Numerical simulation of high- and low-frequency  $L_g$ -wave propagation, *Geophys. J. Int.*, **118**, 47-56.

Gregersen, S. (1984).  $L_g$ -wave propagation and crustal structure differences near Denmark and the North Sea, *Geophys. J. R. Astr. Soc.*, **79**, 217-234.

Hansen, R. A., Ringdal, F. and P. G. Richards (1990). The stability of RMS  $Lg$  measurements and their potential for accurate estimation of yields of Soviet underground nuclear explosions, *Bull. Seism. Soc. Am.*, **80**, 2106-2126.

Herrmann, R. B. (1987). *Computer Programs in Seismology*, Volume IV, Saint Louis Univ., Saint Louis, MO.

Isacks, B. L. and C. Stephens (1975). Conversions of  $S_n$  to  $L_g$  at continental margin, *Bull. Seism. Soc. Am.*, **65**, 235-244.

Jacobson, R. S. (1987). An investigation into the fundamental relationship between attenuation, phase dispersion, and frequency using seismic refraction profiles over sedimentary structures, *Geophysics*, **52**, 72-87.

Jih, R.-S. (1993a). *User's manual of FD2: a software package for modeling seismological problems with 2-dimensional linear finite-difference method*, Report TGAL-93-06, Teledyne Geotech, Alexandria, VA.

Jih, R.-S. (1993b). *Statistical characterization of rugged propagation paths with application to  $R_g$  scattering study*, Report TGAL-93-07, Teledyne Geotech, Alexandria, VA.

Jih, R.-S. (1994). Numerical modeling of crustal phase propagation in irregular waveguides, in *Proceedings of 16th PL/AFOSR Seismic Research Symposium* (7-9 Sept 1994, Thornwood, NY; J. Cipar, J. Lewkowicz, and J. McPhetres, eds.), Report PL-TR-94-2217, Phillips Laboratory, Hanscom AFB, MA, pp. 173-181 (ADA284667).

Jih, R.-S. (1995). Numerical investigation of relative contributions of  $R_g$  scattering and attenuation to

$L_g$  excitation, in *Proceedings of 17th PL/AFOSR Seismic Research Symposium* (12-15 Sept 1995, Scottsdale, AZ; J. Lewkowicz, J. McPhetres, and D. Reiter eds.), Report PL-TR-95-2108, Phillips Laboratory, Hanscom AFB, MA, pp. 401-410.

Jih, R.-S. (1996). *A simple, causal method to incorporate anelastic attenuation into finite-difference calculations*, Report PL-TR-96-2015, Phillips Laboratory, Hanscom AFB, MA.

Jih, R.-S. and C. S. Lynnes (1993). *Studies of regional phase propagation in Eurasia*. Report PL-TR-93-2003 (=TGAL-93-01), Phillips Laboratory, Hanscom AFB, MA (ADA 262801).

Jih, R.-S. and K. L. McLaughlin (1988). *Investigation of explosion generated SV  $L_g$  waves in 2-D heterogeneous crustal models by finite-difference method*, Report AFGL-TR-88-0025 (=TGAL-88-01), Air Force Geophysics Laboratory, Hanscom AFB, MA (ADA 213586).

Jih, R.-S., K. L. McLaughlin and Z. A. Der (1988). Free boundary conditions of arbitrary polygonal topography in a 2-D explicit elastic finite difference scheme, *Geophysics*, **53**, 1045-1055.

Jih, R.-S., R. R. Baumstark, and R. A. Wagner (1995). Simultaneous inversion of event  $m_{Lg}$  and path attenuation coefficient with application to a transportable  $L_g$  magnitude scaling, in *Proceedings of 17th PL/AFOSR Seismic Research Symposium* (12-15 Sept 1995, Scottsdale, AZ; J. Lewkowicz, J. McPhetres, and D. Reiter eds.), Report PL-TR-95-2108, Phillips Laboratory, Hanscom AFB, MA, pp. 411-419.

Kadinsky-Cade, K., M. Barazangi, J. Oliver, and B. L. Isacks (1981). Lateral variations of high-frequency seismic wave propagation at regional distances across the Turkish and Iranian Plateaus, *JGR*, **86**, 9377-9396.

Kennett, B. L. (1985). On regional  $S$ , *Bull. Seism. Soc. Am.*, **75**, 1077-1086.

Kennett, B. L. (1986a).  $L_g$  waves and structural boundaries, *Bull. Seism. Soc. Am.*, **76**, 1133-1141.

Kennett, B. L. (1986b). Wavenumber and wavetype coupling in laterally heterogeneous media, *Geophys. J. R. Astr. Soc.*, **87**, 313-331.

Kennett, B. L. (1989a). On the nature of regional seismic phases - I. Phase representations for  $P_n$ ,  $P_g$ ,  $S_n$ ,  $L_g$ , *Geophys. J.*, **98**, 447-456.

Kennett, B. L. (1989b).  $L_g$ -wave propagation in heterogeneous media, *Bull. Seism. Soc. Am.*, **79**, 860-872.

Kennett, B. L. N., S. Gregersen, S. Mykkeltveit, and R. Newmark (1985). Mapping of crustal heterogeneity in the North Sea Basin via the propagation of  $L_g$  waves, *Geophys. J. R. Astr. Soc.*, **83**, 299-306.

Knopoff, L., F. Schwab, and E. Kausel (1973). Interpretation of  $L_g$ , *Geophys. J.*, **33**, 398-404.

Knopoff, L., R. G. Mitchel, E. G. Kausel, and F. Schwab (1979). A search for the oceanic  $L_g$  phase, *Geophys. J. Roy. Astr. Soc.*, **56**, 211-218.

Levander, A. (1985). Finite-difference calculations of dispersive Rayleigh wave propagation, *Tectonophysics*, **113**, 1-30.

Levshin, A. and K. A. Berteussen (1979). Anomalous propagation of surface waves in the Barents Sea as inferred from NORSAR recordings, *Geophys. J. R. Astr. Soc.*, **56**, 97-118.

Lynnes, C. S. and R. Baumstark (1991). *Phase and spectral ratio discrimination in North America*, Report PL-TR-91-2212(II) (=TGAL-91-06), Phillips Laboratory, Hanscom AFB, MA (ADA 246673).

Martel, L., M. Munasinghe, and G. W. Farnell (1977), Transmission and reflection of Rayleigh wave through a step, *Bull. Seism. Soc. Am.*, **67**, 1277-1290.

Maupin, V. (1989). Numerical modeling of  $L_g$  wave propagation across the North Sea central graben, *Geophys. J. Int.*, **99**, 273-283.

McLaughlin, K. L. and L. M. Anderson (1987). Stochastic dispersion of short-period P waves due to scattering and multipathing, *Geophys. J. R. Astr. Soc.*, **89-3**, 933-963.

McLaughlin, K. L. and R.-S. Jih (1986). *Finite-difference simulations of Rayleigh wave scattering by 2-D rough topography*, Report AFGL-TR-86-0269 (=TGAL-86-09), Air Force Geophysics Laboratory, Hanscom AFB, MA (ADA 179190).

McLaughlin, K. L. and R.-S. Jih (1987). *Finite-difference simulations of Rayleigh wave scattering by shallow heterogeneity*, Report AFGL-TR-87-0322 (=TGAL-87-02), Air Force Geophysics Laboratory, Hanscom AFB, MA (ADA 194961).

Mitchell, B. J. and H. J. Hwang (1987). Effect of low Q sediments and crustal Q on Lg attenuation in the United States, *Bull. Seism. Soc. Am.*, **77**, 1197-1210.

Munasinghe, M. and G. Farnell (1973). Finite-difference analysis of Rayleigh wave scattering at vertical discontinuities, *J. Geophys. Res.*, **78**, 2454-2466.

Ni, J., and M. Barazangi (1983). High-frequency seismic wave propagation beneath the Indian Shield, Himalayan Arc, Tibetan Plateau, and surrounding regions: high uppermost mantle velocities and efficient  $S_n$  propagation beneath Tibet, *Geophys. J. R. Astr. Soc.*, **72**, 665-689.

Nuttli, O. W. (1980). The excitation and attenuation of seismic crustal phases in Iran, *Bull. Seism. Soc. Am.*, **70**, 469-485.

Nuttli, O. W. (1986). Yield estimates of Nevada Test Site explosions obtained from seismic  $L_g$  waves, *J. Geophys. Res.*, **91**, 2137-2151.

Nuttli, O. W. (1988).  $L_g$  magnitudes and yield estimates for underground Novaya Zemlya nuclear explosions, *Bull. Seism. Soc. Am.*, **78**, 873-884.

Oliver, J. and M. Ewing (1957). Higher modes of continental Rayleigh waves, *Bull. Seism. Soc. Am.*, **47**, 187-204.

Patton, H. J. (1988). Application of Nuttli's method to estimate yield of Nevada Test Site explosions recorded on Lawrence Livermore National Laboratory's digital seismic system, *Bull. Seism. Soc. Am.*, **78**, 1759-1772.

Patton, H. J. and S. R. Taylor (1995). Analysis of  $L_g$  spectral ratios from NTS explosions: implications for the source mechanisms of spall and the generation of  $L_g$  waves, *Bull. Seism. Soc. Am.*, **85**, 220-236.

Piwniskii, A. J. (1981). *Deep structure of the earth's crust and upper mantle in the USSR according to geological, geophysical, and seismological data: Dneiper-Donetsk and PriCaspian depressions*, Report UCID-19203, Lawrence Livermore Laboratory, Livermore, CA.

Pomeroy, P. W., W. J. Best, and T. V. McEvilly (1982). Test ban treaty verification with regional data --

a review, *Bull. Seism. Soc. Am.*, **72**, S89-S129.

Press, F. and M. Ewing (1952). Two slow surface waves across North America, *Bull. Seism. Soc. Am.*, **42**, 219-228.

Regan, J. and D. G. Harkrider (1989). Numerical modeling of  $SH$   $L_g$  waves in and near continental margins, *Geophys. J. Int.*, **98**, 107-130.

Ricker, N. H. (1977). *Transient Waves in Visco-elastic Media*, Elsevier Scientific Publishing Co., New York, NY.

Ruzaikin, A. I., I. L. Nersesov, V. I. Khalturin, and P. Molnar (1977). Propagation of  $L_g$  and lateral variation in crustal structure in Asia, *J. Geophys. Res.*, **82**, 307-316.

Savarrensky, E. and N. Valdner (1960). Observations of  $L_g$  and  $R_g$  waves from the Black Sea basin earthquakes, *Ann. Geofis.*, **13**, 129-134.

Singh, S. and R. B. Herrmann (1983). Regionalization of crustal coda Q in the continental United States, *J. Geophys. Res.*, **88**, 527-538.

Toksoz, M. N., A. M. Dainty, and E. E. Charrette (1986). *Development of ultrasonic modeling techniques for the study of seismic wave scattering due to crustal inhomogeneities*, Report AFGL-TR-86-0078, Air Force Geophysics Laboratory, Hanscom AFB, MA (ADA 170062).

Vidale, J. and D. V. Helmberger (1988). Elastic finite-difference modeling of the 1971 San Fernando, California, earthquake, *Bull. Seism. Soc. Am.*, **78**, 122-141.

Zhang, T. and T. Lay (1994). Analysis of short-period regional phase path effects associated with topography in Eurasia, *Bull. Seism. Soc. Am.*, **84**, 119-132.

## DISTRIBUTION LIST

### NON-GOVERNMENT RECIPIENTS

Prof. Thomas Ahrens  
Prof. Donald V. Helmberger  
Dr. Larry J. Burdick  
Division of Geology & Planetary Sciences  
California Institute of Technology  
Pasadena, CA 91125 (3 copies)

Prof. Shelton Alexander  
Prof. Charles A. Langston  
Geosciences Department  
403 Deike Building  
The Pennsylvania State University  
University Park, PA 16802 (2 copies)

Dr. Thomas C. Bache, Jr.  
Dr. Thomas J. Sereno, Jr.  
Dr. Jeffrey W. Given  
Science Applications Int'l Corp.  
10260 Campus Point Drive  
San Diego, CA 92121 (3 copies)

Dr. Douglas R. Baumgardt, Dr. Zoltan A. Der  
ENSCO, Inc.  
5400 Port Royal Road  
Springfield, VA 22151 (2 copies)

Dr. Eric P. Chael, Dr. Dale Breding  
Dr. Larry S. Walker, Dr. Gary Mauth  
Sandia National Laboratory  
Division 9241  
Albuquerque, NM 87185 (4 copies)

Dr. Theodore Cherry  
Science Horizons, Inc.  
710 Encinitas Blvd, Suite 200  
Encinitas, CA 92024

Prof. Steven M. Day  
Dept. of Geological Sciences  
San Diego State University  
San Diego, CA 92182

Dr. Mark D. Fisk  
Mission Research Corporation  
735 State Street  
P.O. Drawer 719  
Santa Barbara, CA 93102

Prof. Cliff Frolich, Dr. Lian-She Zhao  
Institute of Geophysics  
8701 North Mopac  
Austin, TX 78759 (2 copies)

Ms. Lori Grant  
Multimax, Inc.  
311-C Forest Avenue, Suite 3  
Pacific Grove, CA 93950

Prof. Henry L. Gray, Prof. Gary McCartor  
Dept. of Physics  
Southern Methodist University  
Dallas, TX 75275 (2 copies)

Dr. Indra N. Gupta  
Multimax, Inc.  
1441 McCormick Drive  
Landover, MD 20785

Dr. Richard A. Gustafson, Dr. Robert North  
Dr. Jerry Carter  
Center for Monitoring Research  
1300 North 17th Street, Suite 1450  
Arlington, VA 22209-2308 (4 copies)

Dr. Willard J. Hannon  
Lawrence Livermore National Laboratory  
P.O. Box 808  
Livermore, CA 94550

Prof. David G. Harkrider  
Boston College @ PL/GPE  
29 Randolph Road  
Hanscom AFB, MA 01731

Prof. Eugene T. Herrin, Jr.  
Geophysical Laboratory  
Southern Methodist University  
Dallas, TX 75275

Prof. Robert B. Herrmann  
Prof. Brian J. Mitchell  
Dept. of Earth & Atmospheric Sciences  
St. Louis University  
St. Louis, MO 63156 (2 copies)

Prof. Bryan Isacks, Prof. Muawia Barazangi  
Dept. of Geological Sciences  
SNEE Hall  
Cornell University  
Ithaca, NY 14850 (2 copies)

Prof. Lane R. Johnson  
Prof. Thomas V. McEvilly  
Seismographic Station  
University of California  
Berkeley, CA 94720 (2 copies)

Prof. Thomas H. Jordan  
Dept. of Earth, Atmospheric  
and Planetary Sciences  
Massachusetts Institute of Technology  
Cambridge, MA 02139

Prof. Thorne Lay, Prof. Susan Schwartz  
Institute of Tectonics  
University of California, Santa Cruz  
Santa Cruz, CA 95064 (2 copies)

Dr. Randolph Martin, III  
New England Research , Inc.  
76 Olcott Drive  
White River Junction, VT 05001

Dr. Keith L. McLaughlin  
Dr. Jeffrey L. Stevens  
Dr. Terrance G. Barker  
Maxwell Laboratories, S-Cubed Division  
P.O. Box 1620  
La Jolla, CA 92038 (3 copies)

Mr. John R. Murphy, Dr. Theron J. Bennett  
Maxwell Laboratories, S-Cubed Division  
11800 Sunrise Valley Drive, Suite 1212  
Reston, VA 22091 (2 copies)

Dr. Dan N. Hagedorn, Dr. Ray Warner  
Pacific Northwest Laboratories  
Battelle Boulevard  
Richland, WA 99352 (2 copies)

Prof. John A. Orcutt, Prof. Bernard Minster  
Prof. Freeman Gilbert  
IGPP, A-025  
Scripps Institute of Oceanography  
University of California, San Diego  
La Jolla, CA 92093 (3 copies)

Dr. Jay J. Pulli  
Radix Systems, Inc.  
6 Taft Court  
Rockville, MD 20850

Prof. Paul G. Richards, Prof. Lynn R. Sykes  
Prof. William Menke, Prof. Arthur Lerner-Lam  
Prof. David G. Simpson  
Lamont-Doherty Earth Observatory  
of Columbia University  
Palisades, NY 10964 (6 copies)

Dr. Chandan K. Saikia, Dr. Bradley B. Woods  
Woodward-Clyde Consultants  
566 El Dorado Street  
Pasadena, CA 91109-3245 (2 copies)

Prof. Charles G. Sammis, Prof. Keiichi Aki  
Center for Earth Sciences  
University of Southern California  
University Park  
Los Angeles, CA 90089 (2 copies)

Dr. Brian W. Stump, Dr. Steven R. Taylor,  
Dr. Wendee Brunish, Dr. Mark Hodgson  
Dr. Fredrick N. App, Dr. James R. Kamm  
Los Almos National Laboratory  
EES-3, MS C-335  
Los Almos, NM 87545 (6 copies)

Prof. Clifford Thurber, Prof. Robert P. Meyer  
University of Wisconsin-Madison  
Dept. of Geology & Geophysics  
1215 West Dayton Street  
Madison, WI 53706 (2 copies)

Prof. M. Nafi Toksöz, Dr. William Rodi  
Dr. Richard L. Gibson, Dr. Yingping Li  
Earth Resources Laboratory  
Mass. Institute of Technology  
42 Carleton Street  
Cambridge, MA 02142 (4 copies)

Verification Program  
Attn: Dr. Jay Zucca  
Lawrence Livermore National Laboratory  
P.O. Box 808, L205  
Livermore, CA 94550 (12 copies)

Prof. Terry C. Wallace, Prof. Susan L. Beck  
Dept. of Geosciences/SASO  
University of Arizona  
Tucson, AZ 85721 (2 copies)

#### **U.S. GOVERNMENT AGENCIES**

DARPA/OASB/Librarian  
3701 N. Fairfax Drive  
Arlington, VA 22303-1714

Dr. Ralph W. Alewine, III  
Dr. Steven R. Bratt  
Nuclear Treaty Programs Office  
Rosslyn Gateway  
1901 N. Moore Street, Suite 609  
Arlington, VA 22209 (2 copies)

Dr. Robert R. Blandford  
AFTAC/TT, Center for Monitoring Research  
1300 N. 17th Street, Suite 1450  
Arlington, VA 22209

Defense Technical Information Center  
8725 John J. Kingman Road  
Fort Belvoir, VA 22060-6218 (2 copies)

Dr. Anton W. Dainty, Dr. John J. Cipar  
Dr. Katharine Kadinsky-Cade, Mr. Rong-Song Jih  
Earth Sciences Division (PL/GPE)  
Phillips Lab./ Geophysics Directorate  
Hanscom AFB, MA 01731 (4 copies)

Dr. Stanley K. Dickinson  
AFOSR/NM  
110 Duncan Avenue, Suite B115  
Bolling AFB  
Washington, DC 20331-6448

Dr. Dale Glover  
U.S. DIA/DT-IB  
Washington, DC 20301

HQ AFTAC/CA  
(STINFO)  
1030 South Highway A1A  
Patrick AFB, FL 32925-6001

HQ AFTAC/TTR  
1030 South Highway A1A  
Patrick AFB, FL 32925-6001 (12 copies)

HQ AFTAC/TTD  
1030 South Highway A1A  
Patrick AFB, FL 32925-6001 (3 copies)

Dr. Max Koontz, Dr. Joan B. Rohlwing  
Dr. Leslie A. Casey, Dr. Stan Rudnick  
U.S. Dept. of Energy/NN-20  
Forrestal Building  
1000 Independence Avenue  
Washington, DC 20585 (4 copies)

Dr. Leonard E. Johnson  
National Science Foundation  
Division of Earth Sciences  
4201 Wilson Boulevard, Suite 785  
Arlington, VA 22230

Dr. William S. Leith  
Mr. John Rodney Matzko  
U.S. Geological Survey  
920 National Center  
Reston, VA 22092 (2 copies)

Mr. James F. Lewkowicz  
Dr. Delaine T. Reiter, Mrs. Jeanne M. McPhetres  
Earth Sciences Division (PL/GPE)  
Phillips Lab/Geophysics Directorate  
Hanscom AFB, MA 01731 (5 copies)

Dr. Don A. Linger, Dr. Michael Shore  
U.S. DNA  
6801 Telegraph Road  
Alexandria, VA 22310 (2 copies)

Dr. Robert P. Massé  
Denver Federal Center  
Box 25046, Mail Stop 967  
Denver, CO 80225

Office of the Secretary of Defense  
DDR&E  
Washington, DC 20330

Dr. Frank F. Pilote  
HQ AFTAC/TT  
1030 South Highway A1A  
Patrick AFB, FL 32925-6001

Phillips Laboratory / TL  
5 Wright Street  
Hanscom AFB, MA 01731

Phillips Laboratory  
PL/SUL  
3550 Aberdeen Avenue, SE  
Kirtland AFB, NM 87117 (2 copies)

Phillips Laboratory  
PL/XPG  
Hanscom AFB, MA 01731

Dr. Robert E. Reinke  
Field Command, DNA  
FCDNA/FCTTS  
1680 Texas Street, S.E.  
Kirtland AFB, NM 87117-6008

Secretary of the Air Force  
(SAFRD)  
Washington, DC 20330

Dr. Owen J. Sheaks  
Dr. William Roggenthen  
Mr. Alfred Lieberman  
Mr. Richard J. Morrow  
Ms. Mona Dreicer  
U.S. ACDA  
320 21st Street NW  
Washington, DC 20451 (5 copies)

Dr. Lawrence S. Turnbull, Jr.  
Dr. John R. Filson  
Katie Poley  
Sean H. Doran  
U.S. ACIS  
Washington, DC 20505 (4 copies)

Center for Verification Research  
Technical Library  
P.O. Box 1148  
8500 Cinder Bed Road  
Newington, VA 22122-9998

## OTHER RECIPIENTS

Dr. Don Albert  
Lt. Col. Dick Jardine  
U.S. ACRREL  
72 Lyme Road  
Hanover, NH 03755 (2 copies)

Dr. David M. Boore  
Dr. Leif G. Wennerberg  
Dr. Bernard A. Chouet  
U.S. Geological Survey  
345 Middlefield Road, MS 977  
Menlo Park, CA 94025 (3 copies)

Dr. Arthur Frankel  
U.S. Geological Survey  
Denver Federal Center  
Denver, CO 80225

Dr. Richard Lewis  
Earthquake Engineering & Geophysics  
U.S. Army Corps of Engineers  
P.O. Box 631  
Vicksburg, MS 39180

Dr. Ed McDonald  
Naval Research Laboratory  
4555 Overlook Avenue, SW  
Washington, DC 20375

Mr. James Anderson, Mr. Rick Perez  
Teledyne Brown Engineering  
2111 Wilson Boulevard, Suite 900  
Arlington, VA 22201-3058 (2 copies)

Prof. Charles B. Archambeau  
Prof. Danny J. Harvey, Dr. Anatoli L. Levshin  
University of Colorado, JSPC  
Campus Box 583  
Boulder, CO 80309 (3 copies)

Dr. Ralph J. Archuleta  
Dept. of Geological Sciences  
University of California at Santa Barbara  
Santa Barbara, CA 93102

Dr. Jonathan Berger, Dr. Frank Vernon  
Dr. Holly K. Given, Dr. Peter Davis  
IGPP, A-025  
Scripps Institute of Oceanography  
University of California, San Diego  
La Jolla, CA 92093 (4 copies)

Dr. G. A. Bollinger  
Dept. of Geological Sciences  
Virginia Polytechnic Institute  
21044 Derring Hall  
Blacksburg, VA 24061

Prof. Bruce A. Bolt  
Prof. Barbara Romanowicz  
Seismographic Station  
475 McCone Hall  
University of California  
Berkeley, CA 94720 (2 copies)

Prof. Jon F. Claerbout  
Dept. of Geophysics  
Stanford University  
Stanford, CA 94305

Prof. Robert W. Clayton  
Seismological Laboratory  
Division of Geological & Planetary Sciences  
California Institute of Technology  
Pasadena, CA 91125

Prof. Vernon F. Cormier  
Dept. of Geology & Geophysics  
University of Connecticut  
Storrs, CT 06269-2045

Prof. Paul M. Davis, Prof. John Vidale  
Dept. Earth & Space Sciences  
University of California (UCLA)  
Los Angeles, CA 90024 (2 copies)

Prof. Adam Dziewonski  
Prof. Göran Ekström  
Prof. James R. Rice  
Hoffman Laboratory  
Harvard University  
20 Oxford Street  
Cambridge, MA 02138 (3 copies)

Ronald W. Ewing  
Ewing Associates  
11535 Clara Barton Drive  
Fairfax Station, VA 22039

Prof. John Ferguson  
 Prof. George McMechan  
 Center for Lithospheric Studies  
 University of Texas at Dallas  
 P.O. Box 688  
 Richardson, TX 75083-0688 (2 copies)

Prof. Stanley Flatté  
 Applied Sciences Building  
 University of California  
 Santa Cruz, CA 95064

Dr. Alexander Florence, Dr. Stephen Miller  
 SRI International  
 333 Ravenswood Avenue  
 Menlo Park, CA 94025-3493 (2 copies)

Dr. Bengt Fornberg  
 Exxon Engineering & Research Company  
 Clinton Township, Route 22 East  
 Annandale, NJ 08801

Prof. Donald Forsyth  
 Dept. of Geological Sciences  
 Brown University  
 Providence, RI 02912

Dr. Roger Fritzel  
 Pacific Sierra Research  
 1401 Wilson Blvd., Suite 1100  
 Arlington, VA 22209

Dr. Ivan Henson  
 Multimax, Inc.  
 1290 Highway A1A, Suite 206  
 Satellite Beach, FL 32937

Dr. Kevin Hutchenson  
 ENSCO, Inc.  
 445 Pineda Court  
 Melbourne, FL 32940

Prof. Alan Kafka, Prof. John Ebel  
 Dept. of Geology & Geophysics  
 Boston College  
 Chestnut Hill, MA 02167 (2 copies)

Dr. Cyrus P. Knowles  
 JAYCOR  
 1608 Spring Hill Road  
 Vienna, VA 22182

Prof. Leon Knopoff  
 University of California  
 Institute of Geophysics & Planetary Physics  
 Los Angeles, CA 90024

Dr. Richard LaCoss  
 MIT-Lincoln Laboratory  
 M-200B  
 P.O. Box 73  
 Lexington, MA 02173-0073

Prof. Fred K. Lamb  
 University of Illinois  
 Dept. of Physics  
 1110 West Green Street  
 Urbana, IL 61801

Dr. James Lawson  
 Oklahoma Geological Survey  
 P.O. Box 8  
 Leonard, OK 74043

Prof. Alan R. Levander  
 Dept. of Geology & Geophysics  
 Rice University, MS 126  
 Houston, TX 77005

Dr. J. Michael McKisic  
 Tracor Applied Sciences, Inc.  
 1601 Research Boulevard  
 Rockville, MD 20850

Dr. George Mellman  
 Sierra Geophysics  
 11255 Kirkland Way  
 Kirkland, WA 98033

Prof. James Ni, Prof. Thomas Hearn  
 Dept. of Physics  
 New Mexico State University  
 Las Cruces, NM 88003 (2 copies)

Prof. Jeffrey Park  
 Dr. Jonathan Lees  
 Dept. of Geology & Geophysics  
 Yale University  
 P.O. Box 208109  
 New Haven, CT 06520 (2 copies)

Prof. Robert Phinney  
 Geological & Geophysical Sciences  
 Princeton University  
 Princeton, NJ 08544-0636

**Dr. Paul Pomeroy**  
Rondout Associates  
P.O. Box 224  
Stone Ridge, NY 12484

**Dr. Richard Sailor**  
TASC, Inc.  
55 Walkers Brook Drive  
Reading, MA 01867

**Prof. G. T. Schuster**  
Dept. of Geology & Geophysics  
University of Utah  
Salt Lake City, UT 84112

**Prof. R. H. Shumway**  
Division of Statistics  
University of California  
Davis, CA 95616

**Dr. Gregory E. van der Vink**  
IRIS, Inc.  
1616 North Fort Myer Drive, Suite 1050  
Arlington, VA 22209 (2 copies)

**Prof. Stewart W. Smith**  
**Prof. Stephen D. Malone**  
Geophysics AK-50  
University of Washington  
Seattle, WA 98195 (2 copies)

**Prof. Jeremiah Sullivan**  
University of Illinois at Urbana-Champaign  
Dept. of Physics  
1110 West Green Street  
Urbana, IL 61801

**Prof. Pradeep Talwani**  
Dept. of Geological Sciences  
University of South Carolina  
Columbia, SC 29208

**Prof. Leo T. Teng**  
University of Southern California  
University Park  
Los Angeles, CA 90089

**Dr. Karl F. Veith**  
EG&G  
2341 Jefferson Davis Highway, Suite 801  
Arlington, VA 22202

**Dr. William Wortman**  
Mission Research Corporation  
8560 Cinderbed Road, Suite 700  
Newington, VA 22122

**Prof. Francis T. Wu**  
Dept. of Geological Sciences  
State University of New York, Binghamton  
Vestal, NY 13901

## **FOREIGN RECIPIENTS**

Dr. V. V. Adushkin

Dr. I. O. Kitov

Inst. for Dynamics of Geospheres

Russian Academy of Science

Moscow, Russia (2 copies)

Dr. Peter Basham

Earth Physics Branch

Geological Survey of Canada

1 Observatory Crescent

Ottawa, Ontario, CANADA K1A 0Y3

Prof. Ari Ben-Menahem

Dept. of Applied Mathematics

Weizman Institute of Science

Rehovot, ISRAEL 951729

Dr. Michel Bouchon

I.R.I.G.M.-B.P. 68

38402 St. Martin D'Heres

Cedex, FRANCE

Dr. Michel Campillo

Observatoire de Grenoble

I.R.I.G.M.-B.P. 53

38041 Grenoble, FRANCE

Dr. Lawrence A. Drake

Observatorio San Calixto

Casilla 12656, La Paz, BOLIVIA

European-Mediterranean Seismological Centre

CSEM

c/o LPG

BP 12, 91680 Bruyeres-le-Chatel

FRANCE

Dr. Peter Firbas

Institute of Physics of the Earth

Masaryk University Brno

Jecna 29a

612 46 Brno, CZECH REPUBLIC

Prof. Hans-Peter Harjes

Institute for Geophysik

Ruhr University/Bochum

P.O. Box 102148

463 Bochum 1, GERMANY

Dr. Manfred Henger

Fed. Inst. for Geosci. & Nat'l Res.

Postfach 510153

D-3000 Hanover 51, GERMANY

Dr. Eystein Husebye

Inst. for Solid Earth Physics

University of Bergen

Allegation 40

N-5007 Bergen, NORWAY

David Jepsen

Nuclear Monitoring Section

Geology & Geophysics

Bureau of Mineral Resources

G.P.O. Box 378

Canberra, AUSTRALIA

Ms. Eva Jöhannesson

Senior Research Officer

National Defense Research Institute

P.O. Box 27322

S-102 54 Stockholm, SWEDEN

Prof. Brian L.N. Kennett

Research School of Earth Sciences

Institute of Advanced Studies

G.P.O. Box 4

Canberra 2601, AUSTRALIA

Dr. Peter Marshall

Dr. Alan Douglas

Ministry of Defense/Procurement Executive

Blacknest, Brimpton

Reading FG7-4RS

ENGLAND (2 copies)

Dr. Bernard Massinon

Dr. Pierre Mecheler

Societe Radiomana

27 rue Claude Bernard

75005 Paris, FRANCE (2 copies)

Prof. Keith Priestley

Dept. of Earth Sciences

Madingley Rise, Madingley Road

University of Cambridge

Cambridge CB3 0EZ, ENGLAND

**Dr. Frode Ringdal**  
**Dr. Svein Mykkeltveit**  
**NTNF/NORSAR**  
**P.O. Box 51**  
**N-2007 Kjeller, NORWAY (2 copies)**

**Dr. Jorg Schlittenhardt**  
**Federal Inst. for Geosciences &**  
**Natural Resources**  
**Stilleweg 2, D-3000 Hannover 51**  
**GERMANY**

**Dr. A. Shapira**  
**Seismology Division**  
**Inst. for Petroleum Research & Geophysics**  
**Holon, ISRAEL**

**Dr. C. Srinivasan**  
**Seismology Section**  
**National Inst. of Rock Mechanics**  
**New Delhi, INDIA**

**Dr. Tuncay Taymaz**  
**Istanbul Technical University**  
**Dept. of Geophysical Engineering**  
**Maslak-80626, Istanbul, TURKEY**